Mechanistic Underpinnings of Efficient Chemical-to-Electrical Energy Interconversion in Bipolar Membranes

by

Wei Lun Toh

BSc Chemistry, Imperial College London, 2017

Submitted to the Department of Chemistry

in Partial Fulfillment of the Requirements for the Degree of

DOCTOR OF PHILOSOPHY IN CHEMISTRY

at the

MASSACHUSETTS INSTITUTE OF TECHNOLOGY

September 2023

Signature of Author: ………………………………………………………….……………………

Department of Chemistry
August 31, 2023

Certified by: ……………………………………………………..…………………………..…...

Yogesh Surendranath
Professor of Chemistry
Thesis Supervisor

Accepted by: ……………………………………..……………..………………………………..

Adam Willard
Professor of Chemistry
Graduate Officer

This doctoral thesis has been examined by a committee of the Department of Chemistry as follows.

Professor Mircea Dincă …………………………..……………………………………...…

W. M. Keck Professor of Energy

Thesis Committee Chair

Professor Yogesh Surendranath ………………………………………….…………………..

Professor of Chemistry

Thesis Supervisor

Professor Yuriy Román …………………………………….…………………...……………

Robert T. Haslam (1911) Professor of Chemical Engineering and Professor of Chemistry

Thesis Committee Member

Mechanistic Underpinnings of Efficient Chemical-to-Electrical Energy Interconversion in Bipolar Membranes

by

Wei Lun Toh

Submitted to the Department of Chemistry on August 31, 2023
in Partial Fulfillment of the Requirements for the Degree of
Doctor of Philosophy in Chemistry

Abstract

The efficient operation of all electrochemical devices requires an understanding of how electrical and chemical energy can be freely interconverted with minimal losses. One way in which chemical energy can be stored is in the form of ionic gradients. Bipolar membranes (BPMs) are an emerging technology that have the unique ability to convert the chemical potential gradient within a pH gradient into an electric potential gradient in the form of a membrane voltage (*forward bias*) and vice-versa (*reverse bias*). This unprecedented functionality has been utilized to design and construct a suite of electrochemical devices such as water and CO_2 electrolyzers, fuel cells, redox flow batteries, and electrodialyzers that operate with a pH gradient. This in turn has allowed the independent optimization of cathode and anode catalysts, and unlocked new operational modalities such as in operando neutralization for product recovery in CO_2 electrolysis or the extension of the operating voltage window for redox flow batteries, enabling higher energy and power densities. However, despite their utility, the fundamental processes that control the efficiency of chemical-to-electrical energy interconversion in BPMs remain poorly understood, both under open-circuit conditions and under polarization. Hence, the overarching goal of the work in this thesis is to identify these processes and unravel their mechanistic origins in order to develop remediation strategies.

In **Chapter 2**, we describe how *bipolar pairing* interactions can arise from the intimate association of fixed charges at the bipolar junction when one of the phases constituting the junction is mobile, leading to attenuation of the membrane voltage and severe overpotential penalties in reverse bias. We find that the use of layered materials as interfacial additives can inhibit these detrimental interactions and significantly improve electrochemical performance.

In **Chapter 3**, we reveal that BPMs are subject to a process whereby the crossover of coions is coupled to the parasitic neutralization at the bipolar interface, which we term *neutralization shortcircuiting*. We find that for weak electrolyte-containing BPMs, this process buffers the bipolar interface due to the production of the conjugate acid/base, levelling the membrane voltage to a value dictated by the proton affinity of the conjugate acid/base. In addition, this neutralization product can undergo dissociation under reverse bias, reducing the Faradaic efficiency for the water dissociation reaction.

Finally, in **Chapter 4,** we discover that, for BPM cells containing mixtures of strong and weak electrolytes, the weak electrolyte can impose a significant neutralization overpotential on the strong electrolyte in voltage regions where the former is unreactive. This occurs as the weak electrolyte imposes an *ionic blockade* by competing for the same fixed-charge sites in the membrane as the strong electrolyte, inhibiting the transport of the latter. We report on the use of advecting polyelectrolytes and thinner ion exchange membranes as materials strategies for overcoming this transport inhibition, and explain its implications for CO_2 electrolyzers and galvanic cells utilizing forward bias BPMs.

Thesis Supervisor: Yogesh Surendranath

Title: Professor of Chemistry

Respective Contributions

This thesis contains work that was performed collaboratively with other researchers at the Massachusetts Institute of Technology.

In **Chapter 2**, the project was conceptualized by Yogesh Surendranath and the author. An Chu assisted in collection of the electrochemical data. The data was analyzed by the author. The manuscript was written by Yogesh Surendranath and the author with input from An Chu.

In **Chapter 3**, the project was conceptualized by Yogesh Surendranath, Hieu Dinh, and the author. Hieu Dinh, An Chu, and the author collected the electrochemical data. The author performed solution characterization via NMR and ICP-OES. The data was analyzed by Hieu Dinh and the author. The manuscript was written by Yogesh Surendranath and the author, and edited by Yogesh Surendranath, Hieu Dinh, and the author with input from all authors.

In **Chapter 4**, the project was conceptualized by Yogesh Surendranath, Hieu Dinh, and the author. Hieu Dinh, An Chu, and the author collected the electrochemical data. Ethan Sauvé designed and performed the synthesis of polyelectrolytes. The author performed solution characterization via NMR. The data was analyzed by Hieu Dinh and the author. The manuscript was written by Yogesh Surendranath and the author, and edited by Yogesh Surendranath, Hieu Dinh, and the author with input from all authors.

To my family

Table of Contents

List of Figures

List of Tables

List of Abbreviations

AEM	anion exchange membrane
a_i	activity of species i
BHCl	chloride salt of a weak acid BH^+
BPM	bipolar membrane
CEM	cation exchange membrane
c_i	solution concentration of species i
CO_2RR	CO_2 reduction reaction
δ	diffusion boundary layer thickness
D_i	diffusion coefficient of species i
h-BN	hexagonal boron nitride
E_{Don}	Donnan potential at a membrane-solution interface
FE	Faradaic efficiency
GdnHCl	guanidinium chloride
GO	graphene oxide
ICP-OES	inductively coupled plasma-optical emission spectroscopy
IEM	ion exchange membrane
ImHCl	imidazolium chloride
j	current density
j_{coion}	current density for coion crossover under reverse bias
j_{HADR}	current density for weak acid (HA) dissociation under reverse bias
$j_{l\mathrm{im}}$	limiting current density

KA	potassium salt of a weak base A^-
M_w	weight-average molecular weight
N_i	flux (diffusive or migration) of species i
$PDADMA^+$	poly(diallyldimethylammonium)
PSS^-	poly(4-styrenesulfonate)
$PVBTMA^+$	poly((p-vinylbenzyl)trimethylammonium)
PyHCl	pyridinium chloride
SEM-EDS	scanning electron microscopy-energy dispersive spectroscopy
$V_{\Delta\mathrm{pH}}$	theoretical membrane voltage based on solution pH difference
V_J	bipolar junction voltage
V_mem	membrane voltage
WDR	water dissociation reaction

Chapter 1

Introduction

1.1 Chemical Energy Can Be Stored in Ion Gradients

Efficient interconversion between chemical and electrical energy lies at the heart of all electrochemical devices. In most electrolyzers and galvanic cells, this interconversion is mediated by the breakage and formation of chemical bonds in electron transfer processes occurring at the electrode-solution interface as the potential of the electrode is modulated (**Figure 1.1(a)**).[1] However, electrical energy can also be transduced into chemical energy and vice-versa via the formation and levelling of ionic gradients, since ions are charged species that can respond to an applied electric field.[2] Examples of this type of energy conversion include electrodialyzers that drive the selective separation of ionic constituents in an electrolyte solution, which have found application in desalination or the production of caustic solutions, such as in the chlor-alkali process (**Figure 1.1(b)**). Hence, improved understanding and control over processes that efficiently interconvert electrical energy and chemical energy stored in ionic gradients is essential to enabling a wide range of next-generation electrochemical technologies.

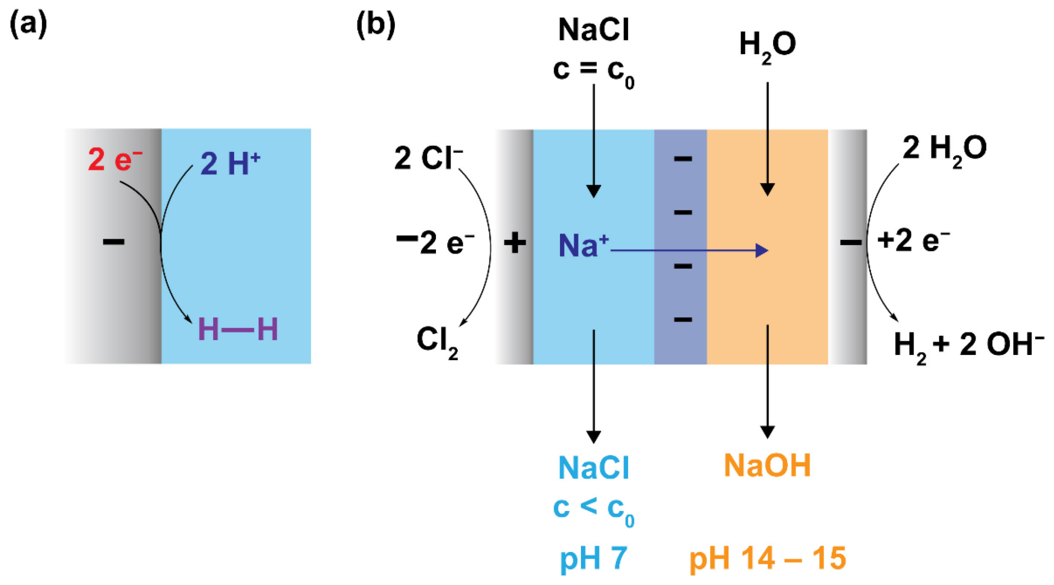

Figure 1.1. Interconversion of electric and chemical energy in electrochemical devices. **(a)** The hydrogen evolution reaction (HER) occurring at the cathode of a water electrolyzer, storing chemical energy in the H-H bond of H_2. **(b)** The chlor-alkali process, whereby the use of a cation exchange membrane (dark blue) that permits only Na^+ transport leads to an ionic gradient across the membrane and enables NaOH to be produced in the catholyte (yellow). Here, chemical energy is stored in the pH gradient across the membrane.

1.2 Structure of Bipolar Membranes

Amongst the slew of electrolyte ions commonly employed, protonic gradients are of particular technological interest and importance since many key electrochemical transformations underpinning our clean energy transition are proton-coupled electron transfer reactions (e.g., the hydrogen evolution reaction (HER) and the oxygen evolution reaction (OER) in water electrolysis). To this end, bipolar membranes (BPMs) have emerged as an exciting electrochemical technology that is able to drive efficient interconversion between protonic and electric potential gradients in solution. This capability originates from their unique structure: BPMs consist of two ion exchange membranes (IEMs), a cation exchange membrane (CEM) and an anion exchange membrane (AEM), laminated onto each other (**Figure 1.2**). Typical structures for the CEM are polymers bearing sulfonate and perfluorosulfonate (trademark name Nafion™, Aquivion®) groups, whereas typical structures for the AEM include quaternary ammonium groups, such as tetraalkylammonium (Fumasep™, Selemion™ [3]), substituted imidazolium (Sustainion™,[4] Aemion™ [5]), and substituted piperidinium (PiperION™ [6]) moieties; and quaternary phosphonium[7] groups (**Figure 1.2**). The fixed polymeric anionic charges within CEMs and cationic charges within AEMs lead to the selective transport of cations and anions, respectively.

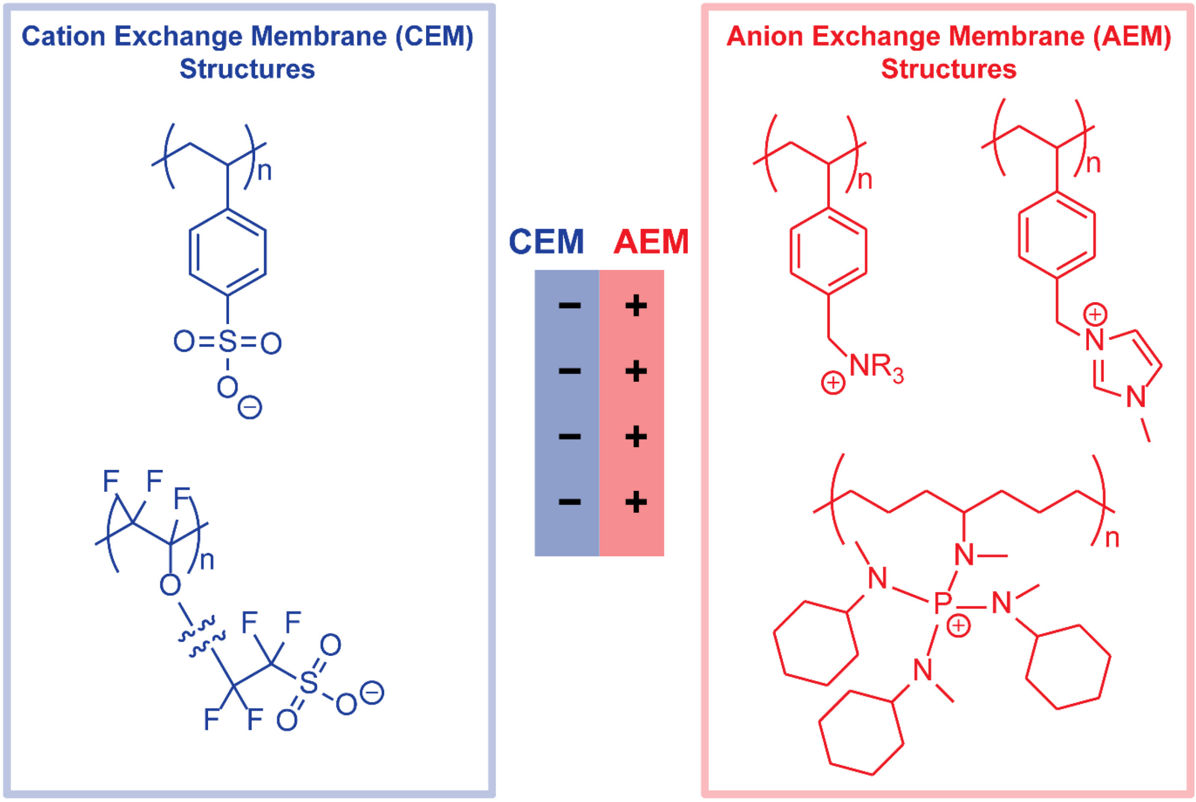

Figure 1.2. A bipolar membrane (BPM) consists of a cation exchange membrane (CEM) laminated onto an anion exchange membrane (AEM). Example structures for CEMs and AEMs are depicted. Note that many of structures are copolymers but only the main polymer chains containing the charged groups are shown here.

1.3 Thermochemistry of the Membrane Voltage in Bipolar Membranes

When exchanged with acid and base, a BPM develops an electric potential drop across its bipolar junction. This arises from the electrochemical equilibrium governing the motion of ions at the bipolar junction.[8] Briefly, H^+ in the acid compartment and OH^- in the base compartment exchange with the Na^+ and Cl^- typically present in commercially sourced CEMs and AEMs. The H^+ and OH^- ions proximal to the bipolar junction within the CEM and AEM, respectively, then undergo neutralization, producing neutral H_2O molecules. This leaves behind excess fixed polymeric charges at the bipolar junction, giving rise to the *bipolar junction voltage*, V_J (**Figure 1.3**). Due to the gradient in the chemical potential of the proton in the CEM and AEM phases, there is a driving force for the diffusion of H^+ ions into the AEM to undergo further neutralization (or, correspondingly, the diffusion of OH^- ions into the CEM). However, the electric field at the bipolar junction induces a migration flux for H^+ of the same magnitude as the diffusive flux but in the opposite direction, and electrostatically repels H^+ from influx into the AEM. Hence, the magnitude of the potential drop corresponds to the proton activity difference between the CEM and AEM is given by **Equation 1.1**.

$$V_\mathrm{J} = -59\ \mathrm{mV} \cdot \log_{10}\left(\frac{\mathrm{a}_{\mathrm{H}^+}^{\mathrm{CEM}}}{\mathrm{a}_{\mathrm{H}^+}^{\mathrm{AEM}}}\right) \qquad \textbf{Equation 1.1}$$

where $\mathrm{a}_{\mathrm{H}^+}^{\mathrm{CEM}}$ and $\mathrm{a}_{\mathrm{H}^+}^{\mathrm{AEM}}$ are the activities of H^+ in the CEM and AEM, respectively. In addition to the potential drop at the bipolar junction, V_J, there are also *Donnan potentials*, E_{Don}, occurring at the membrane-solution interfaces (**Figure 1.3**). Donnan potentials arise when an interface is permeable to either only cations or anions, excluding ions of the opposite charge.[2] Here, the

Donnan potentials are related to the difference in the activity of the mobile ion in the IEM and in solution. $E_{\mathrm{Don\ (Acid|CEM)}}$ and $E_{\mathrm{Don\ (AEM|Base)}}$ are, therefore, given by **Equations 1.2** and **1.3**.

$$E_{\mathrm{Don\ (Acid|CEM)}} = -59\ \mathrm{mV} \cdot \log_{10}\left(\frac{\mathrm{a}_{\mathrm{H^+}}^{\mathrm{acid}}}{\mathrm{a}_{\mathrm{H^+}}^{\mathrm{CEM}}}\right)$$ **Equation 1.2**

$$E_{\mathrm{Don\ (AEM|Base)}} = -59\ \mathrm{mV} \cdot \log_{10}\left(\frac{\mathrm{a}_{\mathrm{H^+}}^{\mathrm{AEM}}}{\mathrm{a}_{\mathrm{H^+}}^{\mathrm{Base}}}\right)$$ **Equation 1.3**

Hence, the overall measurable *membrane voltage* across the BPM, V_{mem}, is given by

$$V_{\mathrm{mem}} = V_{\mathrm{J}} + E_{\mathrm{Don\ (Acid|CEM)}} + E_{\mathrm{Don\ (AEM|Base)}}$$ **Equation 1.4**

$$V_{\mathrm{mem}} = -59\ \mathrm{mV} \cdot \log_{10}\left(\frac{\mathrm{a}_{\mathrm{H^+}}^{\mathrm{acid}}}{\mathrm{a}_{\mathrm{H^+}}^{\mathrm{base}}}\right)$$

$$V_{\mathrm{mem}} = -59\ \mathrm{mV} \cdot (\mathrm{pH_{Base}} - \mathrm{pH_{Acid}})$$

$$V_{\mathrm{mem}} = -59\ \mathrm{mV} \cdot \Delta\mathrm{pH}$$ **Equation 1.5**

where we assume that activities are equal to concentrations. As shown above, V_{mem} is determined only by the difference in pH between the two solutions, and not between the membranes. Consequently, our use of 1 M electrolytes throughout most of the work in this thesis sets the measurements to a standard state reference frame. Finally, although the overall V_{mem} measurement includes two E_{Don} terms, we emphasize that, since we typically employ 1 M electrolytes, which is similar to the fixed charge concentration within the hydrated IEMs, the Donnan potentials are negligible (~0 mV) and not expected to change significantly between different electrolyte conditions or under polarization. Hence, any changes in V_{mem} reflect only changes in V_{J}, allowing us to single out and investigate the electrochemistry of the bipolar junction. This is addressed in more detail in **Supplementary Discussion 3.1** in **Chapter 3**.

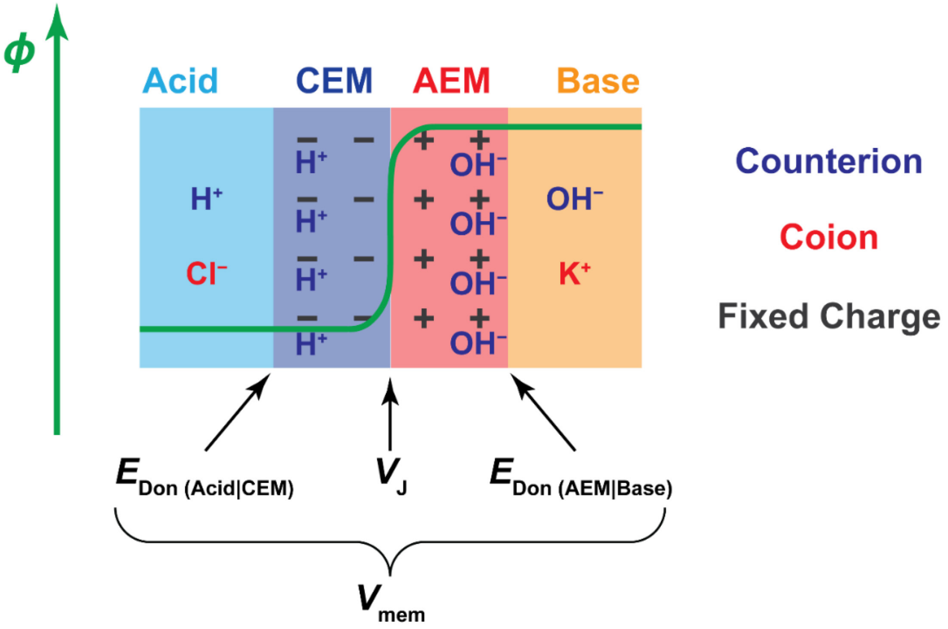

Figure 1.3. Types of ionic charge and potential drops across a BPM. Here, the concentrations of the acid and base solutions are assumed to closely match those of the fixed charges within the IEMs, leading to negligible Donnan potentials.

In reality, the value predicted by **Equation 1.5** often deviates greatly from the open-circuit V_{mem} experimentally measured.[9] In cases where weak electrolytes (acids with $\mathrm{p}K_{\mathrm{a}} > \mathrm{p}K_{\mathrm{a}}\ (\mathrm{H_3O^+}) = 0$; bases with $\mathrm{p}K_{\mathrm{a}} < \mathrm{p}K_{\mathrm{a}}\ (\mathrm{H_2O}) = 14$) are used as buffering constituents, the open-circuit V_{mem} has been found to correlate with the $\mathrm{p}K_{\mathrm{a}}$ of the weak electrolyte present.[9,10] Even in cases when only strong acids and bases were used, deviations in the open-circuit V_{mem} from the prediction by **Equation 1.5** have been observed to persist.[11,12] Since the open-circuit V_{mem} is a direct indicator of how efficiently the pH gradient is being transduced into the electric potential drop at the bipolar junction, these deviations are diagnostic of phenomena that erode the transduction efficiency. We identify and investigate these phenomena in **Chapters 2** and **3**, and explain how these phenomena that exist at open-circuit can also detrimentally affect reverse bias polarization behavior.

1.4 Two Distinct Modes of Operation: Reverse and Forward Bias

Due to the CEM and AEM portions of the BPM being permselective for ions of a particular charge (cationic or anionic), the current-voltage profile for ionic transport in BPMs is analogous to that for electron (and hole) transport in p-n junctions in the semiconductor literature, exhibiting the property of *current rectification*.[13–15] In other words, the voltages required to drive the passage of current in one direction (*reverse bias*) are significantly larger than in the other (*forward bias*), leading to an asymmetric current-voltage profile.

Reverse bias involves applying an external electric field such that counterions within the CEM and AEM (typically $\mathrm{H^+}$ and $\mathrm{OH^-}$, respectively) are driven out of the BPM (**Figure 1.4(a)**). This results in two regimes of operation in the current-voltage curve. Initially, due to the depletion of counterions from the BPM, the crossover of coions (e.g. Cl^- and K^+) occurs and carries the majority of the current through the BPM (**Figure 1.4(c)**, region B). Since the coions are electrostatically repelled by the IEMs, this is an energetically unfavorable process, and hence the reverse bias currents at low overpotentials due to coion crossover are typically low. As the overpotential is raised, the onset of the water dissociation reaction (WDR) occurs once V_{mem} is driven past the thermochemical voltage for WDR, V°_{WDR}, of −830 mV when 1 M electrolytes are used in the acid and base compartments (**Figure 1.4(a)**; **(c)**, region C; **Equation 1.6**).[8,16–18]

$$\mathrm{H_2O} \rightarrow \mathrm{H^+} + \mathrm{OH^-} \qquad \textbf{Equation 1.6}$$

Here, water molecules undergo ionic dissociation at rates enhanced by the electric field within the bipolar junction in a phenomenon known as the *Second Wien Effect*.[14,19] The rate constants of the WDR and the water formation reaction (WFR) are related by the auto-ionization constant of water, i.e.,

$$K_{\mathrm{w}} = \frac{k_{\mathrm{WDR}}}{k_{\mathrm{WFR}}} \qquad \textbf{Equation 1.7}$$

k_{WDR} is known to be as slow as $2\ x\ 10^{-5}$ s^{-1} in bulk solvent, whereas the measured value of $\sim 10^{11}$ M^{-1} s^{-1} for k_{WFR} is thought to be diffusion-limited.[14] Upon polarization, the rate of the WDR gains an exponential dependence on the bipolar junction voltage, leading to a significant increase in the reverse bias currents observed as H^+ and OH^- counterions are produced from the solvent water at the bipolar junction itself. A catalyst layer is often also included between the CEM and the AEM to enhance WDR kinetics. Catalysts that have been shown to be active include metal oxides,[20,21] graphene oxide,[22] and conductive carbons.[21] Here, the catalyst is thought to either have a role in sharpening the interfacial potential drop to augment the electric field enhancement,[21,23] or in contributing surface sites with an accessible pK_a that can protonate or deprotonate water molecules, contributing to a secondary catalysis effect.[24,25] The WDR is the productive process that reverse bias BPMs are conventionally intended to drive, and coion crossover currents are typically regarded as parasitic shunt currents that reduce the efficiency for the WDR. By driving the continuous formation of H^+ and OH^- from H_2O, a reverse bias BPM transduces electric potential gradients in the form of the external field into the chemical potential gradient in the resulting pH gradient.

On the other hand. in forward bias, the polarity of the applied electric field is flipped, such that the counterions H^+ and OH^- are driven into the CEM and AEM, respectively, to undergo a recombination reaction at the bipolar junction, leading to the production of water (**Figure 1.4(b); Equation 1.7**).

$$\mathrm{H^+ + OH^- \rightarrow\ H_2O} \qquad \textbf{Equation 1.7}$$

Since this is a thermodynamically favorable process, the current tends to take off quickly upon applying an overpotential away from the open-circuit voltage. In this mode of operation, the BPM transduces the chemical potential gradient in the form of the pH gradient into an electric potential gradient. Since the polarity of the bipolar junction voltage opposes the polarity of the overall cell, a forward bias BPM is hence able to perform electrical work by offsetting the overall cell voltage across the driving electrodes.

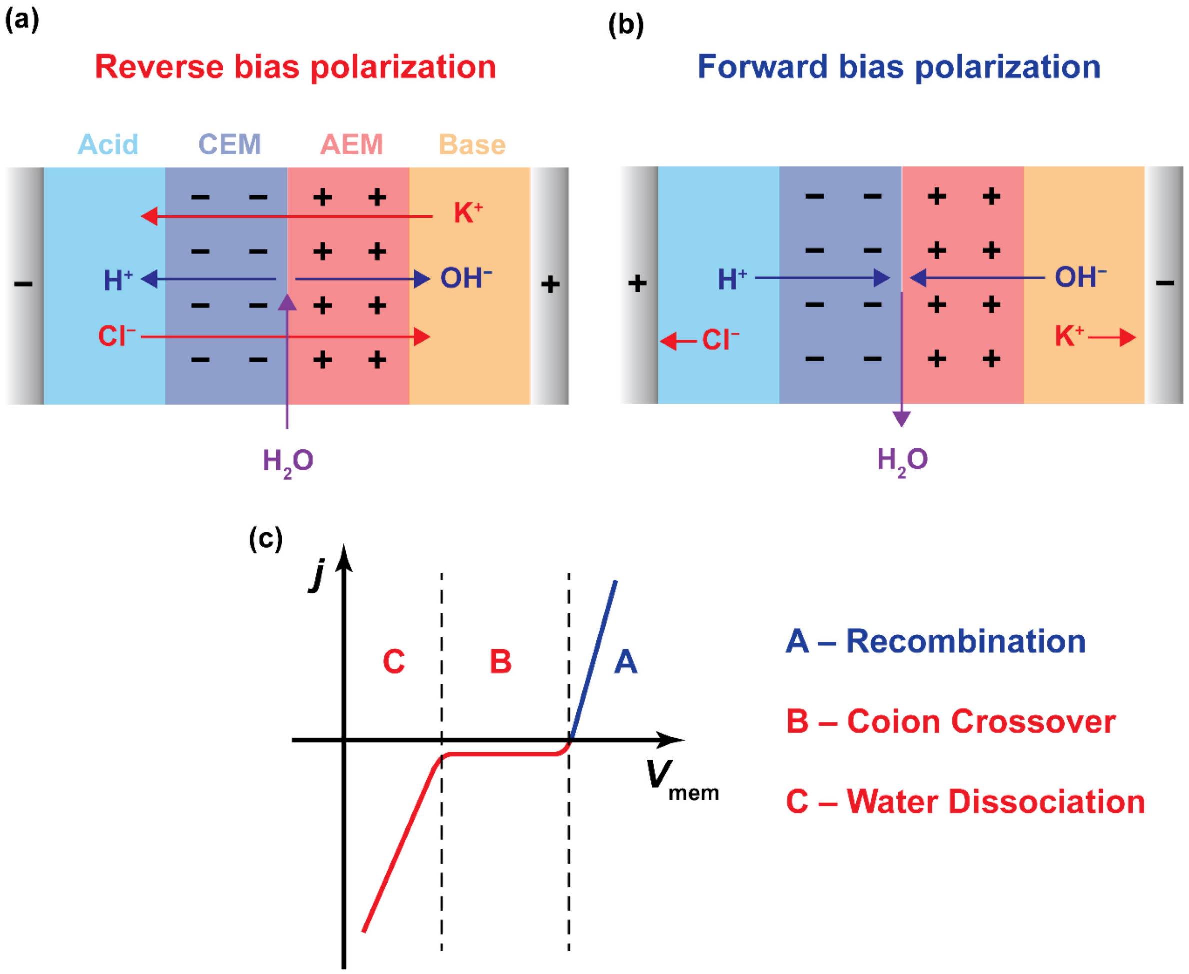

Figure 1.4. Directions of ion motion for counter- and coions when BPMs are operated in (a) reverse and (b) forward bias. (c) Example polarization curve for a BPM showing the forward bias region (blue) and the reverse bias regions (red).

Operation of BPMs in both reverse and forward bias modes has been demonstrated in a wide range of electrochemical devices. Reverse bias BPMs have been more extensively studied due to interest in pairing them with water electrolyzers to enable the use of base-compatible non-precious metal OER catalysts at the anode.[20,26–30] Other emerging applications include CO_2

electrolyzers for local CO_2 regeneration near the cathode[31–38] and bipolar membrane electrodialysis (BPMED) cells.[39,40] Forward bias is an emerging mode of operation and have been studied to a lesser extent as forward bias applications are impeded by the materials challenge of preventing membrane ballooning and delamination as water and other neutralization products (e.g. CO_2) are formed during operation.[35,41,42] Notwithstanding, forward bias BPMs have been incorporated into redox flow batteries exploiting the acid-base recombination to attain higher operating cell voltages.[43–45] Water formation from the acid-base recombination reaction in forward bias BPMS has also been exploited to ensure membrane hydration in self-humidifying fuel cells.[8,46] Other niche applications have been explored in the CO_2 electrolyzer space, and include protonating (bi)carbonates to prevent CO_2 crossover to the anode,[47–49] and performing chemical separation of liquid products in operando.[50,51] Common to many of the abovementioned examples is the presence of complex multi-species electrolyte mixtures, and yet the impact of these mixtures on the forward bias polarization behavior of BPMs remains largely unexplored. This knowledge gap is addressed in detail in **Chapter 4**. As the above examples illustrated, the ability of BPMs to control ionic speciation in the electrolyte enables them to play multifaceted roles in a plethora of electrochemical technologies.

1.5 Layout of the Thesis

Despite the potential utility of BPMs in different classes of electrochemical devices, there is a paucity of understanding surrounding the mechanistic factors that control or undermine efficient transduction of chemical potential gradients into electric potential gradients across the bipolar interface, both at open-circuit and under polarization. An incomplete understanding of the factors that influence the efficiency of energy transduction in BPMs bottlenecks the development and implementation of mature BPM-incorporating electrochemical devices.

Hence, this thesis aims to address this knowledge gap by identifying and examining the mechanistic factors that control the efficiency of chemical-to-electrical energy transduction in BPMs. This is accomplished through complementary approaches such as investigating electrolyte- and membrane-based structure-function-property relationships; comprehensively tracking the fate of coions, counterions, and neutralization products; and applying the theory of electrochemical transport phenomena to interpret complex polarization curves.

We begin by identifying and parsing the factors that influence chemical-to-electrical transduction in BPMs even under open-circuit conditions in **Chapters 2** and **3**, and follow up by studying how these factors impact the polarization behavior in reverse bias.

In **Chapter 2**, we uncover the existence of hitherto unknown *bipolar pairing* effects that can occur when one of the phases constituting the bipolar junction has mobile fixed charges that can pair with fixed charges of the opposite charge. This nonideal behavior leads to charge quenching and V_{mem} suppression, but also significantly worsened overpotentials in reverse bias. However, we reveal that the use of layered interlayer materials is a facile and effective strategy for overcoming this inhibition.

In **Chapter 3**, we examine the effect of using weak electrolytes (e.g. OAc^- in place of OH^-) in BPM cells, and show that the parasitic formation of the conjugate acid/base (e.g. AcOH) via coupling to the coion leakage current can occur at open circuit, in an aggregate process we term *neutralization short-circuiting*. This phenomenon can severely attenuate the V_{mem} away from the thermochemical value based on solution pH differences (**Equation 1.5**) by buffering the bipolar interface. Under polarization, the conjugate acid/base formed at open circuit can also severely attenuate the efficiency for the WDR under reverse bias by contributing parasitic ionization current.

Finally, in **Chapter 4**, we investigate the efficiency losses embedded in the operation of a BPM under forward bias polarization. We perform a detailed study of how the presence of mixed electrolytes (e.g. OH^- mixed with CO_3^{2-}) affects the forward bias polarization behavior of BPMs. Here, we find that when mixed with strong electrolytes, weak electrolytes can impose a substantial transport inhibition on strong electrolytes in the membrane by competing for the same fixed charge sites and taking up sites as inert spectator ions. We term this phenomenon an *ionic blockade*, and show that it greatly limits the V_{mem} that can be harnessed from the pH gradient across the BPM to do electrical work. We detail two materials strategies for mitigating this inhibition, and discuss the implications of this phenomenon on forward bias BPM device archetypes such as CO_2 electrolyzers and redox flow batteries.

In summary, through systematic and detailed mechanistic studies, this thesis aims to further understanding of chemical-to-electrical energy interconversion in BPMs to enable the design of more efficient BPMs and BPM-incorporating devices. This is in the hopes of contributing to accelerating the implementation of next-generation BPM-incorporating electrochemical devices to support our critical clean energy goals.

1.6 Concluding Remarks

We believe that the work in this thesis elucidates a number of experimental approaches and heuristics that will be useful for making assessments about the efficiency of BPM operation, providing guiding principles for further mechanistic investigations into the rich electrochemistry of BPMs. Beyond that, we note that a number of common threads have emerged in our conclusions to the various studies.

First, our studies have collectively and definitively pointed to the need for more selective membranes. However, specifications for the type of selectivity required vary based on the intended application. For example, BPMs with improved coion rejection would be subject to a lower degree of V_{mem} depolarization by minimizing the effect of coion pairing for cells containing strong electrolytes and minimizing the effect of interfacial buffering for cells containing weak electrolytes. This would reduce the overpotentials for reverse bias BPMs driving the WDR, as well as forward bias BPMs operating to harness the pH gradient as electrical work. In addition, these BPMs would also be subject to a lower degree of efficiency losses due to parasitic processes under reverse bias polarization such as coion crossover and buffer ionization reducing the Faradaic efficiency for the WDR. On the other hand, BPMs with improved chemoselectivity for a particular type of counterion would be beneficial for forward bias BPMs operating with mixed electrolytes. By favoring the transport of the strong electrolyte ion, such BPMs could overcome the transport inhibition imposed by unreactive weak electrolyte ions, dramatically raising the limiting current and minimizing V_{mem} losses under high current density operation.[35]

Second, based on our findings on the importance of being able to manipulate speciation near the bipolar interface and application-dependent mechanical property requirements, we also anticipate that new BPM structural archetypes will emerge. Conventional membrane-membrane interfaces, while having been shown to be effective for moderately high current density reverse bias operation (~100 – 200 mA cm^{-2}), face limitations in water transport at very high current densities (>500 mA cm^{-2}),[10,30] as well as in the management of neutralization products formed in operando when operated in forward bias.[35] Our studies in **Chapter 4** demonstrated a novel method to construct functional bipolar interfaces through the use of a polyelectrolyte in place of one of the membranes. This enabled advection near the bipolar interface to affect the transport of reactant ions, but also produced a liquid-membrane interface that was not susceptible to delamination issues. We expect that innovation in methods of constructing bipolar interfaces will result in improved control over near-interfacial transport profiles for reactant and product management, more mechanically robust systems, and possibly even as-yet unknown functionalities such as the introduction of reactants through the bipolar interface in an orthogonal direction from ion current flow.

Looking ahead, the design of next-generation bipolar membranes and interfaces that meet the needs of existing and future electrochemical devices will require an interdisciplinary approach, whereby synthetic polymer chemists iterating on membrane properties work hand-in-hand with electrochemical engineers characterizing membrane electrochemistry and constructing electrochemical cells. As I've become thoroughly familiar with on this PhD journey, the unique capability of BPMs to rectify ionic currents endows it with tremendous potential for revolutionizing the ways in which we design and utilize electrochemical devices. I am excited to see what the future holds for this fascinating technology.

1.5 References

(1) Tributsch, H.; Pohlmann, L. Electron Transfer: Classical Approaches and New Frontiers. *Science.* **1998**, *279* (5358), 1891–1895.

(2) Kontturi, K.; Murtomäki, L.; Manzanares, J. A. *Ionic Transport Processes*; Oxford University Press, 2008; Vol. 9780199533.

(3) Giffin, G. A.; Lavina, S.; Pace, G.; Di Noto, V. Interplay between the Structure and Relaxations in Selemion AMV Hydroxide Conducting Membranes for AEMFC Applications. *J. Phys. Chem. C* **2012**, *116* (45), 23965–23973.

(4) Kutz, R. B.; Chen, Q.; Yang, H.; Sajjad, S. D.; Liu, Z.; Masel, I. R. Sustainion Imidazolium-Functionalized Polymers for Carbon Dioxide Electrolysis. *Energy Technol.* **2017**, *5* (6), 929–936.

(5) Thomas, O. D.; Soo, K. J. W. Y.; Peckham, T. J.; Kulkarni, M. P.; Holdcroft, S. A Stable Hydroxide-Conducting Polymer. *J. Am. Chem. Soc.* **2012**, *134* (26), 10753–10756.

(6) Wang, J.; Zhao, Y.; Setzler, B. P.; Rojas-Carbonell, S.; Ben Yehuda, C.; Amel, A.; Page, M.; Wang, L.; Hu, K.; Shi, L.; Gottesfeld, S.; Xu, B.; Yan, Y. Poly(Aryl Piperidinium) Membranes and Ionomers for Hydroxide Exchange Membrane Fuel Cells. *Nat. Energy* **2019**, *4* (5), 392–398.

(7) Noonan, K. J. T.; Hugar, K. M.; Kostalik, H. A.; Lobkovsky, E. B.; Abruña, H. D.; Coates, G. W. Phosphonium-Functionalized Polyethylene: A New Class of Base-Stable Alkaline Anion Exchange Membranes. *J. Am. Chem. Soc.* **2012**, *134* (44), 18161–18164.

(8) Ünlü, M.; Zhou, J.; Kohl, P. A. Hybrid Anion and Proton Exchange Membrane Fuel Cells. *J. Phys. Chem. C* **2009**, *113* (26), 11416–11423.

(9) Vermaas, D. A.; Wiegman, S.; Nagaki, T.; Smith, W. A. Ion Transport Mechanisms in Bipolar Membranes for (Photo)Electrochemical Water Splitting. *Sustain. Energy Fuels* **2018**, *2* (9), 2006–2015.

(10) Bui, J. C.; Digdaya, I.; Xiang, C.; Bell, A. T.; Weber, A. Z. Understanding Multi-Ion Transport Mechanisms in Bipolar Membranes. *ACS Appl. Mater. Interfaces* **2020**, *12* (47), 52509–52526.

(11) Hohenadel, A.; Powers, D.; Wycisk, R.; Adamski, M.; Pintauro, P.; Holdcroft, S. Electrochemical Characterization of Hydrocarbon Bipolar Membranes with Varying Junction Morphology. *ACS Appl. Energy Mater.* **2019**, *2* (9), 6817–6824.

(12) Al-Dhubhani, E.; Post, J. W.; Duisembiyev, M.; Tedesco, M.; Saakes, M. Understanding the Impact of the Three-Dimensional Junction Thickness of Electrospun Bipolar Membranes on Electrochemical Performance. *ACS Appl. Polym. Mater.* **2023**, *5* (4), 2533–2541.

(13) Lovrecek, B.; Despic, A.; Bockris, J. O. M. Electrolytic Junctions with Rectifying Properties. *J. Phys. Chem.* **1959**, *63* (5), 750–751.

(14) Giesbrecht, P. K.; Freund, M. S. Recent Advances in Bipolar Membrane Design and Applications. *Chem. Mater.* **2020**, *32* (19), 8060–8090.

(15) Pärnamäe, R.; Mareev, S.; Nikonenko, V.; Melnikov, S.; Sheldeshov, N.; Zabolotskii, V.; Hamelers, H. V. M.; Tedesco, M. Bipolar Membranes: A Review on Principles, Latest Developments, and Applications. *J. Memb. Sci.* **2021**, *617*, 118538.

(16) Grew, K. N.; McClure, J. P.; Chu, D.; Kohl, P. A.; Ahlfield, J. M. Understanding Transport at the Acid-Alkaline Interface of Bipolar Membranes. *J. Electrochem. Soc.* **2016**, *163* (14), F1572–F1587.

(17) Grew, K. N.; Chiu, W. K. S. Stability & Kinetics of the Bipolar Membrane Interface: Implications for Electrochemical Technologies. *J. Electrochem. Soc.* **2020**, *167* (16), 164513.

(18) Kole, S.; Venugopalan, G.; Bhattacharya, D.; Zhang, L.; Cheng, J.; Pivovar, B.; Arges, C. G. Bipolar Membrane Polarization Behavior with Systematically Varied Interfacial Areas in the Junction Region. *J. Mater. Chem. A* **2021**, *9* (4), 2223–2238.

(19) Kaiser, V.; Bramwell, S. T.; Holdsworth, P. C. W.; Moessner, R. Onsager's Wien Effect on a Lattice. *Nat. Mater.* **2013**, *12* (11), 1033–1037.

(20) Oener, S. Z.; Foster, M. J.; Boettcher, S. W. Accelerating Water Dissociation in Bipolar Membranes and for Electrocatalysis. *Science.* **2020**, *369* (6507), 1099–1103.

(21) Chen, L.; Xu, Q.; Oener, S. Z.; Fabrizio, K.; Boettcher, S. W. Design Principles for Water Dissociation Catalysts in High-Performance Bipolar Membranes. *Nat. Commun.* **2022**, *13* (1), 3846.

(22) McDonald, M. B.; Freund, M. S. Graphene Oxide as a Water Dissociation Catalyst in the Bipolar Membrane Interfacial Layer. *ACS Appl. Mater. Interfaces* **2014**, *6* (16), 13790–13797.

(23) Bui, J. C.; Corpus, K. R. M.; Bell, A. T.; Weber, A. Z. On the Nature of Field-Enhanced Water Dissociation in Bipolar Membranes. *J. Phys. Chem. C* **2021**, *125* (45), 24974–24987.

(24) Mareev, S. A.; Evdochenko, E.; Wessling, M.; Kozaderova, O. A.; Niftaliev, S. I.; Pismenskaya, N. D.; Nikonenko, V. V. A Comprehensive Mathematical Model of Water Splitting in Bipolar Membranes: Impact of the Spatial Distribution of Fixed Charges and Catalyst at Bipolar Junction. *J. Memb. Sci.* **2020**, *603*, 118010.

(25) Yan, Z.; Zhu, L.; Li, Y. C.; Wycisk, R. J.; Pintauro, P. N.; Hickner, M. A.; Mallouk, T. E. The Balance of Electric Field and Interfacial Catalysis in Promoting Water Dissociation in Bipolar Membranes. *Energy Environ. Sci.* **2018**, *11* (8), 2235–2245.

(26) McDonald, M. B.; Ardo, S.; Lewis, N. S.; Freund, M. S. Use of Bipolar Membranes for Maintaining Steady-State PH Gradients in Membrane-Supported, Solar-Driven Water Splitting. *ChemSusChem* **2014**, *7* (11), 3021–3027.

(27) Vargas-Barbosa, N. M.; Geise, G. M.; Hickner, M. A.; Mallouk, T. E. Assessing the Utility of Bipolar Membranes for Use in Photoelectrochemical Water-Splitting Cells.

ChemSusChem **2014**, *7* (11), 3017–3020.

(28) Luo, J.; Vermaas, D. A.; Bi, D.; Hagfeldt, A.; Smith, W. A.; Grätzel, M. Bipolar Membrane-Assisted Solar Water Splitting in Optimal PH. *Adv. Energy Mater.* **2016**, *6* (13), 1600100.

(29) Mayerhöfer, B.; McLaughlin, D.; Böhm, T.; Hegelheimer, M.; Seeberger, D.; Thiele, S. Bipolar Membrane Electrode Assemblies for Water Electrolysis. *ACS Appl. Energy Mater.* **2020**, *3* (10), 9635–9644.

(30) Oener, S. Z.; Twight, L. P.; Lindquist, G. A.; Boettcher, S. W. Thin Cation-Exchange Layers Enable High-Current-Density Bipolar Membrane Electrolyzers via Improved Water Transport. *ACS Energy Lett.* **2021**, *6* (1), 1–8.

(31) Vermaas, D. A.; Smith, W. A. Synergistic Electrochemical CO2 Reduction and Water Oxidation with a Bipolar Membrane. *ACS Energy Lett.* **2016**, *1* (6), 1143–1148.

(32) Li, Y. C.; Zhou, D.; Yan, Z.; Gonçalves, R. H.; Salvatore, D. A.; Berlinguette, C. P.; Mallouk, T. E. Electrolysis of CO2 to Syngas in Bipolar Membrane-Based Electrochemical Cells. *ACS Energy Lett.* **2016**, *1* (6), 1149–1153.

(33) Zhou, X.; Liu, R.; Sun, K.; Chen, Y.; Verlage, E.; Francis, S. A.; Lewis, N. S.; Xiang, C. Solar-Driven Reduction of 1 Atm of CO2 to Formate at 10% Energy-Conversion Efficiency by Use of a TiO2-Protected III–V Tandem Photoanode in Conjunction with a Bipolar Membrane and a Pd/C Cathode. *ACS Energy Lett.* **2016**, *1* (4), 764–770.

(34) Salvatore, D. A.; Weekes, D. M.; He, J.; Dettelbach, K. E.; Li, Y. C.; Mallouk, T. E.; Berlinguette, C. P. Electrolysis of Gaseous CO2 to CO in a Flow Cell with a Bipolar Membrane. *ACS Energy Lett.* **2018**, *3* (1), 149–154.

(35) Pătru, A.; Binninger, T.; Pribyl, B.; Schmidt, T. J. Design Principles of Bipolar Electrochemical Co-Electrolysis Cells for Efficient Reduction of Carbon Dioxide from Gas Phase at Low Temperature. *J. Electrochem. Soc.* **2019**, *166* (2), F34–F43.

(36) Blommaert, M. A.; Sharifian, R.; Shah, N.; Nesbitt, N.; Smith, W.; Vermaas, D. A. Orientation of Bipolar Membrane Determines the Dominant Ion and Carbonic Species Transport in Membrane Electrode Assemblies for CO2 Reduction. *J. Mater. Chem. A* **2021**.

(37) Siritanaratkul, B.; Forster, M.; Greenwell, F.; Sharma, P. K.; Yu, E. H.; Cowan, A. J. Zero-Gap Bipolar Membrane Electrolyzer for Carbon Dioxide Reduction Using Acid-Tolerant Molecular Electrocatalysts. *J. Am. Chem. Soc.* **2022**, *144* (17), 7551–7556.

(38) Xie, K.; Miao, R. K.; Ozden, A.; Liu, S.; Chen, Z.; Dinh, C.; Huang, J. E.; Xu, Q.; Gabardo, C. M.; Lee, G.; Edwards, J. P.; O'Brien, C. P.; Boettcher, S. W.; Sinton, D.; Sargent, E. H. Bipolar Membrane Electrolyzers Enable High Single-Pass CO2 Electroreduction to Multicarbon Products. *Nat. Commun.* **2022**, *13* (1), 3609.

(39) Sullivan, I.; Goryachev, A.; Digdaya, I. A.; Li, X.; Atwater, H. A.; Vermaas, D. A.; Xiang, C. Coupling Electrochemical CO2 Conversion with CO2 Capture. *Nat. Catal.* **2021**, *4* (11), 952–958.

(40) Sharifian, R.; Wagterveld, R. M.; Digdaya, I. A.; Xiang, C.; Vermaas, D. A. Electrochemical Carbon Dioxide Capture to Close the Carbon Cycle. *Energy Environ. Sci.* **2021**, *14* (2), 781–814.

(41) Shen, C.; Wycisk, R.; Pintauro, P. N. High Performance Electrospun Bipolar Membrane with a 3D Junction. *Energy Environ. Sci.* **2017**, *10* (6), 1435–1442.

(42) Chen, Y.; Wrubel, J. A.; Klein, W. E.; Kabir, S.; Smith, W. A.; Neyerlin, K. C.; Deutsch, T. G. High-Performance Bipolar Membrane Development for Improved Water Dissociation. *ACS Appl. Polym. Mater.* **2020**, *2* (11), 4559–4569.

(43) Yan, Z.; Wycisk, R. J.; Metlay, A. S.; Xiao, L.; Yoon, Y.; Pintauro, P. N.; Mallouk, T. E. High-Voltage Aqueous Redox Flow Batteries Enabled by Catalyzed Water Dissociation and Acid–Base Neutralization in Bipolar Membranes. *ACS Cent. Sci.* **2021**, *7* (6), 1028–1035.

(44) Metlay, A. S.; Chyi, B.; Yoon, Y.; Wycisk, R. J.; Pintauro, P. N.; Mallouk, T. E. Three-Chamber Design for Aqueous Acid–Base Redox Flow Batteries. *ACS Energy Lett.* **2022**, *7* (3), 908–913.

(45) Pärnamäe, R.; Gurreri, L.; Post, J.; van Egmond, W. J.; Culcasi, A.; Saakes, M.; Cen, J.; Goosen, E.; Tamburini, A.; Vermaas, D. A.; Tedesco, M. The Acid–Base Flow Battery: Sustainable Energy Storage via Reversible Water Dissociation with Bipolar Membranes. *Membranes (Basel).* **2020**, *10* (12), 409.

(46) Ünlü, M.; Zhou, J.; Kohl, P. A. Hybrid Polymer Electrolyte Fuel Cells: Alkaline Electrodes with Proton Conducting Membrane. *Angew. Chemie* **2010**, *122* (7), 1321–1323.

(47) O'Brien, C. P.; Miao, R. K.; Liu, S.; Xu, Y.; Lee, G.; Robb, A.; Huang, J. E.; Xie, K.; Bertens, K.; Gabardo, C. M.; Edwards, J. P.; Dinh, C.; Sargent, E. H.; Sinton, D. Single Pass CO2 Conversion Exceeding 85% in the Electrosynthesis of Multicarbon Products via Local CO2 Regeneration. *ACS Energy Lett.* **2021**, *6* (8), 2952–2959.

(48) Tan, Y. C.; Quek, W. K.; Kim, B.; Sugiarto, S.; Oh, J.; Kai, D. Pitfalls and Protocols: Evaluating Catalysts for CO2 Reduction in Electrolyzers Based on Gas Diffusion Electrodes. *ACS Energy Lett.* **2022**, *7* (6), 2012–2023.

(49) Xu, Y.; Miao, R. K.; Edwards, J. P.; Liu, S.; O'Brien, C. P.; Gabardo, C. M.; Fan, M.; Huang, J. E.; Robb, A.; Sargent, E. H.; Sinton, D. A Microchanneled Solid Electrolyte for Carbon-Efficient CO2 Electrolysis. *Joule* **2022**, *6* (6), 1333–1343.

(50) Xia, C.; Zhu, P.; Jiang, Q.; Pan, Y.; Liang, W.; Stavitski, E.; Alshareef, H. N.; Wang, H. Continuous Production of Pure Liquid Fuel Solutions via Electrocatalytic CO2 Reduction Using Solid-Electrolyte Devices. *Nat. Energy* **2019**, *4* (9), 776–785.

(51) Fan, L.; Xia, C.; Zhu, P.; Lu, Y.; Wang, H. Electrochemical CO2 Reduction to High-Concentration Pure Formic Acid Solutions in an All-Solid-State Reactor. *Nat. Commun.* **2020**, *11* (1), 3633.

Chapter 2

Separation of Polymeric Charge Enables Efficient Bipolar Membrane Operation

Abstract

Efficient charge separation is key to the operation of bipolar membranes (BPM). It is well-known that the crossover of coions can quench fixed charges and depolarize the bipolar interface. However, beyond coion crossover, there is a lack of understanding behind the fundamental processes that control charge separation and quenching in BPMs. Herein, we employ polyelectrolytes to investigate the factors controlling charge separation in a cell largely devoid of co-ion crossover. Using ionomeric binders as well as polyelectrolytes, we reveal that mobile fixed charges at the bipolar interface can result in charge pairing and quenching in a process that we term *bipolar pairing*. This phenomenon has the effect of attenuating membrane voltage and inhibiting reverse bias water dissociation kinetics, leading to large overpotential penalties in excess of 7.5 V in some cases. We find that interfacial additives can play a role as spacers to suppress detrimental bipolar pairing interactions on top of acting as catalysts for water dissociation, and that layered materials such as graphene oxide are more effective at this role than nanoparticulate materials such as titanium dioxide. These results unravel a hitherto unknown mechanism of efficiency loss in BPMs, and carry important implications for the design of catalytic layers at bipolar interfaces and bipolar interfaces themselves.

2.1 Introduction

Bipolar membranes (BPMs) are an emerging electrochemical technology that enables the efficient production and separation of acid and base solutions.[1–5] This capability arises from its unique structure, comprising a cation exchange membrane (CEM) laminated onto an anion exchange membrane (AEM).[1–5] Owing to its ability to support a stable pH gradient, BPM have seen application in water electrolyzers,[6–11] CO_2 electrolyzers,[12–19] and BPM electrodialysis (BPMED) cells.[20,21] These examples highlight the abounding opportunities for the application of BPMs in a wide range of next-generation energy technologies. The efficiency of BPM operation is controlled by the magnitude of the potential drop at the bipolar junction.

Generally, differences in potential arise from the separation of charge and the spatial accumulation of charge excess. Electrically polarized interfaces such as the bipolar interface of a BPM can be depolarized by ion pairing interactions. A poignant example widely invoked in the BPM literature is the attenuation in membrane voltage (V_{mem}) due to the crossover of coions and their pairing interactions with excess fixed charges of the BPM.[22,23] However, ion pairing interactions are not exclusive to coions, and it has not been explicitly considered whether interactions between the polymeric charges embedded within the BPM could have a depolarizing effect on the potential drop. This knowledge gap impedes the rational design of BPMs and further optimization of their electrochemical performance.

Herein, we employ polyelectrolytes to exclude the contributions of co-ion leakage to efficiency losses during BPM operation and single out other contributing factors. We find that introducing ionomers as an interfacial additive or replacing one of the membranes constituting the BPM with a polyelectrolyte leads to attenuation of V_{mem} and large increases in reverse bias overpotential losses. Based on these observations, we invoke that the erosion in V_{mem} and polarization kinetics arises from charge quenching interactions of fixed charges at the bipolar interface with mobile fixed charges (*bipolar pairing*). These losses can be mitigated by the inclusion of high specific-area layered materials such as graphene oxide, suggesting that materials, in addition to serving as catalysts, also act as spacers to minimize charge quenching interactions. In contrast, nanoparticulate, non-layered materials such as titanium dioxide were found to be poor at shielding against bipolar pairing interactions. These findings have significant implications for the design of BPM-based devices operating in both reverse and forward bias, and provide guiding principles for the physical construction of BPMs for maximal operating efficiency.

2.2 Coion Crossover Severely Attenuates Membrane Voltage

In this work, homemade BPMs were made by laminating a CEM onto an AEM, either with or without an interlayer additive, and are denoted by the nomenclature (Acid) | CEM | I | AEM | (Base), where I is an interlayer material (see **Experimental Methods** for further detail). Membrane voltages (V_{mem}) across the BPM were measured using a four-electrode cell setup, where the voltage is sensed across a pair of identical reference electrodes (**Figure 2.1(a)**). In addition, as all measurements of V_{mem} were made by sensing the electric potential of the acid solution with respect to the base solution, V_{mem} will be reported as a negative value, with polarization to more negative values indicating reverse bias. Currents are reported based on measurements of electrical current through the external circuit, and hence negative currents correspond to reverse bias polarization. In this study, to simplify the analysis of V_{mem}, we assume that the concentration of fixed charges in the CEM and AEM is 1 M, and that Donnan potentials at the membrane-electrolyte interfaces are constant at 0 mV. Hence, changes in V_{mem} reflect only changes in the bipolar junction voltage (V_{J}).[24]

BPM cells containing strong acid (e.g. HCl, H_2SO_4) and strong base (e.g. NaOH, KOH) are amongst the most well-studied systems in the field.[3,24–26] Thus, in order to acquire a baseline understanding of how the electrochemical performance of a BPM depends on the electrolytes present, we began our experiments with electrochemical measurements of a H_2SO_4 | CEM | AEM | KOH cell. The equilibrated open-circuit V_{mem} recorded for this cell was −560 mV (**Figure 2.1(b)**, blue column). The theoretical open-circuit V_{mem}, $V_{\Delta\mathrm{pH}}$, has been reported to be related to the pH gradient across the BPM (**Equation 2.1**),

$$V_{\Delta\mathrm{pH}} = -59\ \mathrm{mV} \cdot \Delta\mathrm{pH} \qquad \textbf{Equation 2.1}$$

where $\Delta\mathrm{pH} = \mathrm{pH}_{\mathrm{Base}} - \mathrm{pH}_{\mathrm{Acid}}$. Compared to the theoretical $V_{\Delta\mathrm{pH}}$ predicted by **Equation 2.1** (**Figure 2.1(b)**, blue dashed line) based on the measured pH values for the H_2SO_4 and KOH (see **Table S2.1**), this measured value is 240 mV less negative, corresponding to voltage loss equivalent to a 4-unit shallower pH gradient. Consistent with previous reports suggesting that deviations of the experimentally measured V_{mem} from $V_{\Delta\mathrm{pH}}$ are due to coion leakage,[22,23] we attribute the predominant and proximate cause of the severely eroded V_{mem} to the crossover of the coions HSO_4^- and K^+ through the BPM, which is enabled via coupled parasitic neutralization.[24]

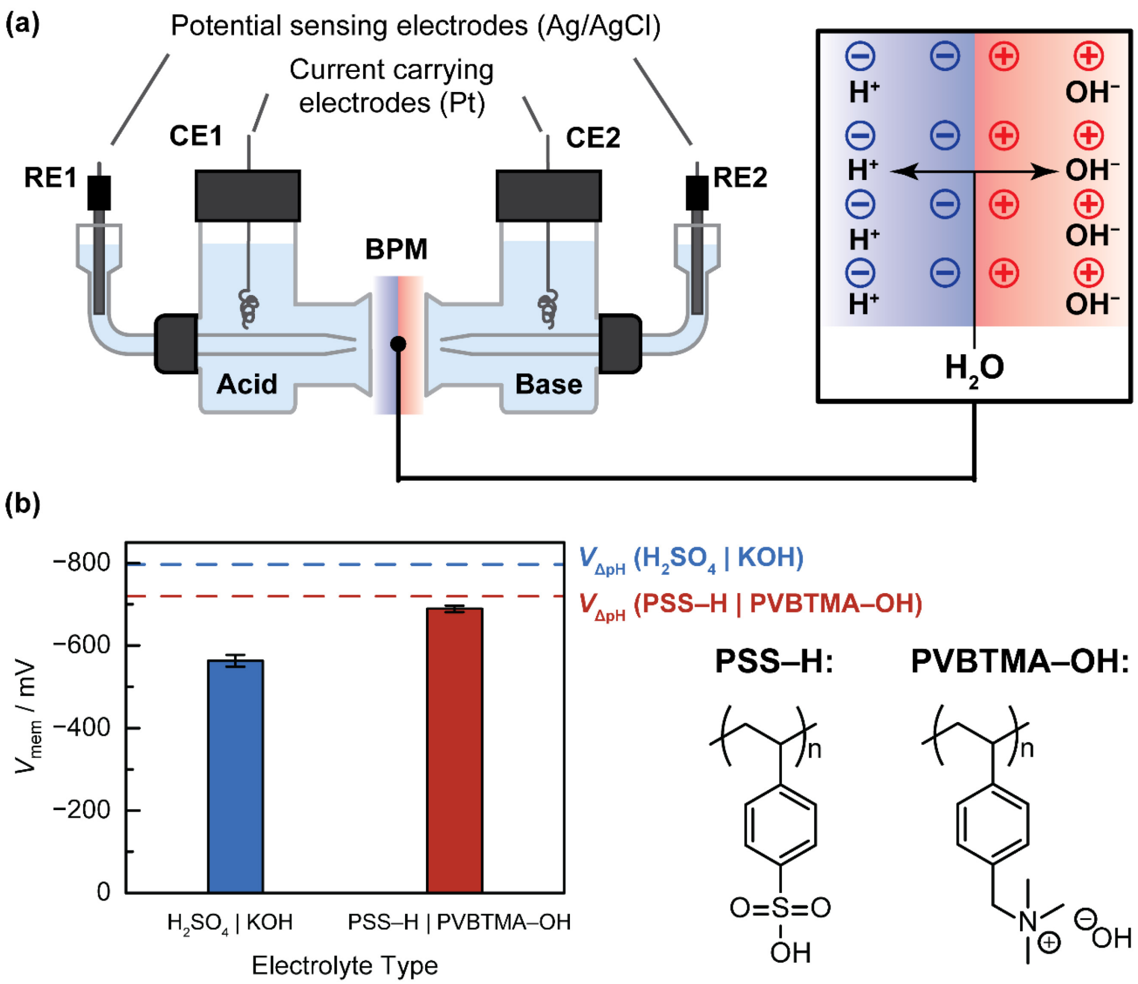

Figure 2.1. (a) Schematic of the electrochemical cell set-up used for electrochemical measurements across the BPM, with a magnified view of the bipolar interface showing the direction of ion motion under reverse bias polarization. **(b)** Open-circuit membrane voltage measurements for the H_2SO_4 | CEM | AEM | KOH and PSS–H | CEM | AEM | PVBTMA–OH electrolyte systems. The horizontal dashed lines indicate the theoretical membrane voltages from **Equation 2.1**. The structures of PSS–H and PVBTMA–OH are shown. Error bars in **(b)** represent the standard deviation of independent triplicate measurements.

In order to eliminate the effect of coion crossover on the open-circuit V_{mem}, we turned to the use of the polyelectrolytes, poly(4-styrenesulfonic acid) (PSS–H) and poly((p-vinylbenzyl)trimethylammonium hydroxide) (PVBTMA–OH) (structures shown in **Figure 2.1**). Due to their high molecular weights, the PSS^- and $PVBTMA^+$ coions are size-excluded from crossing the BPM, shutting down coion crossover entirely.[24,27] We measured an open-circuit V_{mem} of −690 mV for the PSS–H | CEM | AEM | PVBTMA–OH cell (**Figure 2.1(b)**, red column). Importantly, the measured V_{mem} was only 30 mV less negative than the $V_{\Delta\mathrm{pH}}$ for the measured pH difference between PSS–H and PVBTMA–OH, which was −720 mV (**Figure 2.1(b)**, red dashed line; see **Table S2.1** for measured pH values). Using ^{1}H NMR, we verified that there was indeed no crossover of either the PSS$^-$ coion into the PVBTMA–OH solution (**Figure S2.2**) or of the PVBTMA$^+$ coion into the PSS–H solution (**Figure S2.3**) post-experiment. Hence, the smaller difference between V_{mem} and $V_{\Delta\mathrm{pH}}$ for the PSS–H | CEM | AEM | PVBTMA–OH cell than the H_2SO_4 | CEM | AEM | KOH cell unequivocally indicates that the phenomenon of coion crossover can lead to a dramatic attenuation in V_{mem}, and that strategies to prevent coion crossover can mitigate this effect.

In considering how exactly coion crossover leads to changes in V_{mem}, however, we offer the following physical interpretation. Since the magnitude of open-circuit V_{mem} is correlated to the total number of excess fixed charges at the bipolar junction, the role of coion crossover must necessarily be to introduce a quasi-steady-state amount of coions that reside at the bipolar interface. Furthermore, these coions must form strong ion-pair interactions with the unpaired fixed charges present that result in a reduction in the total number of unpaired fixed charges (**Figure 2.2**). We term this phenomenon *coion pairing*, and invoke that the formation of neutral coion-fixed charge contact ion pairs is explicitly the origin of the attenuated V_{mem} for BPM cells containing strong acid and base solutions.

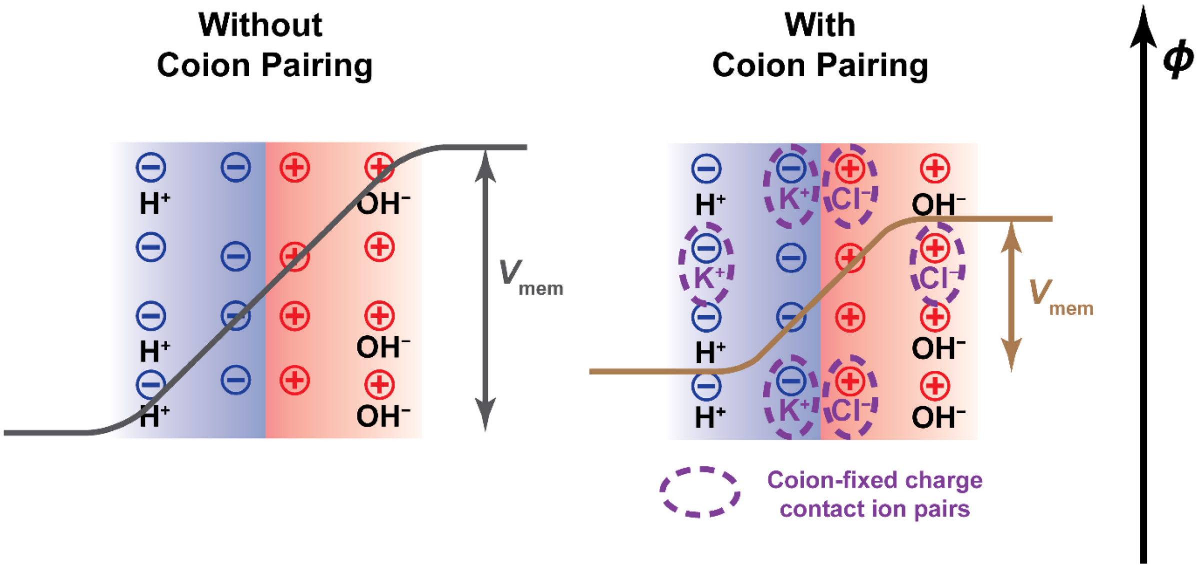

Figure 2.2. Schematic showing how the phenomenon of *coion pairing* resulting from coion crossover leads to the formation of coion-fixed charge contact ion pairs that attenuate V_{mem}.

2.3 Bipolar Pairing Inhibits Electrochemical Performance

Beyond coion crossover, we sought to understand other factors that may influence the measured V_{mem} and lead to deviation from the theoretical $V_{\Delta\mathrm{pH}}$. Ionomers are often used as binders in catalyst ink mixtures to ensure good adhesion with an underlying substrate,[28] and are necessary for stable catalyst operation in BPMs.[6,29] To understand how the inclusion of an ionomeric binder at the bipolar junction may affect BPM performance, we fabricated CEM | I | AEM composites, where I is either a cation exchange ionomer spray-coated directly on the AEM (Nafion D2020), or an anion exchange ionomer spray-coated onto the CEM (Sustainion XA-9). Employing the methodology established above, we used polyelectrolytes in place of H_2SO_4 and KOH in order to disentangle the effect of the ionomer on the V_{mem} from the effect of coion crossover. We observed that open-circuit V_{mem} values for the cells with ionomers, PSS–H | CEM | D2020 | AEM | PVBTMA–OH (−600 mV) and PSS–H | CEM | XA-9 | AEM | PVBTMA–OH (−650 mV), were less negative than the cell without ionomer (−690 mV) by 90 mV and 40 mV, respectively (**Figure 2.3(a)**). Comparing the steady-state reverse bias polarization data for the three cells,, reverse bias polarization kinetics were worse for the polyelectrolyte cells with the inclusion of ionomers across the board, and comparisons at −20 mA cm^{-2} revealed 2.22 and 2.26 V larger overpotentials for the D2020 (V_{mem} = 5.27 V) and XA-9 (V_{mem} = 5.31 V) cells compared to the cell without ionomer (V_{mem} = 3.05 V) (**Figure 2.3(b)**). Repeating these measurements with cells containing H_2SO_4 and KOH, we similarly observed less negative open-circuit V_{mem} values and much larger reverse bias potentials at given current densities for the cells containing ionomers compared to the cell without ionomer (**Figure S2.4**). The observation of attenuated open-circuit V_{mem} and worse reverse bias polarization kinetics when ionomers are included in the bipolar junction whether non-polyelectrolytes or polyelectrolytes are used suggests that detrimental interactions are introduced at ionomer-membrane junctions which occur independently of coion crossover.

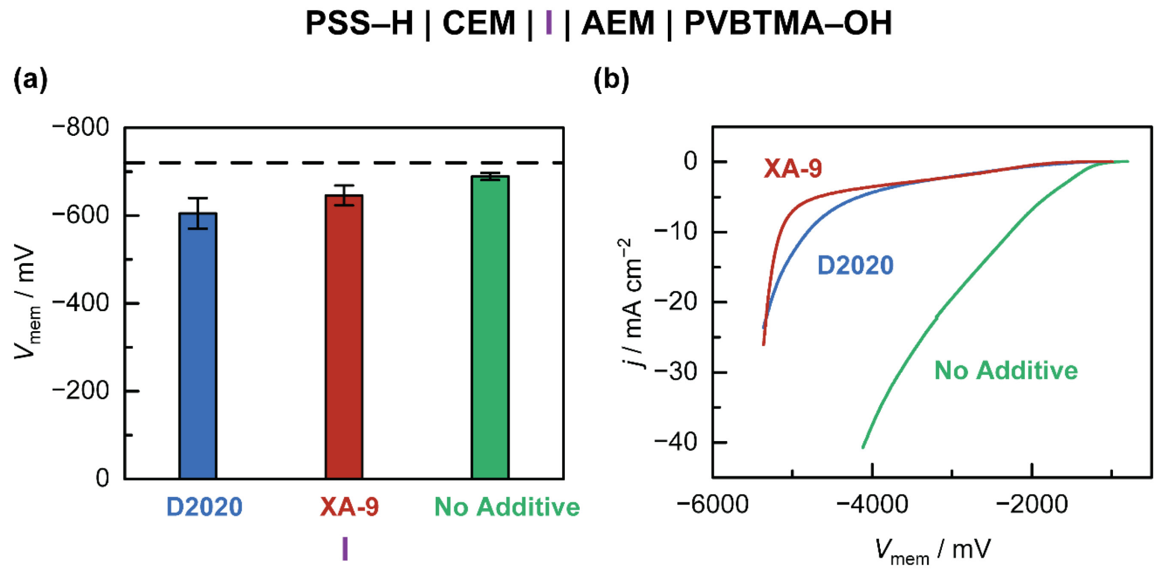

Figure 2.3. (a) Open-circuit membrane voltages and **(b)** reverse bias polarization curves for PSS–H | CEM | I | AEM | PVBTMA–OH cells containing different interlayer additives (I). The horizontal dashed line in (a) indicates the theoretical membrane voltage from **Equation 2.1**. Error bars in **(a)** represent the standard deviation of independent triplicate measurements.

We hypothesized that the detrimental effects from including an ionomer at the bipolar junction originated from charge-pairing interactions between the ionomer and the membrane which could form during the spray-coating process, when the ionomer was still dispersed in solvent and able to freely diffuse on the membrane surface. We further hypothesized that a bipolar junction constructed with fixed charges that have a higher degree of mobility than in a membrane would be susceptible to the same type of interaction. We tested this hypothesis by directly constructing a bipolar junction from a polyelectrolyte | membrane interface with the PSS–H | AEM | PVBTMA–OH cell. Comparing PSS–H | AEM | PVBTMA–OH to PSS–H | CEM | AEM | PVBTMA–OH, where the bipolar junction is a membrane | membrane interface with less mobile fixed charges, we observed an open-circuit V_{mem} that was 90 mV less negative for the former (−600 mV) than the latter (−690 mV) (**Figure 2.4(a)**). Furthermore, reverse bias polarization kinetics were significantly worse for PSS–H | AEM | PVBTMA–OH than PSS–H | CEM | AEM | PVBTMA–OH, requiring a dramatic 7.5 V more overpotential to pass only −2 mA cm^{-2} (**Figure 2.4(b)**). We note that PSS–H and Nafion 117, which is used as the CEM here, both contain sulfonic acids as the ionizable fixed charge moiety. In addition, the PSS–H solution used has a similar concentration of fixed charges as hydrated Nafion 117 (~1.2 M).[30] Hence, we posit that the worse electrochemical performance for PSS–H | AEM | PVBTMA–OH should be predominantly due to differences in fixed charge mobility between the solution-phase PSS–H and membrane-phase Nafion 117.

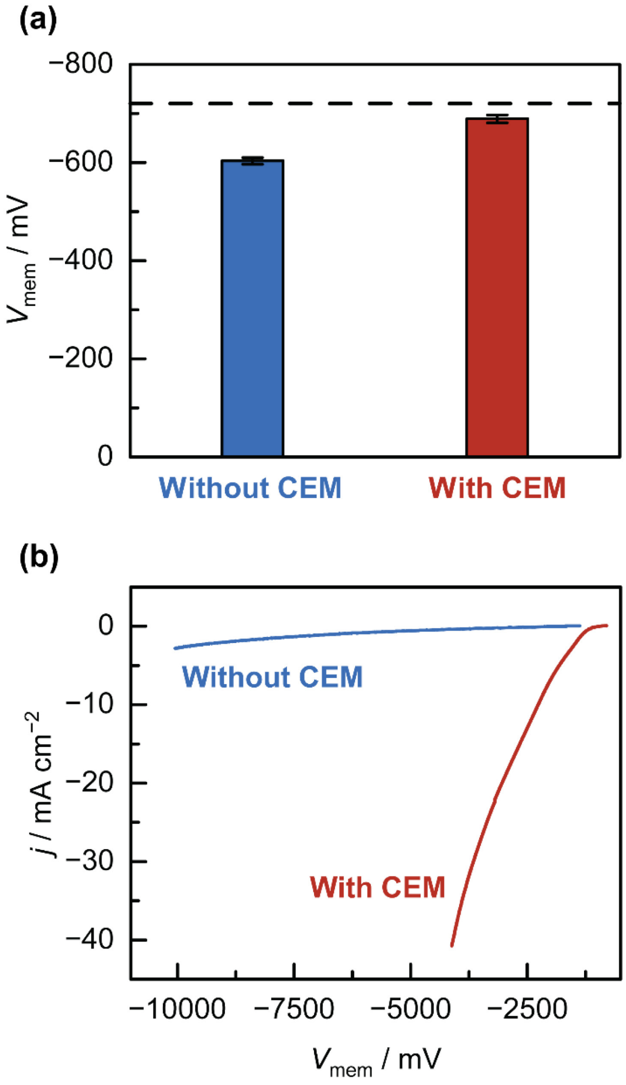

Figure 2.4. Comparison of **(a)** open-circuit membrane voltages and **(b)** reverse bias polarization curves for the PSS–H | AEM | PVBTMA–OH ('Without CEM') and PSS–H | CEM | I | AEM | PVBTMA–OH ('With CEM') cells. The horizontal dashed line in (a) indicates the theoretical membrane voltage from **Equation 2.1**. Error bars in **(a)** represent the standard deviation of independent triplicate measurements.

Consolidating the experimental observations made with the ionomer-coated and polyelectrolye | membrane BPM cells, we find strong evidence for the existence of fixed charge-fixed charge pairing interactions at the bipolar junction. These interactions become more appreciable with increasing mobility of fixed charges due to opposite charges being able to associate more intimately, and manifest in severely eroded open-circuit V_{mem} and reverse bias polarization kinetics (**Figures 2.3 – 2.4**). Since the open-circuit V_{mem} is a direct measure of the concentration of excess fixed charges at the bipolar interface resulting from acid-base neutralization, erosions in its value can be understood as charge pairing interactions quenching the total concentration of excess fixed charges. The existence of this additional and hitherto unaccounted for interaction can further decouple the open-circuit V_{mem} from the thermochemistry of the transmembrane solution pH gradient (**Equation 2.1**), and explains deviations between the experimentally measured V_{mem} and $V_{\Delta\mathrm{pH}}$ in the absence of coion crossover.

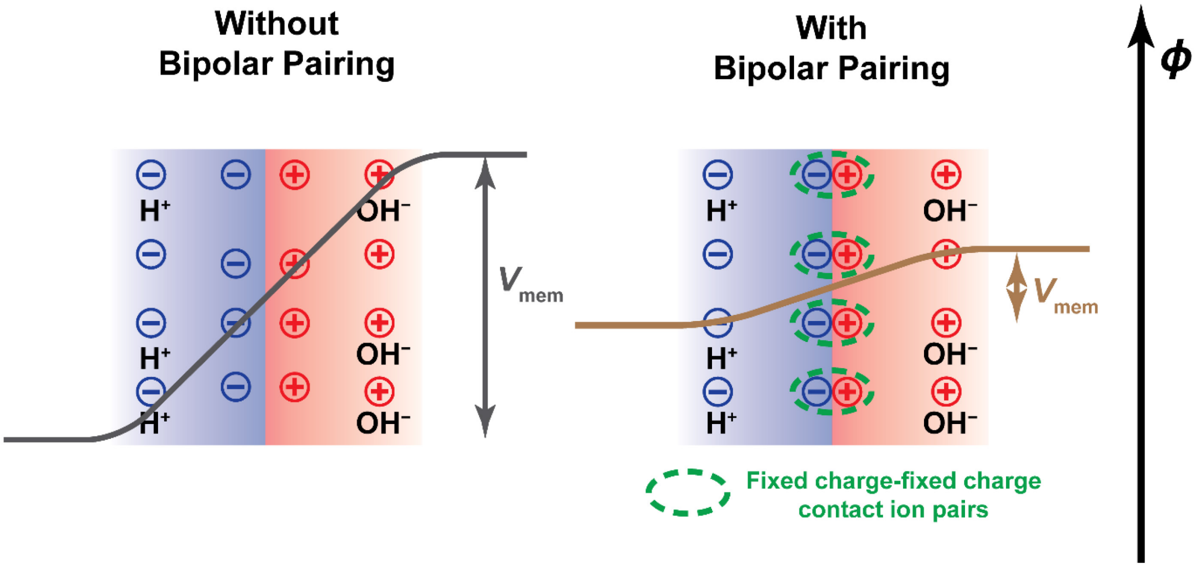

Figure 2.5. Schematic showing how the phenomenon of *bipolar pairing* occurring at the bipolar junction leads to the formation of fixed charge-fixed charge contact ion pairs that attenuate V_{mem}.

Evidence for this fixed charge-fixed charge pairing interaction can also be found in the reverse bias polarization data. In the extreme limit where one of the fixed charge-containing species is solution-phase and has high mobility, as in the case of PSS–H | AEM | PVBTMA–OH, the polarity of the applied electric field under reverse bias polarization drives the mobile fixed charges to become more closely associated with fixed charges of the opposite sign, thereby almost completely shutting off current in reverse bias and leading to near-*total rectification*.[31] We term the formation of fixed charge-fixed charge pairing interactions at the bipolar interface *bipolar pairing*, and, similar to coion pairing, invoke that bipolar pairing reduces the total amount of unpaired fixed charges (**Figure 2.5**). On the surface, this implies that bipolar pairing adds a constant overpotential to reverse bias polarization equivalent to the difference between V_{mem} and $V_{\Delta\mathrm{pH}}$. However, the differences in the current-voltage slopes in **Figures 2.3(b)** and **2.4(b)** imply a secondary effect from bipolar pairing that results in affected cells exhibiting a much weaker sensitivity to the applied voltage. We suggest that on top of lowering V_{mem}, bipolar pairing may result in weaker electric field strengths for a given V_{mem} than a cell without bipolar pairing due to quenching of the most proximal negative and positive fixed charges at the bipolar junction, leading to the potential drop from the residual unquenched fixed charges extending over a larger lengthscale (**Figure 2.5**, right panel). Since the kinetics of the water dissociation reaction (WDR) are strongly electric field-dependent,[2,32] a dampened field at the same V_{mem} would hence lead to worsened reverse bias polarization slopes. The attenuated V_{mem} due to bipolar pairing also imposes, at minimum, a constant overpotential penalty for forward bias operation, but beyond that, the implications of bipolar pairing on the efficiency of forward bias operation are outside of the scope of this study. An alternative explanation for the near-total rectification of current observed with mobile fixed charges is the exclusion of water from the bipolar interface due to the strong association of oppositely charged fixed charges, preventing the formation of an intermediate aqueous phase necessary for water dissociation.[31] This explanation arose from a study in which a surfactant molecule with hydrophobic alkyl chains was employed; this is unlikely to be the case here since PSS–H is a water-soluble polyelectrolyte with a high density of charged groups. Drawing parallels to faradaic electrochemical processes occurring at electrodes, the charge quenching bipolar pairing interactions operative at membrane-based bipolar junctions are analogous to electrode poisoning interactions, insofar as they block active sites and suppress catalytic activity; indeed, in a poignant and structurally relevant example, ionomers used in catalyst inks can also bind directly to electrode surfaces and act as poisons, inhibiting catalysis.[33]

2.4 Interlayer Materials Act as Spacers to Mitigate Charge Quenching Interactions

Having identified a new mechanism that inhibits the electrochemical performance of BPMs, we sought out to find means of remediation. We hypothesized that interlayer additives that prevented bipolar pairing interactions could be utilized to this end. Graphene oxide (GO) is a well-known water dissociation catalyst that has experimentally demonstrated some of the best performance metrics in the field.[29,34–36] Hence, as a first pass, we wanted to understand whether the incorporation of graphene oxide could be beneficial in addressing the effects of the two charge-quenching interactions. For the PSS–H | CEM | I | AEM | PVBTMA–OH series of cells, where I is either GO, anatase TiO_2, or no additive, we observed no significant differences in open-circuit V_{mem} (**Figure 2.6(a)**, GO: −700 mV; TiO_2 : −670 mV ; no additive: −690 mV). Here, we included anatase TiO_2, another reported water dissociation catalyst with record metrics[6,37] but with a non-layered structure, as a counterpoint. SEM characterization of the GO and TiO_2 layers is presented in **Figures S2.5 – S2.6**. For both I = GO and TiO_2, we observed a significant improvement in reverse bias polarization kinetics, measuring a 2.1 and 1.6 V smaller overpotential at −20 mA cm^{-2} for the cells incorporating GO and TiO_2, respectively, than the cell without additives (**Figure 2.6(b)**). These improvements are consistent with GO and TiO_2 being competent WDR catalysts. Repeating the same set of experiments for the PSS–H | I | AEM | PVBTMA–OH series of cells, we observed that the inclusion of GO led to a more significant improvement in the open-circuit V_{mem} of 100 mV from −600 mV (no additive) to −700 mV (GO) (**Figure 2.6(c)**). Unlike GO, however, we note that the inclusion of TiO_2 did not lead to a significant change in the open-circuit V_{mem} (−560 mV for TiO_2 vs −600 mV without additive) (**Figure 2.6(c)**). Comparing the reverse bias polarization curves for GO, TiO_2 and the no-additive cases, we found that GO yielded the lowest overpotential at any given current density, followed by TiO_2, and finally the cell without additives (**Figure 2.6(d)**). Importantly, however, we note that while the polarization curves for PSS–H | CEM | GO | AEM | PVBTMA–OH and PSS–H | GO | AEM | PVBTMA–OH were very similar (**Figure S2.7**), the kinetics for PSS–H | TiO_2 | AEM | PVBTMA–OH were starkly worse than those for PSS–H | CEM | TiO_2 | AEM | PVBTMA–OH (**Figure S2.8**).

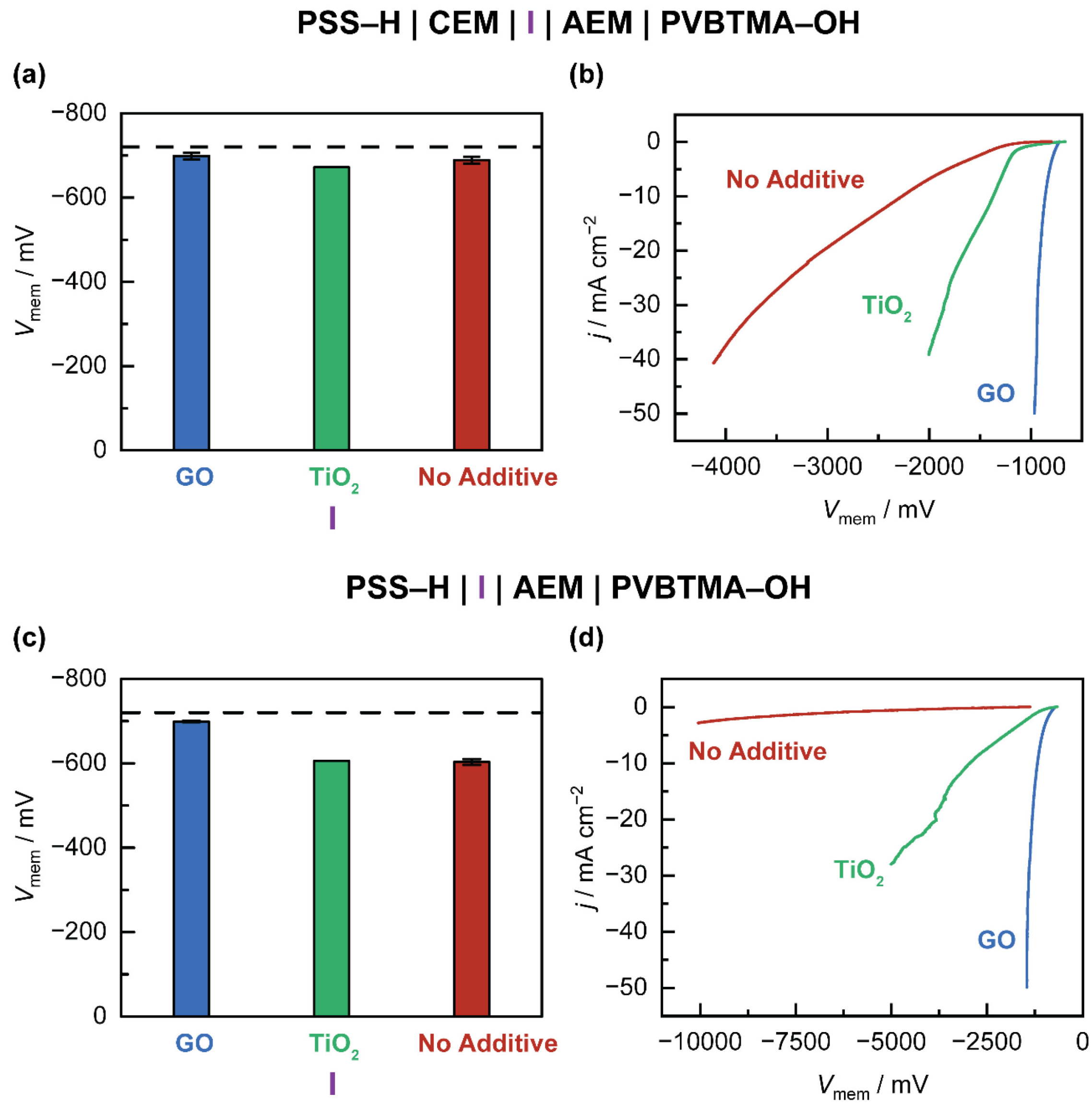

Figure 2.6. Comparison of **(a)** open-circuit membrane voltages and **(b)** reverse bias polarization curves for PSS–H | CEM | I | AEM | PVBTMA–OH cells in the presence and absence of interlayer additives I. Comparison of **(c)** open-circuit membrane voltages and **(d)** reverse bias polarization curves for PSS–H | I | AEM | PVBTMA–OH cells in the presence and absence of interlayer additives I. The horizontal dashed lines in **(a)** and **(c)** indicate the theoretical membrane voltage from **Equation 2.1**. Error bars in **(a)** and **(c)** represent the standard deviation of independent triplicate measurements.

These results can be understood as follows. We suggest that the catalytic properties of the interlayer material (GO or TiO_2) alone cannot explain the observed shifts in V_{mem} upon its inclusion, since the same level of catalytic activity should be at play in both the PSS–H | CEM | I | AEM | PVBTMA–OH and PSS–H | I | AEM | PVBTMA–OH configurations. However, despite the observed improvement in water dissociation kinetics when TiO_2 was included (**Figure 2.6(b)**), there was hardly any difference in the open-circuit V_{mem} for the TiO_2 cell and the cell without additives (**Figure 2.6(a)**). Instead, we suggest that the interlayer material plays a critical secondary role on top of acting as a water dissociation catalyst. This secondary role involves acting as a spacer to prevent the oppositely-charged fixed charges of the bipolar junction from associating closely together to form contact ion pairs and impose charge quenching effects (**Figure 2.7**). The improved open-circuit V_{mem} values consistently obtained when GO was used as an additive ((**Figure 2.6(b), (c)**) is testament to this secondary role, and originates from GO's property of being a high specific area layered material that can cover large swathes of the membrane's surface area (particle size 1 – 7 μm based on manufacturer specifications) (**Figure 2.7**). To explain the differences in how polarization kinetics change for the GO and TiO_2 cells when shifting between the PSS–H | CEM | I | AEM | PVBTMA–OH and PSS–H | I | AEM | PVBTMA–OH configurations, we highlight that the overall reverse bias WDR kinetics are a function of both bipolar pairing interactions (as established above) and WDR catalysis. It is notable that both the PSS–H | CEM | GO | AEM | PVBTMA–OH and PSS–H | GO | AEM | PVBTMA–OH displayed comparable polarization kinetics (**Figure S2.7**) despite PSS–H | CEM | AEM | PVBTMA–OH and PSS–H | AEM | PVBTMA–OH exhibiting dramatically different polarization kinetics (**Figure 2.4(b)**), suggesting that GO is able to effectively prevent bipolar pairing interactions that occur for PSS–H | AEM | PVBTMA–OH, such that the catalytic activity of GO dominates the electrochemical performance. On the other hand, the small, nanoparticulate morphology of the TiO_2 additive (18 nm diameter based on manufacturer specifications) prevented it from effectively acting as a spacer to separate the two phases of the bipolar interface from interacting (**Figure 2.7**), leading to the electrochemical performance of PSS–H | TiO_2 | AEM | PVBTMA–OH being subject to detrimental bipolar pairing interactions not appreciable for PSS–H | CEM | TiO_2 | AEM | PVBTMA–OH (**Figure S2.8**). These findings strongly suggest that the structural morphology of the interfacial additive determines its effectiveness at playing a spacer role.

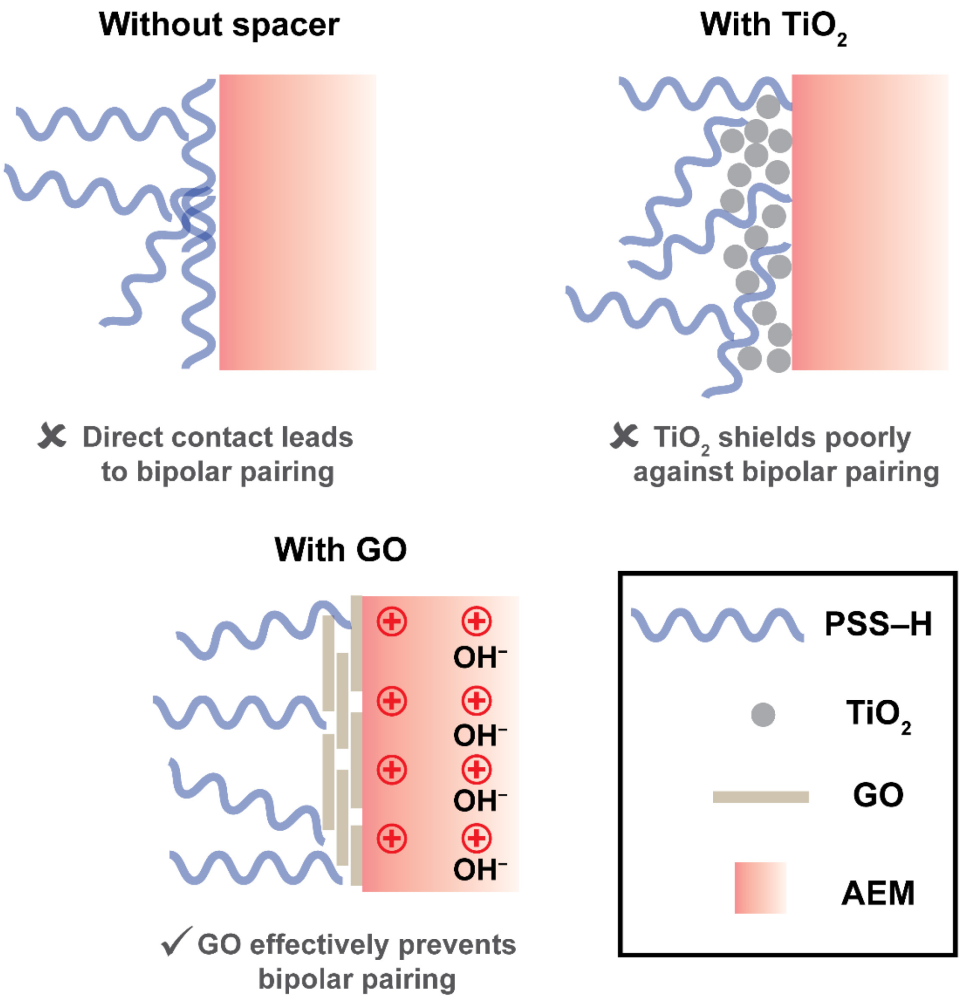

Figure 2.7. The extent of bipolar pairing interactions in the presence of different types of interfacial additives. When no additives are present, the mobile charges of PSS^- can directly interact with the fixed charges of the AEM, leading to significant bipolar pairing. While the nanoparticulate nature of TiO_2 prevents it from shielding against bipolar pairing, the high specific area layered structure of GO makes it an effective agent for blocking these detrimental interactions.

Furthermore, we hypothesized that layered materials are privileged for this type of spacer role and are highly effective at suppressing fixed charge-fixed charge quenching interactions, and, indeed, found appreciable improvements in open-circuit V_{mem} (**Figure S2.9**) and reverse bias polarization kinetics (**Figure S2.10**) when other layered materials (graphene, hexagonal boron nitride, molybdenum disulfide) were used as additives (SEM characterization in **Figures S2.11 – S2.12**). We suggest that differences in the effectiveness of the additive in suppressing bipolar pairing may depend on the molecular details of how each additive associates with and assembles on the AEM, and emphasize that the aggregate reverse bias water dissociation kinetics ultimately depends on both the catalytic activity of the additive and its ability to inhibit bipolar pairing interactions. The notion that certain additives can have a beneficial role in overall catalysis by blocking the deleterious binding of other groups is not unprecedented, and has been demonstrated in the context of preventing electrode poisoning.[38] As a side note, we performed similar experiments with cells containing the non-polyelectrolytes, H_2SO_4 and KOH, and also observed significant improvements in the open-circuit V_{mem} and reverse bias polarization kinetics. This is discussed in **Supplementary Discussion 2.1** but a full investigation of the origin of this phenomenology is beyond the scope of this study. Taken together, the data here support the idea that layered interlayer materials can function as effective spacers to mitigate bipolar pairing interactions, highlighting a key secondary role beyond catalysis.

The findings above have important implications for the construction of catalytic layers at bipolar interfaces, since the inclusion of catalysts often involves the use of binders to ensure mechanical stability and ionic conductivity. We constructed catalytic layers at a bipolar interface through two approaches: sequentially depositing the catalytic graphene oxide layer followed by a cation exchange Nafion D2020 ionomeric binder (PSS–H | D2020 | GO | AEM | PVBTMA–OH); and co-depositing the graphene oxide catalyst and the D2020 binder from a pre-mixed ink (PSS–H | D2020 + GO | AEM | PVBTMA–OH). SEM-EDS characterization revealed good spatial segregation of the D2020 and GO layers in the sequential approach (**Figures S2.14 – S2.15**), and good mixing of the two in the same layer in the mixed approach (**Figure S2.16**). Electrochemical measurements revealed that the sequential approach yielded open-circuit voltages (−670 mV, blue column, **Figure 2.8(a)**) very close to those obtained for PSS–H | GO | AEM | PVBTMA–OH (−700 mV, blue column, **Figure 2.6(c)**) despite the inclusion of D2020, which can form bipolar pairing interactions with the AEM. On the other hand, the open-circuit voltage obtained for the mixed approach (−440 mV, red column, **Figure 2.8(a)**) was significantly less negative than that for PSS–H | GO | AEM | PVBTMA–OH, suggesting the presence of bipolar pairing interactions between D2020 and the AEM. Indeed, comparing the reverse bias polarization curves for the sequential and mixed approaches, we found that while the water dissociation kinetics for the former (blue trace, **Figure 2.8(b))** were comparable to the PSS–H | GO | AEM | PVBTMA–OH cell (blue trace, **Figure 2.6(c)**), the kinetics for the latter were significantly worse (red trace, **Figure 2.8(b)**), which we again attribute to inhibition by bipolar pairing interactions. These observations echo the finding above on the essential role that interlayer additives can play in mitigating detrimental bipolar pairing interactions, but also highlight that a sequential layering strategy is advantageous for constructing binder-inclusive catalytic layers at bipolar interfaces with optimal catalytic activity and robust performance (**Figure 2.8(c)**).

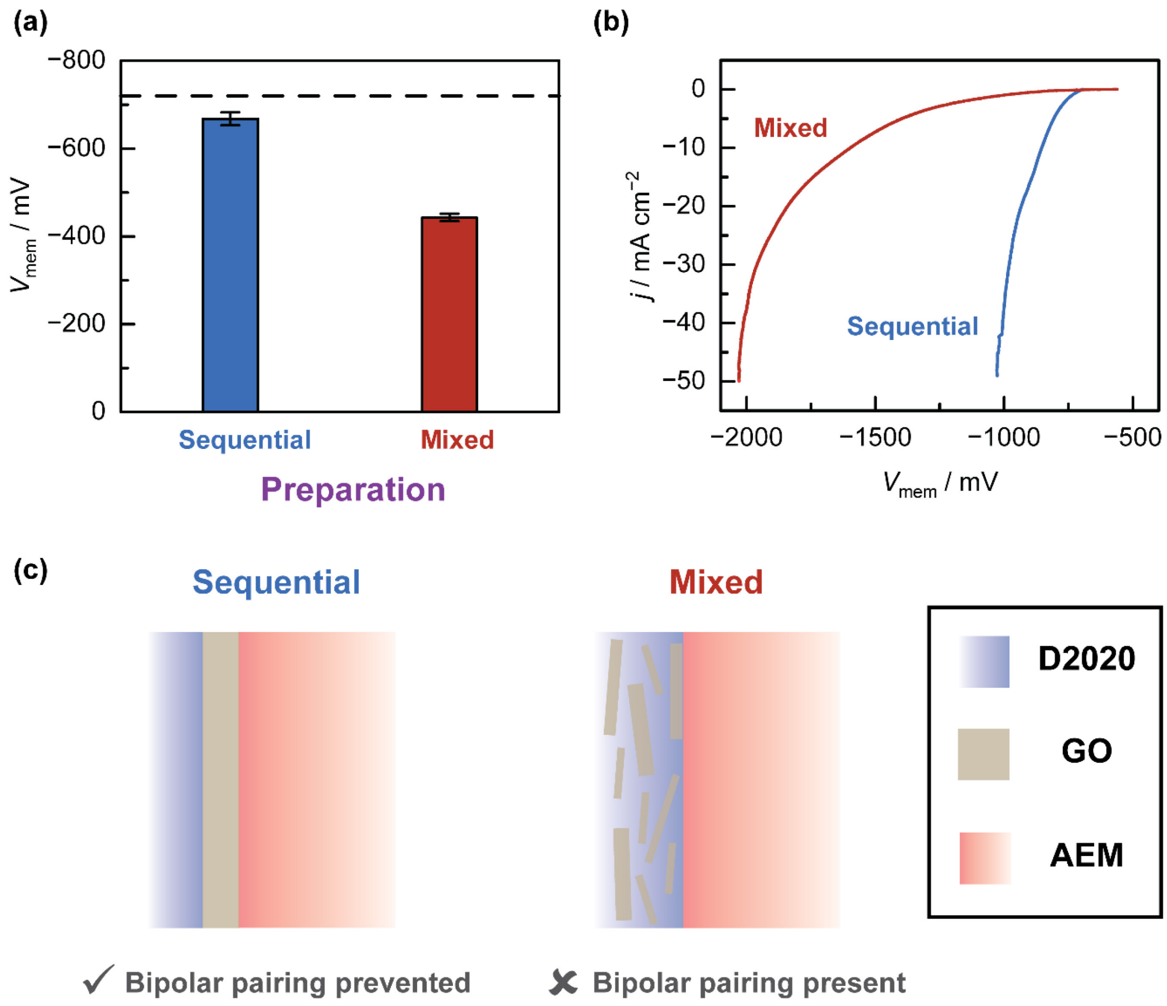

Figure 2.8. Comparison of **(a)** open-circuit membrane voltages and **(b)** reverse bias polarization curves for PSS–H | D2020 | GO | AEM | PVBTMA–OH (Sequential) and PSS–H | D2020 + GO | AEM | PVBTMA–OH (Mixed) cells, showing the impact of the order of catalyst and ionomeric binder deposition to electrochemical performance. **(c)** Schematic showing how the sequential and mixed approaches affect the extent of bipolar pairing interactions present. The horizontal dashed line in **(a)** indicates the theoretical membrane voltage from **Equation 2.1**. Error bars in **(a)** represent the standard deviation of independent triplicate measurements.

2.5 Conclusions

Herein, we systematically investigate the factors that control charge separation and quenching at the bipolar interface of a BPM. Through the judicious use of polyelectrolytes to eliminate coion crossover effects, we reveal that ion pairing between oppositely charged polymeric fixed charges, or bipolar pairing, can also depolarize the bipolar interface. These hitherto overlooked bipolar pairing interactions severely diminish V_{mem}, which imposes an overpotential penalty for operation in both reverse and forward bias. In addition, bipolar pairing interactions can lead to drastically worse reverse bias polarization kinetics. By comparing layered (e.g. GO) and non-layered materials (e.g. TiO_2) as interfacial additives, we identify that a critical contributor to the improvements in water dissociation kinetics when a layered material such as GO is used arises from its ability to mitigate bipolar pairing interactions.

Our studies reveal several key implications for the design and construction of bipolar interfaces for efficient BPM operation. Firstly, our studies highlight the diagnostic utility of open-circuit V_{mem} measurements, which are able to address the thermochemistry of the BPM cell and single out extraneous contributions on top of acid-base neutralization. Importantly, in this study, attenuations in open-circuit V_{mem} were observed to be systematically correlated to worsened reverse bias polarization kinetics, which severely reduces the efficiency of operating BPM cells. Combining observations in changes in open-circuit V_{mem} and polarization kinetics led us to surmise the existence of detrimental bipolar pairing interactions. Secondly, our data show that the direct application of ionomeric binders onto membranes leads to bipolar pairing. This finding runs contrary to conventional wisdom that improved adhesion and interpenetration between the two ion exchange membranes in the BPM should result in improved performance.[39] Fortunately, we find that bipolar pairing can be avoided through a sequential layering approach, whereby a layered catalyst material such as GO is deposited before an ionomer layer. This approach allows the use of ionomeric binders to engender operational stability without incurring performance penalties. Overall, we believe these findings shed timely insights on the microscopic details of how charges can be separated and quenched at the bipolar interface of a BPM, and help demystify aspects of quality BPM construction. These insights will enable the construction of more efficient reverse bias BPMs, and impact their integration into practical devices such as water electrolyzers, CO_2 electrolyzers and electrodialyzers.

2.6 Experimental Methods

Safety Statement

Significant hazards/risks encountered in this study are highlighted with a **CAUTION** label in the relevant Experimental Methods sections, accompanied by an explanation of how they were mitigated.

Chemicals and Materials

Potassium hydroxide (KOH, 99.98%) was purchased from Alfa Aesar and used as received. Poly(sodium 4-styrenesulfonate) (PSS–Na, M_w = 70,000, 30 wt% in H_2O) and hexagonal boron nitride ink (solid content 4.4 – 6.4 wt%) was purchased from Sigma-Aldrich and used as received. Sulfuric acid (OmniTrace, 93-98%) was purchased from VWR and used as received.

Poly(vinylbenzyltrimethyl ammonium chloride (PVBTMA–Cl, M_w = 400,000, 30 wt% in H_2O) was purchased from Scientific Polymer Products and used as received. Platinum wire and mesh (99.995%) used as driving electrodes were purchased from VWR. The CEM Nafion 117, and the AEM Fumasep FAA-3-50 were purchased from Fuel Cell Store and stored dry prior to use. Nafion D2020 (1000 EW, 20 wt% in alcohols) dispersion was purchased from Fuel Cell Store and used as received. Sustainion XA-9 (5% in ethanol) dispersion was purchased from Dioxide Materials and used as received. Graphene oxide (GO) dispersion (4 wt%) was purchased from Graphenea and used as received. Single layer graphene nanoparticles (1 wt% in water) dispersion, titanium oxide nanopowder (TiO_2, anatase, 99.9%, 18 nm) and molybdenum disulfide nanopowder (MoS_2, 30 wt% water dispersion, 6000 nm) were purchased from US Research Nanomaterials and used as received. Dialysis tubing (molecular weight cut-off of 14,000 Da) was obtained from Ward's Science and thoroughly rinsed with Millipore water prior to use. All aqueous electrolyte solutions were prepared with type I water (EMD Millipore, 18.2 MΩ cm resistivity). Glass Ag/AgCl reference electrodes were obtained from CH Instruments and stored in 1 M KCl solution before measurements.

Preparation of Poly(4-Styrenesulfonic Acid) (PSS–H)

PSS–H was prepared in a similar manner to a previous report.[24] To prepare PSS–H samples, 200 mL of a nominal 0.5 M PSS–Na solution were prepared by dilution from the purchased stock solution, transferred into dialysis tubing, and dialyzed against 800 mL of 1 M HCl for 1 h. The HCl was then discarded and replaced with fresh 1 M HCl solution. This procedure was repeated for a total of four times, with the final dialysis step carried out overnight. The dialysis tubing was then thoroughly rinsed and exhaustively dialyzed against Millipore water (with at least 10 exchanges with 1.2 L water) to remove excess HCl. The PSS–H solution was finally concentrated under reduced pressure at 50 °C on a rotary evaporator. An aliquot of this solution was analyzed as is using ICP-OES for S content, and the total volume was adjusted using the measured S concentration to prepare a 1 M PSS–H solution. ^{1}H NMR characterization performed using a 500 MHz Bruker spectrometer was consistent with a previous preparation.[24] The Cl^- content was measured using a chloride ion selective electrode (ISE) (Hach IntelliCAL™ ISECL181 Probe) and found to be negligible (ca. 6.8 mM).

Preparation of Poly(Vinylbenzyltrimethylammonium Hydroxide) (PVBTMA–OH)

To prepare PVBTMA–OH samples, 200 mL of a nominal 0.5 M PVBTMA–Cl solution were prepared by dilution from the purchased stock solution, transferred into dialysis tubing, and dialyzed against 800 mL of 1 M NH_4OH for 1 h. The NH_4OH was then discarded and replaced with fresh 1 M NH_4OH solution. This procedure was repeated for a total of four times, with the final dialysis step carried out overnight. The dialysis tubing was then thoroughly rinsed and exhaustively dialyzed against Millipore water (with at least 10 exchanges with 1.2 L water) to remove excess NH_4OH. The PVBTMA–OH solution was finally concentrated under reduced pressure at 50 °C on a rotary evaporator. The volume of the solution was then adjusted to make a 1 M solution based on the $PVBTMA^+$ present. ^{1}H NMR characterization performed using a 500 MHz Bruker spectrometer was consistent with a previous preparation (**Figure S2.1**).[40] The Cl^- content was measured via ion chromatography performed by Roberton Microlit Laboratories and found to be ~560 mM. However, we emphasize that since Cl^- is a counterion and not a coion in the base compartment, its presence merely dilutes the concentration of OH^{-} but does not impact any of our interpretations.

Preparation of Membrane Composites Containing Interfacial Additives

In the cases whereby interlayer additives were included, an ink dispersion of these materials was spray-coated onto the AEM to make a membrane composite. In a typical sequence, a 0.4 wt% ink of the additive dispersed in a given solvent was prepared and sonicated for at least 15 min prior to use (see **Table S2.2** for solvents used). The FAA-3-50 AEM (3 cm x 3 cm) was heated on a hot plate at 70 °C for 5 minutes while keeping the PET backing intact. 0.5 mL of the ink dispersion were then sprayed onto the heated AEM using an Iwata CM-SB airbrush manipulated with a custom CNC set-up. The AEM composite was then allowed to dry on the hot plate for another 5 min.

For the experiments comparing the effects of different approaches to depositing GO and D2020 onto the AEM on electrochemical performance, the following procedure was used. The sequentially layered D2020 | GO | AEM was prepared by first spray-coating 0.5 mL of a 0.4 wt% dispersion of GO onto the AEM heated at 70 °C and allowing it to dry on the hot plate for 5 min, before spraying 0.5 mL of a 0.4 wt% solution of D2020 onto the same heated AEM. For producing the D2020 + GO | AEM membrane composites whereby the D2020 and GO were co-deposited, equal volumes of 0.4 wt% GO and 0.4 wt% D2020 dispersions were combined and thoroughly mixed, and 1 mL of this mixture was sprayed onto an AEM heated at 70 °C. In both cases, this final composite would then be dried on the hot plate for 5 min.

Preparation of Bipolar Membranes

BPMs used in this study were typically prepared by pressing a dry Nafion 117 CEM onto a dry FAA-3-50 AEM or AEM composite containing an interfacial additive between a pair of glass slides by hand for 1 min. Caution was taken to prevent the trapping of air bubbles.

General Electrochemical Methods

The voltage across the BPM was probed using a four-electrode setup (**Figure 2.1(a)**). For all experiments, the area of the BPM exposed between the two solution compartments was 2 cm^2. In polarization experiments, two glass Ag/AgCl reference electrodes were installed at the ends of the Luggin capillaries. The tips of the capillaries were positioned about 0.3 cm from the BPM surface. Platinum meshes or wires were used as cathode and anode, and each compartment was vented to prevent the build-up of gas during polarization. Acid solutions were added to the compartment facing the CEM, and base solutions were added to the compartment facing the AEM. All electrochemical measurements were performed on either a BioLogic VMP-300 or Gamry Reference 600 potentiostat, and were conducted at ambient temperature (24 ± 1 °C). All glassware and Pt meshes/wires used were cleaned by soaking in a 1:1 mixture by volume of concentrated HNO_3 and H_2SO_4 for at least 30 min before use. For all electrochemical experiments, the V_{mem} values reported were compensated by the drift between the Ag/AgCl reference electrodes measured in a two-electrode setup in 1 M KCl beforehand (typically < 10 mV).

CAUTION: *Concentrated* HNO_3 *and* H_2SO_4 *acids are highly corrosive and should be handled carefully in a fume hood with the appropriate personal protection equipment (PPE), including safety goggles and a corrosion-resistant lab coat and gloves.*

Galvanodynamic Polarization

To obtain the forward and reverse bias polarization curves, galvanodynamic scans were recorded using a scan rate of 10 $\mu A\ cm^{-2}\ s^{-1}$ on either a BioLogic VMP-3 or Gamry REF 600 potentiostat. This scan rate was compared to independent chronopotentiometry measurements and determined to be sufficiently slow to capture steady-state polarization behavior. In cases for which both forward and reverse bias curves needed to be collected, the latter was always collected first since the formation of water and other products in forward bias could delaminate the BPM and affect performance. All polarization curves were typically corrected for Ohmic losses (iR_u) post-experiment using 75 – 80% of uncompensated resistance (R_u) values determined using the Current Interrupt (CI) program on the BioLogic VMP-3 or the galvanostatic electrochemical impedance spectroscopy (GEIS) program on the Gamry REF 600.

Scanning Electron Microscopy – Energy Dispersive Spectroscopy Analysis

Coated membrane composites were imaged using a Zeiss Gemini 450 Scanning Electron Microscope (SEM) equipped with an Everhart Thornley Secondary Electron Detector and an Inlens Secondary Electron Detector. Samples were mounted onto the stage with conductive carbon tape to minimize charging. SEM images were collected at an accelerating voltage of 1 kV. Energy dispersive spectroscopy (EDS) analysis for elemental mapping was performed using the attached Oxford Aztec 100 EDS detector at an accelerating voltage of 5 kV.

2.7 Supplementary Information

2.7.1 Supplementary Discussions

Supplementary Discussion 2.1. Layered interlayer additives improve the open-circuit V_{mem} and reverse bias polarization kinetics for H_2SO_4 | CEM | I | AEM | KOH cells

Having demonstrated that interlayer materials are capable of preventing bipolar pairing interactions, we set out to understand how coion pairing interactions would be affected by the inclusion of interlayer additives. For the H_2SO_4 | CEM | I | AEM | KOH, open-circuit V_{mem} measurements revealed a significant improvement of 200 mV when GO was included (−760 mV) compared to the cell without additives (−560 mV) (**Figure S2.13(a)**). In a similar vein, the GO cell exhibited significantly improved reverse bias kinetics than the cell without additives, showing a 2.8 V lower overpotential at −50 mA cm^{-2} (**Figure S2.13(b)**). While the improvements in polarization kinetics are likely due in large part to the catalytic activity of GO, we suggest that the changes in open-circuit V_{mem} may be reflective of changes in the extent of coion pairing interactions. We propose that the effect of GO in suppressing coion pairing may originate from its innate ability to reject coions, either via electrostatic repulsion with its surface charges, or via the introduction of a low-dielectric environment at the bipolar interface (**Figure S2.13(c)**). Alternatively, the suppression of bipolar pairing interactions through the introduction of GO may enhance the Donnan exclusion of coions from the bipolar junction due to an increase in the total number of unpaired fixed charges (**Figure S2.13(c)**). This would imply synergy between the two roles of GO in suppressing both bipolar and coion pairing interactions. These results are consistent with an earlier study investigating varying interfacial junction morphologies that invoked that coion leakage rates can be controlled not only by the Donnan potentials at membrane | solution interfaces, but also by the interfacial structure of the BPM.[22] Hence, our data suggests that interlayer additives may play a role in preventing coion pairing interactions that erode the efficiency of BPM operation. However, a more thorough investigation of how interlayer additives, particularly layered materials, interact with coions is required, and is outside the scope of this study.

2.7.2 Supplementary Figures & Tables

Table S2.1. Measured pH values of all base solutions used in this study.

Solution	Measured pH
1 M H_2SO_4	0.3
1 M KOH	13.8
1 M PSS–H	0.5
1 M PVBTMA–OH	12.6

Table S2.2. Solvents used to make ink dispersions for spray-coating various interfacial additives.

Additive	Solvent
Nafion D2020	Isopropyl alcohol
Sustainion XA-9	Isopropyl alcohol
Graphene oxide (GO)	Water
Graphene	Water
Hexagonal boron nitride (h-BN)	Cyclohexanone
Molybdenum disulfide (MoS_2)	Water
GO + D2020	1:1 v/v water: isopropyl alcohol

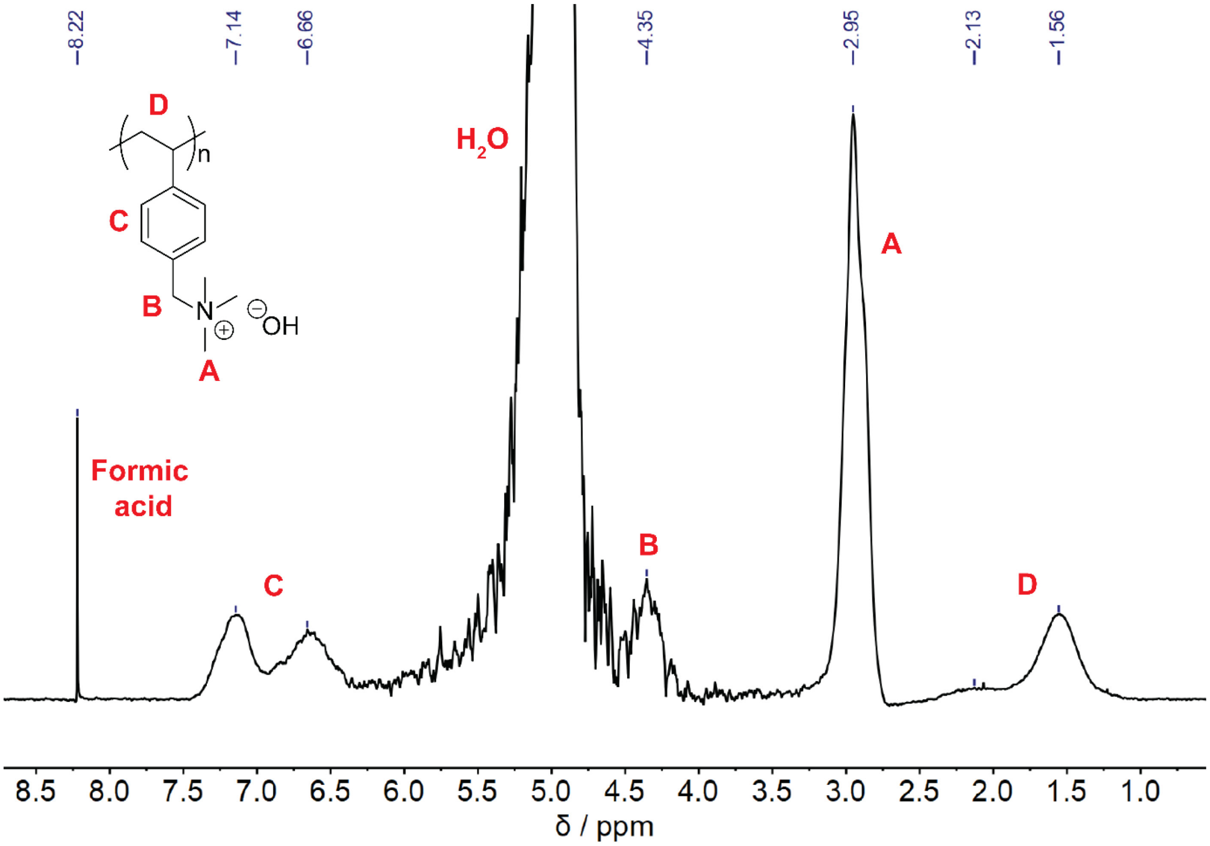

Figure S2.1. ^{1}H NMR spectrum of PVBTMA–OH collected at 500 MHz in a solution containing ~1 M HCl, D_2O and formic acid as the internal standard. Acquired spectrum is in agreement with the literature.[40]

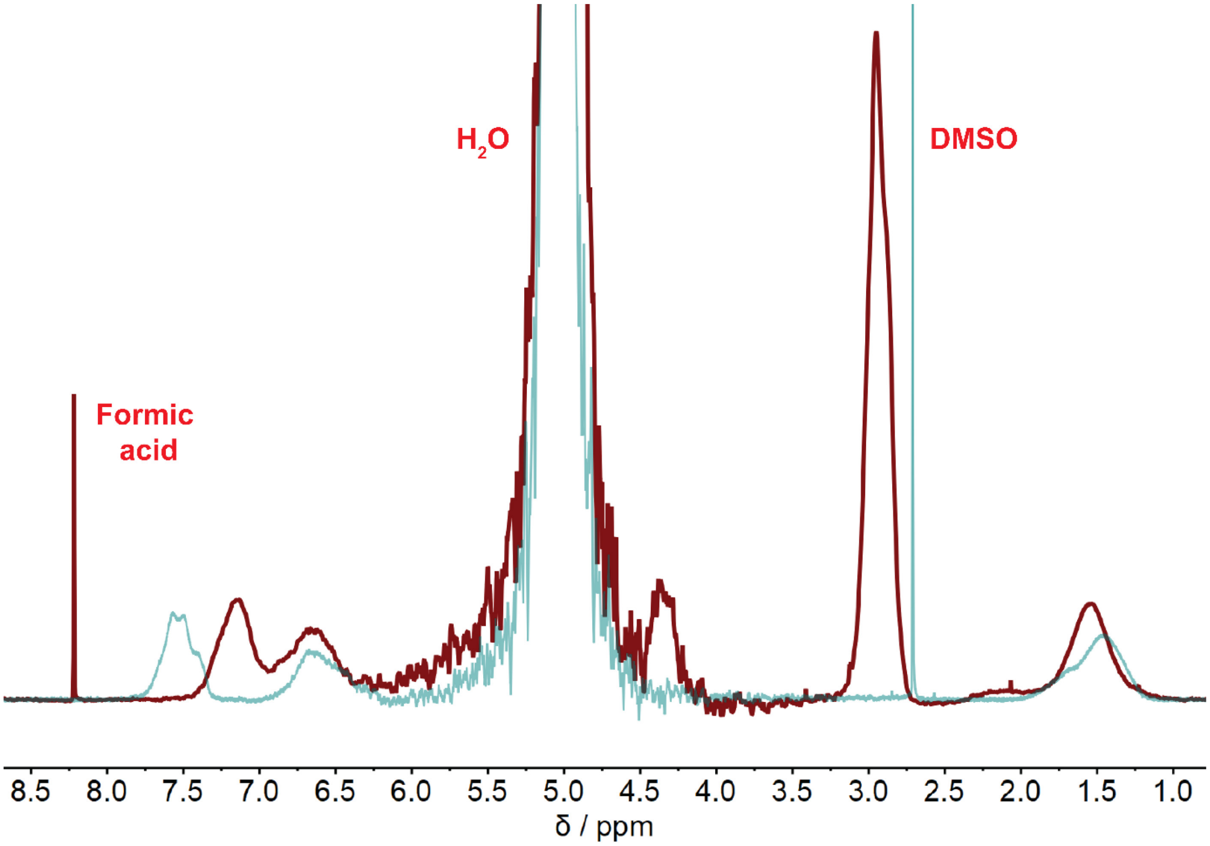

Figure S2.2. Overlay of ^{1}H NMR spectra for an aliquot of the PVBTMA–OH (maroon) solution obtained after a prolonged open-circuit V_{mem} equilibration experiment and a pristine PSS–H (turquoise) solution, indicating the absence of any significant crossover of PSS$^-$ into the PVBTMA–OH compartment.

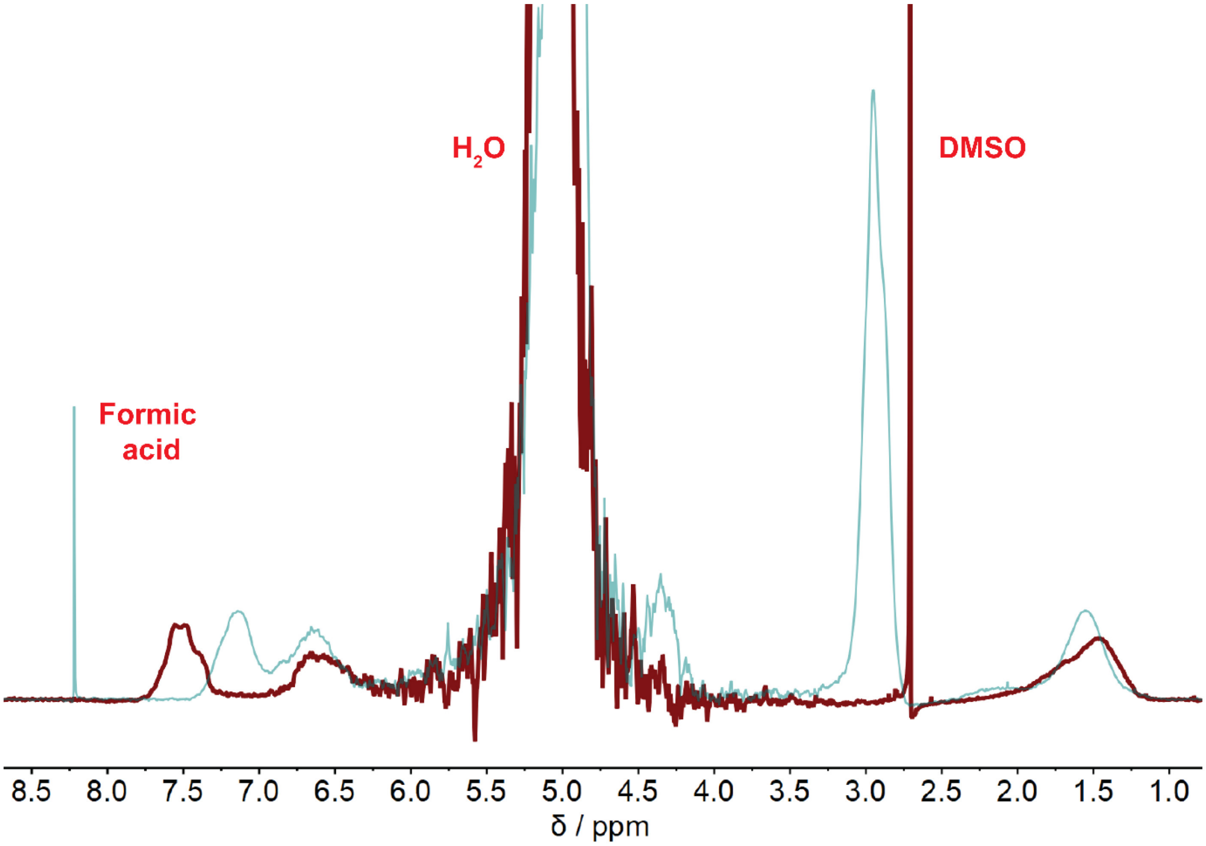

Figure S2.3. Overlay of ^{1}H NMR spectra for an aliquot of the PSS–H (maroon) solution obtained after a prolonged open-circuit V_{mem} equilibration experiment and a pristine PVBTMA–OH (turquoise) solution, indicating the absence of any significant crossover of PVBTMA$^+$ into the PSS–H compartment.

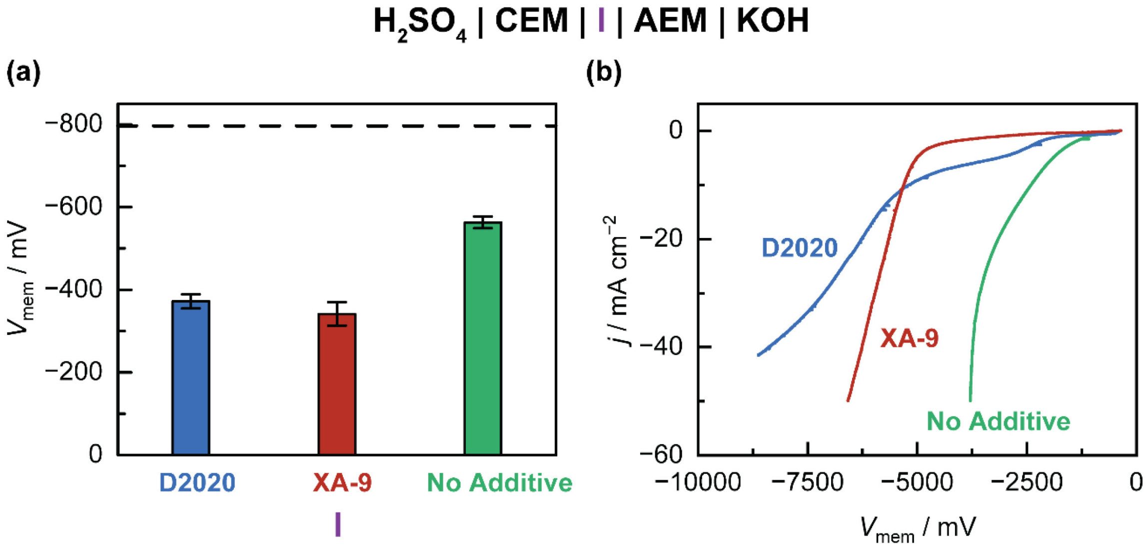

Figure S2.4. (a) Open-circuit membrane voltages and **(b)** reverse bias polarization curves for H_2SO_4 | CEM | I | AEM | KOH cells containing different interlayer additives (I = Nafion D2020 or Sustainion XA-9).

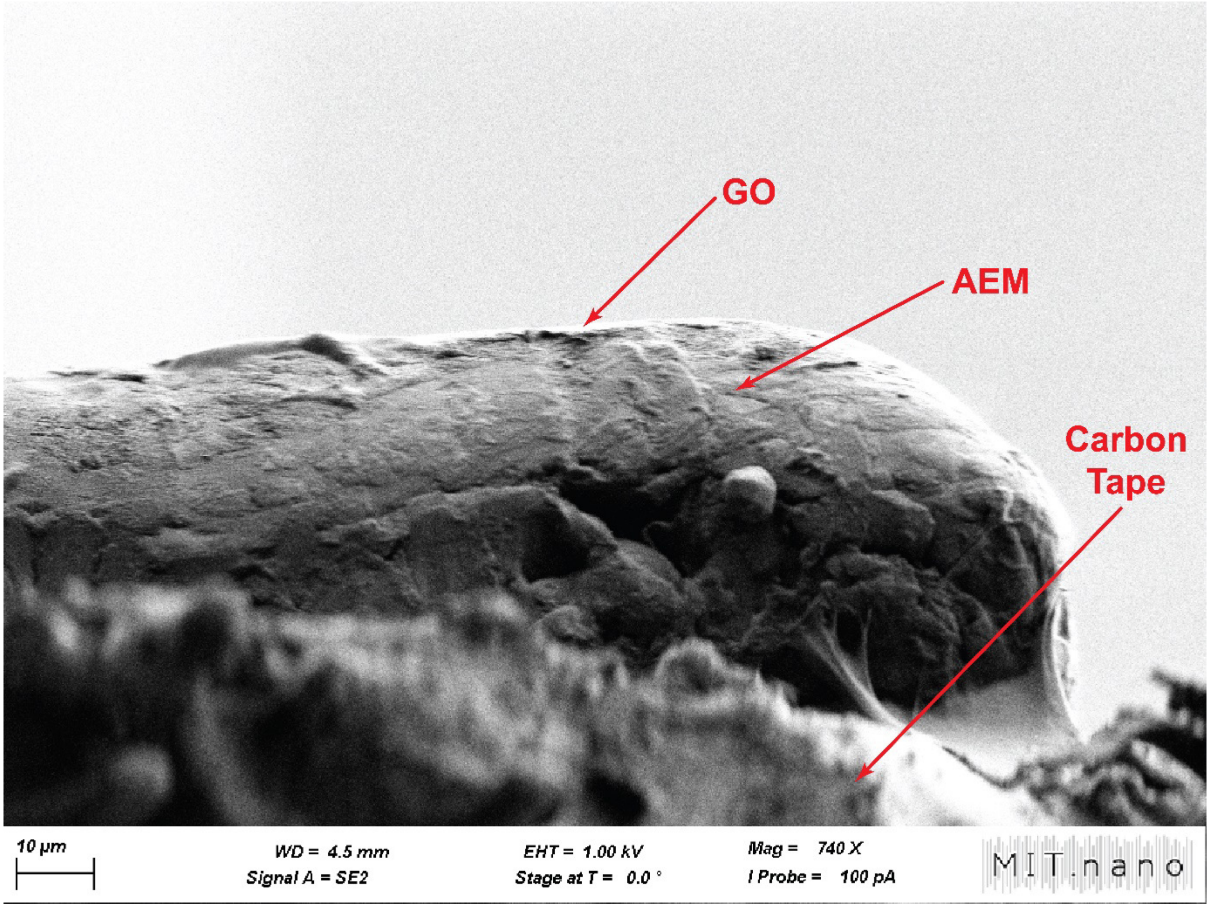

Figure S2.5. SEM image of GO | AEM composite. The GO layer is estimated to be around 1.2 µm.

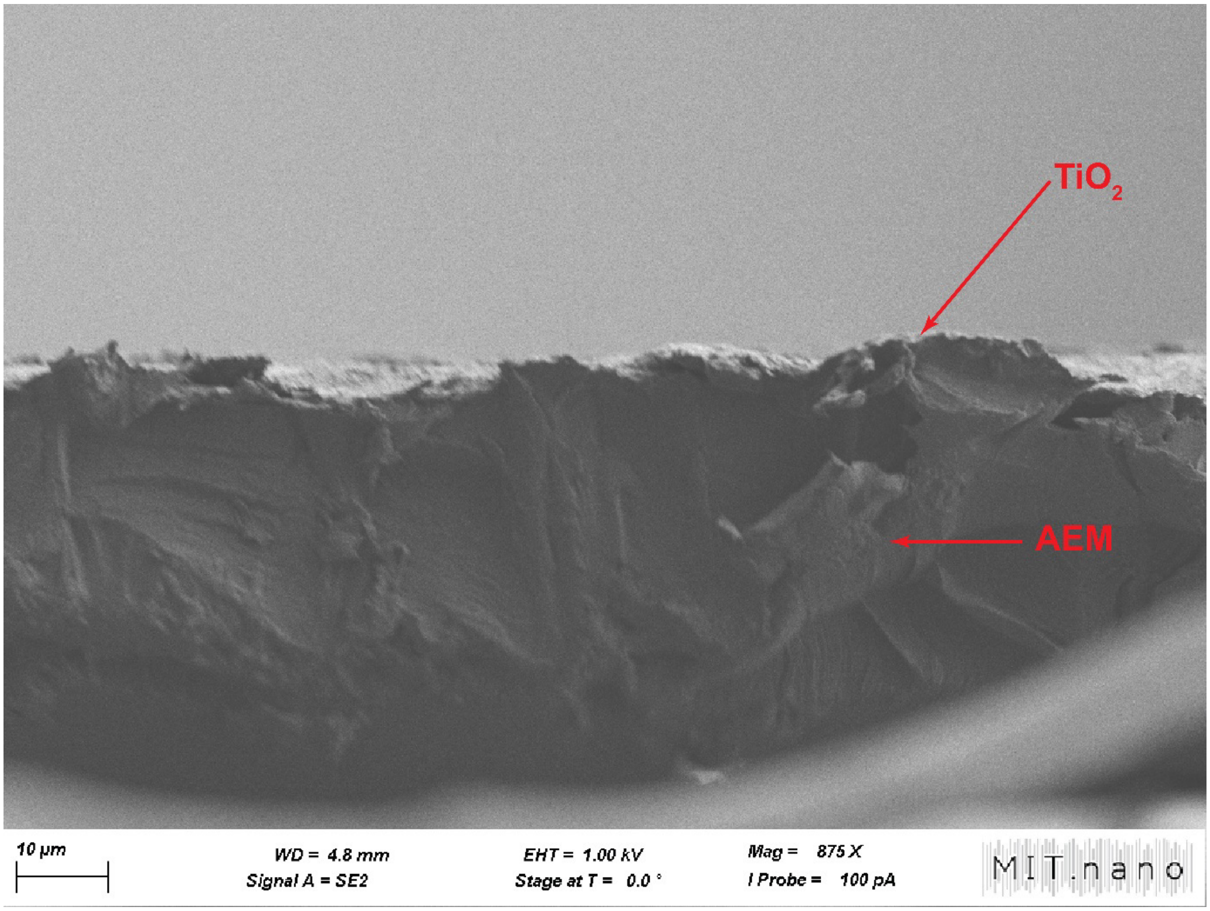

Figure S2.6. SEM image of TiO_2 | AEM composite. The TiO_2 layer is estimated to be around 410 nm.

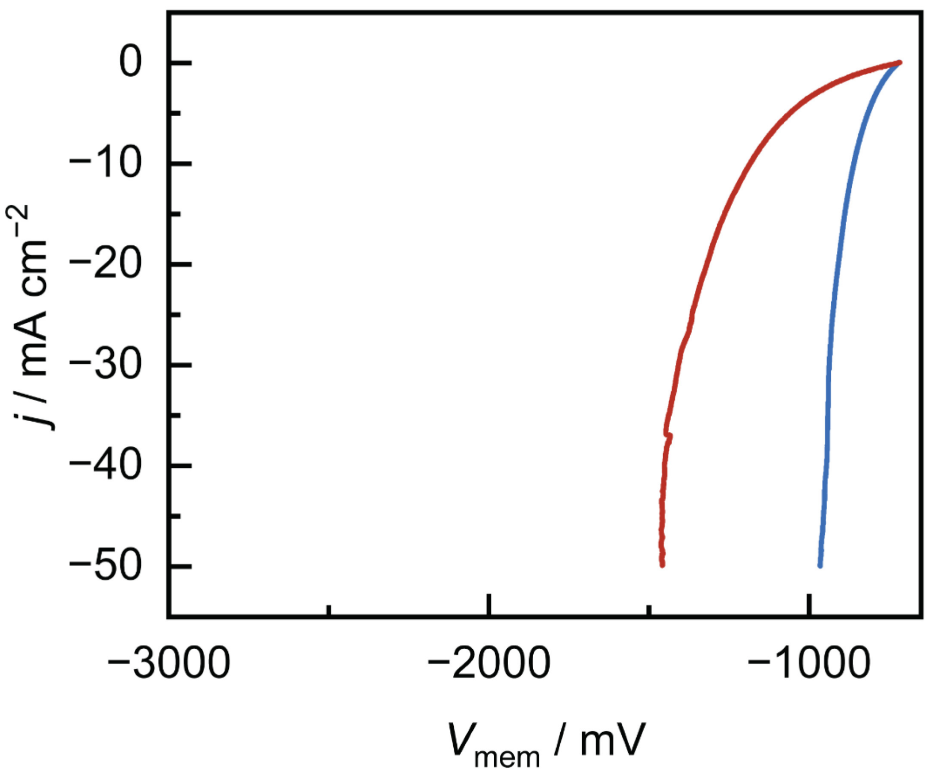

Figure S2.7. Reverse bias polarization curves for the PSS–H | GO | AEM | PVBTMA–OH (red) and PSS–H | CEM | GO | AEM | PVBTMA–OH (blue) cells, showing very similar polarization kinetics.

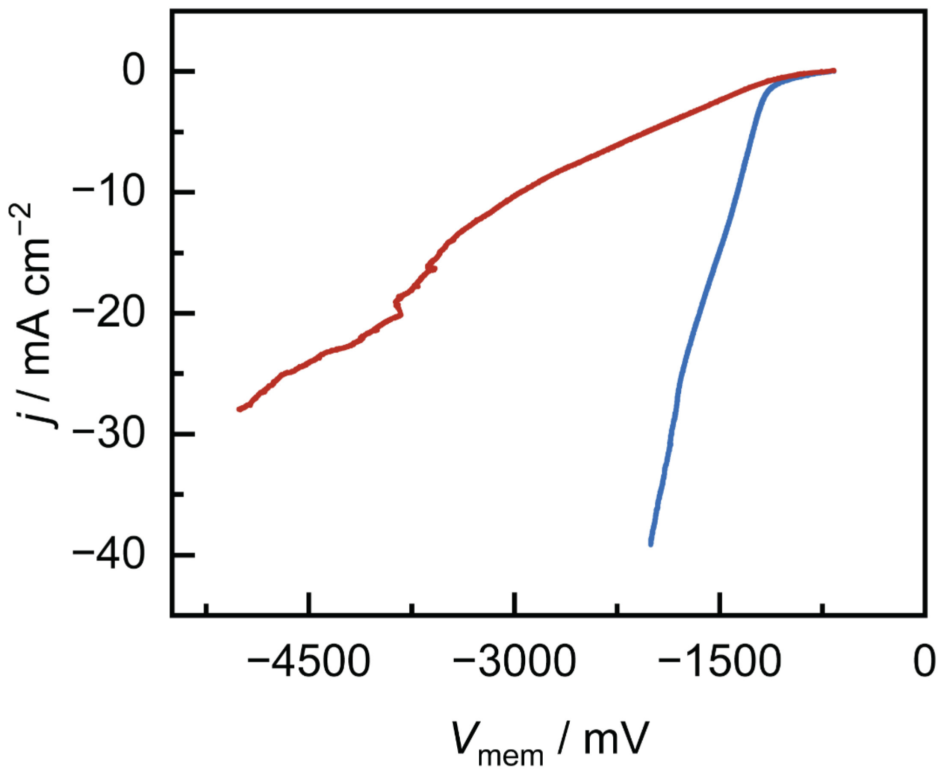

Figure S2.8. Reverse bias polarization curves for the PSS–H | TiO_2 | AEM | PVBTMA–OH (red) and PSS–H | CEM | TiO_2 | AEM | PVBTMA–OH (blue) cells, showing vastly different polarization kinetics.

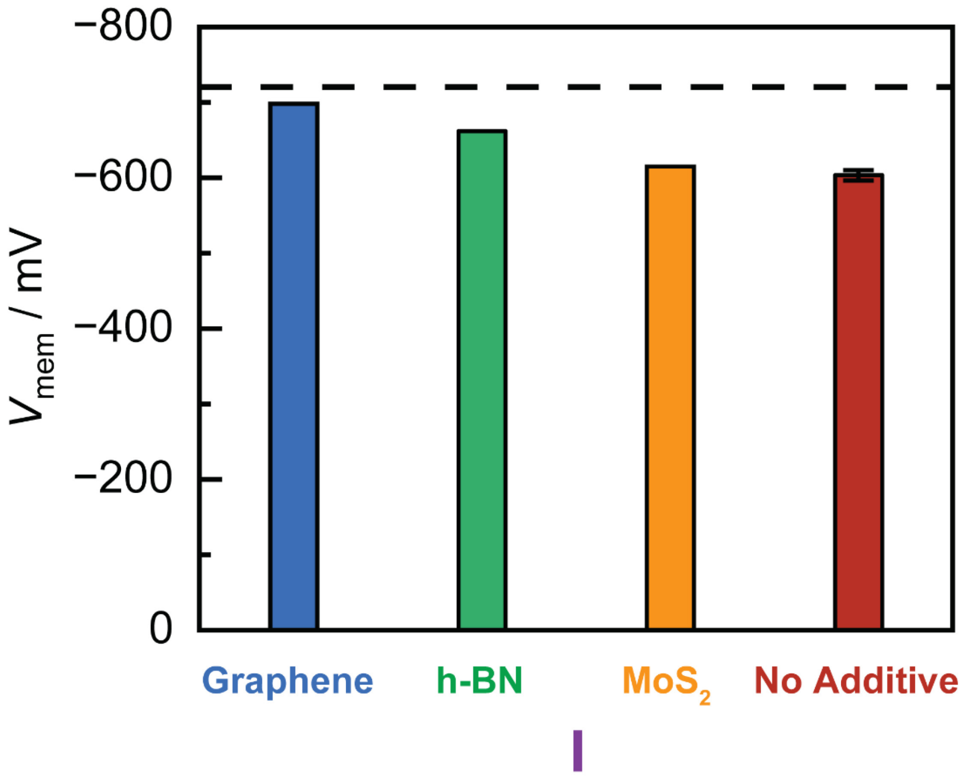

Figure S2.9. Open-circuit membrane voltages for PSS–H | I | AEM | PVBTMA–OH cells containing different layered materials, including graphene, hexagonal boron nitride (h-BN) and molybdenum disulfide (MoS_2). The horizontal dashed lines indicate the theoretical membrane voltage from **Equation 2.1**. Error bars represent the standard deviation of independent triplicate measurements.

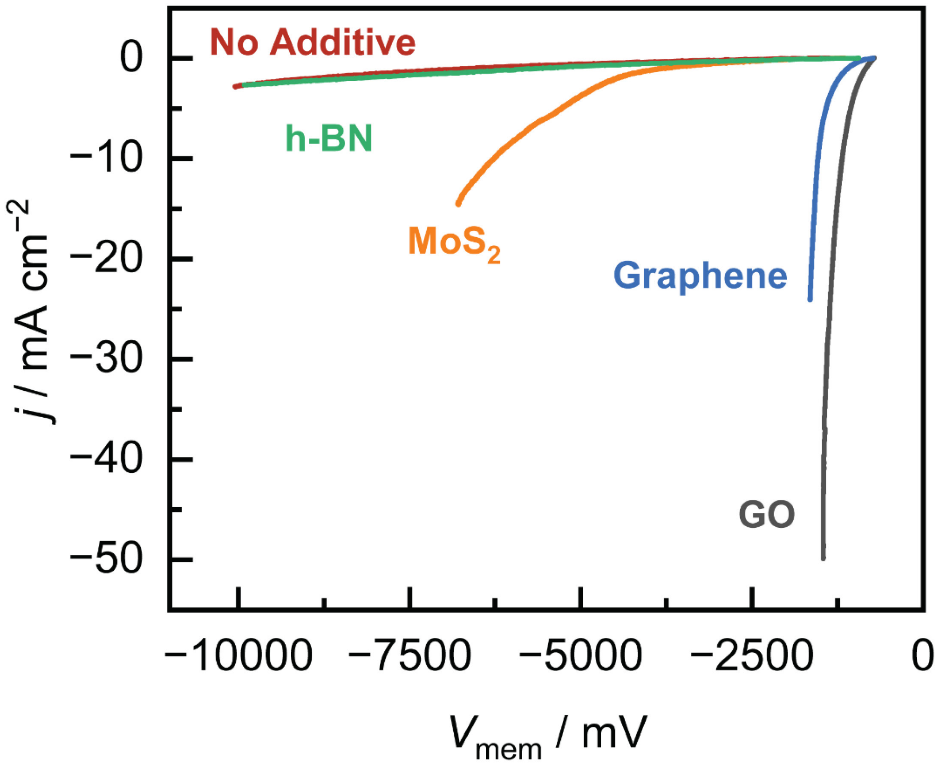

Figure S2.10. Reverse bias polarization curves for the PSS–H | I | AEM | PVBTMA–OH, showing improvements in polarization kinetics with the introduction of layered materials as interfacial additives.

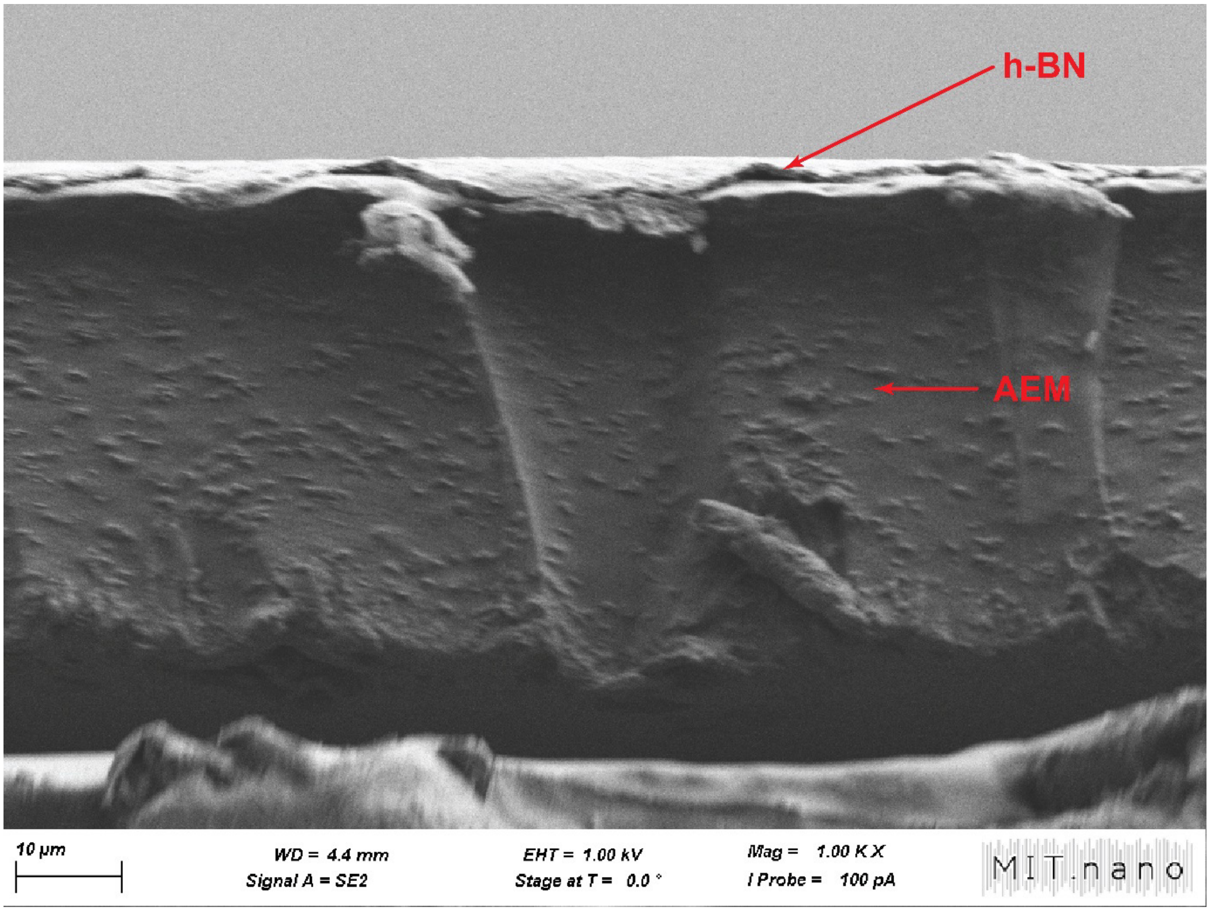

Figure S2.11. SEM image of h-BN | AEM composite. The h-BN layer is estimated to be around 1.1 µm.

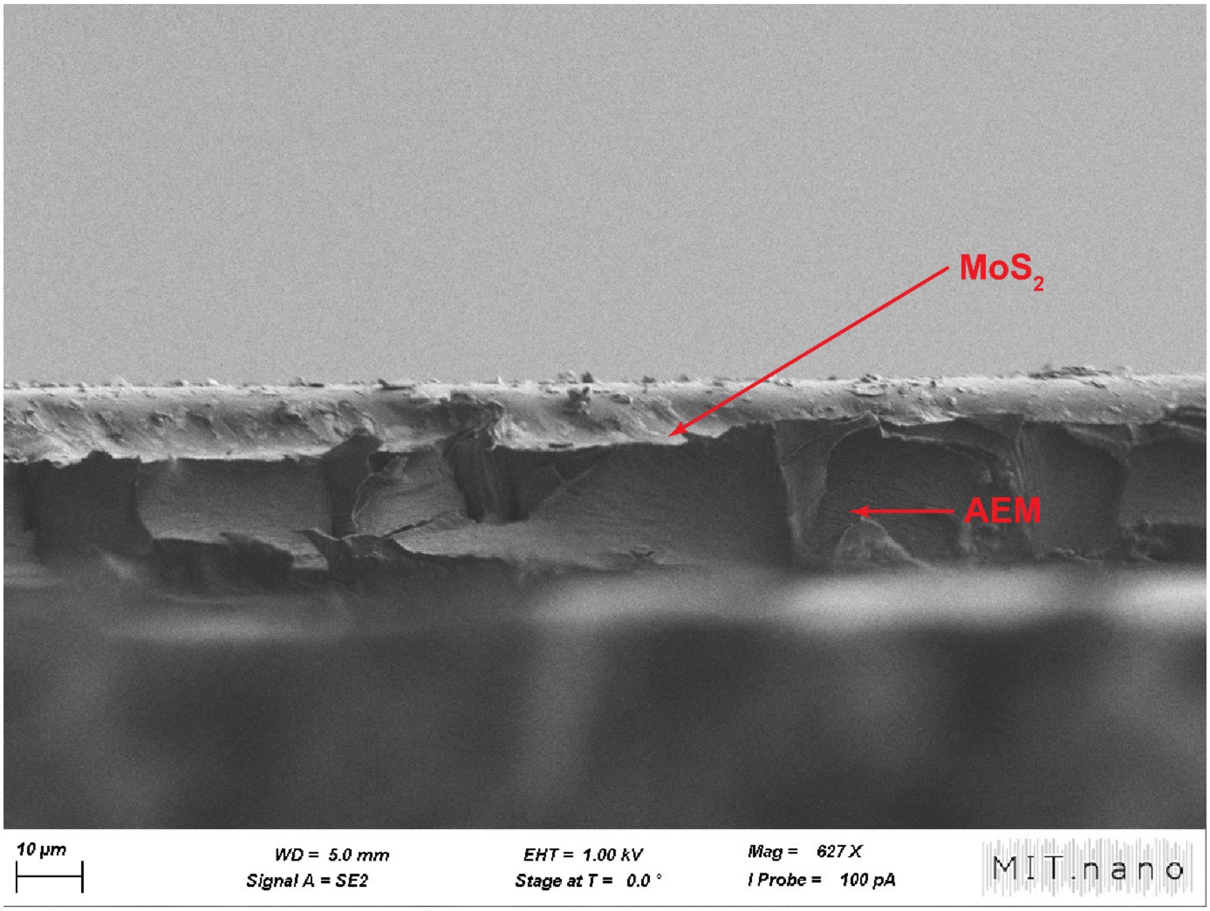

Figure S2.12. SEM image of MoS_2 | AEM composite. The MoS_2 layer is estimated to be around 570 nm.

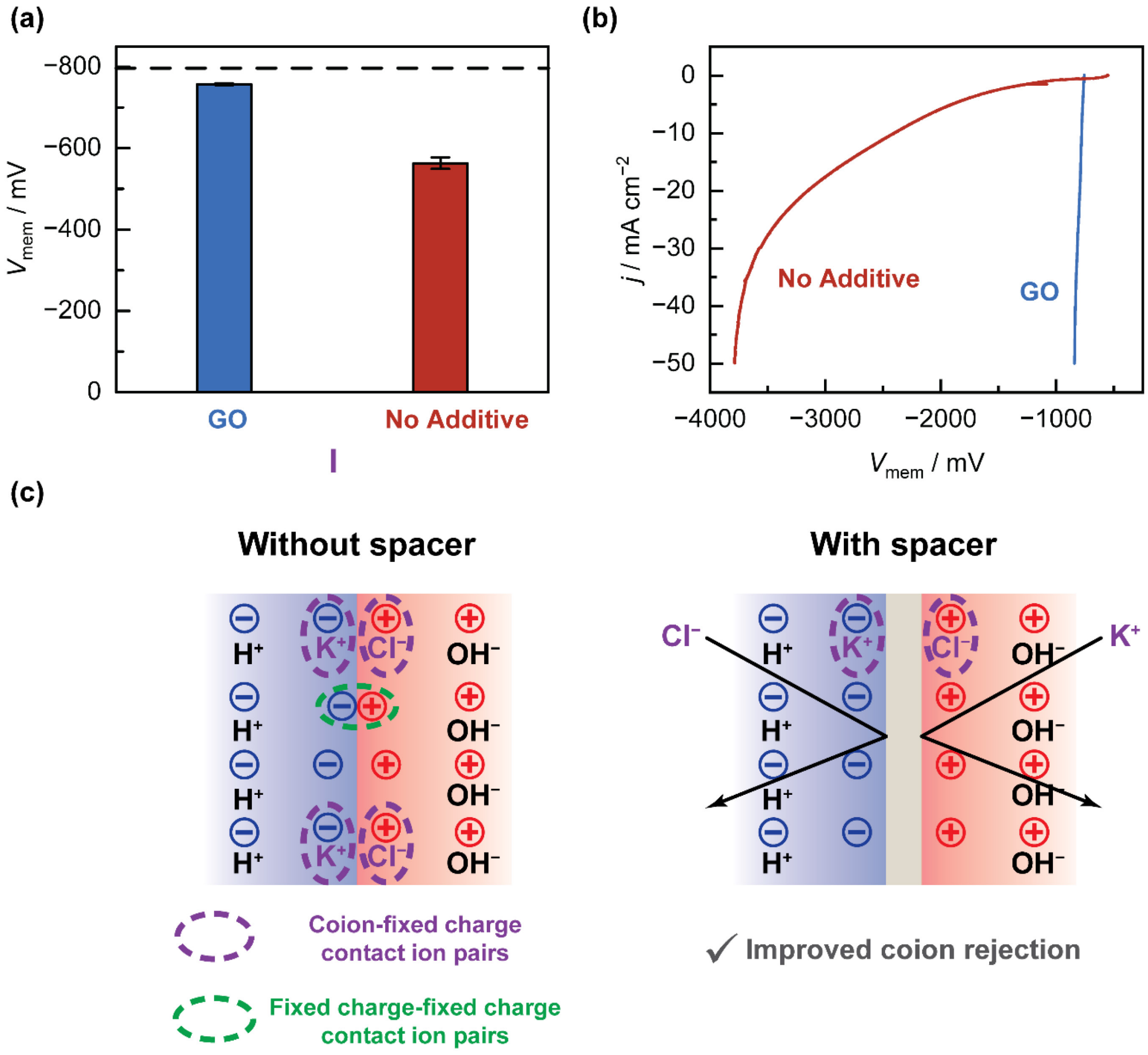

Figure S2.13. Comparison of **(a)** open-circuit membrane voltages and **(b)** reverse bias polarization curves for H_2SO_4 | CEM | I | AEM | KOH cells in the presence and absence of interlayer additives I. **(c)** Proposed configuration of fixed charges and coions at the bipolar interface in the absence and presence of an interlayer additive acting as a spacer to prevent the formation of fixed charge-fixed charge ion pairs, leading to greater Donnan exclusion of coions from the bipolar junction.

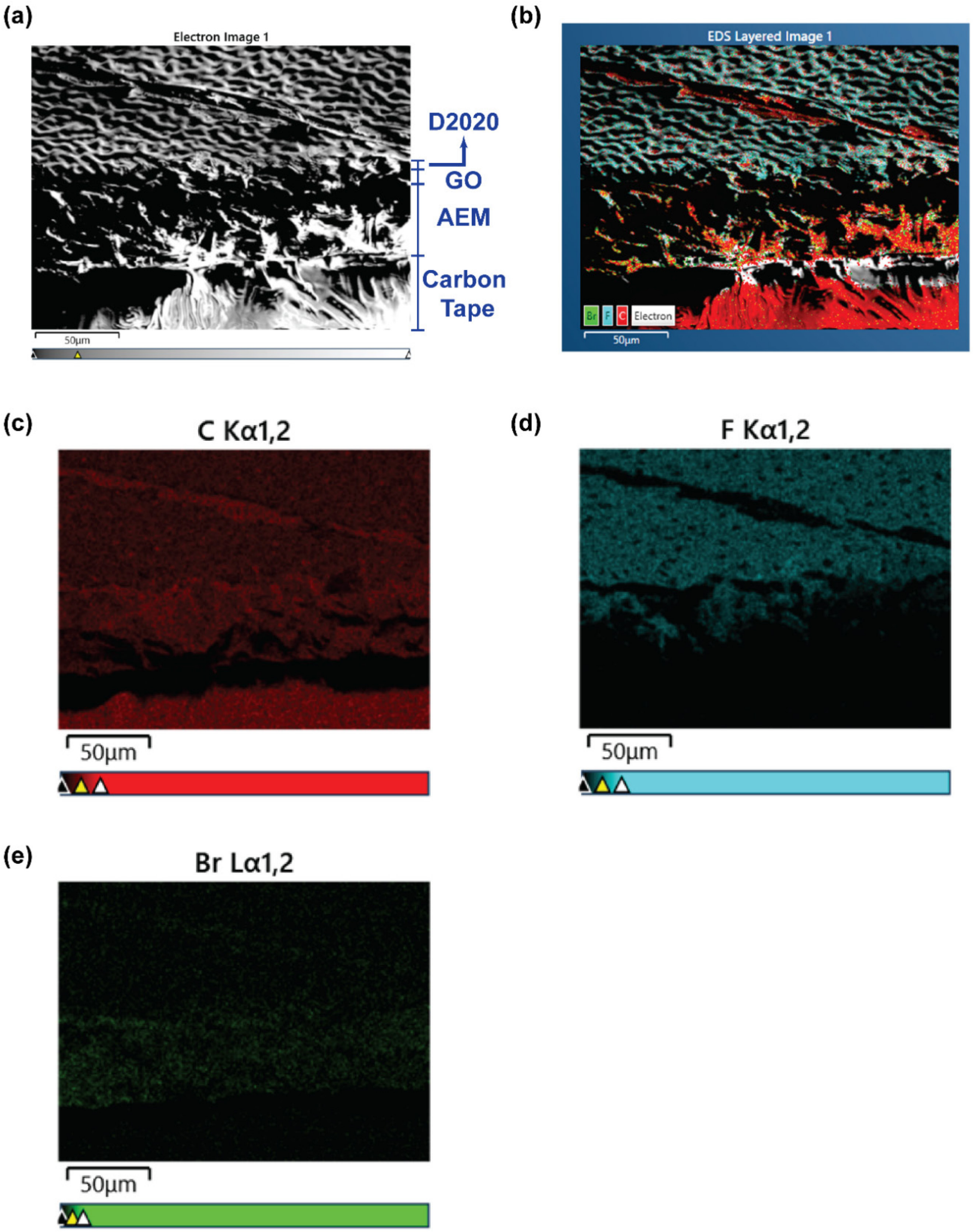

Figure S2.14. SEM-EDS characterization of D2020 | GO | AEM composite prepared via sequential deposition. **(a)** SEM image showing the approximate positions of each layer; **(b)** SEM image overlaid with EDS elemental map for C, F and Br; EDS elemental maps for the individual elements **(c)** C; **(d)** F; and **(e)** Br. The Br signals are attributed to trace residual Br^- in the AEM left behind from its synthesis process, and are used here to distinguish the AEM layer from the GO layer. We note the weak C but and strong F signal intensities in the D2020 layer, indicating the good spatial segregation of the D2020 and GO layers.

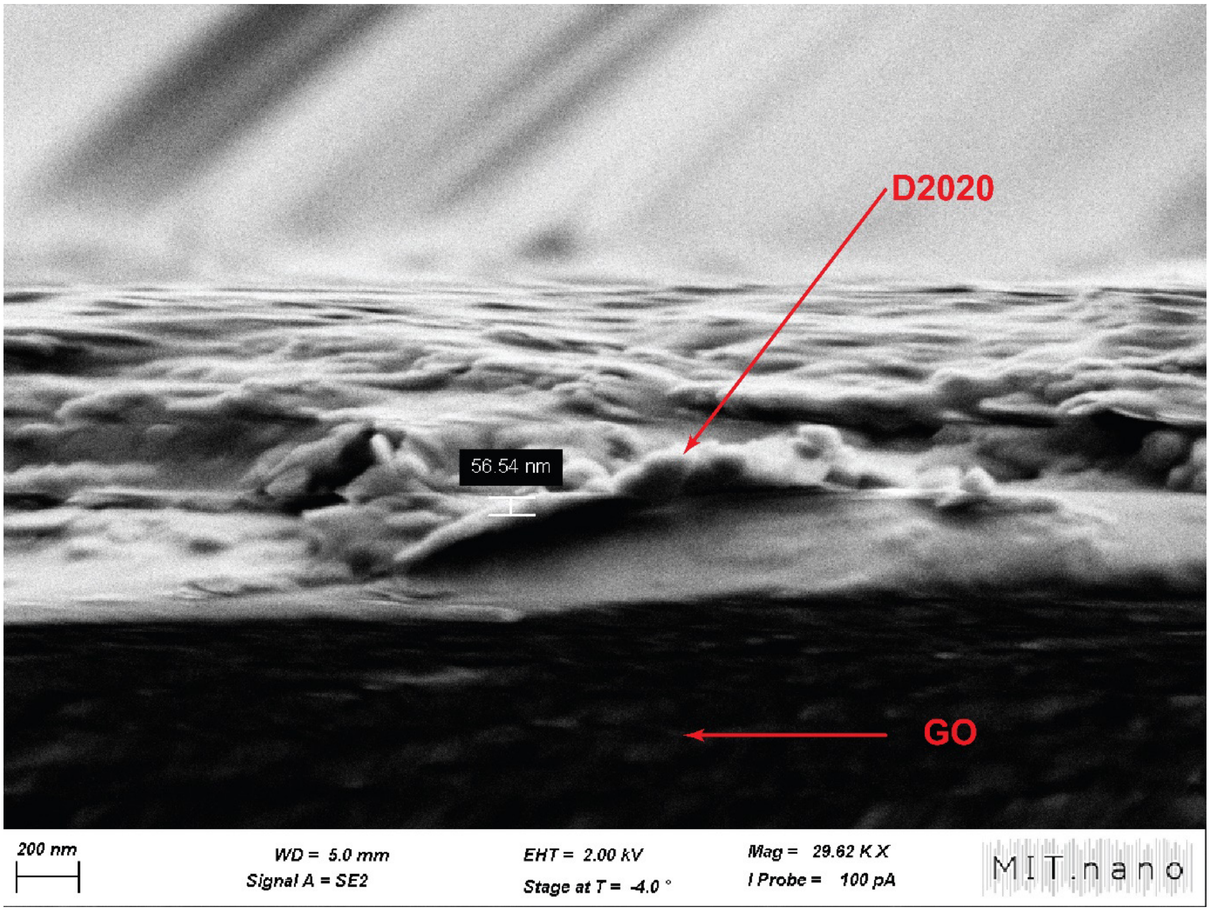

Figure S2.15. SEM image at higher magnification to show the distinct D2020 ionomer layer and GO layers in the D2020 | GO | AEM composite. The D2020 layer is estimated to be around 57 nm. The thickness of the GO layer is assumed to be similar to that of the GO | AEM composite, which is around 1.2 µm (**Figure S2.5**).

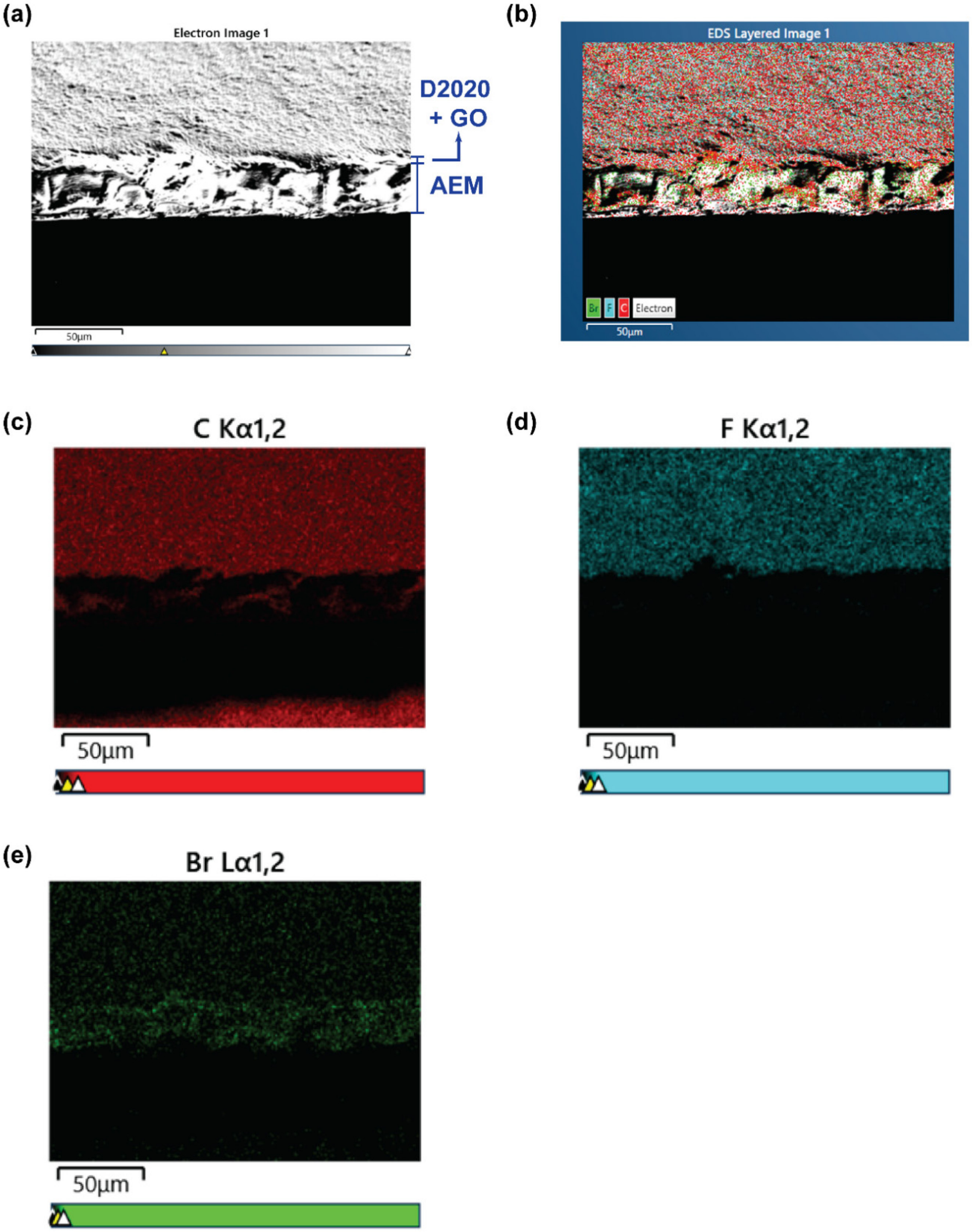

Figure S2.16. SEM-EDS characterization of D2020 + GO | AEM composite prepared via co-deposition from a pre-mixed ink. **(a)** SEM image showing the approximate positions of each layer; **(b)** SEM image overlaid with EDS elemental map for C, F and Br; EDS elemental maps for the individual elements **(c)** C; **(d)** F; and **(e)** Br. The Br signals are attributed to trace residual Br^- in the AEM left behind from its synthesis process, and are used here to distinguish the AEM layer from the GO layer. We note the strong colocalization of C and F signals in the D2020 + GO layer, indicating good mixing.

2.8 References

(1) Pärnamäe, R.; Mareev, S.; Nikonenko, V.; Melnikov, S.; Sheldeshov, N.; Zabolotskii, V.; Hamelers, H. V. M.; Tedesco, M. Bipolar Membranes: A Review on Principles, Latest Developments, and Applications. *J. Memb. Sci.* **2021**, *617*, 118538.

(2) Giesbrecht, P. K.; Freund, M. S. Recent Advances in Bipolar Membrane Design and Applications. *Chem. Mater.* **2020**, *32* (19), 8060–8090.

(3) Blommaert, M. A.; Aili, D.; Tufa, R. A.; Li, Q.; Smith, W. A.; Vermaas, D. A. Insights and Challenges for Applying Bipolar Membranes in Advanced Electrochemical Energy Systems. *ACS Energy Lett.* **2021**, *6*, 2539–2548.

(4) Tufa, R. A.; Blommaert, M. A.; Chanda, D.; Li, Q.; Vermaas, D. A.; Aili, D. Bipolar Membrane and Interface Materials for Electrochemical Energy Systems. *ACS Appl. Energy Mater.* **2021**, *4* (8), 7419–7439.

(5) Yan, Z.; Mallouk, T. E. Bipolar Membranes for Ion Management in (Photo)Electrochemical Energy Conversion. *Accounts Mater. Res.* **2021**, *2* (12), 1156–1166.

(6) Oener, S. Z.; Foster, M. J.; Boettcher, S. W. Accelerating Water Dissociation in Bipolar Membranes and for Electrocatalysis. *Science.* **2020**, *369* (6507), 1099–1103.

(7) McDonald, M. B.; Ardo, S.; Lewis, N. S.; Freund, M. S. Use of Bipolar Membranes for Maintaining Steady-State PH Gradients in Membrane-Supported, Solar-Driven Water Splitting. *ChemSusChem* **2014**, *7* (11), 3021–3027.

(8) Vargas-Barbosa, N. M.; Geise, G. M.; Hickner, M. A.; Mallouk, T. E. Assessing the Utility of Bipolar Membranes for Use in Photoelectrochemical Water-Splitting Cells. *ChemSusChem* **2014**, *7* (11), 3017–3020.

(9) Luo, J.; Vermaas, D. A.; Bi, D.; Hagfeldt, A.; Smith, W. A.; Grätzel, M. Bipolar Membrane-Assisted Solar Water Splitting in Optimal PH. *Adv. Energy Mater.* **2016**, *6* (13), 1600100.

(10) Mayerhöfer, B.; McLaughlin, D.; Böhm, T.; Hegelheimer, M.; Seeberger, D.; Thiele, S. Bipolar Membrane Electrode Assemblies for Water Electrolysis. *ACS Appl. Energy Mater.* **2020**, *3* (10), 9635–9644.

(11) Oener, S. Z.; Twight, L. P.; Lindquist, G. A.; Boettcher, S. W. Thin Cation-Exchange Layers Enable High-Current-Density Bipolar Membrane Electrolyzers via Improved Water Transport. *ACS Energy Lett.* **2021**, *6* (1), 1–8.

(12) Vermaas, D. A.; Smith, W. A. Synergistic Electrochemical CO2 Reduction and Water Oxidation with a Bipolar Membrane. *ACS Energy Lett.* **2016**, *1* (6), 1143–1148.

(13) Li, Y. C.; Zhou, D.; Yan, Z.; Gonçalves, R. H.; Salvatore, D. A.; Berlinguette, C. P.; Mallouk, T. E. Electrolysis of CO2 to Syngas in Bipolar Membrane-Based Electrochemical Cells. *ACS Energy Lett.* **2016**, *1* (6), 1149–1153.

(14) Zhou, X.; Liu, R.; Sun, K.; Chen, Y.; Verlage, E.; Francis, S. A.; Lewis, N. S.; Xiang, C. Solar-Driven Reduction of 1 Atm of CO2 to Formate at 10% Energy-Conversion Efficiency by Use of a TiO2-Protected III–V Tandem Photoanode in Conjunction with a Bipolar Membrane and a Pd/C Cathode. *ACS Energy Lett.* **2016**, *1* (4), 764–770.

(15) Salvatore, D. A.; Weekes, D. M.; He, J.; Dettelbach, K. E.; Li, Y. C.; Mallouk, T. E.; Berlinguette, C. P. Electrolysis of Gaseous CO2 to CO in a Flow Cell with a Bipolar Membrane. *ACS Energy Lett.* **2018**, *3* (1), 149–154.

(16) Pătru, A.; Binninger, T.; Pribyl, B.; Schmidt, T. J. Design Principles of Bipolar Electrochemical Co-Electrolysis Cells for Efficient Reduction of Carbon Dioxide from Gas Phase at Low Temperature. *J. Electrochem. Soc.* **2019**, *166* (2), F34–F43.

(17) Blommaert, M. A.; Sharifian, R.; Shah, N.; Nesbitt, N.; Smith, W.; Vermaas, D. A. Orientation of Bipolar Membrane Determines the Dominant Ion and Carbonic Species Transport in Membrane Electrode Assemblies for CO2 Reduction. *J. Mater. Chem. A* **2021**.

(18) Siritanaratkul, B.; Forster, M.; Greenwell, F.; Sharma, P. K.; Yu, E. H.; Cowan, A. J. Zero-Gap Bipolar Membrane Electrolyzer for Carbon Dioxide Reduction Using Acid-Tolerant Molecular Electrocatalysts. *J. Am. Chem. Soc.* **2022**, *144* (17), 7551–7556.

(19) Xie, K.; Miao, R. K.; Ozden, A.; Liu, S.; Chen, Z.; Dinh, C.; Huang, J. E.; Xu, Q.; Gabardo, C. M.; Lee, G.; Edwards, J. P.; O'Brien, C. P.; Boettcher, S. W.; Sinton, D.; Sargent, E. H. Bipolar Membrane Electrolyzers Enable High Single-Pass CO2 Electroreduction to Multicarbon Products. *Nat. Commun.* **2022**, *13* (1), 3609.

(20) Sullivan, I.; Goryachev, A.; Digdaya, I. A.; Li, X.; Atwater, H. A.; Vermaas, D. A.; Xiang, C. Coupling Electrochemical CO2 Conversion with CO2 Capture. *Nat. Catal.* **2021**, *4* (11), 952–958.

(21) Sharifian, R.; Wagterveld, R. M.; Digdaya, I. A.; Xiang, C.; Vermaas, D. A. Electrochemical Carbon Dioxide Capture to Close the Carbon Cycle. *Energy Environ. Sci.* **2021**, *14* (2), 781–814.

(22) Hohenadel, A.; Powers, D.; Wycisk, R.; Adamski, M.; Pintauro, P.; Holdcroft, S. Electrochemical Characterization of Hydrocarbon Bipolar Membranes with Varying Junction Morphology. *ACS Appl. Energy Mater.* **2019**, *2* (9), 6817–6824.

(23) Al-Dhubhani, E.; Post, J. W.; Duisembiyev, M.; Tedesco, M.; Saakes, M. Understanding the Impact of the Three-Dimensional Junction Thickness of Electrospun Bipolar Membranes on Electrochemical Performance. *ACS Appl. Polym. Mater.* **2023**, *5* (4), 2533–2541.

(24) Dinh, H. Q.; Toh, W. L.; Chu, A. T.; Surendranath, Y. Neutralization Short-Circuiting with Weak Electrolytes Erodes the Efficiency of Bipolar Membranes. *ACS Appl. Mater. Interfaces* **2023**, *15* (3), 4001–4010.

(25) Reiter, R. S.; White, W.; Ardo, S. Communication—Electrochemical Characterization of Commercial Bipolar Membranes under Electrolyte Conditions Relevant to Solar Fuels Technologies. *J. Electrochem. Soc.* **2016**, *163* (4), H3132–H3134.

(26) Vermaas, D. A.; Wiegman, S.; Nagaki, T.; Smith, W. A. Ion Transport Mechanisms in Bipolar Membranes for (Photo)Electrochemical Water Splitting. *Sustain. Energy Fuels* **2018**, *2* (9), 2006–2015.

(27) Toh, W. L.; Dinh, H.; Chu, A.; Sauvé, E.; Surendranath, Y. Ionic Blockades Control the Efficiency of Energy Recovery in Forward Bias Bipolar Membranes. *ChemRxiv* **2023**.

(28) Holdcroft, S. Fuel Cell Catalyst Layers: A Polymer Science Perspective. *Chem. Mater.* **2014**, *26* (1), 381–393.

(29) Lucas, É.; Bui, J.; Hwang, M.; Wang, K.; Bell, A.; Weber, A.; Ardo, S.; Atwater, H.; Xiang, C. Asymmetric Bipolar Membrane for High Current Density Electrodialysis Operation with Exceptional Stability. *ChemRxiv* **2023**.

(30) Lehmani, A.; Turq, P.; Périé, M.; Périé, J.; Simonin, J.-P. Ion Transport in Nafion® 117 Membrane. *J. Electroanal. Chem.* **1997**, *428* (1–2), 81–89.

(31) Suendo, V.; Eto, R.; Tanioka, A. Ionic Rectification Properties of a Bipolar Interface Consisting of a Cationic Surfactant and Cation-Exchange Membrane. *J. Colloid Interface Sci.* **2002**, *250* (2), 507–509.

(32) Kaiser, V.; Bramwell, S. T.; Holdsworth, P. C. W.; Moessner, R. Onsager's Wien Effect on a Lattice. *Nat. Mater.* **2013**, *12* (11), 1033–1037.

(33) Berlinger, S. A.; McCloskey, B. D.; Weber, A. Z. Probing Ionomer Interactions with Electrocatalyst Particles in Solution. *ACS Energy Lett.* **2021**, *6* (6), 2275–2282.

(34) McDonald, M. B.; Freund, M. S. Graphene Oxide as a Water Dissociation Catalyst in the Bipolar Membrane Interfacial Layer. *ACS Appl. Mater. Interfaces* **2014**, *6* (16), 13790–13797.

(35) Chen, Y.; Wrubel, J. A.; Klein, W. E.; Kabir, S.; Smith, W. A.; Neyerlin, K. C.; Deutsch, T. G. High-Performance Bipolar Membrane Development for Improved Water Dissociation. *ACS Appl. Polym. Mater.* **2020**, *2* (11), 4559–4569.

(36) Powers, D.; Mondal, A. N.; Yang, Z.; Wycisk, R.; Kreidler, E.; Pintauro, P. N. Freestanding Bipolar Membranes with an Electrospun Junction for High Current Density Water Splitting. *ACS Appl. Mater. Interfaces* **2022**, *14* (31), 36092–36104.

(37) Chen, L.; Xu, Q.; Oener, S. Z.; Fabrizio, K.; Boettcher, S. W. Design Principles for Water Dissociation Catalysts in High-Performance Bipolar Membranes. *Nat. Commun.* **2022**, *13* (1), 3846.

(38) Chen, F.; Chen, S.; Wang, A.; Wang, M.; Guo, L.; Wei, Z. Blocking the Sulfonate Group in Nafion to Unlock Platinum's Activity in Membrane Electrode Assemblies. *Nat. Catal.* **2023**.

(39) Shen, C.; Wycisk, R.; Pintauro, P. N. High Performance Electrospun Bipolar Membrane with a 3D Junction. *Energy Environ. Sci.* **2017**, *10* (6), 1435–1442.

(40) Ting, J. M.; Wu, H.; Herzog-Arbeitman, A.; Srivastava, S.; Tirrell, M. V. Synthesis and Assembly of Designer Styrenic Diblock Polyelectrolytes. *ACS Macro Lett.* **2018**, *7* (6), 726–733.

Chapter 3

Neutralization Short-Circuiting with Weak Electrolytes Erodes the Efficiency of Bipolar Membranes

Adapted and reprinted with permission from:

Dinh, H. Q.; Toh, W. L.; Chu, A. T.; Surendranath, Y. ACS Appl. Mater. Interfaces **2023**, 15 (3), 4001–4010. Copyright 2023 American Chemical Society

Abstract

Bipolar membranes (BPMs) are critical components of a variety of electrochemical energy technologies. Many electrochemical applications require the use of buffers to maintain stable, non-extreme pH environments, yet the impact of buffers or weak acids/bases on the electrochemical behavior of BPMs remains poorly understood. We demonstrate that for a cell containing weak electrolytes, internal pH gradients within an AEM or CEM are generated from ionic short-circuiting processes at open-circuit. Short-circuiting results from the coupling of co-ion crossover and parasitic neutralization and leads to buffering of the bipolar interface. This phenomenon, which we term *neutralization short-circuiting*, serves to erode BPM efficiency by attenuating the open-circuit membrane voltage and introducing parasitic reverse bias currents associated with weak acid/base dissociation at the interface. These findings establish a mechanistic basis for the operation of BPM cells in the presence of weak acid/base electrolytes.

3.1 Introduction

Electrochemical charge transfer and electrocatalysis is highly sensitive to the pH and electrolyte environment at each electrode interface. For many electrochemical processes, cathodic and anodic half-reactions are favored in disparate pH or electrolyte environments. Thus, strategies for operating an electrochemical cell with a pH gradient between the catholyte and anolyte are required to optimize the performance of many electrochemical devices. This pH gradient can be generated and maintained using a bipolar membrane (BPM), which consists of a cation exchange membrane (CEM) laminated onto an anion exchange membrane (AEM).[1–5] A catalyst layer is often also included in the bipolar junction between the CEM and the AEM in order to accelerate dissociation[6] or recombination reactions. BPMs display the property of ionic current rectification, allowing them to sustain differential pH and electrolyte environments optimized for cathodic and anodic half-reactions. As a result, BPMs can be operated in either reverse or forward bias polarization mode. In reverse bias polarization, electric potential gradients are transduced into chemical potential gradients, and this commonly involves the electric field-enhanced ionic dissociation of water to produce hydronium and hydroxide ions.[2,3,7,8] This mode of BPM operation has been widely applied in water electrolyzers,[6,9–13] CO_2 electrolyzers,[14–21] and bipolar membrane electrodialysis (BPMED) cells.[22,23] Alternatively, under forward bias polarization, chemical potential gradients are transduced into electric potential gradients, and this occurs via harvesting the neutralization free energy for a given acid-base pair to produce a membrane voltage.[24] This mode has been employed in redox flow batteries exploiting acid-base recombination to reach higher operating cell voltages.[25–27] Acid-base recombination has also been exploited in other contexts as well, such as to prevent CO_2 crossover to the anode,[28–30] to recover liquid products in

CO_2 electrolyzers,[31,32] as well as to maintain optimal humidity in fuel cells.[33,34] As these examples illustrate, the development of a fundamental understanding of acid-base reactivity at BPMs could enable a suite of new and improved energy technologies.

The operation of BPMs with extreme pH gradients (e.g. pH 0 | 14, 1 | 13) has been extensively studied.[3,35,36] In contrast, there exists limited understanding of BPM operation under buffered intermediate pH conditions, which contain weak electrolytes.[36–40] This is despite the fact that weak acids and bases in the form of organic moieties[2,9,41] or inorganic compounds[6,9] have been demonstrated to be efficient interlayer catalysts for water dissociation. Here, weak electrolytes refer to charged bases whose conjugate acids have a $pK_a < 14$ (e.g. OAc^-) or charged acids with a $pK_a > 0$ (e.g. NH_4^+). In other words, weak electrolytes consist of dominant charged proton carriers other than OH^- and H_3O^+. This knowledge gap persists despite the requirement for weak electrolytes in order to sustain intermediate pH operation in many electrochemical devices. For example, intermediate pH operation is often required to maximize AEM stability,[42,43] increase durability of water-splitting photoelectrodes,[3,37] and maintain high cycle stability in redox flow batteries.[44,45] These considerations emphasize the importance of uncovering mechanistic details on the operation of BPMs in the presence of weak acids and bases.

The operation of BPMs is affected by the transport of two categories of ions. Counter-ions possess the opposite charge to a given membrane, whereas co-ions possess the same charge as a given membrane and are prevented from entering the membrane by Donnan exclusion.[46,47] For example, for the cell HCl | CEM | AEM | NaOH, where the CEM is interfaced with HCl solution and the AEM is interfaced with NaOH solution, H^+ and OH^- are counter-ions to the CEM and the AEM, respectively, whereas Cl^- and Na^+ are co-ions to the CEM and AEM, respectively. In the ideal limit in which the H^+ and OH^- are the only mobile ions transiting the BPM, the membrane voltage (V_{mem}) across a BPM is simply given by the pH differential (ΔpH) across the membrane:[10,33,35]

$$
\begin{aligned}
V_{\Delta\mathrm{pH}} &= -59\ \mathrm{mV} \cdot (\mathrm{pH}_{\mathrm{Base}} - \mathrm{pH}_{\mathrm{Acid}}) \\
&= -59\ \mathrm{mV} \cdot \Delta\mathrm{pH} \qquad \textbf{Equation 3.1}
\end{aligned}
$$

where $V_{\Delta\mathrm{pH}}$ is the ΔpH-pinned membrane voltage, $\mathrm{pH}_{\mathrm{Base}}$ refers to the pH of the base solution and $\mathrm{pH}_{\mathrm{Acid}}$ refers to the pH of the acid solution. However, in any real system, membranes are never perfectly permselective.[48] Thus, co-ions can also transit across the membrane. This so-called *co-ion crossover* phenomenon is known to erode the transmembrane voltage and lead to a sigmoidal current-voltage profile characterized by a potential-independent current plateau, often referred to as the *limiting current*.[1,2] For buffered non-extreme pH environments, the presence of the buffer constituents introduces additional complexity. Indeed, for weak electrolyte systems, **Equation 3.1** is known to overpredict membrane voltages,[36] and, in some cases, the membrane voltage has been observed to correlate with the $\mathrm{p}K_{\mathrm{a}}$ of buffering constituents, rather than the pH differential.[36,38] The mechanistic origin of both of these observations remains unclear. In addition, while contributions from buffering species to the limiting current have been analyzed computationally,[38,40] no supporting experimental characterizations have been reported hitherto. Given that the membrane voltage and limiting current are key descriptors of the efficiency for water dissociation and acid-base recombination in BPMs, these pervasive knowledge gaps have prevented systematic improvement of BPM efficiency under the intermediate pH conditions often required for device function.

Herein, we demonstrate that ionic short-circuiting reactions resulting from the coupling of co-ion crossover with weak electrolyte neutralization generate a substantial internal pH gradient within the AEM or CEM portion of the BPM. This gradient serves to suppress the transmembrane voltage to a value dictated by the pK_a of the weak electrolyte, rather than the full pH differential across the BPM. We further find that ionization of the neutral conjugate acid or base generated via short-circuiting augments the limiting current observed in reverse bias. Both effects erode the efficiency of BPM operation. These findings highlight the critical role of parasitic neutralization reactions in defining the polarization behavior of BPMs in weak electrolyte-containing media and motivate new strategies for electrolyte management to maximize BPM efficiency.

3.2 Neutralization Short-Circuiting Produces Internal pH Gradients in Bipolar Membranes

To analyze ion transfer processes occurring in BPMs, we examined the commercial BPM, Fumasep FBM, in a four-electrode set-up (**Figure S3.1**). In this work, unless otherwise stated, we will use the nomenclature (Acid) | (Base) to refer to a cell containing 1 M of acid on the CEM side and 1 M of base on the AEM side of the BPM. These cells will all be of the type HCl/H_2SO_4 | KA or BHCl | KOH, where A^- represents a weak base and BH^+ represents a weak acid. In addition, as all measurements of membrane voltage (V_{mem}) were made by sensing the electric potential of the acid solution with respect to the base solution, V_{mem} will be reported as a negative value, with polarization to more negative values indicating reverse bias. Currents are reported based on measurements of electrical current through the external circuit, and hence negative currents correspond to reverse bias polarization. In this study, we assume that the concentration of fixed charges in the CEM and AEM are 1 M, and hence Donnan potentials at the membrane-electrolyte interfaces are assumed to be 0 mV (see **Supplementary Discussion 3.1** for details and justification).

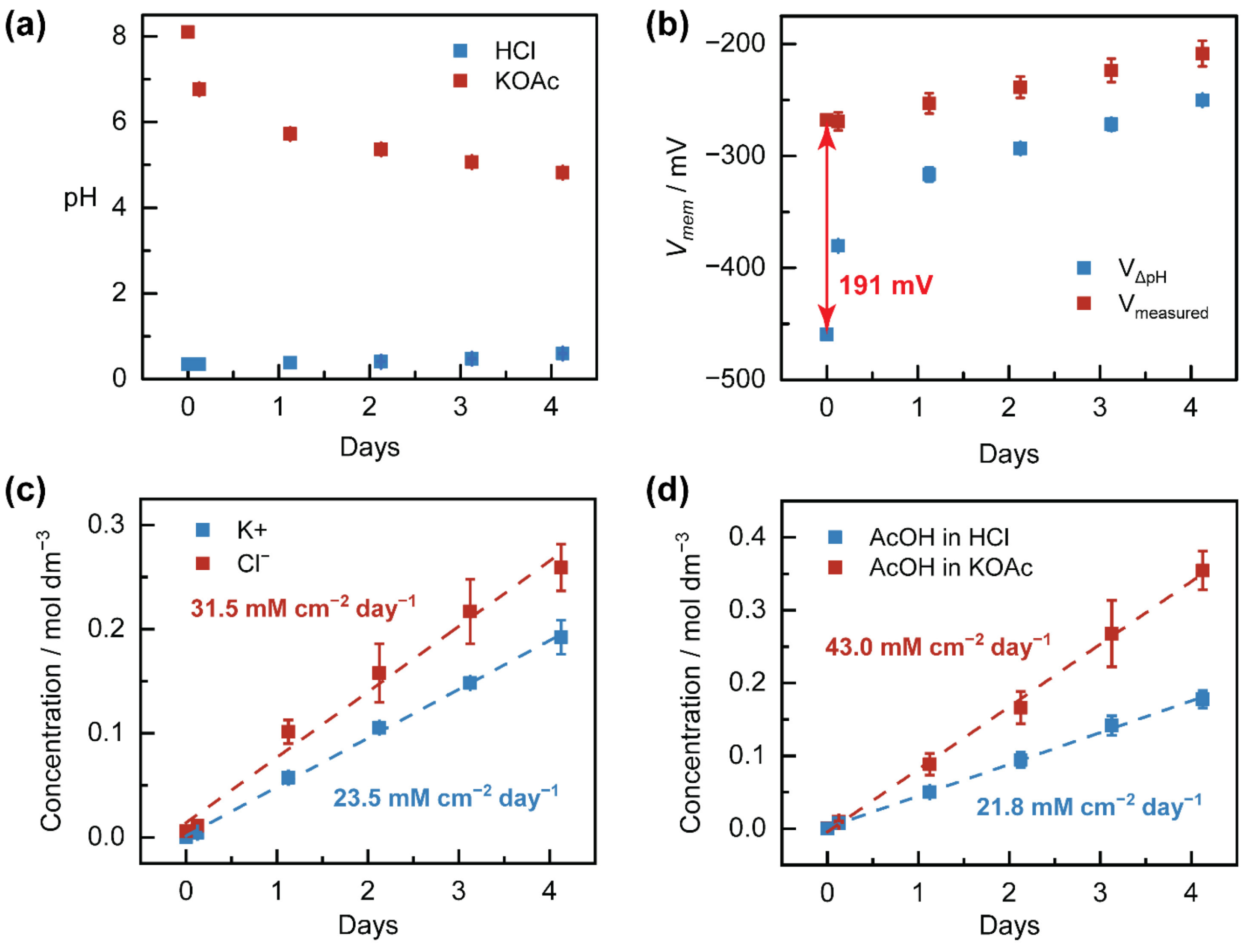

Figure 3.1. Plots showing the time evolution of **(a)** pH of HCl and KOAc solutions, **(b)** open-circuit membrane voltage, **(c)** crossover concentrations of co-ions K+ and Cl$^-$, **(d)** AcOH concentration in HCl and KOAc solutions for the cell HCl | KOAc measured over 4 days. Rates reported are normalized to the surface area of the membrane (2 cm^2). Measurements were performed in duplicate (n = 2) and error bars represent the absolute difference between duplicate points.

In order to study the effect of using weak electrolytes in BPM cells, we employed HCl | KOAc as a model cell and began by examining its properties at open-circuit. The open-circuit condition ensures that no *net* ionic current flows across the membrane. Despite this constraint, we observe that the pH of the two solutions drifted over the course of four days: the pH of the KOAc solution decreased from 8.1 to 4.8 and that of the HCl solution increased from 0.3 to 0.6 (**Figure**

3.1(a)). KOAc displayed a much larger change than the strong acid HCl, owing to its initial pH being closer to neutral and the logarithmic nature of the pH scale. In addition, the absolute value of V_{mem} also increased from −268 mV to −209 mV (**Figure 3.1(b)**). The measured V_{mem} deviated greatly from $V_{\Delta\mathrm{pH}}$ (**Equation 3.1**), with the deviation being as large as 191 mV in the initial time points, equivalent to ~3.2 pH units. Instead, V_{mem} was found to be close to $-59\ mV \cdot pK_a(AcOH)$. During this same period, we also analyzed aliquots taken from the two compartments and measured the concentration of crossover co-ions (K^+ in HCl; Cl^- in KOAc) and AcOH in each solution using ICP-OES and ^1H NMR respectively. The rates of crossover of both co-ions were found to be appreciable, with ~0.18 M K^+ and ~0.25 M Cl^- having been transferred across the BPM after four days (**Figure 3.1(c)**). Comparable concentrations of AcOH had also accumulated in the two compartments over four days, with ~0.18 M in HCl and 0.35 M in KOAc (**Figure 3.1(d)**). Specifically for the KOAc solution, the AcOH present could be determined using the measured pH and the Henderson-Hasselbalch equation (see **3.6 Experimental Methods** for calculation). The foregoing observations indicate that the HCl | KOAc cell is subject to progressive co-ion crossover concomitant with the generation of acetic acid.

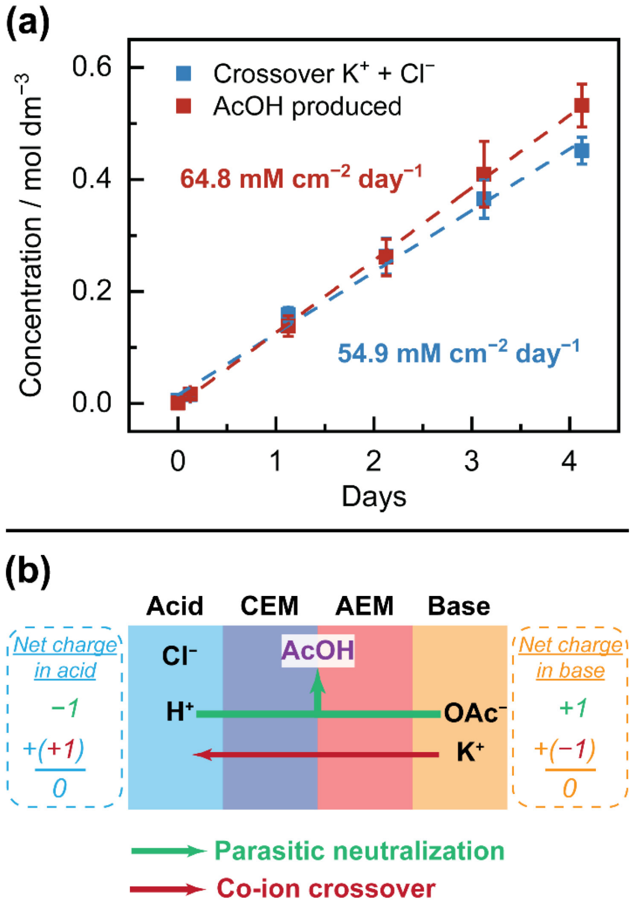

Figure 3.2. (a) Time evolution plot comparing the concentrations of total crossover K^+ and Cl^- with AcOH produced for the HCl | KOAc cell, showing a nearly 1:1 ratio between transfer rates. Rates reported are normalized to the surface area of the membrane (2 cm^2). **(b)** Charge balance diagram showing how the coupling of co-ion crossover with parasitic neutralization conserves electroneutrality, using K^+ as an example. A similar scheme for Cl^- crossover is presented in **Figure S3.11**.

The co-ion crossover rates correspond to the rate of acid-base neutralization. Specifically, for the HCl | KOAc cell, we find a ~1:1 correspondence between the total amount of co-ions that cross over and total amount of AcOH formed. This correspondence holds across the entire time series, indicating similar rates of the two processes (**Figure 3.2(a)**). Similarly, for the NH_4Cl | KOH cell, where NH_3 is formed as the neutralization product, we find that the total co-ion crossover rate matches the NH_3 accumulation rate, with conservations of the same stoichiometric ratio (**Figure S3.9**). These observations are in line with the understanding that crossover of a co-ion leads to a charge imbalance between the two solutions. This charge imbalance can be alleviated by coupling to parasitic neutralization of acid and base at the bipolar junction. Thus, stoichiometric balance between co-ion crossover and acid-base neutralization allows for electroneutrality to be conserved in the system (**Figure 3.2(b); Figure S3.11**). This overall process can be understood as a form of *ionic short-circuiting*, whereby leakage ionic current from the two coupled processes of co-ion crossover and counter-ion recombination flow at open-circuit due to the imperfect permselectivities of the two membranes. In order to distinguish this particular phenomenon from the short-circuit processes that can occur for ion flow in BPM reverse electrodialysis (RED) devices,[49,50] we term this overall process *neutralization short-circuiting*. Co-ion crossover has long been acknowledged as an issue that compromises the energy efficiency of BPM cells and the purity of acid and base streams generated from water dissociation under reverse bias polarization.[39,51] Indeed, using total co-ion crossover rates, the overall neutralization short-circuiting rate could be expressed as an electrical current, and was found to be 1.53 mA cm^{-2} (**Supplementary Discussion 3.2**) which was found to be in good agreement with the computed sum of 1.8 mA cm^{-2} for the open-circuit co-ion crossover of K^+ and Cl^- in a pH 0 | 7 1 M HCl | 1 M $K_iH_jPO_4$ cell incorporating the same FBM.[38] Importantly, in a typical HCl | KOH cell, the product of acid-base neutralization is water, which cannot be directly quantified against the 55 M bulk water background in the medium. Hence, by replacing the commonly used KOH in BPM cells with KOAc, we were able to directly observe the AcOH and quantify the rate for parasitic neutralization. By comparing the co-ion crossover and parasitic neutralization rates, these data evince a quantitative correspondence between the two processes as the basis for neutralization short-circuiting.

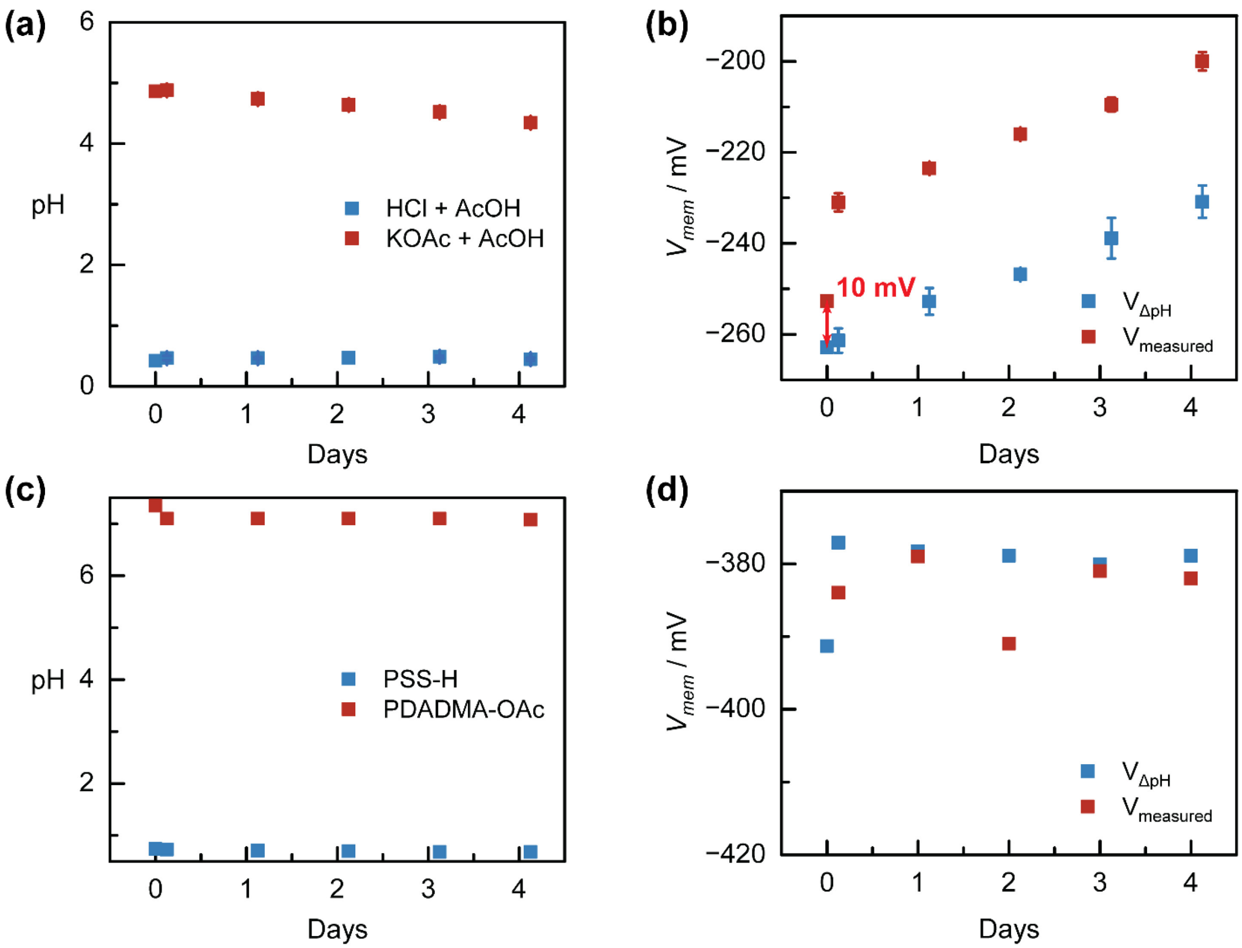

Figure 3.3. Plots showing the time evolution of **(a)** pH of HCl and KOAc solutions, and **(b)** open-circuit membrane voltage for the cell HCl + AcOH | KOAc + AcOH, as well as the time evolution of **(c)** pH of PSS–H and PDADMA–OAc solutions, and **(d)** open-circuit membrane voltage for the cell PSS–H | PDADMA–OAc measured over 4 days. For **(a)** and **(b)**, measurements were performed in duplicate (n = 2) and error bars represent the absolute difference between duplicate points.

To investigate the effect of the concentration of the neutralization product (i.e. the conjugate acid or base of the weak electrolyte ion) on the neutralization short-circuiting mechanism, we performed similar open-circuit crossover experiments with the cell HCl + AcOH | KOAc + AcOH, wherein 1 M AcOH was added to the solution on both sides of the BPM. The pH values of both solutions were found to be more stable over time, remaining at ~0.4 for the HCl side and decreasing only by ~0.6 units from 4.9 to 4.3 for KOAc side (**Figure 3.3(a)**). In this cell, we find that V_{mem} matches $V_{\Delta\mathrm{pH}}$ within ~10 mV (**Figure 3.3(b)**) as opposed to the 191 mV discrepancy observed for the HCl | KOAc cell (**Figure 3.1(b)**) at the earliest timepoint. Additionally, we note that the magnitude of V_{mem} for the HCl + AcOH | KOAc + AcOH (−253 mV) is comparable to the value for the HCl | KOAc cell (−268 mV) on day 0, despite the dramatically different pH differential between the solutions across the BPM for HCl | KOAc (0 | 8.3) and HCl + AcOH | KOAc + AcOH (0 | 4.76). As an aside, we observed notable differences in co-ion crossover rates between the HCl | KOAc and HCl + AcOH | KOAc + AcOH cells, and these are shown in **Figure S3.3** and discussed in **Supplementary Discussion 3.3.** The observation that addition of 1 M AcOH to the electrolyte solutions does not significantly change V_{mem} lends further support to the aforementioned finding that neutralization short-circuiting leads to acetic acid generation at the bipolar interface in the HCl | KOAc cell.

The foregoing data led us to postulate that a BPM cell devoid of co-ions would be free from co-ion crossover and therefore be immune to neutralization short-circuiting. To test this hypothesis, we employed polyelectrolytes, which are polymers containing charged monomer units. Specifically, we replaced the Cl^- and K^+ present in the HCl | KOAc cell with poly(4-styrene sulfonate) (PSS^-) and poly(diallyldimethylammonium) ($PDADMA^+$), respectively. PSS–H and PDADMA–OAc were prepared via ion-exchange dialysis using commercial PSS-Na and PDADMA–Cl as starting materials (see **3.6 Experimental Methods**). Owing to the high molecular weight of these polyelectrolytes (average of 70 kDa for PSS^- and 100 kDa for $PDADMA^+$, respectively), we envisioned that crossover across the BPM would be physically inhibited due to size-exclusion. We performed the same open-circuit crossover experiments for the PSS–H | PDADMA–OAc cell, and found that, in contrast to the HCl | KOAc cell, the pH of both the PSS–H and PDADMA–OAc solutions remained unchanged over time at ~0.7 and ~7.1 respectively (**Figure 3.3(c)**). In addition, as opposed to the HCl | KOAc cell, V_{mem} matched $V_{\Delta\mathrm{pH}}$ throughout the experiment (**Figure 3.3(d)**). Analysis of aliquots taken from the two solutions for the crossover of the polyelectrolyte co-ions revealed negligible rates of crossover (**Figure S3.6**). Examination of the day four aliquot of the PSS–H solution via NMR revealed that ~13.5 mM AcOH had been produced at the end of four days (**Figure S3.6**). We attribute this small crossover to trace oligomeric impurities present in PSS–H. Nonetheless, with polyelectrolytes, the generated AcOH is far smaller than the 0.53 M AcOH generated in HCl | KOAc cell (**Figure 3.1(d)**). Taken together, these results establish that co-ion crossover enables parasitic neutralization at the bipolar interface, and that neutralization short-circuiting at open-circuit can be dramatically inhibited by sterically blocking co-ion transport.

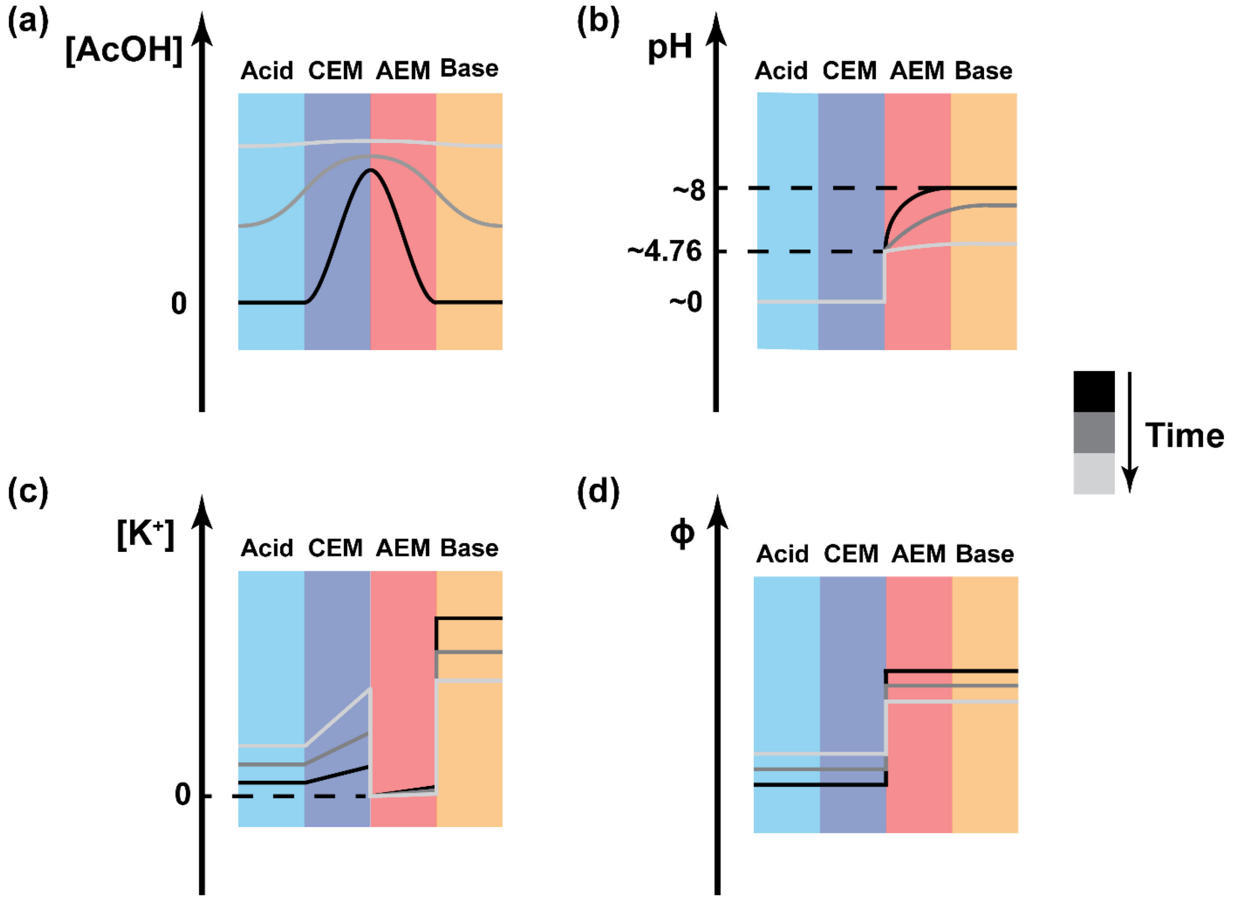

Figure 3.4. Theorized time evolution of **(a)** AcOH concentration profile, (b) pH profile, (c) K^+ concentration profile (as an example co-ion) and (d) electrostatic potential profile for the HCl | KOAc cell held at open-circuit. The actual potential drop may not be symmetric as depicted in (d).

The foregoing data allow us to propose the following model for the behavior of BPMs in the presence of weak electrolytes. Theorized profiles of AcOH concentration, the pH, K^+ concentration, and the electrostatic potential as a function of time are shown in **Figure 3.4**, and have been qualitatively sketched based on previously reported transport modelling on a similar cell (1 M HCl | 1 M $K_iH_jPO_4$, pH 0 | 7).[38] Specifically, we posit that production of AcOH enabled by co-ion crossover leads to a high local concentration of AcOH at the bipolar junction in the HCl | KOAc cell (**Figure 3.4(a), black trace**). This in turn has the effect of buffering the pH on the

AEM side containing OAc^{-}, but has no effect on the pH on the CEM side, where pH << pK_a (AcOH). The production of a large concentration of AcOH on the order of the OAc^{-} concentration within the near-interfacial region of the AEM occurs within a short-timescale, prior to the first timepoint (30 min). As a result, the pH difference between the near-interfacial regions of the CEM and AEM decreases from 0 | 8.1 to 0 | ~4.76 (**Figure 3.4(b), black trace**), in line with the pK_a for AcOH of 4.76. Since V_{mem} is only sensitive to the acid-base neutralization thermochemistry at the bipolar junction, it becomes pinned to $\sim -59\text{ mV}\cdot(4.76-0) = -59\text{ mV}\cdot \mathrm{p}K_{\mathrm{a}}(\mathrm{AcOH})$ as opposed to $-59\text{ mV}\cdot\Delta\mathrm{pH} = -59\text{ mV}\cdot(8.3-0)$, even though the pH of the bulk solutions has not significantly changed. Since the pH is sensitive to the ratio of [AcOH]:[OAc^{-}], the gradient in AcOH across the AEM translates into a pH gradient between the bulk value of 8.3 and the putative interfacial value of 4.76. We stress that V_{mem} becomes decoupled from the bulk solution pH differential as it is only determined by the excess fixed charge that arises as a result of the neutralization equilibrium at the bipolar interface. The concentration profile of K^{+} (as an example co-ion) and electrostatic potential profile at the very beginning of the experiment are also plotted in **Figure 3.4** (black trace). We highlight that small amounts of co-ion crossover early in the experiment are sufficient for the bipolar interface to be buffered by the AcOH produced.

This interfacial buffering behavior for HCl | KOAc stands in stark contrast to the HCl | KOH cell, where parasitic neutralization generates water as the product. Since the bulk solvent is already water, the presence of additional water does not appreciably change the pH within either the CEM or AEM, meaning the interfacial pH gradient is the same magnitude as the pH gradient between the two solutions, and V_{mem} pins to $V_{\Delta\text{pH}}$. Over time, due to continual co-ion crossover, parasitic neutralization at the bipolar junction, and the diffusion of AcOH out of the bipolar junction, the concentrations of AcOH as well as crossover co-ions in the two bulk solutions increase (**Figure 3.4(a), gray trace**)**.** However, the interfacial concentration of AcOH has already reached a high value at early times and continues to increase only by a small extent, leading to small changes in ΔpH at the bipolar junction (**Figure 3.4(b), gray trace**) and the corresponding V_{mem} (**Figure 3.1(b); Figure 3.4(d), gray trace**). Since V_{mem} is controlled by the gradient in electrochemical potential of the proton across the BPM, the pH of the HCl solution is not changing significantly over time, and V_{mem} has been decoupled from the pH of the KOAc solution due to interfacial buffering, we ascribe further increases in the value of V_{mem} beyond the initial timepoints after taking interfacial buffering into account for both the HCl | KOAc (**Figure 3.1(b))** and HCl + AcOH | KOAc + AcOH cells (**Figure 3.3(b))** to further increases in the concentration of AcOH in the near-interfacial region of the AEM, which lowers the pH in the same region. The bulk K^+ concentration in KOAc decreases as it continues to cross over (**Figure 3.4(c), gray trace**)**.** At an even later timepoint, co-ions and AcOH continue to accumulate in the two bulk solutions as the pH of KOAc and the electrostatic potential drop continues to increase (**Figure 3.4, white trace**). However, the concentration gradient of AcOH will not become level and the electrostatic potential drop will not stop increasing until co-ion crossover has ceased. This should occur at long timescales when global equilibrium has been attained across the BPM, which in turn occurs when the electrochemical potential of the proton has equalized across the two solutions and membranes, both co-ions have attained the same concentration in both compartments, and the pH and composition of the two solutions becomes the same, (i.e. 0.5 M KCl, 0.5 M AcOH) and V_{mem} reaches ~0 mV. In fact, this global equilibrium condition for neutralization short-circuiting also applies to the HCl | KOH cell, except that because water is produced as the neutralization product and released into an aqueous environment, there is effectively no gradient in proton activity and therefore pH within either membrane, and V_{mem} here is not susceptible to buffering effects.

In contrast, when co-ion crossover is prevented, as is the case with PSS–H | PDADMA–OAc, continual AcOH production cannot occur. The trace amount of AcOH generated from the Nernst-Planck equilibrium attained at the bipolar junction does not significantly perturb the pH in the near-interfacial region of the OAc$^-$-containing AEM, and eventually diffuses into the two solutions. Hence, the interfacial pH gradient is similar in magnitude to the pH difference between the two bulk solutions, and V_{mem} is pinned to $V_{\Delta\mathrm{pH}}$. Therefore, we conclude that the pinning of V_{mem} to $-59\ mV \cdot pK_a(AcOH)$ for the HCl | KOAc cell arises from interfacial buffering made possible by a continuous co-ion crossover-coupled parasitic neutralization reaction to produce AcOH.

3.3 Unbuffered Weak Electrolyte-Containing Cells Are Universally Buffered at the Bipolar Interface

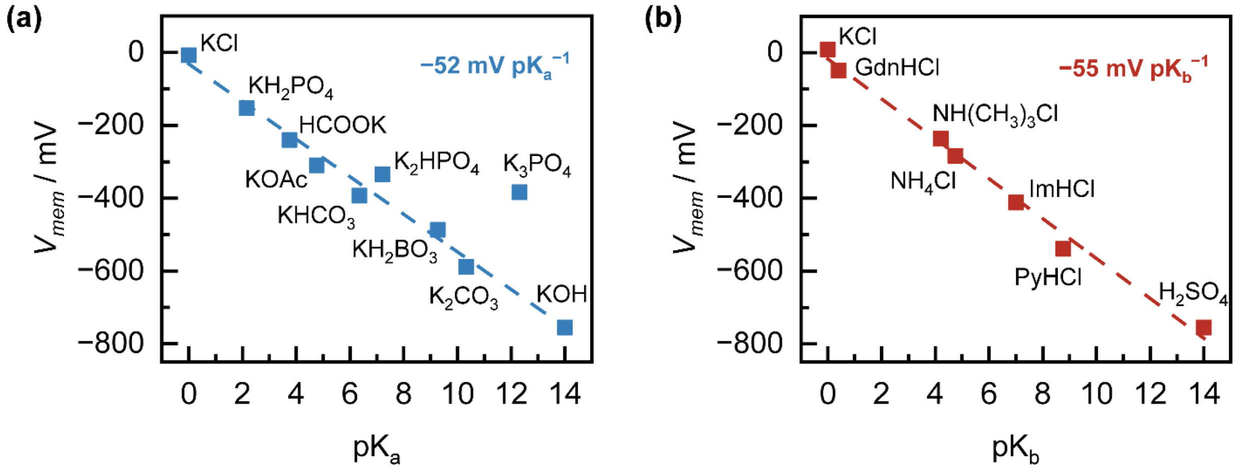

Figure 3.5. Plots of open-circuit membrane voltage vs **(a)** pK_a of conjugate acid neutralization product (HA) generated for H_2SO_4 | KA cells, and **(b)** pK_b of conjugate base neutralization product (B) generated for BHCl | KOH cells. The pH and pK_a values of all solutions used are listed in **Table S3.2** and **Table S3.3**. Continuous open-circuit V_{mem} measurements are presented in **Figure S3.14** – **Figure S3.29**. The K_3PO_4 outlier was excluded for linear regression in **(a)**.

Based on the foregoing mechanistic model, we postulated that the V_{mem} correlation with pK_a would hold across all weak acids/bases. To test the hypothesis, we examined the open circuit V_{mem} (OCV) of a series of H_2SO_4 | KA cells, where A^- is the conjugate base of a weak acid HA. We find that the OCV scales by −52 mV pK_a^{-1} (**Figure 3.5(a)**) but shows no correlation with the $V_{\Delta pH}$ (**Figure S3.13(a)**). An analogous −55 mV pK_b^{-1} scaling trend holds across a series of BHCl | KOH cells where BH^+ is the conjugate acid of a weak base B (**Figure 3.5(b)**). Similarly, this acid variation series displays no correlation between OCV and the $V_{\Delta pH}$ either (**Figure S3.13(b)**). These near-Nernstian slopes allow us to state generally that, when concentrations of electrolytes used are 1 M, for a H_2SO_4 | KA cell,

$$V_{\mathrm{mem}}\,(\mathrm{H_2SO_4} \mid \mathrm{KA}) \approx -59\ \mathrm{mV} \cdot \mathrm{p}K_{\mathrm{a}}(\mathrm{HA}) \qquad \textbf{Equation 3.2}$$

and for a BHCl | KOH cell,

$$V_{\mathrm{mem}}\,(\mathrm{BHCl} \mid \mathrm{KOH}) \approx -59\ \mathrm{mV} \cdot \left(14 - \mathrm{p}K_{\mathrm{a}}(\mathrm{BH^+})\right)$$

$$= -59\ \mathrm{mV} \cdot \mathrm{p}K_{\mathrm{b}}(\mathrm{B}) \qquad \textbf{Equation 3.3}$$

In the case of H_2SO_4 | KA cells, **Equation 3.2** holds true not only for monoprotic bases A^-, but also for diprotic bases A^{2-}, whereby V_{mem} is pinned to pK_{a} of HA^- (e.g. $A^{2-} = CO_3^{2-}$, HPO_4^{2-} in **Figure 3.5(a)**). The H_2SO_4 | K_3PO_4 cell notably deviates from this relation. Instead, the open-circuit V_{mem} for H_2SO_4 | K_3PO_4 is more closely pinned to the pK_{a} of $H_2PO_4^-$. This suggests that the near-interfacial region of the AEM is enriched in $H_2PO_4^-$ and HPO_4^{2-} with a low local concentration of PO_4^{3-}. We attribute this phenomenon to the rate of HPO_4^{2-} and $H_2PO_4^-$ accumulation outpacing that of PO_4^{3-} diffusion towards the bipolar interface, which could in turn be due to the higher-valent PO_4^{3-} species experiencing a larger attenuation in its diffusion coefficient within the AEM than lower-valent $H_2PO_4^-$ and HPO_4^{2-} species.[52] This leads to the near-interfacial region of the AEM having a pH close to the pK_{a} of $H_2PO_4^-$. Although we can find the phenomenological trends in **Equation 3.2** and **Equation 3.3** to hold quite broadly, we stress that the precise value of V_{mem} will depend on the charge density of the membrane, the rate of conjugate acid/base production due to co-ion crossover, and the rate of diffusion of the conjugate acid/base away from the bipolar junction, since these are the factors that will determine the speciation local to the bipolar junction. The correlation of V_{mem} to the pK_{a} of a species within the BPM has been observed but remained unexplained.[36,38] In this study, through the use of single-component weak electrolyte solutions instead of complex electrolyte mixtures to set a particular pH,[36] we were able to isolate the relationship between V_{mem} and the identity of electrolyte. These findings establish that the phenomenon of pK_{a}-pinned V_{mem} results from interfacial buffering arising from neutralization short-circuiting.

3.4 Open-Circuit Dynamics Impact Reverse Bias Polarization Behavior

The foregoing understanding of the pH gradients that develop between the BPM junction and the bulk solution informs on the qualitative and quantitative features of the polarization curve in reverse bias. Under reverse bias, the field-enhanced water dissociation reaction (WDR) can occur at voltages past its thermodynamic dissociation voltage, V_{WDR}, of −830 mV.[33,53–55] However, due to the non-ideal permselectivities of the CEM and the AEM, current can flow at voltages well positive of V_{WDR} due to parasitic co-ion crossover. The majority of the limiting (and underlimiting) current which appears at underpotentials to V_{WDR} is commonly attributed to co-ion crossover,[36,37,39,56] though some contribution from WDR has been invoked at voltages near V_{WDR}.[40] Buffer reactions have also been implicated as contributors to the limiting current in previous computational studies involving phosphate buffers,[38,40] and the impact of pK_{a} on Na^+ co-ion crossover under polarization in a HX/KX | CEM | AEM | NaOH cell (where HX/KX represent a buffer couple) has been examined.[39] However, to the best of our knowledge, no experimental studies exist that systematically examine the extent to which these buffer reactions impact reverse bias polarization when the weak electrolyte is a counter-ion to the BPM, or the interplay of buffer reactions in such a scenario with field-driven co-ion crossover.

Having established above that neutralization short-circuiting at open-circuit generates a reservoir of the neutralization product at the junction, we sought to isolate the impact of this phenomenon on the polarization behavior of the system. We held a H_2SO_4 | KOAc cell at open-circuit for varying time durations and then recorded steady-state galvanodynamic scans. We found that the reverse bias limiting current, j_{lim}, increased from −3.7 mA cm^{-2} following 30 min at open-circuit to −6.4 mA cm^{-2} following five days at open-circuit (**Figure 3.6(a)**). We stress that this increase in j_{lim} is at odds with the expected progressive decrease in co-ion crossover flux over time as concentrations of K^+ and HSO_4^-/SO_4^{2-} in the KOAc and H_2SO_4 compartments, respectively decrease.

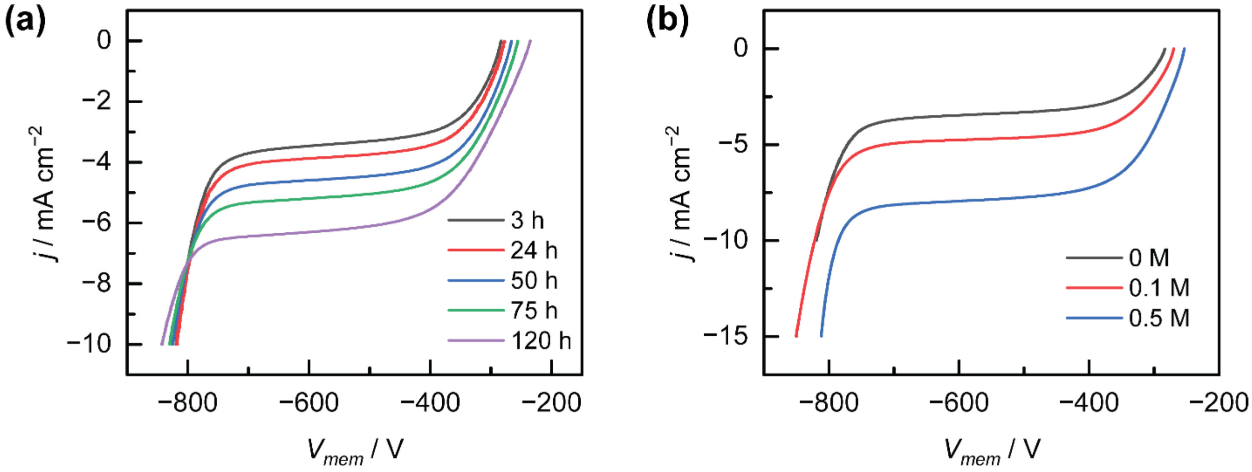

Figure 3.6. Reverse bias polarization curve of **(a)** H_2SO_4 | KOAc at varying timepoints and **(b)** H_2SO_4 | KOAc with varying concentrations of added AcOH after 3 h of equilibration.

Instead, similar to how water dissociates in reverse bias at its thermodynamic breakdown voltage of −830 mV,[33,53–55] weak acids and bases can also undergo ionization at the bipolar junction to generate charge carriers. Here, AcOH can dissociate to produce H^+ and OAc^-, i.e.

$$\mathrm{AcOH} + \mathrm{H_2O} \rightarrow \mathrm{H_3O^+} + \mathrm{AcO^-} \qquad \textbf{Equation 3.4}$$

which can then conduct current. The increase in j_{lim} with time would then be consistent with the accumulation of AcOH in the cell due to neutralization short-circuiting at open-circuit as discussed above **(Figure 3.1(d)**). In addition, the increase in j_{lim} with time was found to be linear (**Figure S3.30(a)**), similar to neutralization short-circuiting rates (**Figure 3.1(c) – (d)**). Indeed, when AcOH is explicitly added to the cell H_2SO_4 | KOAc, j_{lim} measured after the same equilibration time (3 h) was found to increase from −3.7 mA cm^{-2} to −8.1 mA cm^{-2} for AcOH concentrations ranging from 0 to 0.5 M (**Figure 3.6(b)**). AcOH dissociation can proceed via either a *direct mechanism* (whereby AcOH transfers a proton onto H_2O) or an *indirect mechanism* (whereby a fast H_2O autoionization step produces OH^- which then deprotonates AcOH). However, with the present data, we are unable to determine which mechanism is operative. Although buffer reactions have been invoked in models,[38,40] direct experimental insight into their effect on polarization behavior has yet to be attained. Here, our results are consistent with AcOH dissociation being the origin of the additional current when AcOH concentration is raised.

To rule out the possibility that the increase in j_{lim} with increasing AcOH concentration resulted from enhancing co-ion crossover rates, we measured polarization curves with polyelectrolytes, using the PSS–H | PDADMA–OAc cell and varying concentrations of added AcOH. Despite the incorporation of polyelectrolytes that inhibit co-ion crossover, we nonetheless observed that j_{lim} substantially increased upon addition of AcOH from −1.2 mA cm^{-2} at 0 M AcOH to −10.8 mA cm^{-2} at 1 M AcOH (**Figure S3.31**). Importantly, despite inhibition of co-ion transfer, the rate of increase in j_{lim} as a function of AcOH concentration added for the H_2SO_4 | KOAc (**Figure S3.30(b)**) and PSS–H | PDADMA–OAc (**Figure S3.31(b)**) cells were very similar with slopes of −8.6 vs −9.6 mA cm^{-2} (mol dm^{-3}) $^{-1}$ respectively, evincing that the changes in j_{lim} arise predominantly from AcOH dissociation. Furthermore, in contrast to open-circuit behavior, the similar slopes suggest that co-ion crossover and AcOH dissociation are decoupled and independent when driven under reverse bias.

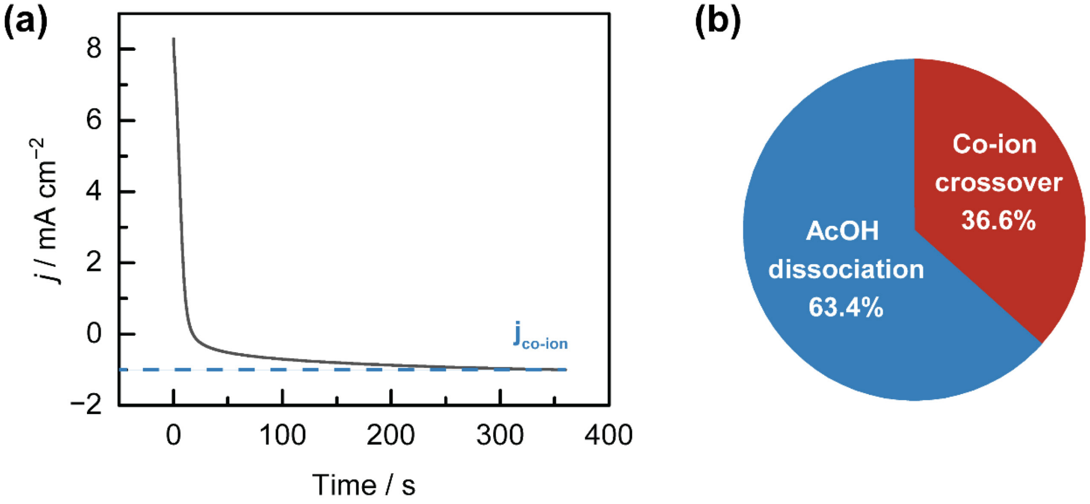

Figure 3.7. (a) Chronoamperometric measurement at −600 mV (not iR-corrected) immediately following galvanostatic polarization at −9 mA cm^{-2} for 15 min for a H_2SO_4 | KOAc cell which had been equilibrated at open-circuit for 3 h. **(b)** Breakdown of limiting current into partial current contributions from co-ion crossover and AcOH dissociation.

We next sought to quantify the magnitude of the reverse bias current arising from weak acid dissociation. We first measured the aggregate baseline limiting current, j_{lim}. To do this we equilibrated a HCl | KOAc cell for 3 h at open-circuit and then collected a galvanodynamic scan in reverse bias, measuring a j_{lim} value of −2.7 mA cm^{-2} (**Figure S3.32**). In this section, V_{mem} values reported are not iR-corrected to allow direct comparisons between different measurements. Subsequently, we electrodialyzed any AcOH generated via neutralization short-circuiting away from the bipolar interface by passing −9 mA cm^{-2} for 15 min. During this electrolysis, V_{mem} reached a steady-state value of ~−920 mV, sufficient to dissociate AcOH and water. Immediately following this electrolysis, we recorded a chronoamperogram at −600 mV, in the middle of the limiting current region (refer to **Figure S3.32)**. The current transient decayed rapidly from positive currents (due to H$^+$/OH$^-$ recombination) and reached a quasi-stable value at ~−1 mA cm^{-2} after 6 min (**Figure 3.7(a)**). We attribute this value to an upper-limit estimate of the co-ion crossover partial current ($j_{\mathrm{co\text{-}ion}}$), since all of the dissociable AcOH had been electrodialyzed as H$^+$ and OAc$^-$ out of the bipolar junction at ~−920 mV and −600 mV is at a significant underpotential to water dissociation. The increasingly negative current after quasi-stabilization at ~6 min is consistent with the slow back-diffusion of AcOH from the bulk solutions into the bipolar junction, contributing partial current, j_{HADR}, arising from AcOH (or HA) dissociation. Subtracting the estimated $j_{\mathrm{co\text{-}ion}}$ from the aggregate j_{lim} measured in the initial galvanodynamic experiment yields an estimate for j_{HADR} of −1.73 mA cm^{-2} for the 3 h-equilibrated cell. This partial current accounted for 63.4% of j_{lim} (**Figure 3.7(b)**). Over longer equilibration periods, $j_{\mathrm{co\text{-}ion}}$ is expected to decrease and j_{HADR} is expected to increase due to the neutralization short-circuiting process, meaning j_{HADR} will occupy an increasingly larger share of j_{lim} over time. Although a number of computational studies of current breakdown in BPMs exist,[38,40] to our knowledge, this is the first study to experimentally quantify the various contributions to reverse bias current. This type of current transient measurement could be adopted to benchmark future theoretical studies and transport models of BPMs. Together, these studies demonstrate that ionization of weak acids/bases generated from open-circuit neutralization short-circuiting can be a significant contributor to reverse bias currents.

3.5 Conclusions

Herein, we investigate the ion transfer processes occurring across bipolar membranes operated with weak electrolytes at intermediate pH values. We find that the presence of weak electrolytes at pH values far removed from their pK_a radically alters the membrane voltage and polarization characteristics of a BPM relative to buffer-free systems operating at pH extremes. We find that this is due to ionic short-circuiting reactions with weak electrolytes leading to the generation of conjugate acids/bases at the interface, and we term this overall process neutralization short-circuiting. Importantly, in contrast to the strong electrolytes H_3O^+ and OH^- used to operate with extreme pH gradients, the ionization of weak electrolytes is sensitive to the presence of their conjugate acid/base, resulting in pronounced internal pH gradients across the AEM or CEM, respectively. These pH gradients serve to attenuate the open-circuit V_{mem} of the BPM and the ionization of conjugate acids/bases accumulated from short-circuiting augments the reverse bias limiting current.

These findings have several important implications for BPMs operated under intermediate pH conditions. First, due to the phenomenon of interfacial buffering, BPM cells intended for converting the chemical potential gradient between two electrolyte solutions into an electrical potential gradient may not recover a voltage difference corresponding to the full pH differential across the cell. Instead, the attenuated open-circuit V_{mem} caps the maximum voltage that can be extracted under forward bias polarization of the BPM. We have demonstrated that the membrane voltage is attenuated due to accumulation of the conjugate acid/base, and that attenuation is most pronounced at pH values far removed from the pK_a. Hence, we anticipate that extracting electrical work corresponding to the full pH differential will require strategies for efficiently removing the conjugate acid/base from the BPM interface.

Second, the ionization of the conjugate acid/base accumulated from neutralization short-circuiting can impact the efficiency for water dissociation. Although conjugate acid/base ionization did not affect the qualitative behavior in the water dissociating regime of the polarization curve (**Figure 3.6**), current for HADR is expected to persist even after WDR onset. Since the conjugate acid/base accumulates at open circuit, its parasitic dissociation will have a more pronounced effect on water dissociation efficiency for applications in which BPMs are operated intermittently.

Finally, the phenomenon of weak acid/base ionization at the bipolar interface carries implications for electrochemical cells where neutral weak acids and bases are generated as reaction products at the electrodes. These neutral weak acids/bases can diffuse to the BPM interface and undergo ionization and electrodialysis in BPMs in reverse bias, which can complicate their separation and recovery from the electrolyte. For example, in the context of CO_2 reduction or organic oxidation, the cathode and anode generate neutral weak acids (e.g. formic acid, acetic acid in CO_2 electrolysis;[57] lactic acid[58,59] and 2,5-furandicarboxylic acid[60] in glycerol and biomass oxidation electrolysis, respectively) which will diffuse to the bipolar interface and undergo dissociation and electrodialysis. This effect is expected to be particularly pronounced in the limit of high single-pass conversion that generates concentrated product streams.

Collectively, these implications motivate additional efforts to manage the transport of both ions and neutral species in BPMs. By exposing the role of parasitic weak electrolyte neutralization reactions in BPMs, this study lays the foundation for advancing BPM applications under intermediate pH conditions.

3.6 Experimental Methods

Safety Statement

Significant hazards/risks encountered in this study are highlighted with a **CAUTION** label in the relevant **Experimental Methods** sections, accompanied by an explanation of how they were mitigated.

Chemicals and Materials

Potassium hydroxide (KOH, 99.98%), potassium formate (HCOOK, 99%), boric acid (H_3BO_3, Puratronic, 99.9995%), sodium acetate (CH_3COONa, 99.997%), ammonium chloride (NH_4Cl, 99.999%) were purchased from Alfa Aesar and used as received. Potassium chloride (KCl, 99%), potassium acetate (CH_3COOK, 99%), potassium bicarbonate ($KHCO_3$, 99.95%), potassium phosphate monobasic (KH_2PO_4, 99.5%), potassium phosphate dibasic trihydrate ($K_2HPO_4 \bullet 3H_2O$, 99%), acetic acid (CH_3COOH, glacial, 99.7%), potassium phosphate tribasic (K_3PO_4, >98%), ammonium acetate (CH_3COONH_4, 97%), trimethylamine hydrochloride ($N(CH_3)_3 \bullet HCl$, 98%), guanidine hydrochloride ($CH_5N_3 \bullet HCl$, 99%), imidazole hydrochloride ($C_3H_4N_2 \bullet HCl$, >98%), pyridine hydrochloride ($C_5H_5N \bullet HCl$, 98%), poly(sodium 4-

styrenesulfonate) (PSS-Na, Mw = 70,000, 30 wt. % in H_2O), poly(diallyldimethylammonium chloride) (PDADMA–Cl, Mw < 100,000, 35 wt. % in H_2O) and diethyl ether (Et_2O, anhydrous, >99%) were purchased from Sigma-Aldrich and used as received. Sulfuric acid (OmniTrace, 93-98%) and hydrochloric acid (OmniTrace, 34−37%) were purchased from VWR and used as received. Potassium carbonate (K_2CO_3, 99.995%) was purchased from Beantown Chemical and used as received. Platinum wire and mesh (99.995%) used as driving electrodes were purchased from VWR. All aqueous electrolyte solutions were prepared with type I water (EMD Millipore, 18.2 MΩ·cm resistivity). The commercial bipolar membrane Fumasep FBM was purchased from Fuel Cell Store and stored in Millipore water before use. Dialysis tubing (molecular weight cut-off of 14,000 Da) was obtained from Ward's Science and thoroughly rinsed with Millipore water before use. Glass Ag/AgCl reference electrodes were obtained from CH Instruments and stored in 1 M KCl solution in between measurements.

Preparation of Poly(4-Styrenesulfonic Acid) (PSS–H)

To prepare PSS–H samples, 200 mL of a nominal 0.5 M PSS-Na solution were made by dilution from the purchased stock solution, transferred into dialysis tubing, and dialyzed against 800 mL of 1 M HCl for 1 h. The HCl was then discarded and replaced with fresh solution. This procedure was repeated for a total of four times, with the final dialysis step carried out overnight. The dialysis tubing was then thoroughly rinsed and exhaustively dialyzed against Millipore water at a 5:1 volume ratio for 1 h periods at least 8 times to remove excess HCl. The tubing solution was finally concentrated under reduced pressure at 50 °C on a rotary evaporator. An aliquot of this solution was analyzed using ICP-OES for S and Cl^- content, and the total volume was adjusted using the S measurement to make a 1 M PSS–H solution. ^1H NMR characterization of the obtained product was performed using a 500 MHz Bruker spectrometer (**Figure S3.4**).

Preparation of Poly(Diallyldimethylammonium Acetate) (PDADMA–OAc)

To prepare PDADMA–OAc samples, 200 mL of 0.5 M PDADMA–Cl solution were made by dilution from the purchased stock solution, transferred into dialysis tubing and dialyzed against 800 mL of 1 M NH_4OAc for 1 h. The NH_4OAc was then discarded and replaced with fresh solution. This procedure was repeated for a total of four times, with the final dialysis step carried out overnight. Following this, the dialysis tubing was thoroughly rinsed and exhaustively dialyzed against Millipore water at a 5:1 volume ratio for 1 h periods at least 8 times to remove excess NH_4OAc. The tubing solution was then dehydrated under reduced pressure at 50 °C on a rotary evaporator. This also served to drive the thermal decomposition of any excess NH_4OAc and the evacuation of the NH_3 formed. The resulting resin was dissolved in ~200 mL of EtOH and slowly precipitated out of a ~1 L Et_2O solution to remove any excess AcOH left behind from NH_4OAc decomposition. The Et_2O was then decanted, and the residue redissolved in EtOH and reduced to dryness on the rotary evaporator. The resulting solid was dried in a 40 °C vacuum oven overnight. The next day, the dried solid was dissolved in Millipore water and an aliquot of this solution was analyzed by ^1H NMR to determine the OAc^- concentration. Assuming a 1:1 stoichiometry between the fixed charges of $PDADMA^+$ and OAc^-, the total volume was adjusted accordingly to make a 1 M PDADMA–OAc solution. An aliquot of this solution was analyzed using the Cl^- ion-selective electrode (see below section, **Measurements of Ion Concentrations**) to determine the Cl^- content. ^1H NMR characterization of the obtained product was performed using a 500 MHz Bruker spectrometer (**Figure S3.5**).

General Electrochemical Methods

The voltage across the BPM was probed using a four-electrode setup (**Figure S3.1**). For all experiments, the area of the BPM exposed between the two solution compartments was 2 cm^2. In polarization experiments, two glass AgCl/Ag reference electrodes were installed at the ends of the Luggin capillaries. The tips of the capillaries were placed approximately 0.5 cm from each face of the BPM. Platinum meshes or wires were used as cathode and anode, and each compartment was vented to prevent the build-up of gas during polarization. Acid solutions were added to the compartment facing the CEM, and base solutions were added to the compartment facing the AEM. All electrochemical measurements were made on either a BioLogic VMP-300 or Gamry Reference 600 potentiostat, and were performed at ambient temperature (24 ± 1 °C). All glassware and Pt meshes/wires used were cleaned by soaking in a 1:1 mixture by volume of concentrated HNO_3 and H_2SO_4 for at least 30 min prior to use.

CAUTION: *Concentrated HNO_3 and H_2SO_4 acids are highly corrosive and should be handled carefully in a fume hood with the appropriate personal protection equipment (PPE), including safety goggles and a corrosion-resistant lab coat and gloves.*

Cataloguing Open-Circuit Membrane Voltage for pK_a and pK_b-Scaling Studies

To record the open-circuit membrane voltages for the pK_a and pK_b-scaling studies (**Figure 3.5**), continuous open-circuit voltage measurements of the BPM were recorded upon solution addition. The membrane voltage typically reached a stable value within ~3 h. After the open-circuit

V_{mem} had passed a minimum and stabilized to within ± 1 mV h^{-1}, the value reached was recorded and plotted in **Figure 3.5**. In all cases, the V_{mem} reported was compensated by the drift between the Ag/AgCl reference electrodes measured in a two-electrode setup in 1 M KCl beforehand (typically < 5 mV).

Measurements of Ion Concentrations

Inductively coupled plasma-optical emission spectroscopy (ICP-OES) (Agilent 5100 ICP-OES SVDV) was employed to measure the concentrations of K^+ and PSS^- (as [S]) ions present in aliquots from open-circuit crossover experiments. Aliquots were typically diluted by 40 times and filtered through a membrane filter of 0.25 μm pore size before measurements. K^+ concentrations were determined at 766.491 nm, and [S] at 182.562 nm.

Cl^- concentrations were determined using a chloride ion selective electrode (ISE) (Hach IntelliCAL™ ISECL181 Probe).

Open-Circuit Crossover Experiments

To study the coupling of co-ion crossover and parasitic neutralization under open-circuit conditions, the cell was set up and monitored over the course of four days. 25 mL of each electrolyte solution were added to their respective compartments and the entire cell was kept unperturbed in a closed chamber with open vials of water to maintain humidity. Luggin capillaries were not installed in order to avoid obstructing the membrane. Each day, the two solutions would be thoroughly mixed, and 250 μL aliquots would be taken from each solution. The day zero timepoints for V_{mem} were measured after 30 min of membrane equilibration. The concentrations of crossover ions were determined using either ICP-OES or a Cl^- ISE, and the concentrations of the produced acetic acid and ammonia were quantified by ^1H NMR (see below). The pH of each compartment was measured using either a VWR or Orion A121 pH electrode, and reference electrodes were briefly inserted to measure the open-circuit V_{mem} each day. The volume of the solution in each compartment was not found to change significantly after four days.

Quantitative ^1H NMR for Determination of Acetic Acid and Ammonium Concentration

^1H NMR was required for the quantification of various compounds during polyelectrolyte preparation or open-circuit experiments, and a list of all the calibrant solutions with their different use cases is given in **Table S3.1**. In a typical routine, 50 μL of an aliquot collected from the as-synthesized polyelectrolyte or an open-circuit experiment were added to 450 μL of a calibrant mixture. All NMR spectra were collected on a 400 or 500 MHz Bruker spectrometer.

A particular issue that arose was the need to deconvolute acetic acid from acetate in the base compartment of the HCl | KOAc cell or ammonia from ammonium in the acid compartment of the NH_4Cl | KOH cell, as the acidic calibrant solutions converted all acetate to acetic acid and all ammonia to ammonium. Using acetate/acetic acid as an example, the concentration of acetic acid in aliquots collected from the base compartment could be determined via two methods of calculation.

(a) From NMR measurements

Firstly, the ratio of acetic acid to acetate was calculated using the Henderson-Hasselbalch equation with the measured pH and the known pK_a of acetic acid as inputs. This calculated acid/base ratio was then applied to the measured concentration of total acetate/acetic acid species in the base solution from ^{1}H NMR to obtain the concentration of acetic acid in the base produced from neutralization short-circuiting.

(b) From ICP-OES measurements

Here, we considered that all of the acetate ions must be charge-paired with alkali metal cations (M^+), but that the M^+ present could be paired with either acetate or the Cl^- anion from crossover. Hence, the total acetate concentration was found by subtracting the concentration of M^+ that would be charge-paired with Cl^- from the total concentration of M^+ determined by ICP-OES. Finally, the acetic acid concentration could be determined by applying the acetic acid to acetate ratio found from pH measurements to this calculated acetate concentration.

Similar calculations were applied to determine the concentration of ammonia in ammonium chloride solution in the NH_4Cl | KOH open-circuit experiments. Good correspondence was found between the NMR and ICP-OES methods of quantification (**Figure S3.2**).

Reverse Bias Galvanodynamic Polarization

To obtain the reverse bias polarization curves, galvanodynamic scans were typically collected from 0 to −30 mA cm^{-2}, using a scan rate of 10 µA cm^{-2} s^{-1}. This scan rate was compared to independent chronopotentiometry measurements and determined to be sufficiently slow to capture steady-state polarization behavior. All polarization curves were typically corrected for

Ohmic losses (iR_u) using 85% of uncompensated resistance (R_u) values determined using the Current Interrupt (CI) program on the BioLogic VMP−3 potentiostat.

3.7 Supplementary Information

3.7.1 Supplementary Discussions

Supplementary Discussion 3.1. Breakdown of potentials in a BPM cell

The overall membrane voltage, V_{mem}, measured across a BPM is the sum of the bipolar junction potential, V_{J}, and two Donnan potentials, $E_{\text{Don(Acid | CEM)}}$ and $E_{\text{Don(AEM | Base)}}$ arising at the acid | CEM and AEM | base interfaces respectively.[2]

$$V_{\text{mem}} = E_{\text{Don(Acid | CEM)}} + V_{\text{J}} + E_{\text{Don(AEM | Base)}}$$

The bipolar junction potential, V_{J} ,is given by

$$V_{\text{J}} = -60\text{ mV} \cdot (\text{pH}_{\text{AEM}} - \text{pH}_{\text{CEM}})$$

where pH_{AEM} refers to the pH within the AEM, pH_{CEM} refers to the pH within the CEM and, chemical activities have been swapped for concentrations, assuming no non-idealities.

The Donnan potential, $E_{\text{Don(IEM | Solution)}}$, is given by

$$E_{\text{Don(IEM | Solution)}} = \frac{-60\text{ mV}}{z_i} \cdot \log_{10}\left(\frac{c_{i,m}}{c_i}\right)$$

where $c_{i,m}$ refers to the concentration of a given charged species i within the membrane, c_i refers to the concentration of i within the solution, and z_i is the charge of i. Here, we assume that only counter-ions are able to freely transit a given membrane.

Using these equations, we can calculate theoretical V_{mem} values for cells containing BPMs of different fixed charge concentrations, while keeping the solution concentrations the same.

For a cell containing a BPM with fixed charge concentrations of **1 M** in both the CEM and AEM, the following potentials result.

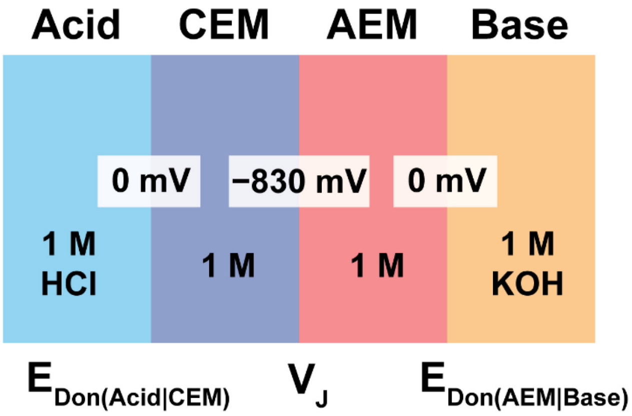

$$V_{\text{mem}} = 60 + (-950) + 60 = -830 \text{ mV}$$

For a cell containing a BPM with fixed charge concentrations of **10 M** in both the CEM and AEM, the following potentials result.

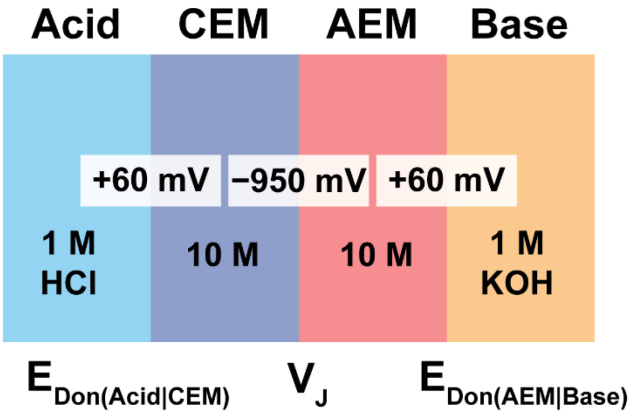

$$V_{\text{mem}} = 0 + (-830) + 0 = -830 \text{ mV}$$

Hence, as demonstrated here, V_{mem} is sensitive only to the solution concentrations and not to the fixed charge concentration of the BPM.

As such, in order to simplify our analysis of V_{mem} and focus on changes to V_J, we assumed that fixed charge concentrations are 1 M in this study, leading to Donnan potentials of 0 mV and $V_{\text{mem}} = V_J$. Since solution concentrations in the acid and base compartments do not change significantly, Donnan potentials also do not change significantly during the course of the experiments reported in this study, meaning that Donnan potentials can be safely ignored as a constant, and that changes in V_{mem} reflect changes only in V_J.

In reality, we note that fixed charge concentrations of ~6 M have been reported for the commercial BPM, Fumasep FBM.[39] This implies Donnan potentials of ~46 mV are present at each membrane-solution interface, and that Donnan exclusion of co-ions is hence in effect to prevent significant co-ion fluxes.

We also note that the equation presented above for $E_{\mathrm{Don(IEM\,|\,Solution)}}$ is an approximation and that a more mathematically rigorous value of $E_{\mathrm{Don(IEM\,|\,Solution)}}$ can be found following the theory in a previous report.[38]

Supplementary Discussion 3.2. Calculations of neutralization short-circuit current from open-circuit crossover experiments

For the HCl | KOAc cell, the absolute K^+ crossover rate is 46.9 mmol dm^{-3} day^{-1}, and the absolute Cl^- crossover rate is 62.9 mmol dm^{-3} day^{-1} (without normalization to membrane surface area). The electrolyte volume is 25 mL per compartment.

Hence, the neutralization short-circuit current for K^+ is:

$$j_{\mathrm{K+,short-circuit}} = \frac{(\mathrm{K^+\ crossover\ rate}) * (\mathrm{Volume\ of\ compartment}) * \mathrm{F}}{(\mathrm{Membrane\ Area})}$$

$$= \frac{0.0469\ \mathrm{mol}}{1\ \mathrm{dm}^3} * \frac{1}{1\ \mathrm{day}} * \frac{1\ \mathrm{day}}{(3600 * \ 24)\mathrm{s}} * \frac{1\ \mathrm{dm}^3}{1000\ \mathrm{mL}} * 25\ \mathrm{cm}^3 * \frac{96485\ \mathrm{C}}{1\ \mathrm{mol}} * \frac{1}{2\ \mathrm{cm}^2}$$

$$= \ 0.65\ \mathrm{mA\ cm}^{-2}$$

where F is Faraday’s constant.

A similar calculation performed for Cl^- returns a $j_{\mathrm{Cl-,short-circuit}}$ of 0.88 mA cm^{-2}.

The total neutralization short-circuit current for HCl | KOAc is hence <u>1.53 mA cm^{-2}</u>.

Supplementary Discussion 3.3. Analysis of differences in co-ion crossover rates between HCl | KOAc and HCl + AcOH | KOAc + AcOH cells reveals selective negative feedback mechanisms

The rate of K^+ crossover was very similar (~1.1X) between HCl | KOAc (23.5 mM cm^{-2} day^{-1}, **Figure S3(c)**, blue) and HCl + AcOH | KOAc + AcOH (22.0 mM cm^{-2} day^{-1} , **Figure S3.3 (c)**, red). In contrast, however, the rate of Cl^- crossover was almost twice as fast for HCl | KOAc (31.5 mM cm^{-2} day^{-1}, **Figure S3(d)**, blue) than for HCl + AcOH | KOAc + AcOH (15.9 mM cm^{-2} day^{-1}, **Figure S3(d)**, red). We contend that differences in V_{mem} between HCl | KOAc and HCl + AcOH | KOAc + AcOH cannot explain the asymmetric changes in K^+ and Cl^- crossover rates, as the differences are small and would be expected to indiscriminately affect both co-ions. In an analogous fashion, when we compared NH_4Cl | KOH with NH_4Cl + NH_3 | KOH + NH_3, we found that the K^+ crossover rate was higher by 3.4 times (**Figure S3.8(e)**), but the Cl^- crossover rate had only changed by 1.4 times (**Figure S3.8(f)**). These findings are in agreement with a previous report that observed a dependence of Na^+ crossover rates on the opposing electrolyte at open-circuit.[39] Taken together, these observations that only Cl^- crossover rates for HCl | KOAc cells are reduced due to AcOH addition and only K^+ crossover rates for NH_4Cl | KOH cells are reduced due to NH_3 addition imply these *co-ions are selectively subjected to negative feedback mechanisms that affect their respective crossover rates over time* (**Figure S3.12**). However, uncovering the mechanistic origins of these feedback mechanisms is outside the scope of this work and is the subject of ongoing studies.

Supplementary Discussion 3.4. Note on correlations between crossover rates of individual co-ions and AcOH accumulation rates in individual solutions

Although a correlation seems to exist between the rate of K^+ crossover into HCl and AcOH accumulation in HCl as well as between the rate of Cl^- crossover into KOAc and AcOH accumulation in KOAc (**Figure 3.1(c)-(d)**), we refrain from interpreting this as we do not observe a similar correlation for the NH_4Cl | KOH cell (compare **Figure S3.8(e)-(f)** with **Figure S3.10**), and believe this is simply a coincidence. Instead, the partition of AcOH and NH_3 between the acid and base compartments should be dependent on their differential diffusive properties within the CEM and AEM, respectively.

3.7.2 Supplementary Figures & Tables

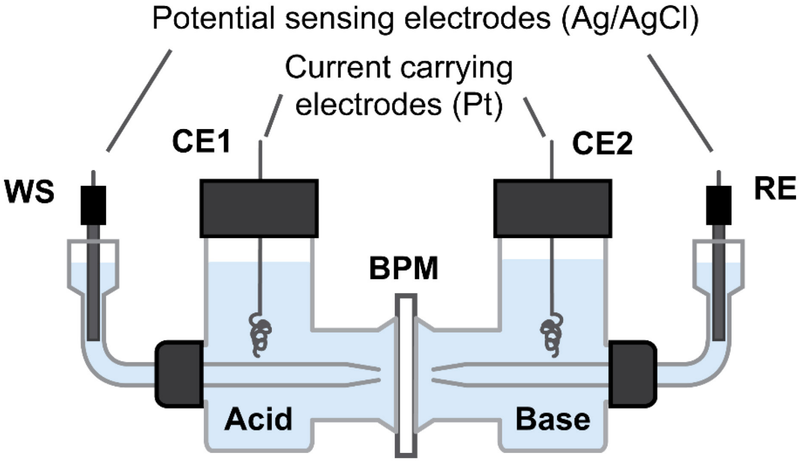

Figure S3.1. Illustration of the four-electrode set up, showing the placement of the working sense (WS) electrode, reference electrode (RE), and counter electrodes 1 (CE1) and 2 (CE2) in the acid and base solutions.

Table S3.1. List of calibrant solutions used for ^{1}H NMR analysis. Internal standards are indicated with an asterisk.

Calibrant Solution	Composition	Use Cases
A	8 parts 1 M HCl, 1 part D_2O, 1 part 0.1 M DMSO*	▪ Characterization of as-synthesized PSS–H ▪ AcOH quantification in HCl | KOAc and PSS–H | KOAc open-circuit experiments
B	8 parts 1 M HCl, 1 part D_2O, 1 part 0.1 M maleic acid*	▪ AcOH quantification for as-synthesized PDADMA–OAc ▪ AcOH quantification in HCl | PDADMA–OAc open-circuit experiments
C	8 parts 1 M HCl, 1 part CD_3CN, 1 part 0.1 M DMSO*	▪ NH_4^+ quantification for as-synthesized PDADMA–OAc
D	7 parts 1 M HCl, 2 parts CD_3CN, 1 part 0.1 M DMSO*	▪ NH_4^+ quantification in NH_4Cl | KOH open-circuit experiments
E	8 parts 1 M HCl, 1 part D_2O, 1 part 0.1 M formic acid*	▪ PSS–H and PDADMA$^+$ quantification in PSS–H | PDADMA–OAc open-circuit experiments

Table S3.2. Measured pH values of all base solutions used in this study. pK_a values were taken from the literature.[61]

Solution	pK_a (conjugate acid)	Measured pH
1 M KOH	14	14.1
1 M K_3PO_4	12.32	12.5
1 M K_2CO_3	10.33	10.3
1 M KH_2BO_3	9.27	11.1
1 M K_2HPO_4	7.21	7.5
1 M $KHCO_3$	6.35	8.6
1 M KOAc	4.76	8.3
1 M HCOOK	3.75	9.0
1 M KH_2PO_4	2.16	4.6
1 M KCl	0*	6.2
1 M PDADMA–OAc	n.d.	7.57

*Due to solvent levelling in aqueous solution.

Table S3.3. Measured pH values of all acid solutions used in this study. pK_a values were taken from the literature.[61]

Solution	**pK_a**	**Measured pH**
1 M HCl	0*	0.3
1 M H_2SO_4	0*	0.1
1 M pyridinium chloride (PyHCl)	5.23	2.6
1 M imidazolium chloride (ImHCl)	6.99	3.6
1 M NH_4Cl	9.25	5.1
1 M trimethylammonium chloride ($NH(CH_3)_3Cl$)	9.80	4.3
1 M Guanidinium chloride (GdnHCl)	13.6	5.2
1 M KCl	14	6.2
1 M PSS–H	n.d.	1.00

*Due to solvent levelling in aqueous solution.

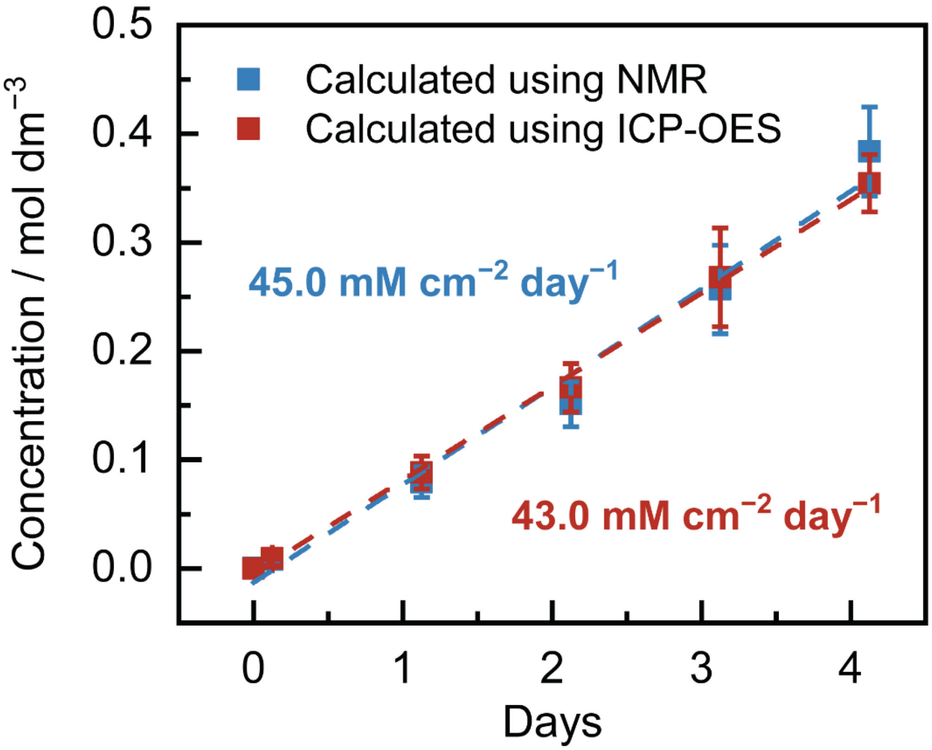

Figure S3.2. Plot showing the good correspondence between the concentrations of AcOH in KOAc solutions calculated using either the NMR or ICP-OES methods. Rates reported are normalized to the surface area of the membrane (2 cm^2).

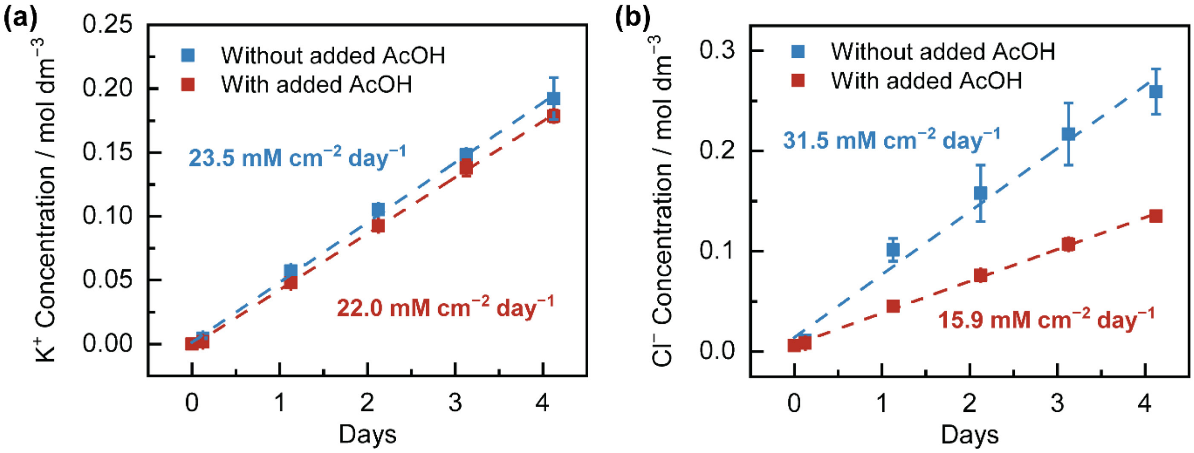

Figure S3.3. Plots showing the time evolution of crossover concentrations of **(a)** co-ion K+ and **(b)** Cl$^-$ for the cell HCl + AcOH | KOAc + AcOH measured over 4 days. **(a)** and **(b)** compare co-ion crossover rates with the cell HCl | KOAc. Rates reported are normalized to the surface area of the membrane (2 cm^2). Measurements were performed in duplicate (n = 2) and error bars represent the absolute difference between duplicate points.

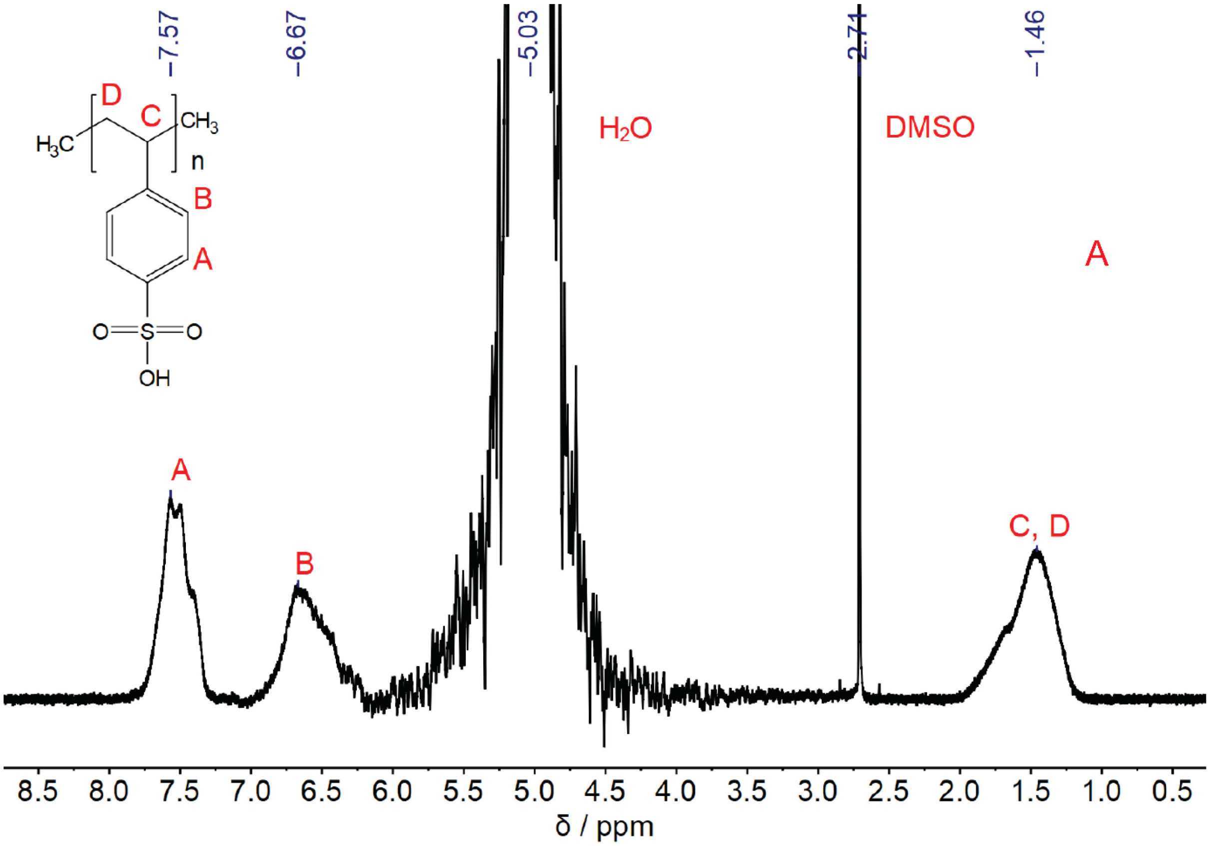

Figure S3.4. ^{1}H NMR spectrum of as-prepared PSS–H collected at 500 MHz using calibrant solution A. Acquired spectrum is in agreement with the literature.[62]

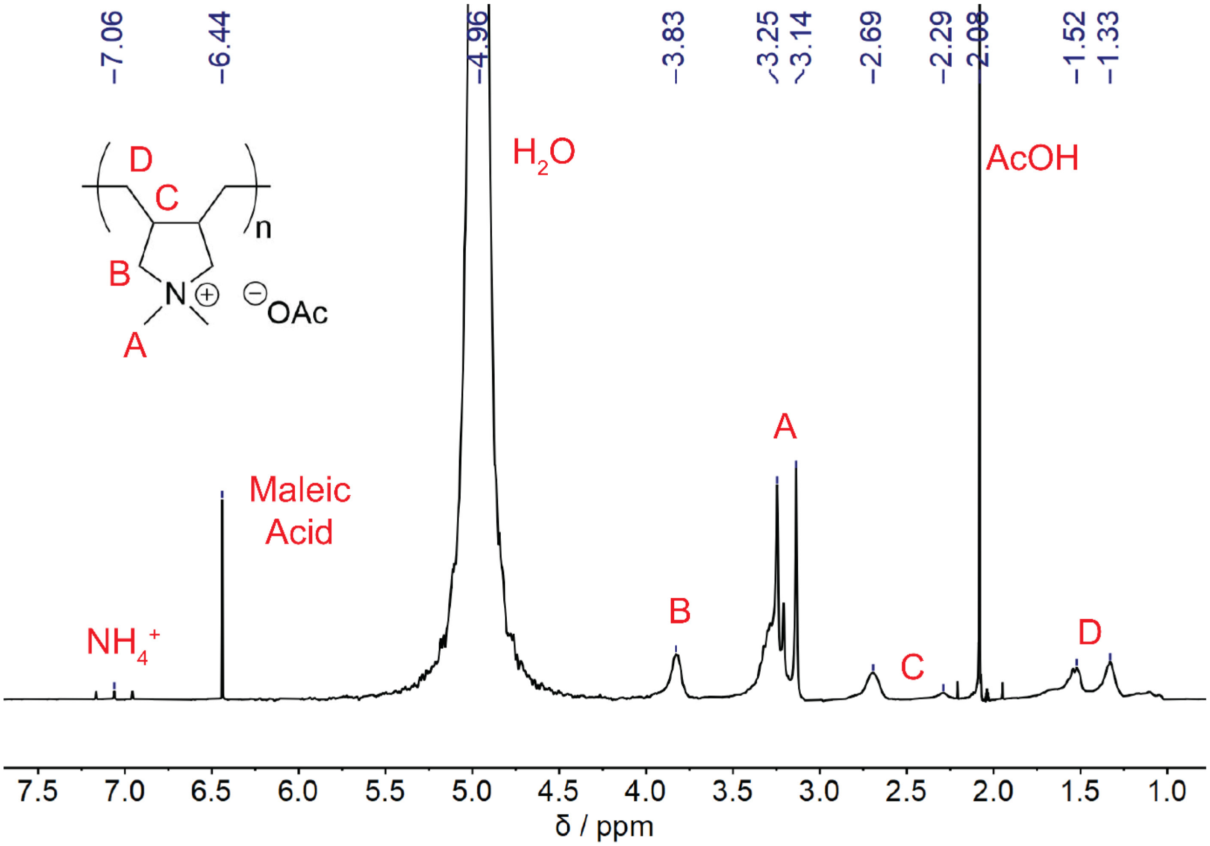

Figure S3.5. ^{1}H NMR spectrum of as-prepared PDADMA–OAc collected at 500 MHz using calibrant solution B**.** Acquired spectrum is in agreement with the literature.[63]

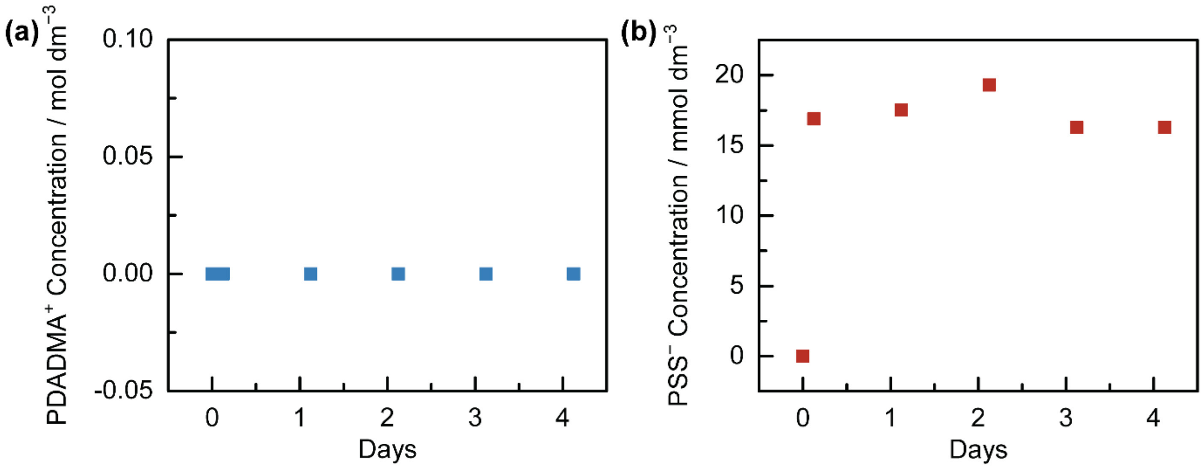

Figure S3.6. Plots showing the time evolution of crossover concentrations of **(a)** PDADMA$^+$ in PSS–H solution determined via NMR (see **Figure S3.7**) and **(b)** PSS$^-$ in PDADMA–OAc solutions (via measurement of all S-containing species) determined via ICP-OES for the cell PSS–H | PDADMA–OAc measured over 4 days. The small concentration of crossover PSS$^-$ detected is attributed to trace oligomeric species remaining in the PSS–H solution after dialysis.

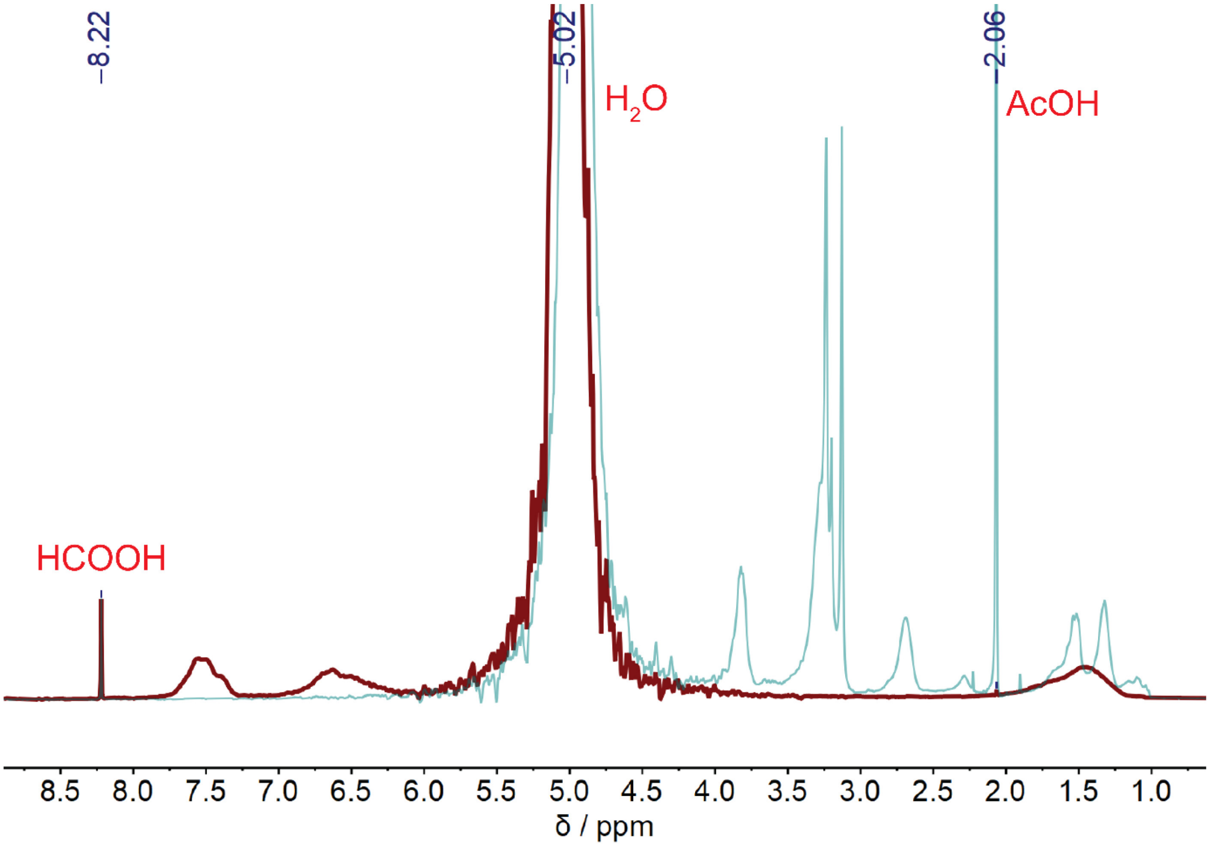

Figure S3.7. Overlay of ^{1}H NMR spectra for day 4 aliquots taken from the PSS–H (maroon) and PDADMA–OAc (turquoise) solutions for the PSS–H | PDADMA–OAc cell, indicating the absence of any significant crossover of PSS$^-$ into the PDADMA–OAc compartment or of PDADMA$^+$ into the PSS–H compartment. Integration of the trace AcOH signal in PSS–H reveals a concentration of 13.5 mM. The spectra were collected using calibrant solution E with a delay time (d1) of 50 s.

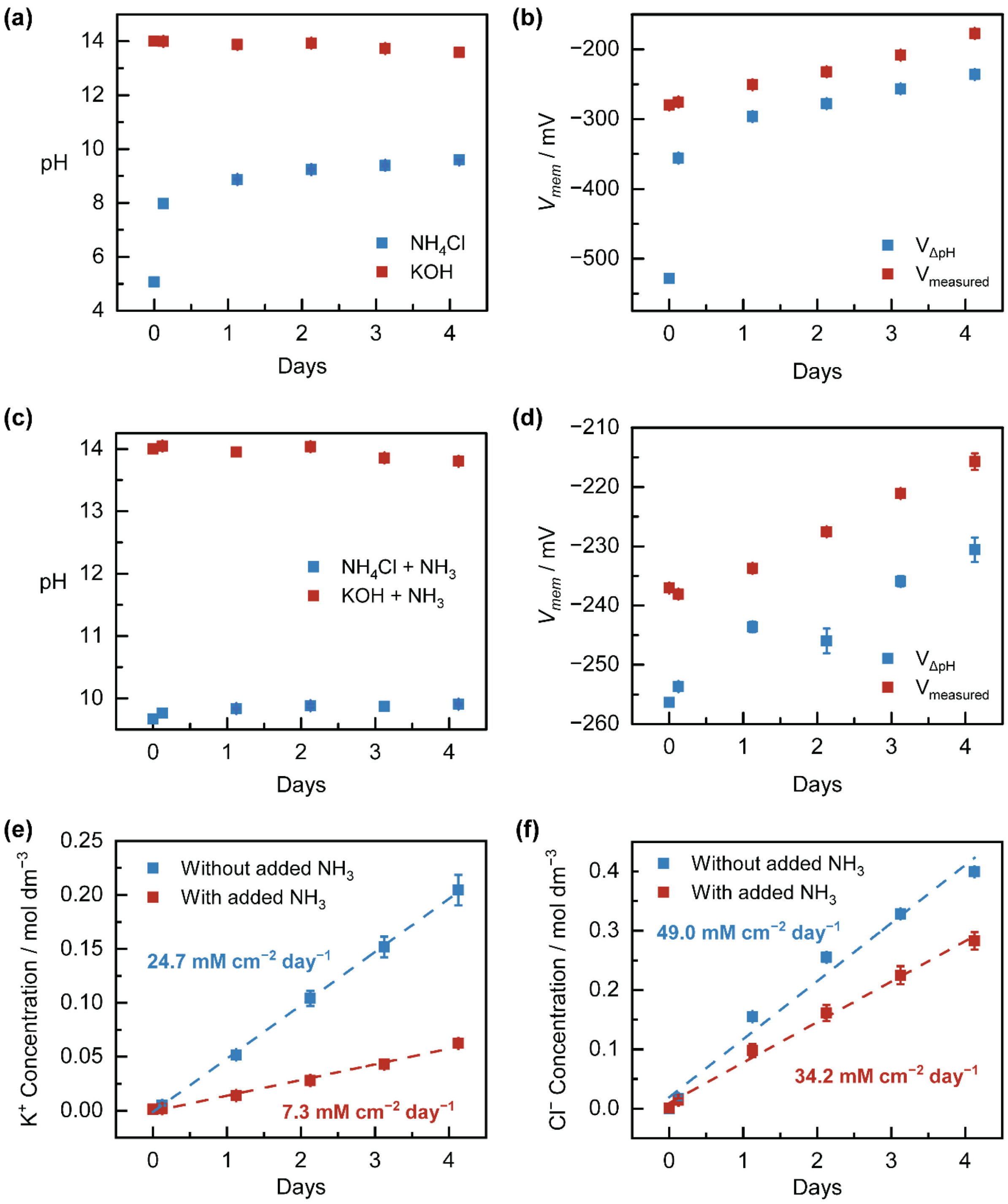

Figure S3.8. Plots showing the time evolution of pH of NH_4Cl and KOH solutions and open-circuit membrane voltage for the NH_4Cl | KOH cell **(a, b)**; pH of NH_4Cl and KOH solutions and open-circuit membrane voltage for the $NH_4Cl + NH_3$ | $KOH + NH_3$ cell **(c, d)**; and crossover concentrations of **(e)** K^+ and **(f)** Cl^- comparing the NH_4Cl | KOH and $NH_4Cl + NH_3$ | $KOH + NH_3$ cells. Rates reported are normalized to the surface area of the membrane (2 cm^2). Measurements were performed in duplicate (n = 2) and error bars represent the absolute difference between duplicate points.

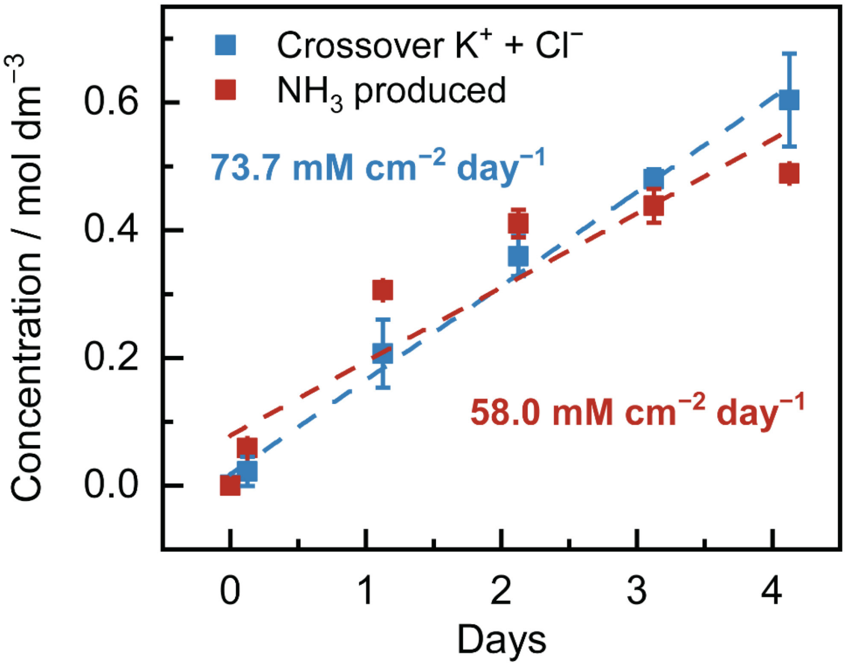

Figure S3.9. Time evolution plot comparing the concentrations of crossover K^+ and Cl^- with NH_3 produced for the NH_4Cl | KOH cell, showing a nearly 1:1 ratio between transfer rates. Rates reported are normalized to the surface area of the membrane (2 cm^2). The deviation from linearity for the increase in NH_3 concentration in the later timepoints is attributed to the evaporative loss of volatile NH_3.

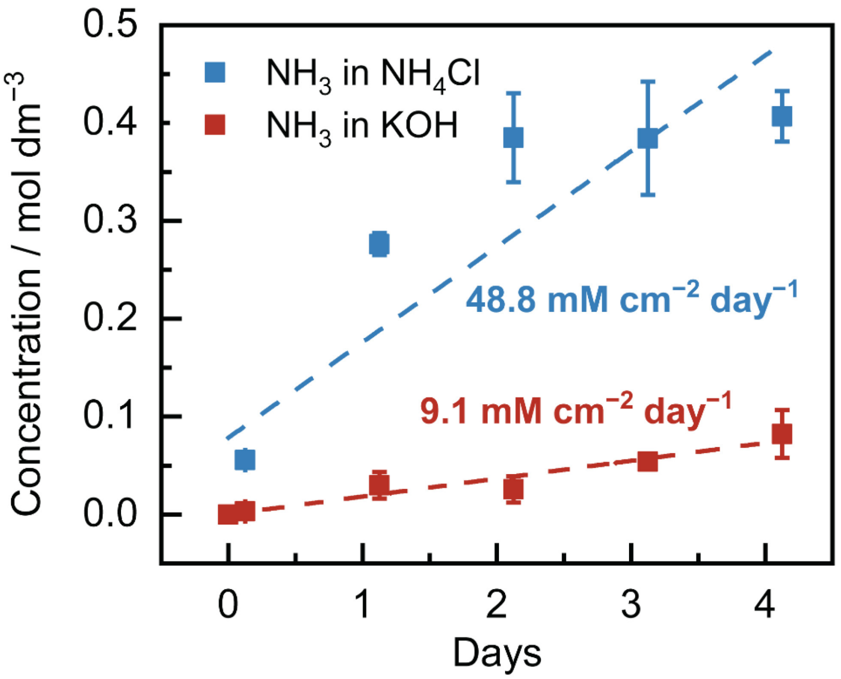

Figure S3.10. Plot showing the time evolution of NH_3 concentration in NH_4Cl and KOH solutions for the cell NH_4Cl | KOH measured over 4 days. Rates reported are normalized to the surface area of the membrane (2 cm^2). Measurements were performed in duplicate (n = 2) and error bars represent the absolute difference between duplicate points. The deviation from linearity for the increase in NH_3 concentration in NH_4Cl in the later timepoints is attributed to the evaporative loss of volatile NH_3.

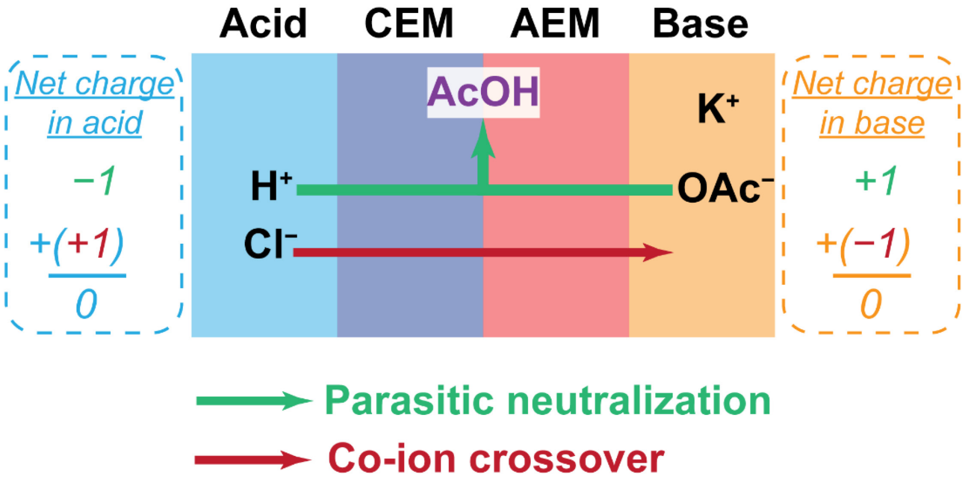

Figure S3.11. Charge balance diagram showing how the coupling of co-ion crossover with parasitic neutralization conserves electroneutrality for Cl$^-$ crossover.

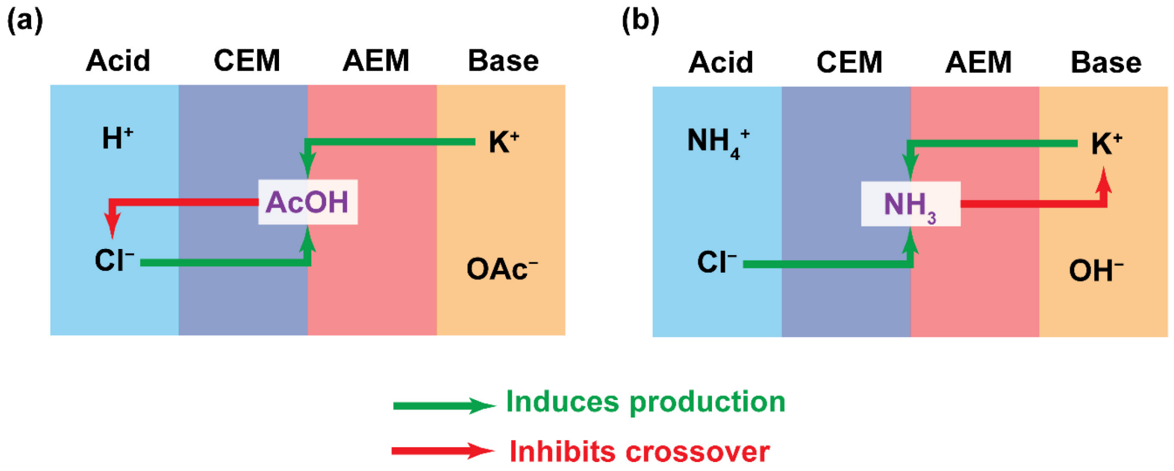

Figure S3.12. Interactions between crossover co-ions K$^+$ and Cl$^-$ and the AcOH produced from parasitic neutralization for the cells **(a)** HCl | KOAc and **(b)** NH_4Cl | KOH. In **(a)**, a negative feedback loop occurs for Cl$^-$ but not for K$^+$. In (b), a negative feedback loop occurs for K$^+$ but not for Cl$^-$.

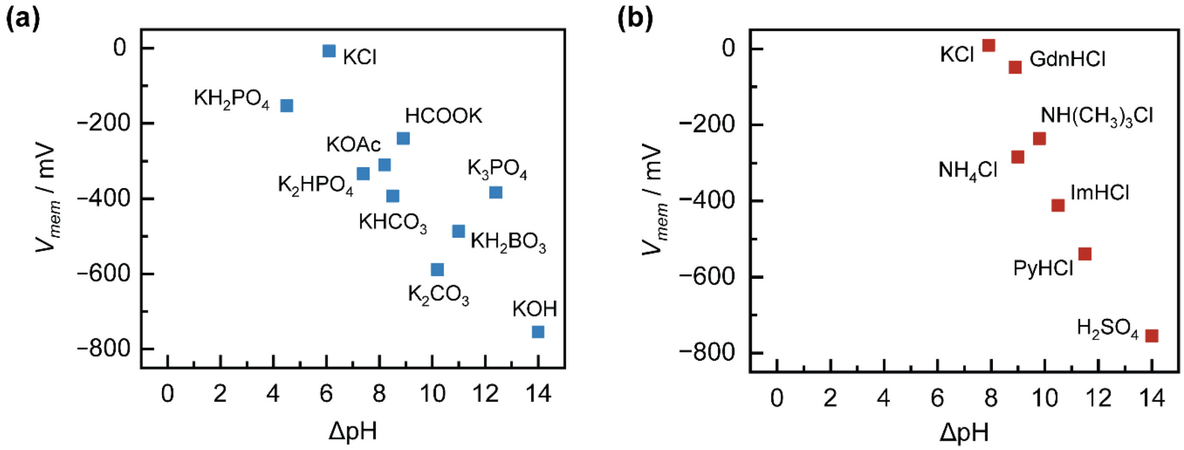

Figure S3.13. Plot of open-circuit V_{mem} vs ΔpH for **(a)** H_2SO_4 | KA and **(b)** BHCl | KOH cells.

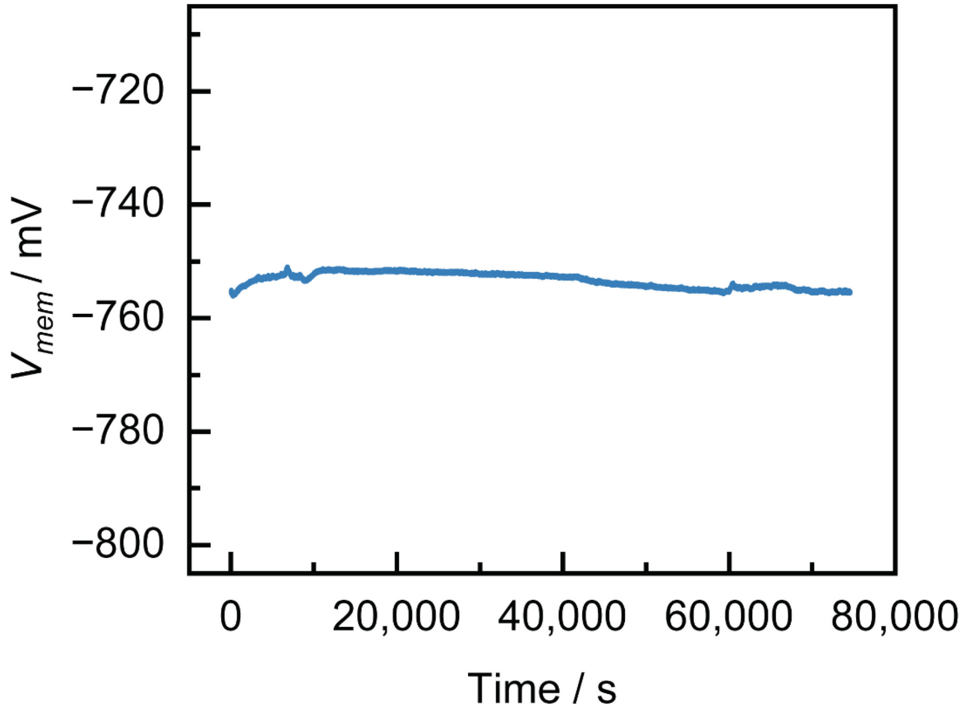

Figure S3.14. Time evolution of open-circuit membrane voltage for the H_2SO_4 | KOH cell.

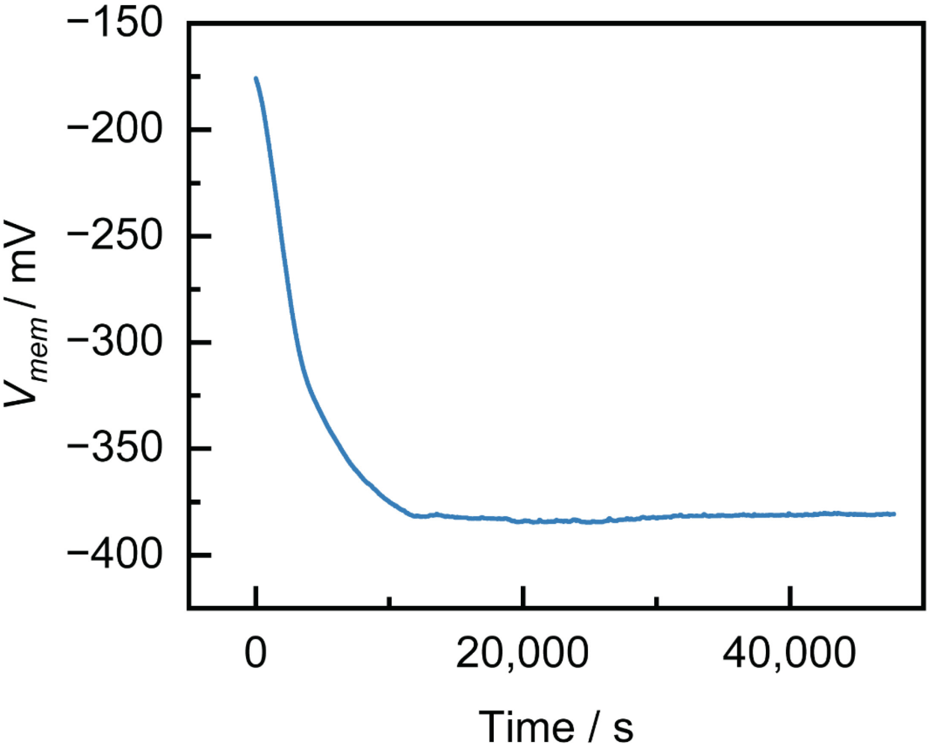

Figure S3.15. Time evolution of open-circuit membrane voltage for the H_2SO_4 | K_3PO_4 cell.

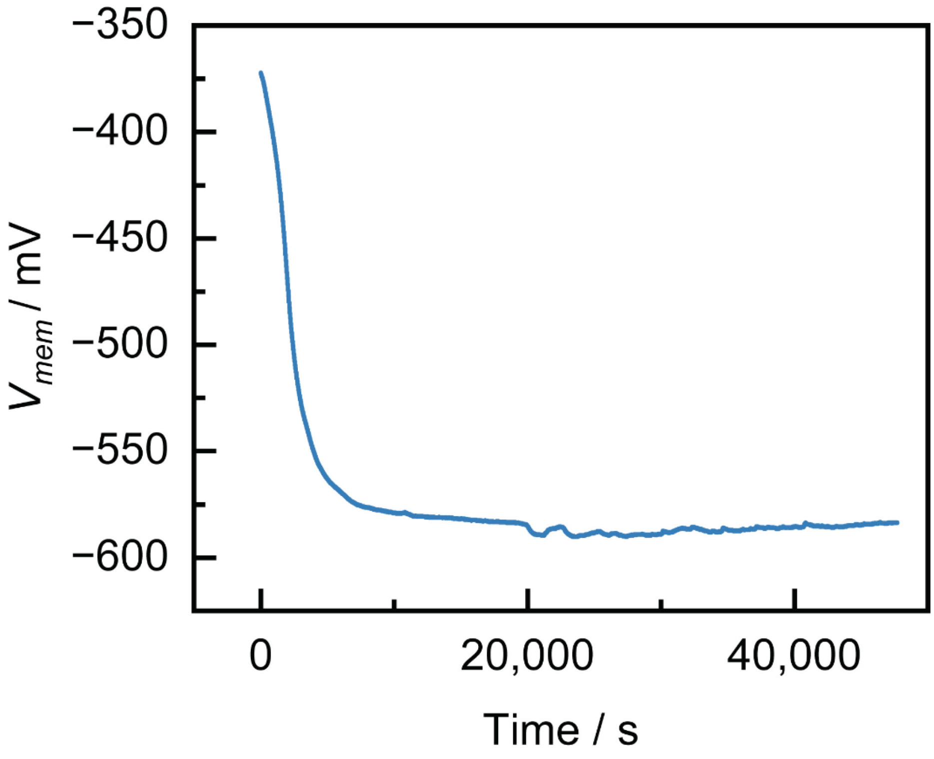

Figure S3.16. Time evolution of open-circuit membrane voltage for the H_2SO_4 | K_2CO_3 cell.

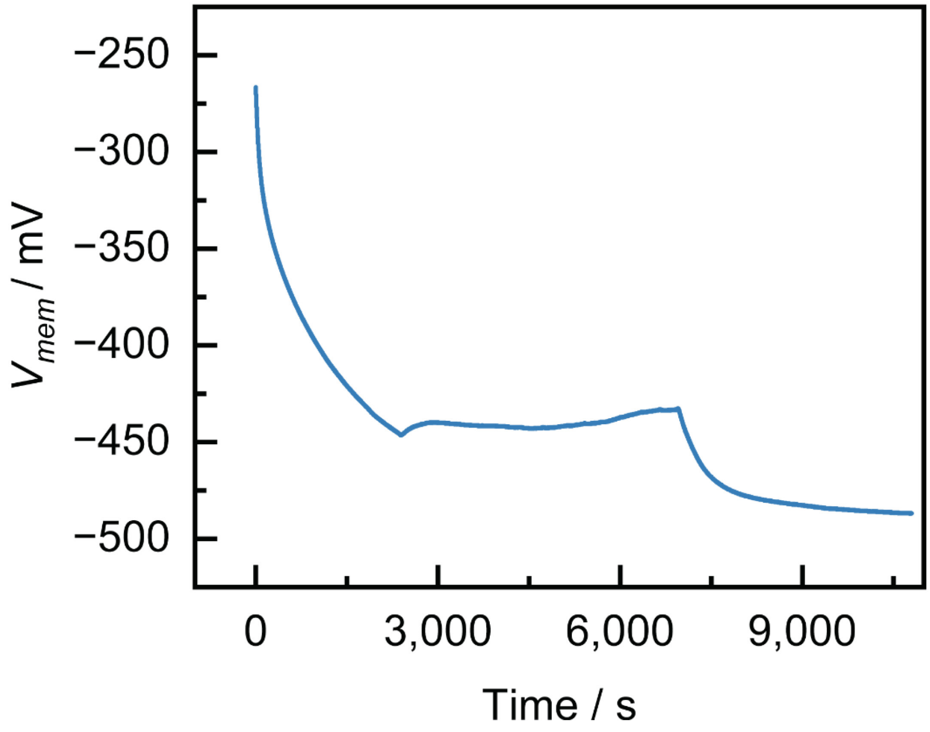

Figure S3.17. Time evolution of open-circuit membrane voltage for the H_2SO_4 | KH_2BO_3 cell.

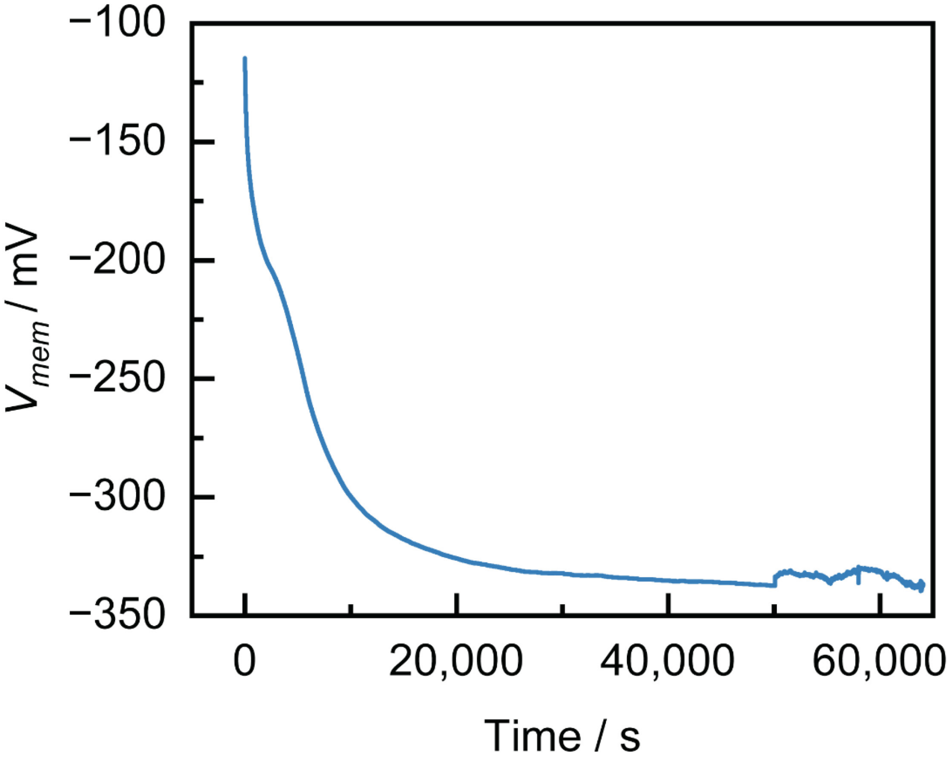

Figure S3.18. Time evolution of open-circuit membrane voltage for the H_2SO_4 | K_2HPO_4 cell.

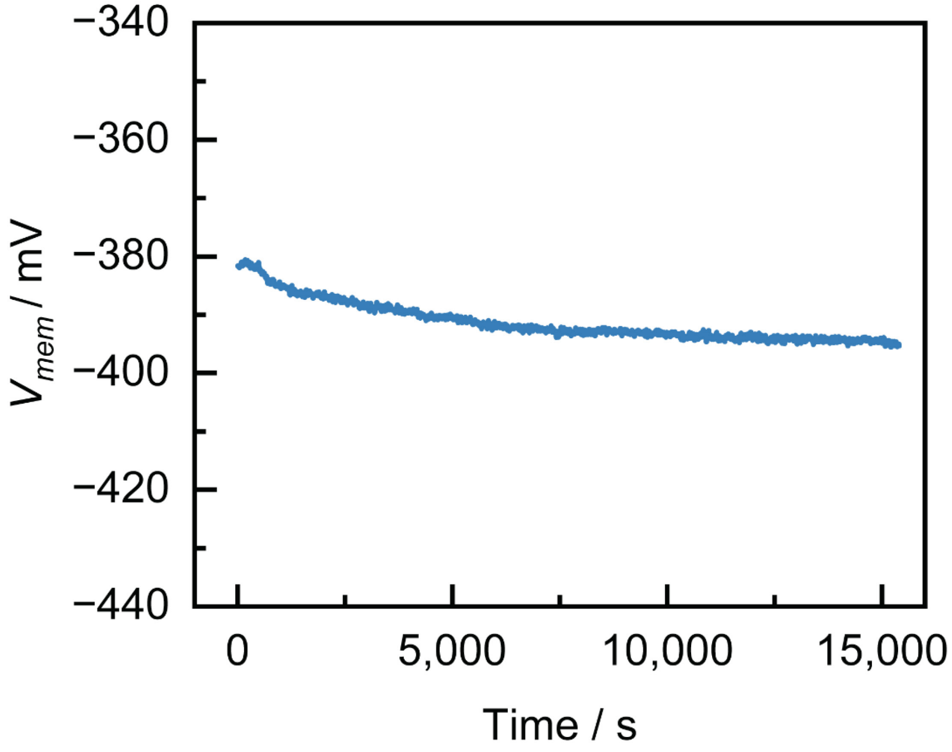

Figure S3.19. Time evolution of open-circuit membrane voltage for the H_2SO_4 | $KHCO_3$ cell.

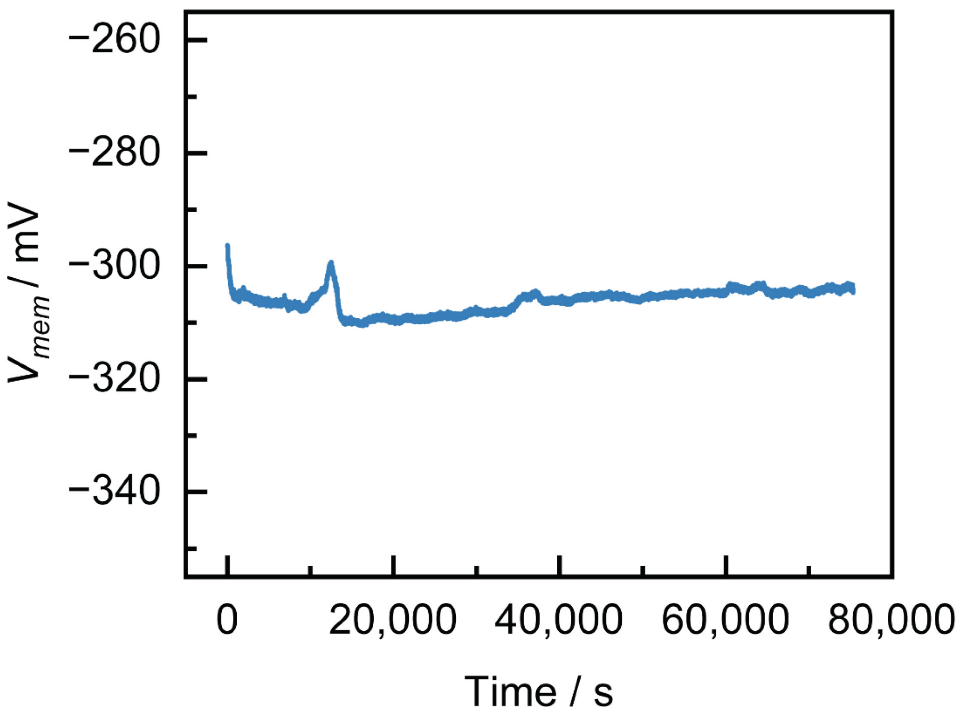

Figure S3.20. Time evolution of open-circuit membrane voltage for the H_2SO_4 | KOAc cell.

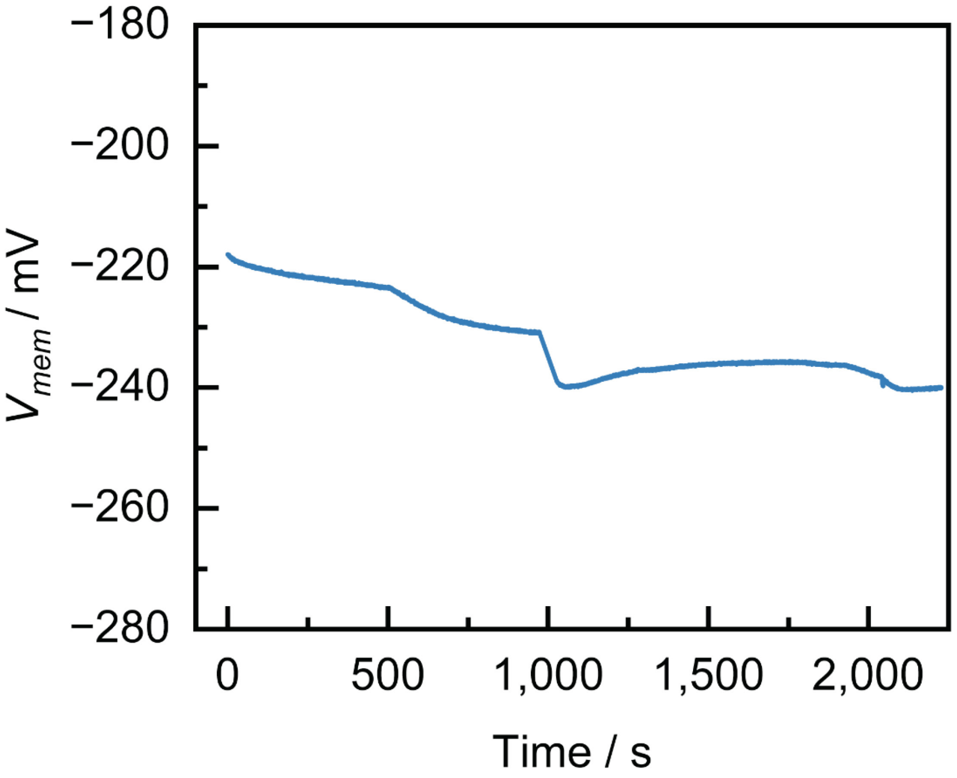

Figure S3.21. Time evolution of open-circuit membrane voltage for the H_2SO_4 | HCOOK cell.

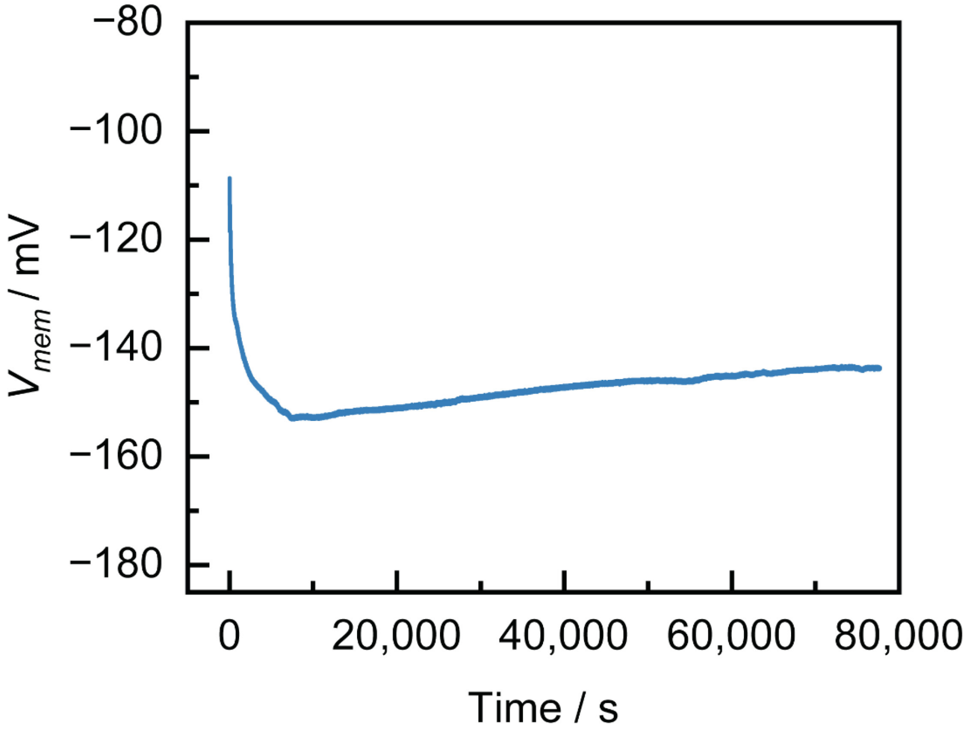

Figure S3.22. Time evolution of open-circuit membrane voltage for the H_2SO_4 | KH_2PO_4 cell.

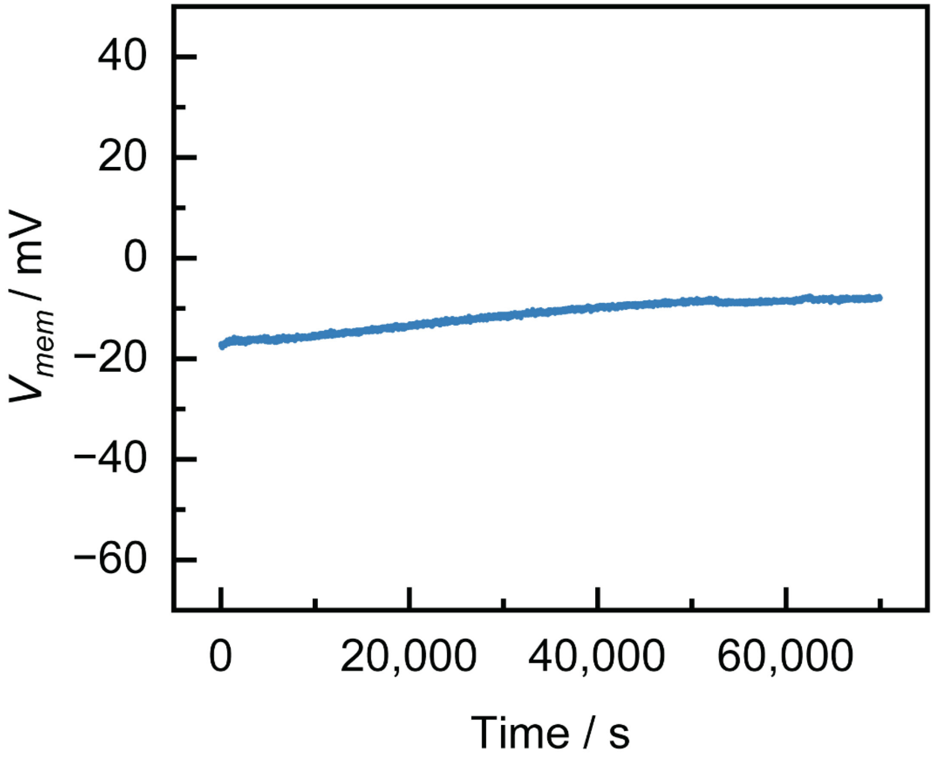

Figure S3.23. Time evolution of open-circuit membrane voltage for the H_2SO_4 | KCl cell.

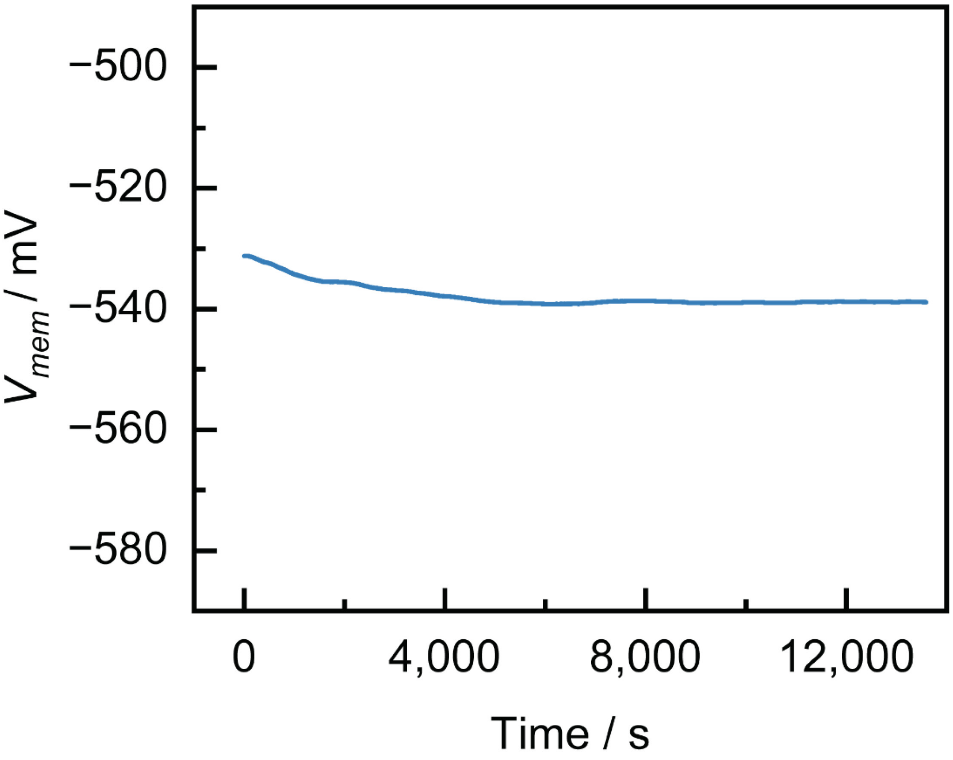

Figure S3.24. Time evolution of open-circuit membrane voltage for the PyHCl | KOH cell.

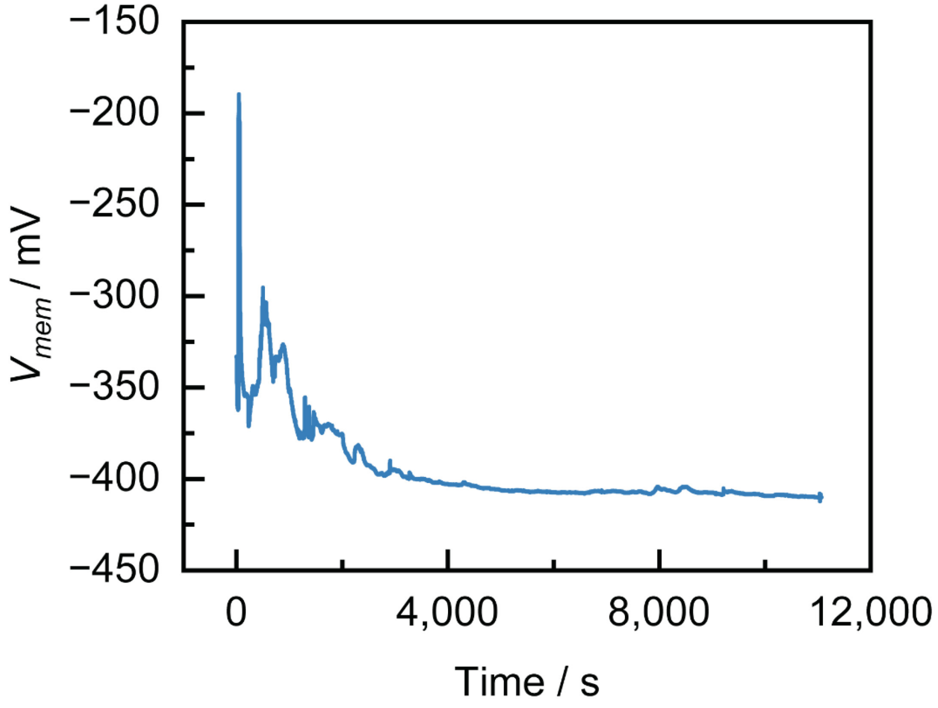

Figure S3.25. Time evolution of open-circuit membrane voltage for the ImHCl | KOH cell.

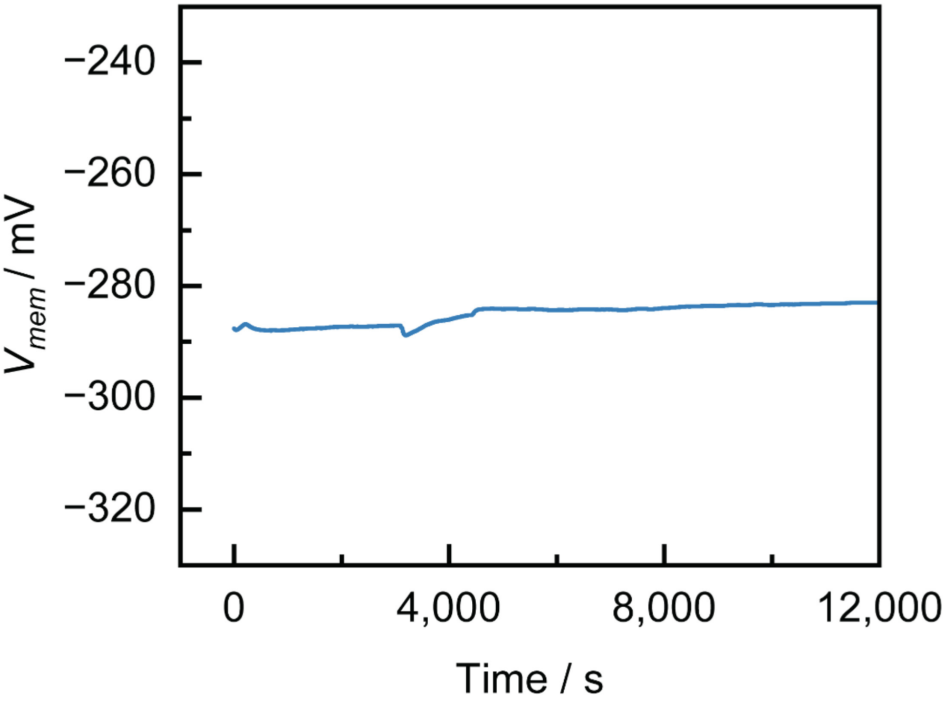

Figure S3.26. Time evolution of open-circuit membrane voltage for the NH_4Cl | KOH cell.

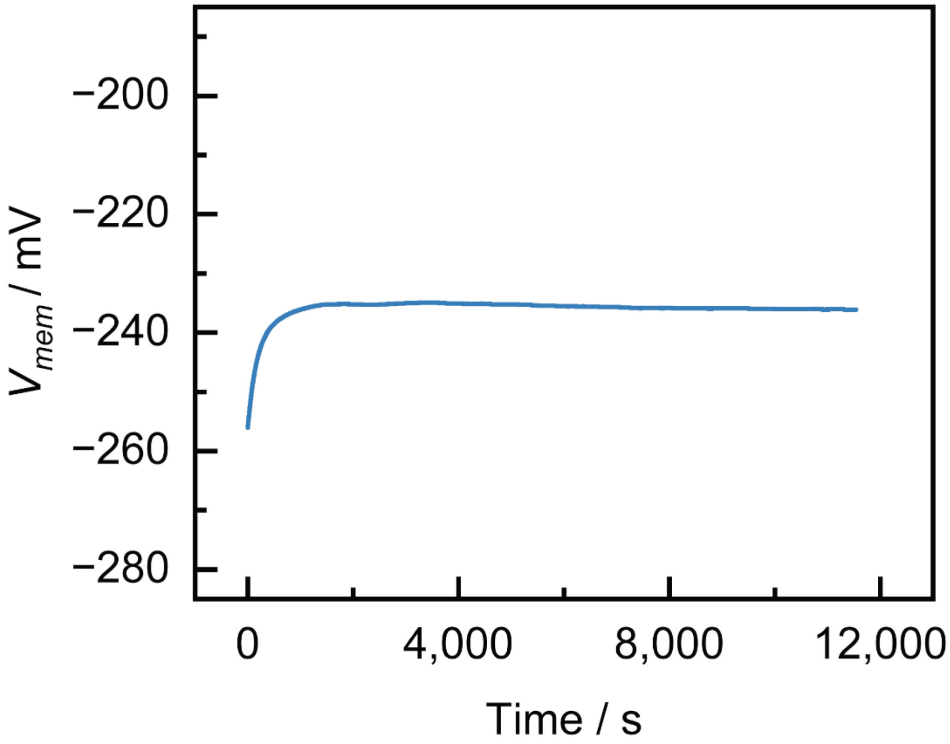

Figure S3.27. Time evolution of open-circuit membrane voltage for the $NH(CH_3)_3Cl$ | KOH cell.

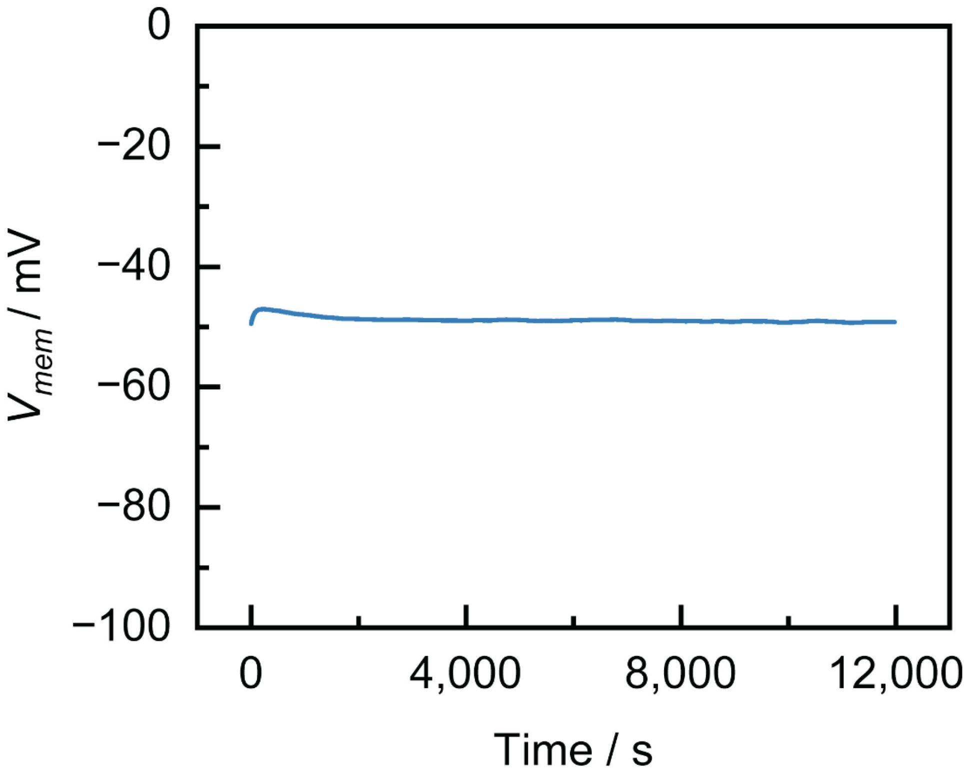

Figure S3.28. Time evolution of open-circuit membrane voltage for the GdnHCl | KOH cell.

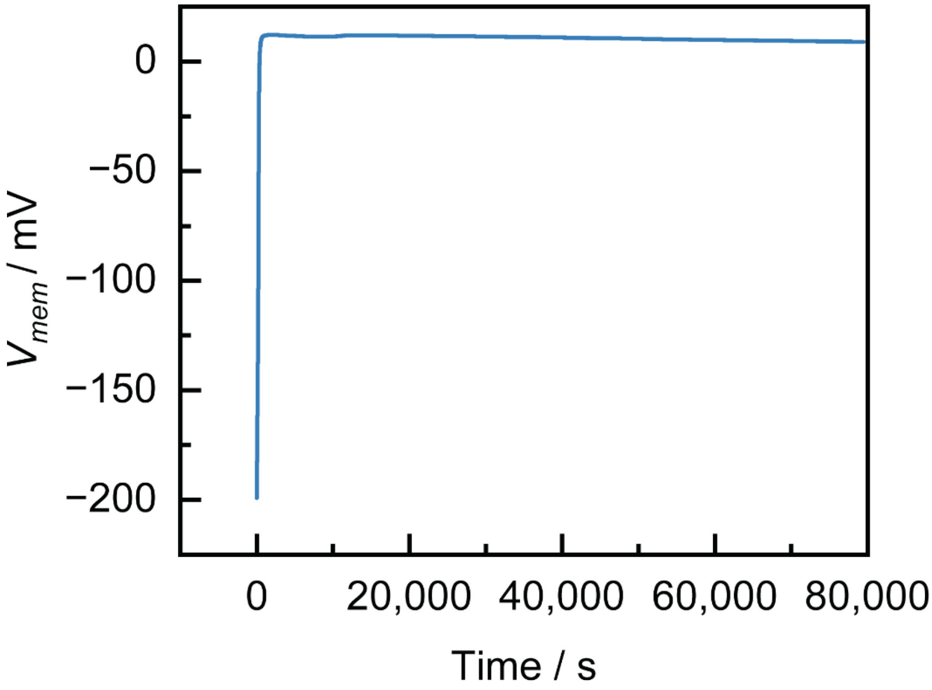

Figure S3.29. Time evolution of open-circuit membrane voltage for the KCl | KOH cell.

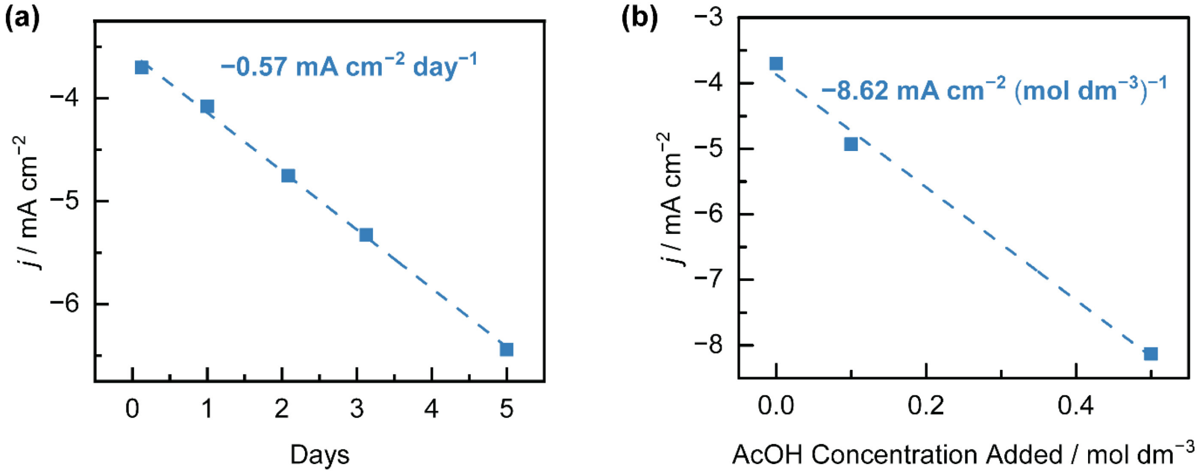

Figure S3.30. Variation of j_{lim} as a function of **(a)** the number of days that a H_2SO_4 | KOAc cell has been held at open-circuit without added AcOH and **(b)** the concentration of AcOH added to separate H_2SO_4 | KOAc cells polarized after 3 h of equilibration.

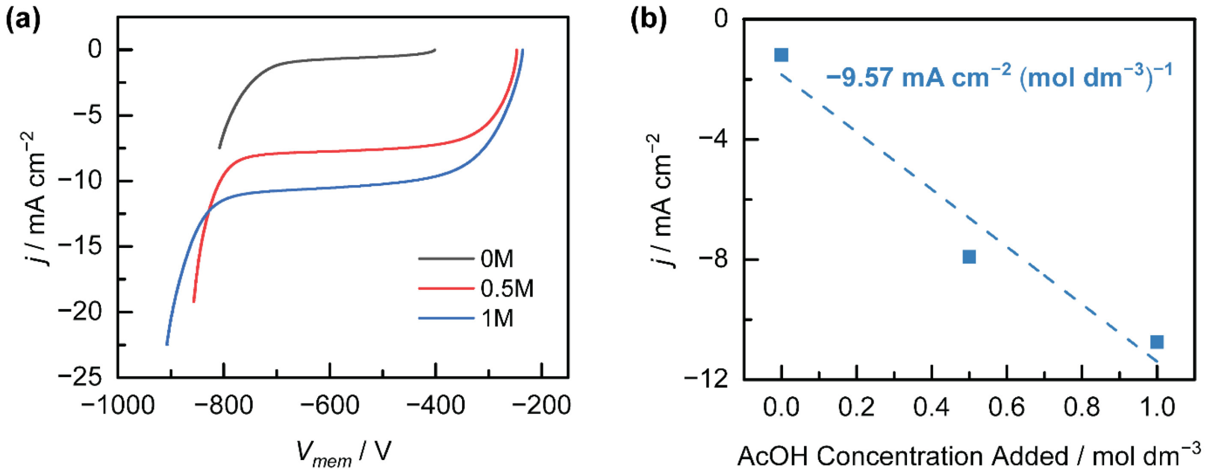

Figure S3.31. **(a)** Reverse bias polarization curves and **(b)** plot of j_{lim} against concentration of AcOH added for separate PSS–H | PDADMA–OAc cells after 3 h of equilibration.

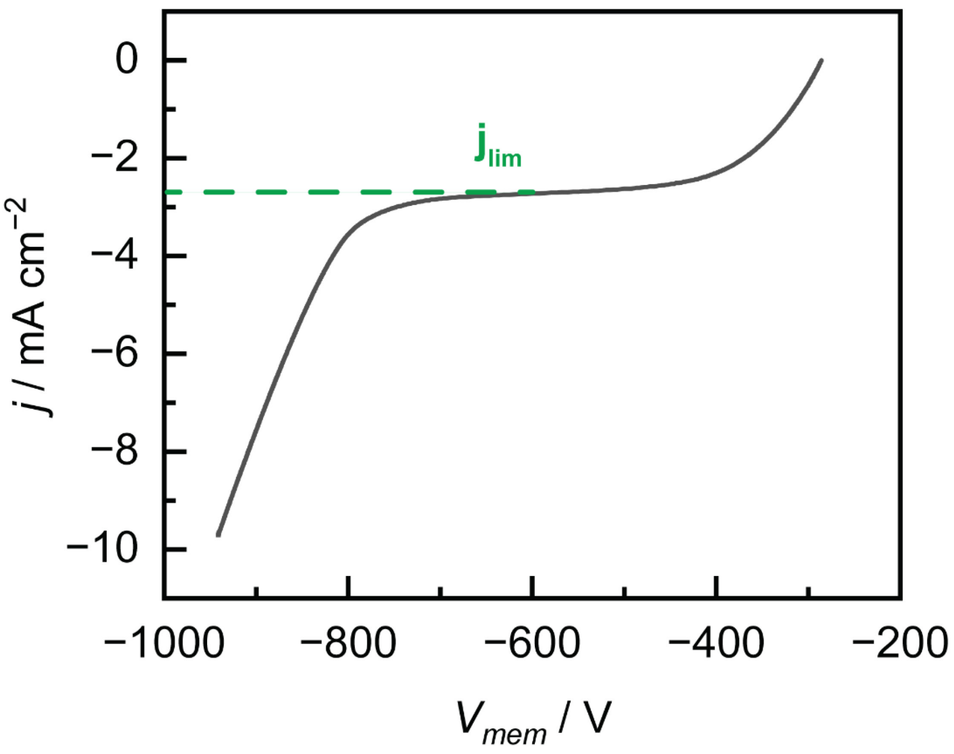

Figure S3.32. Reverse bias polarization curve of H_2SO_4 | KOAc after 3 h equilibration at open-circuit (not iR-corrected).

3.8 References

(1) Pärnamäe, R.; Mareev, S.; Nikonenko, V.; Melnikov, S.; Sheldeshov, N.; Zabolotskii, V.; Hamelers, H. V. M.; Tedesco, M. Bipolar Membranes: A Review on Principles, Latest Developments, and Applications. *J. Memb. Sci.* **2021**, *617*, 118538.

(2) Giesbrecht, P. K.; Freund, M. S. Recent Advances in Bipolar Membrane Design and Applications. *Chem. Mater.* **2020**, *32* (19), 8060–8090.

(3) Blommaert, M. A.; Aili, D.; Tufa, R. A.; Li, Q.; Smith, W. A.; Vermaas, D. A. Insights and Challenges for Applying Bipolar Membranes in Advanced Electrochemical Energy Systems. *ACS Energy Lett.* **2021**, *6*, 2539–2548.

(4) Tufa, R. A.; Blommaert, M. A.; Chanda, D.; Li, Q.; Vermaas, D. A.; Aili, D. Bipolar Membrane and Interface Materials for Electrochemical Energy Systems. *ACS Appl. Energy Mater.* **2021**, *4* (8), 7419–7439.

(5) Yan, Z.; Mallouk, T. E. Bipolar Membranes for Ion Management in (Photo)Electrochemical Energy Conversion. *Accounts Mater. Res.* **2021**, *2* (12), 1156–1166.

(6) Oener, S. Z.; Foster, M. J.; Boettcher, S. W. Accelerating Water Dissociation in Bipolar Membranes and for Electrocatalysis. *Science.* **2020**, *369* (6507), 1099–1103.

(7) Simons, R.; Khanarian, G. Water Dissociation in Bipolar Membranes: Experiments and Theory. *J. Membr. Biol.* **1978**, *38* (1–2), 11–30.

(8) Ramírez, P.; Rapp, H.-J.; Mafé, S.; Bauer, B. Bipolar Membranes under Forward and Reverse Bias Conditions. Theory vs. Experiment. *J. Electroanal. Chem.* **1994**, *375* (1–2), 101–108.

(9) McDonald, M. B.; Ardo, S.; Lewis, N. S.; Freund, M. S. Use of Bipolar Membranes for Maintaining Steady-State PH Gradients in Membrane-Supported, Solar-Driven Water Splitting. *ChemSusChem* **2014**, *7* (11), 3021–3027.

(10) Vargas-Barbosa, N. M.; Geise, G. M.; Hickner, M. A.; Mallouk, T. E. Assessing the Utility of Bipolar Membranes for Use in Photoelectrochemical Water-Splitting Cells. *ChemSusChem* **2014**, *7* (11), 3017–3020.

(11) Luo, J.; Vermaas, D. A.; Bi, D.; Hagfeldt, A.; Smith, W. A.; Grätzel, M. Bipolar Membrane-Assisted Solar Water Splitting in Optimal PH. *Adv. Energy Mater.* **2016**, *6* (13), 1600100.

(12) Mayerhöfer, B.; McLaughlin, D.; Böhm, T.; Hegelheimer, M.; Seeberger, D.; Thiele, S. Bipolar Membrane Electrode Assemblies for Water Electrolysis. *ACS Appl. Energy Mater.* **2020**, *3* (10), 9635–9644.

(13) Oener, S. Z.; Twight, L. P.; Lindquist, G. A.; Boettcher, S. W. Thin Cation-Exchange

Layers Enable High-Current-Density Bipolar Membrane Electrolyzers via Improved Water Transport. *ACS Energy Lett.* **2021**, *6* (1), 1–8.

(14) Vermaas, D. A.; Smith, W. A. Synergistic Electrochemical CO2 Reduction and Water Oxidation with a Bipolar Membrane. *ACS Energy Lett.* **2016**, *1* (6), 1143–1148.

(15) Li, Y. C.; Zhou, D.; Yan, Z.; Gonçalves, R. H.; Salvatore, D. A.; Berlinguette, C. P.; Mallouk, T. E. Electrolysis of CO2 to Syngas in Bipolar Membrane-Based Electrochemical Cells. *ACS Energy Lett.* **2016**, *1* (6), 1149–1153.

(16) Zhou, X.; Liu, R.; Sun, K.; Chen, Y.; Verlage, E.; Francis, S. A.; Lewis, N. S.; Xiang, C. Solar-Driven Reduction of 1 Atm of CO2 to Formate at 10% Energy-Conversion Efficiency by Use of a TiO2-Protected III–V Tandem Photoanode in Conjunction with a Bipolar Membrane and a Pd/C Cathode. *ACS Energy Lett.* **2016**, *1* (4), 764–770.

(17) Salvatore, D. A.; Weekes, D. M.; He, J.; Dettelbach, K. E.; Li, Y. C.; Mallouk, T. E.; Berlinguette, C. P. Electrolysis of Gaseous CO2 to CO in a Flow Cell with a Bipolar Membrane. *ACS Energy Lett.* **2018**, *3* (1), 149–154.

(18) Pătru, A.; Binninger, T.; Pribyl, B.; Schmidt, T. J. Design Principles of Bipolar Electrochemical Co-Electrolysis Cells for Efficient Reduction of Carbon Dioxide from Gas Phase at Low Temperature. *J. Electrochem. Soc.* **2019**, *166* (2), F34–F43.

(19) Blommaert, M. A.; Sharifian, R.; Shah, N.; Nesbitt, N.; Smith, W.; Vermaas, D. A. Orientation of Bipolar Membrane Determines the Dominant Ion and Carbonic Species Transport in Membrane Electrode Assemblies for CO2 Reduction. *J. Mater. Chem. A* **2021**.

(20) Siritanaratkul, B.; Forster, M.; Greenwell, F.; Sharma, P. K.; Yu, E. H.; Cowan, A. J. Zero-Gap Bipolar Membrane Electrolyzer for Carbon Dioxide Reduction Using Acid-Tolerant Molecular Electrocatalysts. *J. Am. Chem. Soc.* **2022**, *144* (17), 7551–7556.

(21) Xie, K.; Miao, R. K.; Ozden, A.; Liu, S.; Chen, Z.; Dinh, C.; Huang, J. E.; Xu, Q.; Gabardo, C. M.; Lee, G.; Edwards, J. P.; O'Brien, C. P.; Boettcher, S. W.; Sinton, D.; Sargent, E. H. Bipolar Membrane Electrolyzers Enable High Single-Pass CO2 Electroreduction to Multicarbon Products. *Nat. Commun.* **2022**, *13* (1), 3609.

(22) Sullivan, I.; Goryachev, A.; Digdaya, I. A.; Li, X.; Atwater, H. A.; Vermaas, D. A.; Xiang, C. Coupling Electrochemical CO2 Conversion with CO2 Capture. *Nat. Catal.* **2021**, *4* (11), 952–958.

(23) Sharifian, R.; Wagterveld, R. M.; Digdaya, I. A.; Xiang, C.; Vermaas, D. A. Electrochemical Carbon Dioxide Capture to Close the Carbon Cycle. *Energy Environ. Sci.* **2021**, *14* (2), 781–814.

(24) Ding, Y.; Cai, P.; Wen, Z. Electrochemical Neutralization Energy: From Concept to Devices. *Chem. Soc. Rev.* **2021**, *50* (3), 1495–1511.

(25) Pärnamäe, R.; Gurreri, L.; Post, J.; van Egmond, W. J.; Culcasi, A.; Saakes, M.; Cen, J.;

Goosen, E.; Tamburini, A.; Vermaas, D. A.; Tedesco, M. The Acid–Base Flow Battery: Sustainable Energy Storage via Reversible Water Dissociation with Bipolar Membranes. *Membranes (Basel).* **2020**, *10* (12), 409.

(26) Yan, Z.; Wycisk, R. J.; Metlay, A. S.; Xiao, L.; Yoon, Y.; Pintauro, P. N.; Mallouk, T. E. High-Voltage Aqueous Redox Flow Batteries Enabled by Catalyzed Water Dissociation and Acid–Base Neutralization in Bipolar Membranes. *ACS Cent. Sci.* **2021**, *7* (6), 1028–1035.

(27) Metlay, A. S.; Chyi, B.; Yoon, Y.; Wycisk, R. J.; Pintauro, P. N.; Mallouk, T. E. Three-Chamber Design for Aqueous Acid–Base Redox Flow Batteries. *ACS Energy Lett.* **2022**, *7* (3), 908–913.

(28) O'Brien, C. P.; Miao, R. K.; Liu, S.; Xu, Y.; Lee, G.; Robb, A.; Huang, J. E.; Xie, K.; Bertens, K.; Gabardo, C. M.; Edwards, J. P.; Dinh, C.; Sargent, E. H.; Sinton, D. Single Pass CO2 Conversion Exceeding 85% in the Electrosynthesis of Multicarbon Products via Local CO2 Regeneration. *ACS Energy Lett.* **2021**, *6* (8), 2952–2959.

(29) Tan, Y. C.; Quek, W. K.; Kim, B.; Sugiarto, S.; Oh, J.; Kai, D. Pitfalls and Protocols: Evaluating Catalysts for CO2 Reduction in Electrolyzers Based on Gas Diffusion Electrodes. *ACS Energy Lett.* **2022**, *7* (6), 2012–2023.

(30) Xu, Y.; Miao, R. K.; Edwards, J. P.; Liu, S.; O'Brien, C. P.; Gabardo, C. M.; Fan, M.; Huang, J. E.; Robb, A.; Sargent, E. H.; Sinton, D. A Microchanneled Solid Electrolyte for Carbon-Efficient CO2 Electrolysis. *Joule* **2022**, *6* (6), 1333–1343.

(31) Xia, C.; Zhu, P.; Jiang, Q.; Pan, Y.; Liang, W.; Stavitski, E.; Alshareef, H. N.; Wang, H. Continuous Production of Pure Liquid Fuel Solutions via Electrocatalytic CO2 Reduction Using Solid-Electrolyte Devices. *Nat. Energy* **2019**, *4* (9), 776–785.

(32) Fan, L.; Xia, C.; Zhu, P.; Lu, Y.; Wang, H. Electrochemical CO2 Reduction to High-Concentration Pure Formic Acid Solutions in an All-Solid-State Reactor. *Nat. Commun.* **2020**, *11* (1), 3633.

(33) Ünlü, M.; Zhou, J.; Kohl, P. A. Hybrid Anion and Proton Exchange Membrane Fuel Cells. *J. Phys. Chem. C* **2009**, *113* (26), 11416–11423.

(34) Ünlü, M.; Zhou, J.; Kohl, P. A. Hybrid Polymer Electrolyte Fuel Cells: Alkaline Electrodes with Proton Conducting Membrane. *Angew. Chemie* **2010**, *122* (7), 1321–1323.

(35) Reiter, R. S.; White, W.; Ardo, S. Communication—Electrochemical Characterization of Commercial Bipolar Membranes under Electrolyte Conditions Relevant to Solar Fuels Technologies. *J. Electrochem. Soc.* **2016**, *163* (4), H3132–H3134.

(36) Vermaas, D. A.; Wiegman, S.; Nagaki, T.; Smith, W. A. Ion Transport Mechanisms in Bipolar Membranes for (Photo)Electrochemical Water Splitting. *Sustain. Energy Fuels* **2018**, *2* (9), 2006–2015.

(37) Vermaas, D. A.; Sassenburg, M.; Smith, W. A. Photo-Assisted Water Splitting with Bipolar Membrane Induced PH Gradients for Practical Solar Fuel Devices. *J. Mater. Chem. A* **2015**, *3* (38), 19556–19562.

(38) Bui, J. C.; Digdaya, I.; Xiang, C.; Bell, A. T.; Weber, A. Z. Understanding Multi-Ion Transport Mechanisms in Bipolar Membranes. *ACS Appl. Mater. Interfaces* **2020**, *12* (47), 52509–52526.

(39) Blommaert, M. A.; Verdonk, J. A. H.; Blommaert, H. C. B.; Smith, W. A.; Vermaas, D. A. Reduced Ion Crossover in Bipolar Membrane Electrolysis via Increased Current Density, Molecular Size, and Valence. *ACS Appl. Energy Mater.* **2020**, *3* (6), 5804–5812.

(40) Lin, M.; Digdaya, I. A.; Xiang, C. Modeling the Electrochemical Behavior and Interfacial Junction Profiles of Bipolar Membranes at Solar Flux Relevant Operating Current Densities. *Sustain. Energy Fuels* **2021**, *5* (7), 2149–2158.

(41) Mareev, S. A.; Evdochenko, E.; Wessling, M.; Kozaderova, O. A.; Niftaliev, S. I.; Pismenskaya, N. D.; Nikonenko, V. V. A Comprehensive Mathematical Model of Water Splitting in Bipolar Membranes: Impact of the Spatial Distribution of Fixed Charges and Catalyst at Bipolar Junction. *J. Memb. Sci.* **2020**, *603*, 118010.

(42) Varcoe, J. R.; Atanassov, P.; Dekel, D. R.; Herring, A. M.; Hickner, M. A.; Kohl, P. A.; Kucernak, A. R.; Mustain, W. E.; Nijmeijer, K.; Scott, K.; Xu, T.; Zhuang, L. Anion-Exchange Membranes in Electrochemical Energy Systems. *Energy Environ. Sci.* **2014**, *7* (10), 3135–3191.

(43) Blommaert, M. A.; Vermaas, D. A.; Izelaar, B.; in 't Veen, B.; Smith, W. A. Electrochemical Impedance Spectroscopy as a Performance Indicator of Water Dissociation in Bipolar Membranes. *J. Mater. Chem. A* **2019**, *7* (32), 19060–19069.

(44) Wedege, K.; Dražević, E.; Konya, D.; Bentien, A. Organic Redox Species in Aqueous Flow Batteries: Redox Potentials, Chemical Stability and Solubility. *Sci. Rep.* **2016**, *6* (1), 39101.

(45) Tabor, D. P.; Gómez-Bombarelli, R.; Tong, L.; Gordon, R. G.; Aziz, M. J.; Aspuru-Guzik, A. Mapping the Frontiers of Quinone Stability in Aqueous Media: Implications for Organic Aqueous Redox Flow Batteries. *J. Mater. Chem. A* **2019**, *7* (20), 12833–12841.

(46) Donnan, F. G. The Theory of Membrane Equilibria. *Chem. Rev.* **1924**, *1* (1), 73–90.

(47) Higuchi, A.; Nakagawa, T. Membrane Potential and Permeation of Salts across Bipolar Membranes. *J. Memb. Sci.* **1987**, *32* (2–3), 267–280.

(48) Luo, T.; Abdu, S.; Wessling, M. Selectivity of Ion Exchange Membranes: A Review. *J. Memb. Sci.* **2018**, *555*, 429–454.

(49) Rubinstein, I.; Pretz, J.; Staude, E. Open Circuit Voltage in a Reverse Electrodialysis Cell. *Phys. Chem. Chem. Phys.* **2001**, *3* (9), 1666–1667.

(50) Culcasi, A.; Gurreri, L.; Zaffora, A.; Cosenza, A.; Tamburini, A.; Cipollina, A.; Micale, G. Ionic Shortcut Currents via Manifolds in Reverse Electrodialysis Stacks. *Desalination* **2020**, *485*, 114450.

(51) Moussaoui, R. El; Pourcelly, G.; Maeck, M.; Hurwitz, H. D.; Gavach, C. Co-Ion Leakage through Bipolar Membranes Influence on I–V Responses and Water-Splitting Efficiency. *J. Memb. Sci.* **1994**, *90* (3), 283–292.

(52) Miyoshi, H. Diffusion Coefficients of Ions through Ion-Exchange Membranes for Donnan Dialysis Using Ions of the Same Valence. *Chem. Eng. Sci.* **1997**, *52* (7), 1087–1096.

(53) Grew, K. N.; McClure, J. P.; Chu, D.; Kohl, P. A.; Ahlfield, J. M. Understanding Transport at the Acid-Alkaline Interface of Bipolar Membranes. *J. Electrochem. Soc.* **2016**, *163* (14), F1572–F1587.

(54) Grew, K. N.; Chiu, W. K. S. Stability & Kinetics of the Bipolar Membrane Interface: Implications for Electrochemical Technologies. *J. Electrochem. Soc.* **2020**, *167* (16), 164513.

(55) Kole, S.; Venugopalan, G.; Bhattacharya, D.; Zhang, L.; Cheng, J.; Pivovar, B.; Arges, C. G. Bipolar Membrane Polarization Behavior with Systematically Varied Interfacial Areas in the Junction Region. *J. Mater. Chem. A* **2021**, *9* (4), 2223–2238.

(56) Strathmann, H.; Krol, J. .; Rapp, H.-J.; Eigenberger, G. Limiting Current Density and Water Dissociation in Bipolar Membranes. *J. Memb. Sci.* **1997**, *125* (1), 123–142.

(57) Lee, M.-Y.; Park, K. T.; Lee, W.; Lim, H.; Kwon, Y.; Kang, S. Current Achievements and the Future Direction of Electrochemical CO2 Reduction: A Short Review. *Crit. Rev. Environ. Sci. Technol.* **2020**, *50* (8), 769–815.

(58) Fan, L.; Liu, B.; Liu, X.; Senthilkumar, N.; Wang, G.; Wen, Z. Recent Progress in Electrocatalytic Glycerol Oxidation. *Energy Technol.* **2021**, *9* (2), 2000804.

(59) Yadegari, H.; Ozden, A.; Alkayyali, T.; Soni, V.; Thevenon, A.; Rosas-Hernández, A.; Agapie, T.; Peters, J. C.; Sargent, E. H.; Sinton, D. Glycerol Oxidation Pairs with Carbon Monoxide Reduction for Low-Voltage Generation of C2 and C3 Product Streams. *ACS Energy Lett.* **2021**, *6* (10), 3538–3544.

(60) Li, S.; Sun, X.; Yao, Z.; Zhong, X.; Cao, Y.; Liang, Y.; Wei, Z.; Deng, S.; Zhuang, G.; Li, X.; Wang, J. Biomass Valorization via Paired Electrosynthesis Over Vanadium Nitride-Based Electrocatalysts. *Adv. Funct. Mater.* **2019**, *29* (42), 1904780.

(61) Haynes, W. M.; Lide, D. R.; Bruno, T. J. *CRC Handbook of Chemistry and Physics*, 97th ed.; CRC Press, 2016.

(62) Coughlin, J. E.; Reisch, A.; Markarian, M. Z.; Schlenoff, J. B. Sulfonation of Polystyrene: Toward the "Ideal" Polyelectrolyte. *J. Polym. Sci. Part A Polym. Chem.* **2013**, *51* (11), 2416–2424.

(63) Donovan, S.; Atkinson, A. J.; Fischer, N.; Taylor, A. E.; Kieffer, J.; Croue, J. P.; Westerhoff, P.; Herckes, P. Nuclear Magnetic Resonance Enables Understanding of Polydiallyldimethylammonium Chloride Composition and N -Nitrosodimethylamine Formation during Chloramination. *Environ. Sci. Water Res. Technol.* **2021**, *7* (6), 1050–1059.

Chapter 4

Ionic Blockades Control the Efficiency of Energy Recovery in Forward Bias Bipolar Membranes

Portions of this chapter have been published:

Wei Lun Toh,[‡] Hieu Q. Dinh,[‡] An T. Chu, Ethan, R. Sauvé, Yogesh Surendranath. *ChemRxiv*. Preprint. https://chemrxiv.org/engage/chemrxiv/article-details/642faa3e736114c9630e5df7

[‡]These authors contributed equally.

Abstract

Limited understanding exists about the operation of bipolar membranes (BPMs) in forward bias to convert protonic gradients into electrical work, despite its emerging role in many electrochemical devices. In these device contexts, the BPM is typically exposed to complex electrolyte mixtures, but their impact on polarization remains poorly understood. Herein, we develop a mechanistic model explaining the forward bias polarization behavior of BPMs in mixed electrolytes with different acidities/basicities. This model invokes that weak acids/bases accumulate in the BPM and impose an ionic blockade that inhibits the recombination of stronger acids/bases, resulting in a substantial neutralization overpotential. We demonstrate the utility of our model to fuel cells and redox flow batteries, and introduce two materials design strategies for mitigating this inhibition. Lastly, we apply our findings to enhance the energy efficiency of carbonate management in CO_2 electrolyzers. This work highlights how non-equilibrium local environments at membrane-membrane interfaces can define the efficiency of protonic-to-electrical energy conversion.

4.1 Introduction

The interconversion of chemical and electrical potential energy gradients underpins the function of electrochemical energy technologies.[1] Typically, this interconversion is mediated by charge transfer reactions at electrode-electrolyte interfaces.[2] However, electrical energy can also be converted into chemical energy in solution, via the formation of ion gradients across membrane-electrolyte interfaces.[3] This mode of energy conversion is key to ion separations and electrodialysis and can be used to enhance the efficiency, selectivity, and durability of flow batteries, fuel cells, and electrolyzers.[3] Thus, mechanistic understanding of ion transfer processes across membrane-electrolyte interfaces is critical for addressing frontier challenges in energy and sustainability.

Bipolar membranes (BPMs) are an emerging electrochemical technology that enables the interconversion of protonic free energy gradients in solution into electrical potential gradients.[4–8] This capability arises from their unique structure comprising a cation exchange membrane (CEM) laminated onto an anion exchange membrane (AEM), giving rise to the property of ionic current rectification and allowing the maintenance of a stable pH gradient between the catholyte and the anolyte.[4–8] BPMs can be operated in both reverse and forward bias modes. In reverse bias, an applied potential drives the dissociation of water or other proton donors into charged acid and base species.[5,6,9,10] This mode transduces electrical work into a chemical protonic gradient, and allows the continuous generation of acid and base. As a result, it has been extensively studied and applied to water electrolyzers,[11–16] CO_2 electrolyzers,[17–24] and bipolar membrane electrodialysis (BPMED) cells.[25,26] In contrast, in forward bias, the spontaneous recombination of charged acids and bases at the bipolar junction is employed to generate a potential difference that can be used to drive electrical work in an external circuit.[27–29] Consequently, this mode of operation transduces a proton gradient into electrical potential, which can be used to reduce the overall voltage of an electrolytic cell or increase the overall voltage of a galvanic cell. Indeed, forward bias BPMs have been applied to access larger cell voltages in redox flow batteries.[28–30] The foregoing examples showcase the opportunities BPMs offer for interconverting protonic and electrical energy.

Despite its immense potential, there is limited understanding of the factors that control the efficiency of protonic to electrical energy conversion under forward bias polarization. Existing BPM studies have predominantly examined the reverse bias mode,[5] and the studies on forward bias have largely examined the recombination of only binary electrolytes (i.e. containing only one type of cation and one type of anion), commonly hydronium and hydroxide (**Figure 4.1**),[31–33] with only a few reports investigating the effect of salt and buffer ions.[10,32,34] To our knowledge, there have been no systematic studies of BPMs in electrolyte mixtures that contain two or more species of different acidities and basicities. This is despite the prevalence of mixed electrolytes in variety of device contexts. For example, in H_2 fuel cells and CO_2 electrolyzers, in addition to hydroxide ions, (bi)carbonates invariably co-exist as a result of CO_2 absorption.[35] In addition, in CO_2 electrolyzers, weak organic bases such as acetate and formate can be produced as liquid products of CO_2 reduction.[36] This knowledge gap of how mixed electrolytes affect the speciation and polarization behavior within forward bias BPMs severely hampers the utilization of this bias mode in complex electrolyte environments.

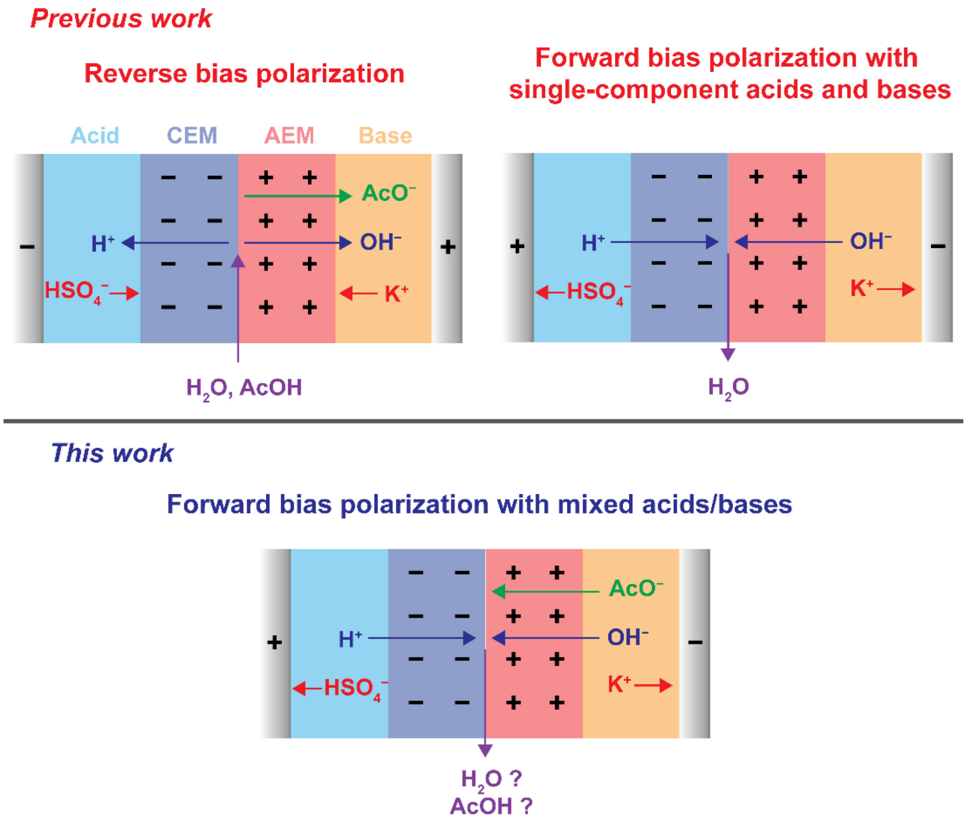

Figure 4.1. Existing understanding of ionic processes in BPMs. BPM cells operating in reverse bias and in forward bias with single-component acids and bases have been extensively studied, but the behaviour of a forward bias cell containing mixed acids or bases is poorly understood.

Herein, we develop a mechanistic model to explain the forward bias polarization behavior of a BPMs in the presence of mixed electrolytes. We show that each constituent in the mixture undergoes neutralization at a distinct membrane voltage dictated by its pK_a. Critically, we find that the presence of even a minority concentration of weak acids/bases can impose a large overpotential for the neutralization of stronger acids/bases. We show that this *neutralization overpotential* manifests in a potential-independent limiting current for forward bias operation, and results from an ionic blockade imposed by the accumulation of unreactive weak acid/base ions in the BPM. We demonstrate the utility of this model in the context of fuel cells and redox flow batteries and apply this model to develop improved BPM materials with reduced neutralization overpotentials. Finally, we apply our findings to enhance energy recovery in the context of reversing electrolyte carbonation during CO_2 electrolysis. Our studies provide a mechanistic framework for understanding the current-voltage behavior of BPMs in mixed electrolytes and enable high-efficiency protonic to electrical energy conversion.

4.2 Mechanism of Forward Bias Polarization in Mixed Electrolytes

In this work, two types of BPMs were employed: a homemade BPM, denoted by the nomenclature (Acid) | CEM | AEM | (Base), and the commercial Fumasep FBM, denoted by (Acid) | FBM | (Base) (see **4.7 Experimental Methods** for further detail). Unless the membranes are the subject of the experiment, FBM will be used, and these notations will be abbreviated to (Acid) | (Base) in the text. In addition, as all measurements of membrane voltage (V_{mem}) were made by sensing the electric potential of the acid solution with respect to the base solution, V_{mem} will be reported as a negative value, with polarization to less negative values indicating forward bias. Currents are reported based on measurements of electrical current through the external circuit, and hence positive currents correspond to forward bias polarization. In this study, to simplify the analysis of V_{mem}, we assume that the concentration of fixed charges in the CEM and AEM is 1 M, and that Donnan potentials at the membrane-electrolyte interfaces are constant at 0 mV. Hence, changes in V_{mem} reflect only changes in the bipolar junction voltage (V_J).[37] Here, we will use the term *weak electrolytes* to refer to charged bases whose conjugate acids have a $\mathrm{p}K_a < 14$ (e.g., OAc^-) or charged acids with a $\mathrm{p}K_a > 0$ (e.g., NH_4^+), and the term *strong electrolytes* to refer to H^+ and OH^-.

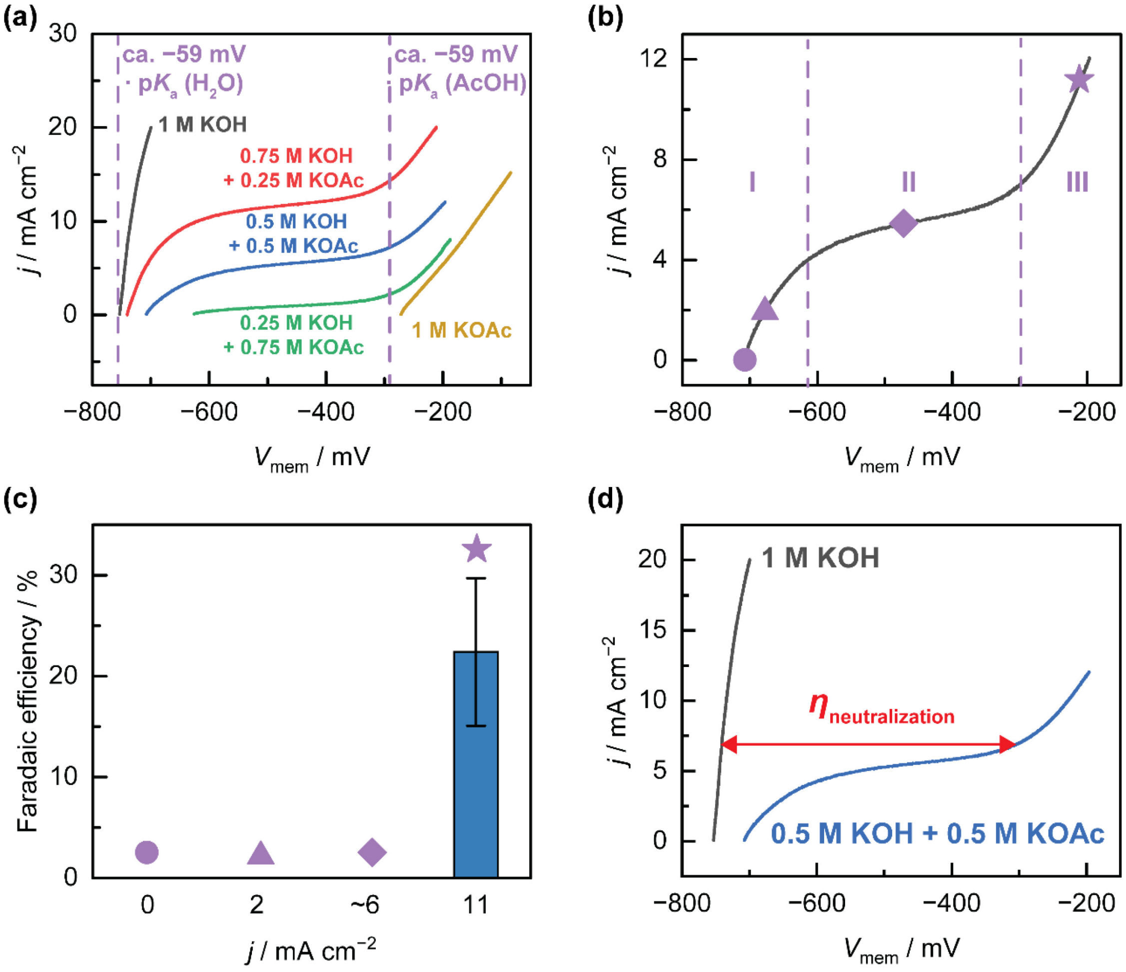

Figure 4.2. Electrochemical characterization of BPMs containing KOH-KOAc mixtures. **(a)** Forward bias polarization curve of 1 M H_2SO_4 | FBM | x M KOH + y M KOAc (where x + y = 1). **(b)** Forward bias polarization curve of 1 M H_2SO_4 | FBM | 0.5 M KOH + 0.5 M KOAc, with different regions delineated. **(c)** Faradaic efficiency for AcOH based on analysis of aliquots taken from acid compartment after controlled current or voltage polarization at points indicated in (b). The error bar in **(c)** represents the standard deviation of three independent replicates. **(d)** Forward bias polarization curve of 1 M H_2SO_4 | FBM | 1 M KOH and 1 M H_2SO_4 | FBM | 0.5 M KOH + 0.5 M KOAc, with the neutralization overpotential, $\eta_{neutralization}$, marked for 7.5 mA cm^{-2}.

Forward bias polarization is gated by acid-base equilibria. In order to understand how mixed electrolytes influence forward bias polarization behavior, we investigated a BPM cell containing a mixture of a hydroxide and acetate in the catholyte paired with a sulfuric acid anolyte. Specifically, we employed cells of the type 1 M H_2SO_4 | x M KOH + y M KOAc (x+y = 1), where

OAc^- = acetate. KOH and KOAc were chosen due to the large separation in the pK_a values for their conjugate acids (14 vs 4.75), allowing us to sample behavior over a wide basicity range. The open-circuit V_{mem} values for catholytes containing 1 M KOH, 0.75 M KOH + 0.25 M KOAc and 0.25 M KOH + 0.75 M KOAc were found to be close to −59 mV·ΔpH (where ΔpH = $pH_{catholyte}$ − $pH_{anolyte}$) or, equivalently, −59 mV·pK_a (H_2O), whereas that for the catholyte containing 1 M KOAc was close to −59 mV·pK_a (AcOH) (**Figure 4.2(a)**). The pK_a-pinned open-circuit V_{mem} value, or V_{pKa}, for the latter case is consistent with our findings in our previous study,[37] in which we showed that ionic short-circuiting processes led to buffering of the bipolar interface by the acid-base couple present (H_2O/OH^- and $AcOH/OAc^-$, respectively). In the case of 1 M H_2SO_4 | 0.75 M KOH + 0.25 M KOAc and 1 M H_2SO_4 | 0.25 M KOH + 0.75 M KOAc, the presence of OH^- ensures a high pH in the region of the AEM close to the bipolar interface, resulting in the open-circuit V_{mem} being dominated by the H^+/OH^- recombination couple and pinned to ca. −59 mV·ΔpH despite the presence of OAc^-. These open-circuit membrane voltages reflect the expected pH gradients at the bipolar interface.

The forward bias polarization curves display a high degree of complexity when mixed electrolytes are used. For the 1 M H_2SO_4 | 1 M KOH and 1 M H_2SO_4 | 1 M KOAc cells, we observed a monotonic current rise (**Figure 4.2(a)**), which must correspond to the recombination reactions in **Equation 4.1** and **Equation 4.2**, respectively.

$$H^{+} + OH^{-} \rightarrow H_2O \qquad \textbf{Equation 4.1}$$

$$H^{+} + OAc^{-} \rightarrow AcOH \qquad \textbf{Equation 4.2}$$

Indeed, surveying other cells of the type 1 M H_2SO_4 | 1 M KA containing the monoprotic base A^- revealed similar forward bias polarization curves with monotonic current rising from the respective open-circuit V_{mem} values set by the pK_a of each HA (**Figure S4.3**). In contrast to these single-component catholytes, in the presence of a mixture of hydroxide and acetate, the current rise is interrupted by a broad limiting current plateau (**Figure 4.2(a),** red and blue traces). As the KOH: KOAc concentration ratio increases from 0.25:0.75 to 0.5:0.5, the limiting current density increases from 7.3 mA cm^{-2} to 29 mA cm^{-2}. This potential-independent limiting current is observed despite the large undepleted pool of OH^- in the bulk electrolyte that could undergo protonation at the bipolar interface. In addition, the V_{mem} at which additional current flows beyond the limiting plateau was found to overlap with the open-circuit V_{mem} of 1 M H_2SO_4 | 1 M KOAc, occurring at ca. −59 mV·pK_a (AcOH) (**Figure 4.2(a)**). When an analogous series of cells of the type x M H_2SO_4 + y M NH_4Cl | 1 M KOH (x + y = 1) were polarized in forward bias (**Figure S4.4**), we observed identical behavior to the 1 M H_2SO_4 | x M KOH + y M KOAc cells. Additionally, consistent with previous experimental[37,38] and computational[32] reports, we observe that the presence of polyprotic buffer species in the cell 1 M H_2SO_4 | 1 M $K_xH_yPO_4$ (x + y = 3), gave multiple limiting current plateaus with inflection points coinciding with ca. −59 mV·pK_a (H_3PO_4) (−130 mV), ca. −59 mV·pK_a ($H_2PO_4^-$) (−430 mV) and ca. −59 mV·pK_a (HPO_4^-) (−620 mV), respectively (**Figure S4.5**). Together, these data reveal that the sigmoidal current-voltage profile is universal to electrolyte mixtures with species of different acidities, regardless of whether those species arise from a common polyprotic acid (e.g., phosphates), or are structurally distinct (e.g., the OH^{-}/OAc^{-} and H^{+}/NH_4^{+} mixtures).

The foregoing experiments show how electrolyte mixtures impact the current-voltage behavior, but do not shed light on which reaction (**Equation 4.1** or **Equation 4.2**) is occurring at each voltage. We postulated that net protonation of a given species can only occur at V_{mem} values more positive than its corresponding $V_{\mathrm{p}K\mathrm{a}}$. In order to determine the identity of the species being protonated at the bipolar junction, we polarized the 1 M H_2SO_4 | 0.5 M KOH + 0.5 M KOAc cell galvanostatically or potentiostatically within the three distinct regions of the polarization curve (**Figure 4.2(b)**; chronopotentiograms/chronoamperograms in **Figure S4.6 –Figure** S4.10), and analyzed aliquots taken from the acid compartment via ^{1}H NMR to determine the AcOH concentration. No AcOH was detected for polarizations in the underlimiting (I) and limiting (II) regions of the polarization curve (**Figure 4.2(c)**). Only when the cell was polarized in the overlimiting (III) region, where $V_{\mathrm{mem}} > V_{\mathrm{p}K\mathrm{a}\ (\mathrm{AcOH})}$, did we observe an appreciable concentration of AcOH, corresponding to ca. 22% faradaic efficiency (FE) relative to the total ionic current (**Figure 4.2(c)**; see section below for quantitative analysis of observed FE). AcOH was also produced at appreciable FEs when the cell was polarized to higher currents (22, 33 mA cm^{-2}) in the overlimiting region (**Figure S4.11**). On the other hand, when the 1 M H_2SO_4 | 1 M KOAc cell was polarized at the same current densities, quantitative FE was observed for AcOH formation (**Figure S4.12**). The observation that AcOH is produced in net only when $V_{\mathrm{mem}} > V_{\mathrm{pKa}\ (\mathrm{AcOH})}$ suggests that V_{mem} is directly correlated to the interfacial pH gradient and speciation at the bipolar junction. Since the pH within the CEM, which contains the strong acid H^{+}, is unlikely to change, this observation implies that the increase in V_{mem} from −760 mV to −280 mV is consistent with the near-interfacial region of the AEM decreasing in pH from ca. 13 to ca. 4.76. This in turn indicates an accumulation of OAc^{-} and depletion of OH^{-} near the bipolar interface. This correlation of V_{mem} to the interfacial acid-base chemistry is discussed further in **Supplementary Discussion 4.1**. Indeed, when open-circuit V_{mem} measurements of the 1 M H_2SO_4 | x M KOH + y M KOAc cells were performed immediately after collection of the forward bias polarization curves, the open-circuit transients for return to the unpolarized equilibrium state were found to parallel the polarization curves, with inflection points conserved at the same $V_{pK_a(AcOH)}$ value (**Figure S4.15**). These observations highlight the strong correlation between the speciation at the bipolar interface, the interfacial pH differential, and V_{mem}.

Importantly, these results highlight that a substantial overpotential is imposed on the neutralization of a strong electrolyte (OH^{-}) by the presence of the weaker electrolyte (OAc^{-}). Despite the fact that OH^{-} protonation is exergonic at all voltages positive of the open-circuit value, the current plateaus in the presence of OAc^{-}, even in electrolyte mixtures where OAc^{-} is the minority species (**Figure 4.2(a)**). Consequently, accessing an OH^{-} neutralization current in excess of the limiting value requires the application of a substantial *neutralization overpotential*, $\eta_{neutralization}$, which subtracts from the thermodynamic potential available in the H^{+}/OH^{-} neutralization reaction. For example, at 7.5 mA cm^{-2}, even though OH^{-} is expected to carry all the neutralization current, V_{mem} for 1 M H_2SO_4 | 1 M KOH is −740 mV, but V_{mem} for 1 M H_2SO_4 | 0.25 M KOH + 0.75 M KOAc is −300 mV, which translates into $\eta_{neutralization} = 440$ mV (**Figure 4.2(d)**). We note that this neutralization overpotential will increase as the concentration of the weak acid/base increases and for pK_a/pK_b values further removed from that of the strong acid/base. Collectively, the foregoing findings evince that the net protonation of a given species A^{-} can only occur at $V_{\mathrm{mem}} < \mathrm{V}_{\mathrm{p}K\mathrm{a}\ (\mathrm{HA})}$, and that the presence of a weak electrolyte can result in large overpotentials for the neutralization of a strong electrolyte.

Forward bias limiting currents arise from interfacial ionic blockades. In order to shed additional light on the factors controlling the limiting current and the neutralization overpotential, we conducted several experiments varying the electrolyte composition. First, for cells of the type 1 M H_2SO_4 | x M KOH + x M KOAc (x = 0.5 or 0.75), we held the concentration ratio between KOH and KOAc constant at 1:1 but increased the absolute concentration of KOH/KOAc from 0.5 to 0.75 M, and found that j_{lim} remained unchanged at ca. 4.3 mA cm^{-2} (**Figure 4.3(a)**). This shows that j_{lim} is sensitive to the concentration ratio of mixed electrolytes but not to their absolute concentrations.

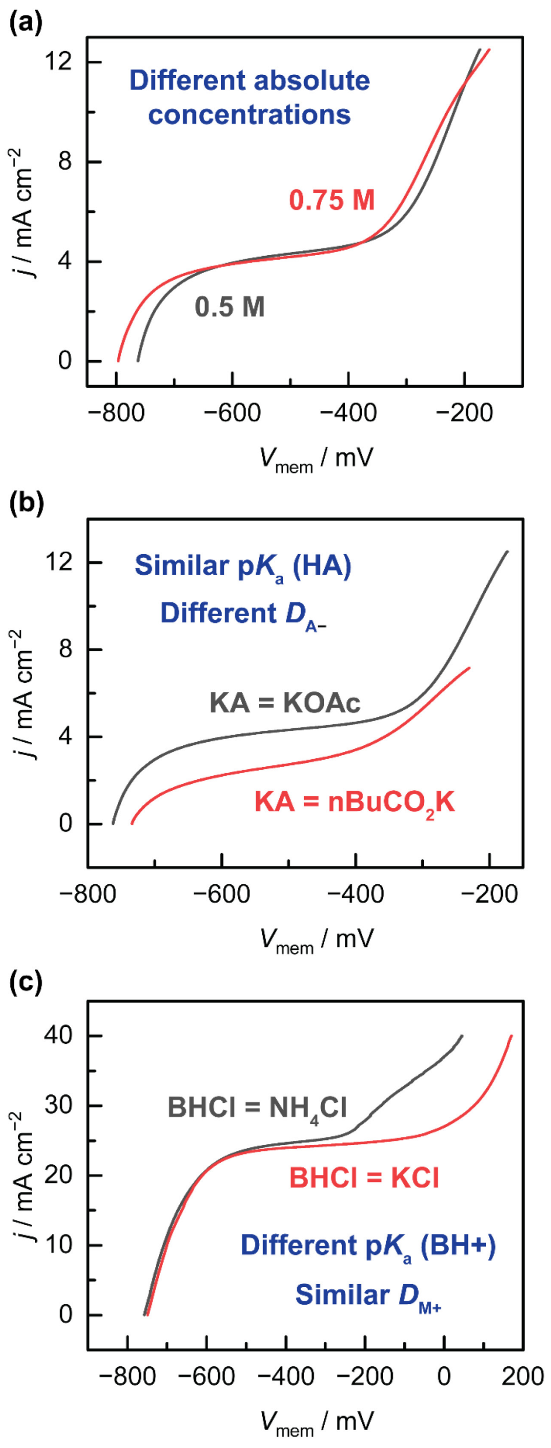

Figure 4.3. Electrochemical characterization of BPMs with varied electrolyte properties. Forward bias polarization curves for **(a)** 1 M H_2SO_4 | FBM | x M KOH + x M KOAc (x = 0.5 or 0.75), **(b)** 1 M H_2SO_4 | FBM | 0.5 M KOH + 0.5 M KA (A^- = OAc^- or $nBuCO_2^-$), and **(c)** 0.5 M H_2SO_4 + 0.5 M MCl | FBM | 1 M KOH (M^+ = NH_4^+ or K^+). We attribute the slight differences in polarization date for 1 M H_2SO_4 | FBM | 0.5 M KOH + 0.5 M KOAc between **Figures 4.2** and **4.3** and to the lot-to-lot variability in FBM.

Next, we substituted acetate for n-butyrate in the analyte compartment. Specifically, for cells of the type 1 M H_2SO_4 | 0.5 M KOH + 0.5 M KA (A^- = OAc^- or $nBuCO_2^-$, where $nBuCO_2$ = butyrate), acetate and butyrate have similar proton affinities (pK_a = 4.76 for AcOH, 4.82 for $nBuCO_2H$) but distinct diffusion coefficients (D_{OAc-} = 1.089 x 10^{-5} cm^2 s^{-1}, $D_{nBuCO2-}$ = 0.868 x 10^{-5} cm^2 s^{-1}).[39] This substitution leads to a lower j_{lim} for the $nBuCO_2K$ cell (ca. 2.7 mA cm^{-2}) than the KOAc cell (ca. 4.3 mA cm^{-2}) (**Figure 4.3(b)**), correlated with $D_{nBuCO2-}$ being lower than D_{OAc-}. We note that V_{mem} for the current onset in the overlimiting region is conserved between the two cells, owing to $V_{pKa\,(AcOH)} \approx V_{pKa(nBuCO2H)}$. Conversely, with cells of the type 0.5 M H_2SO_4 + 0.5 M MCl | 1 M KOH (M^+ = NH_4^+ or K^+) (note that the electrolyte mixture is now in the acid instead of the base compartment), we selected unreactive ions with similar diffusion coefficients (D_{NH4+} = D_{K+} = 1.957 x 10^{-5} cm^2 s^{-1}) but different proton affinities (pK_a = 9.25 for NH_4^+, 14 for K^+ (H_2O)).[39] Since K^+ is not deprotonatable, it can be considered a weak acid in the extreme whose acidity is levelled to that of H_2O (see **Supplementary Discussion 4.2**). Here, j_{lim} was found to be almost identical in value between the two cells (ca. 24 mA cm^{-2}) (**Figure 4.3(c)**), indicating that the diffusive properties of the unreactive ion, rather than its proton affinity, defines the limiting current density. To determine whether j_{lim} depended on the diffusion coefficient of only the unreactive electrolyte or both the unreactive and reactive electrolyte, we examined the cell with 0.5 M NH_4Cl + 0.5 M KCl | 1 M KOH, and measured a j_{lim} that was significantly lower (ca. 7 mA cm^{-2}) than that with the 0.5 M H_2SO_4 + 0.5 M KCl anolyte (24 mA cm^{-2}) (**Figure S4.16**). These findings demonstrate that j_{lim} depends on the diffusion coefficients of both the unreactive and reactive electrolyte, but not on the acid-base thermochemistry of either electrolyte.

Collectively, the foregoing data depicting the effect of electrolyte composition on forward bias polarization suggest a transport model whereby different reactive species in the mixed electrolyte (e.g., OH^{-} vs OAc^{-}) compete for a finite number of fixed charge sites to charge-pair with in the membrane (e.g., AEM). Specifically, we propose that site competition on the order of the depletion layer thickness (ca. 4 – 10 nm)[32,40] controls speciation at the near-interfacial region (within several nm) of the bipolar junction and consequently the V_{mem}, and that site competition on diffusional lengthscales (ca. 10s – 100s of μm) controls speciation within the bulk of the AEM and consequently the value of j_{lim}. Our putative model reflects the following boundary conditions: (a) the composition within the AEM near the AEM | Base interface is controlled by the Donnan equilibria for OH^{-} and OAc^{-};[32] (b) OH^{-} and OAc^{-} are the only mobile charges within the AEM, and hence their concentrations must sum to the fixed charge concentration everywhere in the AEM except at the interfacial depletion region; (c) V_{mem} directly reports on the interfacial pH gradient, and hence reveals the speciation of OH^{-}, OAc^{-} and AcOH at the bipolar interface.[32,40] Applying these constraints, postulated concentration profiles as a function of the region of the polarization curve in the near-interfacial and bulk regions of the AEM for OH^{-}, OAc^{-} and AcOH are depicted in **Figure 4.4(a)**, and postulated pH profiles across the BPM in the same regions are depicted in **Figure 4.4(b)**. These profiles are in qualitative agreement with a previous computational study.[32]

At open-circuit, we postulate that the concentration ratio of OH^{-}:OAc^{-} in the bulk of the AEM becomes identical to that in the base solution upon complete equilibration (**Figure S4.17**). The concentrations of OH^{-} and OAc^{-} near the interface, however, depend on neutralization equilibria attained between H^{+}, OH^{-} and OAc^{-}, which we envision to lead to a much lower OH^{-}:OAc^{-} ratio than that in the bulk due to the higher reactivity of OH^{-} compared to OAc^{-} (**Figure S4.17**).

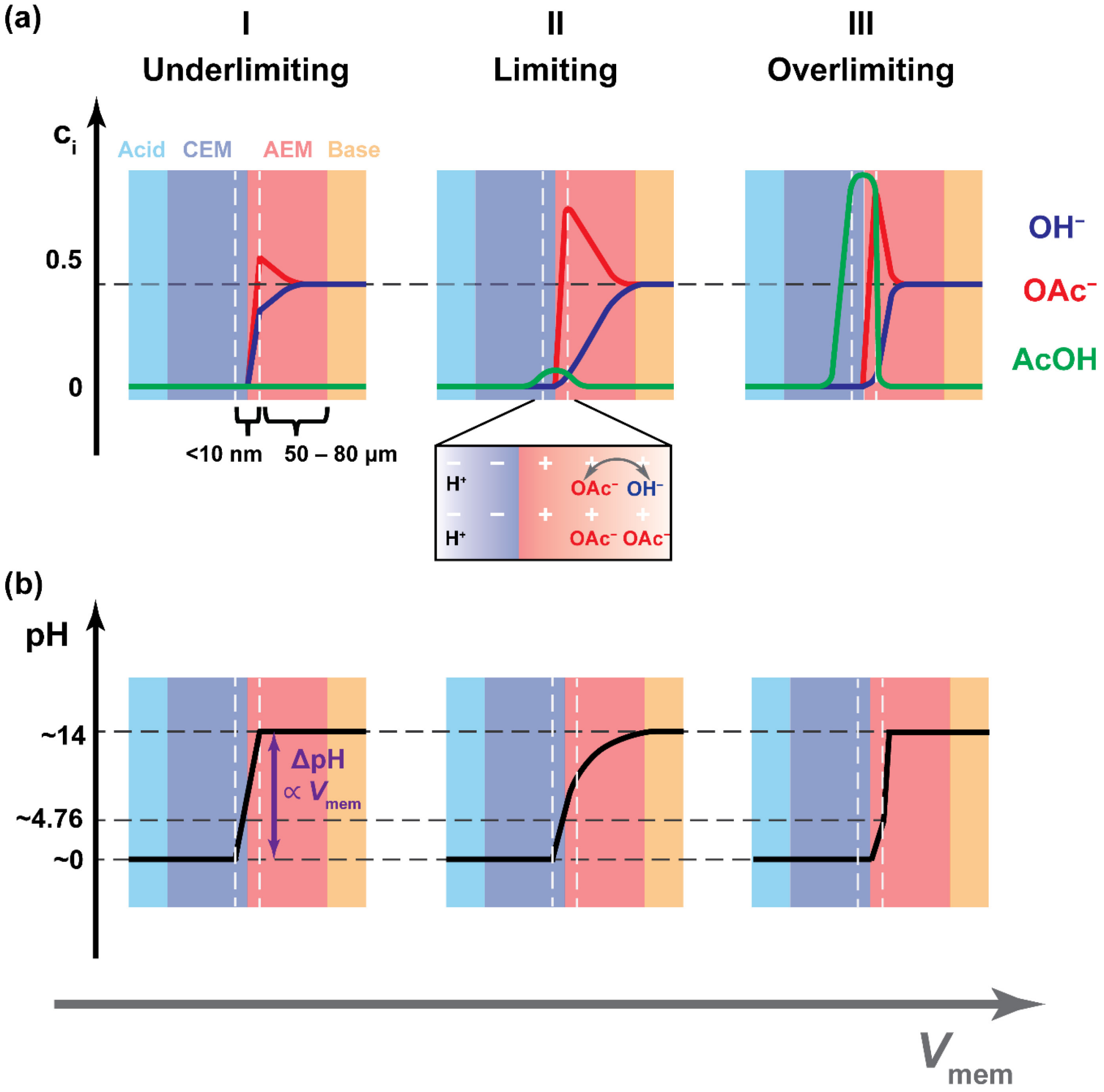

Figure 4.4. Concentration and pH profiles across BPMs as a function of polarization region. **(a)** Postulated concentration profiles of OH$^-$, OAc$^-$, and AcOH in different regions of the polarization curve (as demarcated in **Figure 4.2(b)**). Vertical dashed lines indicate the near-interfacial regions, where equilibration of the proton activity with the electric potential profile in the bipolar interface is rapid. **(b)** pH profiles in different regions of the polarization curve. Profiles in **(a)** and **(b)** are qualitatively plotted based on the initial quasi-steady-state conditions attained upon short-duration polarization of the cell (whereby concentrations of OH$^-$ and OAc$^-$ in the solution have not significantly changed). The fixed charge concentration in the AEM is assumed to be 1 M to simplify the analysis.

As the cell is polarized into the underlimiting region (region I), the net protonation of OH^- according to **Equation 4.1** allows the passage of current at the bipolar interface, resulting in the steep current-voltage slope (**Figure 4.2(b)**, region I). Since $V_{pKa\ (H2O)} < V_{mem} < V_{pKa\ (AcOH)}$, OH^- is the only base species capable of being protonated in net within this region. This results in the near-interfacial region of the AEM being gradually depleted in reactive OH^- and enriched in unreactive OAc^- with increasing V_{mem} (**Figure 4.4(a)**, region I). Since the applied field across the BPM induces the migration of both OH^- and OAc^- towards the bipolar interface, the unreactive OAc^- accumulates in the bulk of the AEM while the reactive OH^- depletes (**Figure 4.4(a)**, region I).

Entering the limiting region (region II), the current flatlines and becomes roughly voltage-independent (**Figure 4.2(b)**, region II). Since $V_{pKa\ (H2O)} < V_{mem} < V_{pKa\ (AcOH)}$, the majority of the current is still due to OH^- protonation, as the interfacial pH gradient does not yet permit significant net OAc^- protonation. We propose that current passed at the bipolar interface is now limited by OH^- diffusion. The near-interfacial region of the AEM is now almost completely depleted of the reactive OH^- and dominated by the unreactive OAc^- (**Figure 4.4(a)**, region II). Due to the rigidity of fixed charge groups within the AEM, the transport of OH^- to reach the interfacial region must be accompanied by coupled motion with OAc^-, the only other mobile species, in order to avoid electrical charge gradients and maintain electroneutrality. This results in a type of net place-exchange mechanism for OH^- transport, whereby a OH^- ion diffusing towards the interface swaps sites with an OAc^- ion diffusing away from the interface (**Figure 4.4(a)**, region II, blowup), leading to the observed potential-independent polarization curve. The observation that j_{lim} depends on the OH^-:OAc^- concentration ratio (**Figure 4.2(a)**) and the diffusion coefficient of both the reactive and unreactive species (**Figure 4.3(b) – (c), Figure S4.16**) is evidence for this electrolyte exchange mechanism, and furthermore suggests that the overall process is rate-limited by the aggregate place exchange dynamics. We term this overall phenomenon an *ionic blockade*, and emphasize its two key mechanistic aspects: firstly, both the strong and weak electrolytes compete for the same fixed charge sites for occupancy within the membrane; and, secondly, the weak electrolyte is unreactive under the applied membrane voltages and therefore has the net effect of inhibiting the transport of the reactive strong electrolyte to the bipolar interface. Consequently, the concentration of OH^- in the bulk of the AEM continues to decrease, whereas the concentration of OAc^- continues to increase as V_{mem} is swept more positively. However, while we invoke that the overall process for OH^- transport to the bipolar interface must involve aggregate place exchange with the unreactive OAc^- present to conserve electroneutrality, we are unable to infer whether the limiting region can be entirely explained by depletion and concentration polarization of OH^- within the AEM, or whether there are also ion-ion correlations between OH^- and OAc^- that attenuate the diffusivity of the former on the molecular level.[41] Hence, while our qualitative model captures the key mechanistic principles, we emphasize that a detailed computational model would be better suited to quantitative calculations of concentration profiles and transport fluxes, as well as dissecting the nuances of correlated ion transport. An alternative explanation for the limiting region is that net protonation current can only be passed when the AcOH at the bipolar interface diffuses into the AEM and reacts with OH^-, but this is a less plausible mechanism (see **Supplementary Discussion 4.3**). Another consideration was how the presence of electrolyte mixtures in both acid and base compartments would impact overall polarization. Comparing the polarization curve for 0.5 M H_2SO_4 + 0.5 M KCl | 0.5 M KOH + 0.5 M KOAc to that for 1 M H_2SO_4 | 0.5 M KOH + 0.5 M KOAc, we found that the former exhibited a lower j_{lim}, indicating that electrolyte exchange rates in both the CEM (H^+/K^+) and AEM (OH^-/OAc^-) contribute to controlling the overall j_{lim} (**Figure S4.19).** Finally, to rule out the co-ion playing a significant role in controlling j_{lim}, we polarized the cells 1 M H_2SO_4 | 0.625 M MOH + 0.375 M MOAc ($M^+ = Li^+$, Na^+ or K^+) and found a minor dependence on the identity of the co-ion (**Figure S4.20**). Together, the evidence suggests that the ionic blockade imposed by unreactive weak acids/bases in the CEM/AEM is the origin of the aforementioned neutralization overpotential.

Finally, as the cell is polarized past $V_{\mathrm{p}K\mathrm{a\ (AcOH)}}$, the current rapidly takes off again (**Figure 4.2(b)**, region III). This is due to the net protonation of OAc^- being turned on, which allows for the unfettered flow of both OH^- and OAc^-. The concentration of OH^- rises in the bulk of the AEM and the concentration of OAc^- decreases as the concentration polarization from the ionic blockade is reduced. In this region, the current is expected to partition between OH^- protonation and OAc^- protonation as per their relative migration fluxes through the AEM (**Equation 4.3**, derivation in **Supplementary Discussion 4.4**).

$$\frac{N_{\mathrm{OH-}}}{N_{\mathrm{OAc-}}} = \frac{D_{\mathrm{OH-}}c_{\mathrm{OH-}}}{D_{\mathrm{OAc-}}c_{\mathrm{OAc-}}}$$

Equation 4.3

This explains the 22% FE for AcOH production (**Figure 4.2(c)**), which results from $D_{\mathrm{OAc-}}$: $D_{\mathrm{OH-}}$ = 1:4 when the solution OH^-:OAc^- concentration ratio is kept at 1:1. Further evidence corroborating our model of site competition comes from the open-circuit equilibration data, where we find that relative diffusive fluxes of OH^- and OAc^- control the near-interfacial composition of the AEM and the resulting V_{mem} (**Supplementary Discussion 4.5**). We note that some of the AcOH present in the AEM can be neutralized by OH^-, leading to an asymmetric concentration profile favoring AcOH diffusion into the AEM that leads to a disparity between the FE measured with our methodology (see **4.7 Experimental Methods**) compared to that predicted by **Equation 4.3**. Indeed, we see FEs decreasing to below ca. 20% at higher current densities (**Figure S4.11**; **Figure S4.23**), but postulate that this asymmetry in acetic acid diffusion is a minor contributor at modest current densities (**Figure 4.2(c)**). Collectively, our studies on electrolyte variation have established a mechanistic basis for the forward bias current-voltage behavior of BPMs containing mixed electrolytes of different acidities/basicities.

4.3 Implications of Mechanistic Model for Galvanic Cells

The preceding mechanistic picture is relevant to a number of BPM galvanic cell types including H_2 fuel cells[42,43] and aqueous redox flow batteries.[28,29] For example, BPMs can be employed in fuel cells to pair facile hydrogen oxidation kinetics in acid with the use of earth-abundant catalysts for oxygen reduction in base.[42] The production of water at the bipolar junction in forward bias also endows fuel cells with the property of self-humidification.[42] However, the operation of fuel cells can be complicated by the formation and accumulation of (bi)carbonates in the alkaline electrolyte due to exposure to ambient CO_2.[35]

To understand the effect of trace carbonate on the performance of a H_2SO_4 | KOH BPM fuel cell, we measured polarization curves of cells of the type 1 M H_2SO_4 | FBM | x M KOH + y M K_2CO_3 (x + 2y = 1) (**Figure 4.5(a)**). We find that even with pristine KOH solutions, a limiting current region develops, due to the presence of trace carbonate from CO_2 absorption. Importantly, the limiting current decreases dramatically from ca. 45 to ca. 14 mA cm^{-2} as the concentration of K_2CO_3 present increases from trace levels to 0.125 M. Following from the model developed above, this limiting current results from the accumulation of CO_3^{2-} and HCO_3^{-} species at the BPM junction, inhibiting OH^{-} transport to the interface. In this case, it is expected that only OH^{-} and CO_3^{2-} are protonated at currents below the limiting current, and that HCO_3^{-} is only protonated at currents above the limiting current. Operating the BPM at a V_{mem} that results in bicarbonate protonation and CO_2 formation is an option, but the resulting ca. 450 mV neutralization overpotential will sap the power output of the fuel cell, particularly given that the peak power point of most hydrogen fuel cells occurs in the high-current range at $V_{\mathrm{mem}} > -200$ mV. Importantly, ionic blockading by (bi)carbonates occurs even when these species are minority constituents of the strongly alkaline electrolyte and the bulk of the current is carried by OH^{-} ions (**Figure 4.5(b)**). In addition, gas evolution at the bipolar junction can lead to delamination, which can be problematic for conventional bipolar membranes (see below for a detailed discussion of this topic). We note that if the basic solution progressively accumulates (bi)carbonate, operating in the under-limiting and limiting regions will not clear these species from the cell, and so periodic polarization in the over-limiting region may be necessary to re-establish the hydroxide pool. Notwithstanding, our model explains the pernicious effect of even trace (bi)carbonates on the efficiency of forward bias BPM fuel cells. This motivates the development of strategies for raising the limiting current (see below) to enable access to high power densities for fuel cells as well as other galvanic devices, such as redox flow batteries (see **Supplementary Discussion 4.6**).

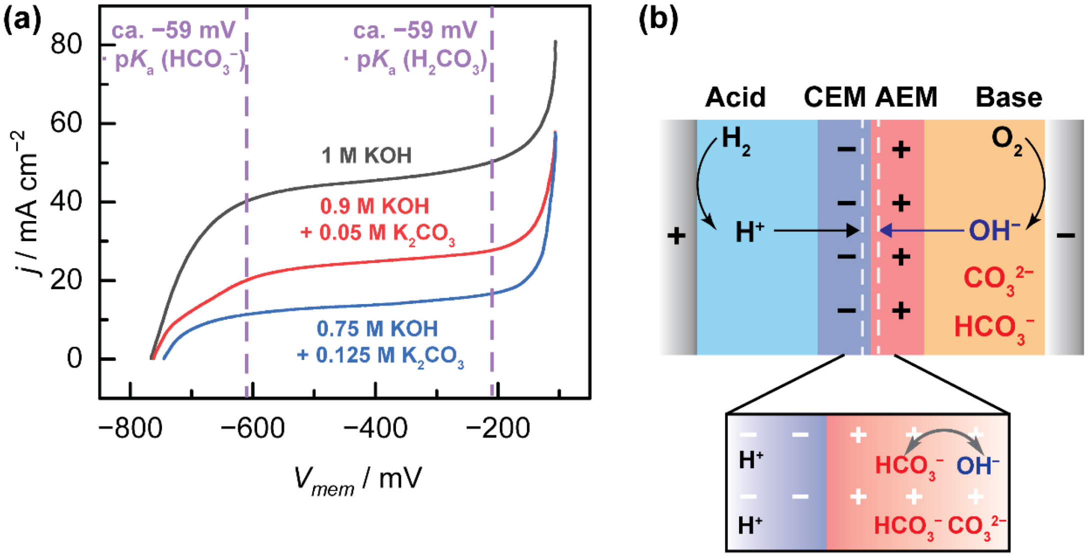

Figure 4.5. Electrochemical characterization of BPMs with varying concentrations of CO_2 dissolved in KOH. **(a)** Forward bias polarization curves for the cells 1 M H_2SO_4 | FBM | x M KOH + y M K_2CO_3 (x + 2y = 1). Note that the current takeoff in the high current region is pinned to the pK_a of 3.49 for H_2CO_3. **(b)** Cell schematic showing the faradaic reactions at the electrodes and the ionic reactions within the BPM for a forward bias BPM H_2 fuel cell. CO_3^{2-} and HCO_3^- ions formed from CO_2 absorption into the alkaline electrolyte accumulate in the AEM and inhibit OH^- transport.

4.4 Materials Design Enhances Limiting Current for Galvanic Cells

Analysis of forward bias BPM galvanic cells using our mechanistic framework revealed the importance of high limiting currents, and motivated us to explore the experimental handles that were available to control the limiting current. We first investigated the effect of varying the properties of the membrane. Using cells of the type 0.5 M NH_4Cl + 0.5 M H_2SO_4 | CEM | FAA-3-50 | 1 M KOH, where the CEM was varied in thickness, we observed that j_{lim} (considered at V_{mem} = −450 mV) decreased from 44 mA cm^{-2} to 26.6 mA cm^{-2} as the CEM thickness increased from 9 µm to 124 µm (**Figure 4.6(a)**). However, as the CEM thickness increased past the threshold value of 124 µm to 178 µm and subsequently 254 µm, j_{lim} remained invariant at ca. 12.5 mA cm^{-2}

(**Figure 4.6(a)**). We suggest that this non-monotonic change in j_{lim} can be attributed to the relative lengthscale of the thickness of the CEM (*m*) relative to the thickness of the diffusional boundary layer (δ) for the electrolyte exchange mechanism described in the preceding section (albeit applied to H^+/NH_4^+ exchange here) (**Figure 4.6(b)**). Although we previously established that the overall electrolyte exchange rate depends on both the reactive and unreactive ion, for simplicity, only the concentration profile for NH_4^+ has been depicted here. We note that the concentration profiles for NH_4^+ and H^+ should be inversely correlated, since no other counterions for the AEM exist. When $m > \delta$, then the diffusional boundary layer is entirely contained within the CEM and varying m has no bearing on the rate of NH_4^+/H^+ exchange (**Figure 4.6(b)**). Conversely, when $m < \delta$, then variations in m result in changes in the rate of NH_4^+/H^+ rate. This is due to the effective diffusion coefficient of NH_4^+ being lower in the CEM than in solution, i.e. $D_{\text{NH4+ (CEM)}} < D_{\text{NH4+ (Solution)}}$. Consequently, the rate of NH_4^+ diffusion exchange is slower within the CEM than in solution. In addition, the ionic blockade effect of NH_4^+ on H^+ transport only occurs within the CEM, where there are no mobile anions occur. Hence, the smaller the value of *m*, the faster the net NH_4^+/H^+ exchange, and the higher the value of j_{lim} (**Figure 4.6(b)**). This analysis brackets δ between 50 and 124 μm for the experiments in **Figure 4.6(a)**. These membrane thickness variation data demonstrate a materials handle for tuning j_{lim} and further support the notion that sluggish diffusion impeded by ionic place-exchange in the membrane is the origin of the limiting current.

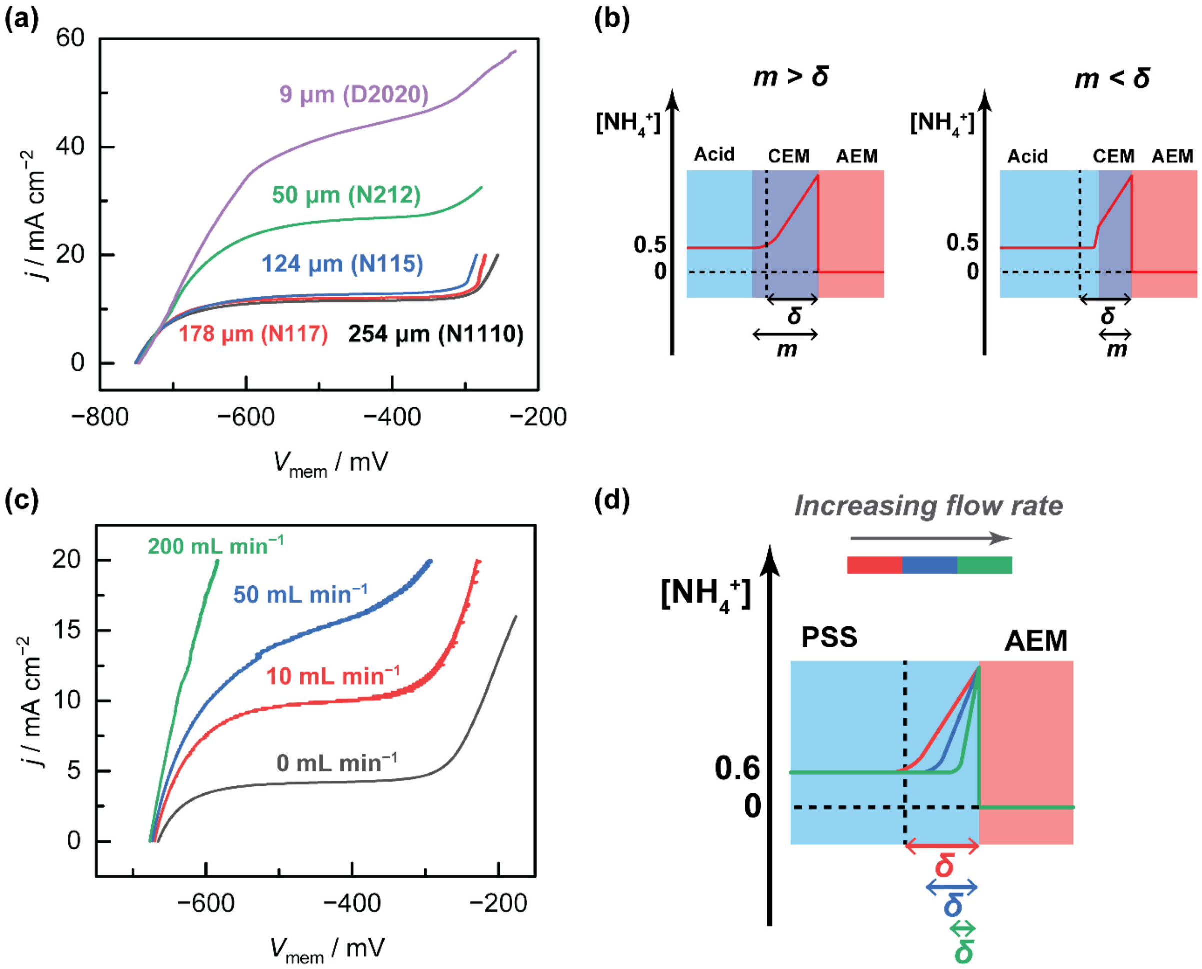

Figure 4.6. Materials design strategies to raise limiting current densities. **(a)** Forward bias polarization curve of 0.5 M H_2SO_4 + 0.5 M NH_4Cl | CEM | AEM | 1 M KOH, wherein CEM thickness = 9, 50, 124, 178 or 254 µm (see **Table S4.3** for list of CEMs used). **(b)** Putative concentration profiles for NH_4^+ in the CEM and acid solution when CEM thickness (m) is larger or smaller than the diffusional boundary layer thickness (δ). **(c)** Forward bias polarization curve of 0.4 M PSS–H + 0.6 M PSS–NH_4 | AEM | 1 M KOH with varying flow rates. **(d)** Concentration profile for NH_4^+ in the PSS solution as a function of flow rate.

Finally, with mounting evidence that the limiting region is diffusively controlled, we sought to design a BPM system that afforded dynamic control over the current-voltage characteristics of the limiting region. In electrochemical systems, improved transport of species to a reactive surface of an electrode can be induced by introducing advection (e.g., by stirring the solution or the use of a rotating electrode setup).[44] In order to set up a system where advection could be directly applied to the bipolar interface, we employed a hybrid liquid-membrane system with the cell 0.4 M PSS–H + 0.6 M PSS–NH_4 | AEM | 1 M KOH, where the CEM and the H^+- and NH_4^+-containing acid solution of a conventional BPM setup are replaced with a poly(4-styrene sulfonate) (PSS^-) solution. Owing to its high molecular weight (M_w ca. 70 kDa on average), the PSS^- co-ion is size-excluded from crossing the AEM, and is able to form a stable bipolar interface, with the PSS–H solution playing the dual role of CEM and acid solution.[37] With this cell type, we were able to collect polarization curves with different flow rates applied to the bipolar interface. Indeed, as the flow rate increased from 0 to 200 mL min^{-1}, the current density considered at the same V_{mem} of −600 mV increased nearly fivefold from 3.4 mA cm^{-2} to 17.4 mA cm^{-2} (**Figure 4.6(c)**). Analogous to conventional hydrodynamic electrochemical methods (e.g. rotating electrodes),[44] this correlation can be explained by the thickness of the diffusional boundary layer shrinking with increasing flow rate, leading to steeper concentration gradients for NH_4^+ and faster H^+/NH_4^+ exchange rates (**Figure 4.6(d)**). The polyelectrolyte advection data here are in agreement with the limiting region being diffusion-controlled, and demonstrate a facile methodology for controlling the value of j_{lim} in this region.

Together, the strategies introduced above provide additional levers for managing electrolyte speciation across the BPM, mitigating the effect of ionic blockades, and decreasing overpotential losses in BPM electrochemical devices.

4.5 Implications for Forward Bias BPM CO_2 Electrolyzers

The electrocatalytic CO_2 reduction reaction (CO_2RR) enables the production of carbon-based feedstocks and fuels powered by renewable electrical energy sources, and is a keystone transformation underpinning the clean energy transition.[45,46] Selective CO_2 reduction requires an alkaline environment at the cathode interface.[47–50] However, the absorption of CO_2 into alkaline solutions is a thermodynamically favorable process and leads to the formation of (bi)carbonates over time, lowering the energy efficiency for electrolysis.[51,52] To circumvent this issue, CO_2 electrolyzers operating with acidic electrolytes (**Figure 4.7(a)**), which avoid carbonate formation, have been developed.[47–50] However, these systems universally rely on the presence of alkali metal cations in the electrolyte to engineer an alkaline pH swing local to the cathode surface.[51,53] This leads to the development of a large pH gradient between the alkaline cathode surface and the bulk acidic electrolyte, which can add a significant but oft-overlooked concentration overpotential to the overall cell voltage. Therefore, while attractive for avoiding carbonate formation and allowing improved CO_2 utilization, the operation of acidic CO_2 electrolyzers invariably incurs large energy losses in the form of large pH swing overpotentials.

Forward bias BPM systems comprising a basic catholyte and an acidic anolyte have been employed in CO_2 electrolyzers to enable regeneration of CO_2 from carbonated electrolytes in operando and increase overall CO_2 utilization (**Figure 4.7(b)**).[54–57] However, owing to the limited understanding of the mechanism of forward-bias BPM operation in carbonate electrolytes, the utilization of this device construct for energy recovery has been largely ignored.[54–56] In contrast to acidic CO_2 electrolyzers that operate with a locally alkaline pH swing, the incorporation of a BPM between the acid and base compartments theoretically engenders the ability to transduce the chemical potential gradient into an electrical potential gradient that can offset part of the cell voltage (**Figure 4.7(c)**). Hence, forward bias BPM CO_2 electrolyzers represent an attractive and potentially more energy-efficient alternative to acidic CO_2 electrolyzers. However, the lack of understanding of forward bias operation with carbonate electrolytes impedes the development of strategies to further improve the efficiency of CO_2 electrolyzers via BPM incorporation.

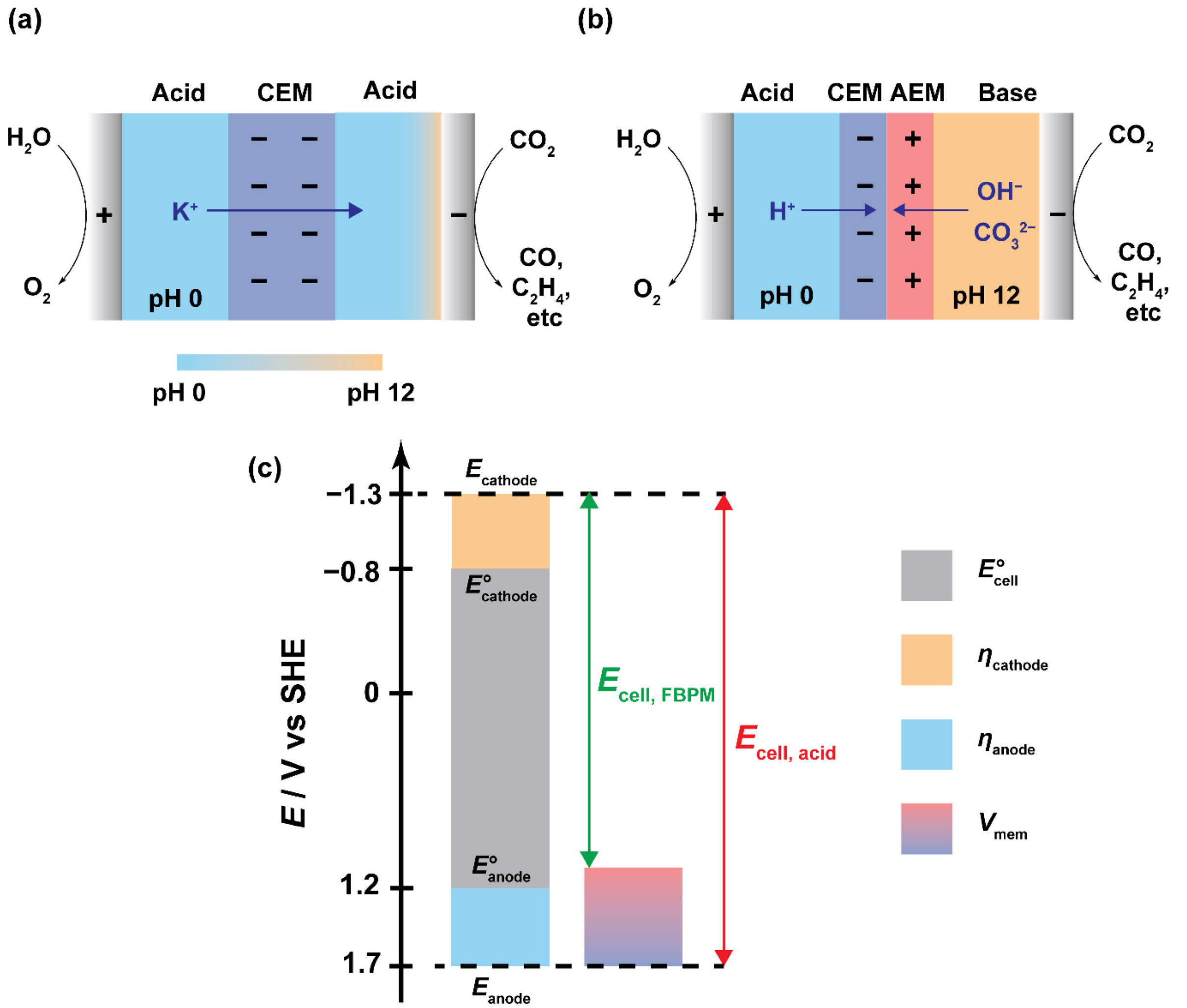

Figure 4.7. Comparing pH swing and forward bias BPM CO_2 electrolyzers. Cell schematics for **(a)** an acidic CO_2 electrolyzer employing an interfacial pH swing and **(b)** a forward bias BPM CO_2 electrolyzer. **(c)** Corresponding cell voltage breakdowns for **(a)** and **(b)**, showing the voltage offset enabled by the BPM. $\boldsymbol{E}^{\mathbf{o}}_{\mathbf{anode}}$ and $\boldsymbol{E}^{\mathbf{o}}_{\mathbf{cathode}}$ refer to thermodynamic cell potentials in pH 0 and 12, respectively. Ohmic losses are assumed to be identical between the two types of cells and are not treated in this analysis. Approximate values are taken from the literature.[51,53]

In order to understand the intrinsic forward bias polarization behavior of a BPM cell containing (bi)carbonates, we collected polarization curves for for 1 M H_2SO_4 | 1 M $K_xH_yCO_3$ (x + y = 2). Analogous to the 1 M H_2SO_4 | x M KOH + y M KOAc mixed electrolyte cells, the open-circuit V_{mem} values for the K_2CO_3 cell and the $KHCO_3$ cell were found to pin to ca. −59 mV·pK_a (HCO_3^-) and ca. −59 mV·pK_a (H_2CO_3) (**Figure 4.8(a)**). In addition, we observed polarization behavior for both cells that was analogous with the 1 M H_2SO_4 | x M KOH + y M KOAc cells: the $KHCO_3$ cell showed current takeoff from the open-circuit voltage (**Figure 4.8(a)**) similar to the 1 M H_2SO_4 | 1 M KOAc cell (**Figure 4.2(a)**), whereas the K_2CO_3 cell exhibited a plateau current between V_{mem} values pinned to ca. −59 mV·pK_a (HCO_3^-) and ca. −59 mV·pK_a (H_2CO_3) (**Figure 4.8(a)**, analogous to the 1 M H_2SO_4 | x M KOH + y M KOAc (x = 0.5, y = 0.5 or x = 0.75, y = 0.25) cells (**Figure 4.2(a)**). Applying the foregoing mechanistic model, we expect that only CO32− will be protonated in net in the underlimiting and limiting regions, and that net HCO_3^- protonation and CO_2 evolution can only occur at $V_{mem} > V_{pKa\,(H2CO3)}$ = ca. −380 mV (**Figure 4.8(a)**). Operating at membrane voltages lower than this value will lead to progressive accumulation of the bicarbonate in the catholyte (**Figure 4.8(b)**) and thus operation at membrane voltages greater than this value is essential for continuous CO2 clearance and steady state operation (**Figure 4.8(c)**). Consequently, the maximum electrical work recoverable is −380 mV rather than the −710 mV corresponding to the full 0-12 pH differential across a typical CO_2 electrolyzer.[53,58] Nonetheless, this recovered voltage is a substantial fraction (54%), of that required to sustain the pH gradient, which is otherwise lost to heat in acidic pH swing CO_2 electrolyzers (**Figure 4.7(a)**). These findings establish a quantitative basis for the expected Vmem for a forward bias BPM regenerating CO_2, and highlight the leveling effect that the pK_a of H_2CO_3 can have on the resultant V_{mem}.

High-current forward bias BPM operation requires efficient CO_2 removal. We polarized a 1 M PSS–H | AEM | 1 M K_2CO_3 cell and found that lower overpotentials were required compared to the 1 M H_2SO_4 | FBM | 1 M K_2CO_3 cell at high current densities in the overlimiting region (**Figure 4.8(d)**). We invoke that the FBM traps small pockets of CO_2 within the bipolar junction that occlude the bipolar interface and reduce the total electroactive surface area, and attribute the improved electrochemical performance of the PSS–H cell to the non-trapping liquid-membrane interface formed between PSS–H and the AEM. In addition, in contrast to the FBM cells, we observe a second plateau for the 1 M H_2SO_4 | CEM | AEM | 1 M $K_xH_yCO_3$ cells outfitted with homemade BPMs in the overlimiting region that is absent for the former (**Figure S4.25**). We postulate that the second plateau is the result of significant CO_2 evolution rates severely reducing the bipolar interfacial contact area and leading to some degree of membrane delamination for the more loosely attached homemade BPMs. Alternative approaches that avoid the trapping of CO_2 (e.g., a porous[56] or microchanneled[55] CEM structure) have also been found to result in improved device performance, but these studies expose, for the first time, the mechanistic importance of CO_2 removal for optimal I-V characteristics. Taken together, these observations suggest that polarization of a (bi)carbonate-containing BPM cell in the over-limiting region can be inhibited by the trapping and accumulation of CO_2, and that a hybrid liquid-membrane interface strategy can circumvent this issue by allowing rapid CO_2 clearance.

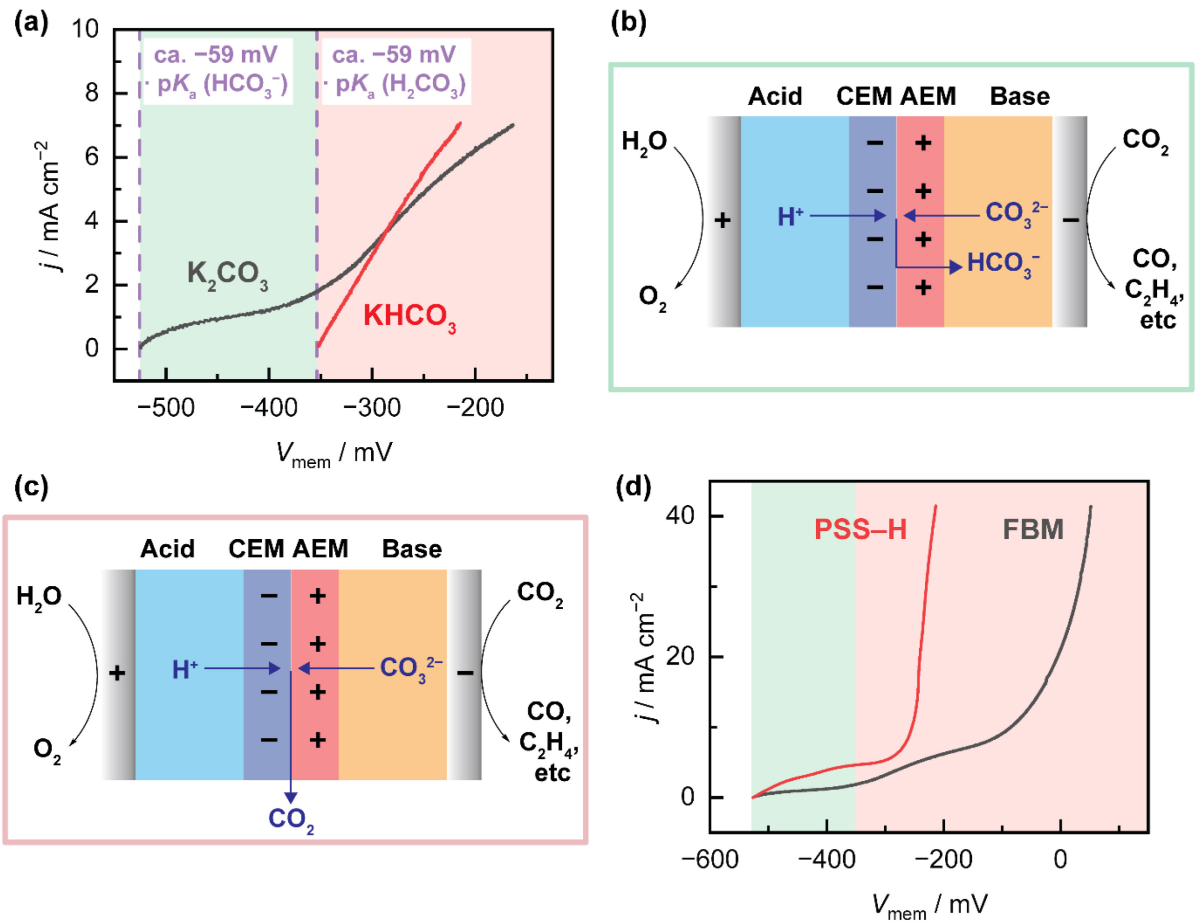

Figure 4.8. Modes of operation for forward bias BPM CO_2 electrolyzers. **(a)** Forward bias polarization curve of 1 M H_2SO_4 | FBM | 1 M $K_xH_yCO_3$ (where x + y = 2). Current-voltage regions where HCO_3^- is produced are shaded in green, and regions where CO_2 is produced are shaded in red. Cell schematics and polarization curves for a forward bias BPM CO_2 electrolyzer with a fully carbonated catholyte (e.g., 1 M K_2CO_3) operating in **(b)** the under-limiting and limiting regions (corresponding to the green regions) and **(c)** the over-limiting region (corresponding to the red regions). **(d)** Forward bias polarization curve of 1 M PSS–H | AEM | 1 M K_2CO_3 and 1 M H_2SO_4 | FBM | 1 M K_2CO_3.

Revisiting BPM CO_2 electrolyzers where the forward bias mode is implemented to allow the recovery of liquid products from the CO_2RR,[59,60] a similar analysis can be performed for the impact of the region of operation on the speciation at the bipolar interface (**Figure S4.26**). Using a CO_2 electrolyzer that produces acetate in an alkaline catholyte as an example, our earlier findings (**Figure 4.2(c)**) reveal that acetate is only protonated at $V_{mem} > V_{pKa(AcOH)}$ in the overlimiting region, and not in the underlimiting or limiting regions. This implication highlights two distinct modes of operation that are possible for such a device: (a) operating in the overlimiting region and continuously generating protonated liquid CO_2RR products at the bipolar interface, or (b) operating in the underlimiting and limiting regions and preferentially protonating hydroxide so as to concentrate acetate in the catholyte to enable more energy-efficient downstream separations outside the device. Operating in the concentrator mode would enable the recovery of a large V_{mem} from the pH gradient to offset the cell voltage, but would require strategies for raising j_{lim} to match the currents passed at the electrodes, which can be accomplished via the use of a thin AEM layer or a flowing cationic polyelectrolyte (in place of the AEM) as discussed above. Hence, our studies illustrate how the current-voltage profile of the forward bias BPM platform can be a powerful atlas for manipulating ion speciation at the bipolar interface and controlling catholyte composition in a CO_2 electrolyzer.

4.6 Conclusions

Herein, by systematically varying the properties of electrolyte mixtures and membranes, we establish a general mechanistic framework for understanding the forward bias current-voltage profile of weak electrolyte-containing BPM cells. We find that the net protonation of a given acid/base onsets at voltages beyond those pinned by their pK_a values. Furthermore, we reveal that an ionic blockade exerted by unreactive counterions can lead to limiting currents in forward bias. We expose the factors controlling this limiting current as well as materials design strategies for augmenting its magnitude, paving the way for designing galvanic cells that incorporate forward bias BPMs. Finally, we perform a detailed analysis on the implications of our studies to CO_2

electrolyzers, revealing how forward bias BPM electrolyzers can operate at lower cell voltages and higher efficiencies than acidic electrolyzers, as well as how knowledge of the current-voltage profile enables versatility in controlling ion speciation at the bipolar interface for performing liquid CO_2RR product recovery.

The results here shine a spotlight on the non-linear current-voltage relationship of forward bias BPMs interfaced with electrolyte mixtures, and the large, oft-overlooked overpotentials that can arise at the bipolar junction. Particularly pernicious is the levelling effect that even trace quantities of weak acids/bases (e.g., HCO_3^-) in the electrolyte can have on V_{mem} when they accumulate in the bipolar membrane and inhibit the transport of stronger acids and bases (e.g., OH^-, CO_3^{2-}), leading to large neutralization overpotentials (**Figure 4.5**). The limiting current density is expected to depend on the intrinsic transport rates of ions in the BPM, which is controlled by the ion exchange capacity, as well as the relative transport rates of strong and weak electrolytes. Since the ionic blockade effect ultimately stems from conventional ion-exchange membranes being highly charge-selective for counterions over coions but not chemoselective between ions of the same charge (e.g., for OH^- vs OAc^- or CO_3^{2-} in AEMs), we suggest that the development of membranes highly chemoselective for the transport of strong electrolytes could effectively mitigate the inhibition and significantly augment limiting current densities towards technologically relevant values (>100 mA cm^{-2}). For example, specific complexation interactions with a metal oxide have been exploited to engineer highly phosphate-selective membranes.[61] As a final note, although not discussed here, an important secondary consideration for forward bias operation at high current densities is the need for facile product (water, CO_2, etc) removal from the bipolar interface in order to avoid membrane ballooning and delamination. Together, the conclusions presented here provide a basis for predicting and understanding the forward bias polarization of

BPMs with a multiplicity of mobile ions, and pave the way for the rational design of next-generation forward bias BPM applications.

4.7 Experimental Methods

Chemicals and Materials

Potassium hydroxide (KOH, 99.98%), potassium formate (HCOOK, 99%), boric acid (H_3BO_3, Puratronic, 99.9995%), sodium acetate (CH_3COONa, 99.997%), ammonium chloride (NH_4Cl, 99.999%) were purchased from Alfa Aesar and used as received. Potassium chloride (KCl, 99%), potassium acetate (CH_3COOK, 99%), potassium bicarbonate ($KHCO_3$, 99.95%), potassium phosphate monobasic (KH_2PO_4, 99.5%), potassium phosphate dibasic trihydrate ($K_2HPO_4.3H_2O$, 99%), acetic acid (CH_3COOH, glacial, 99.7%), potassium phosphate tribasic (K_3PO_4, >98%), ammonium acetate (CH_3COONH_4, 97%), trimethylamine hydrochloride ($N(CH_3)_3.HCl$, 98%), guanidine hydrochloride ($CH_5N_3.HCl$, 99%), imidazole hydrochloride ($C_3H_4N_2.HCl$, >98%), pyridine hydrochloride ($C_5H_5N.HCl$, 98%), poly(sodium 4-styrenesulfonate) (PSS–Na, M_w = 70,000, 30 wt. % in H_2O), and poly(diallyldimethylammonium chloride) (PDADMA-Cl, M_w < 100,000, 35 wt. % in H_2O) were purchased from Sigma-Aldrich and used as received. Sulfuric acid (OmniTrace, 93-98%) and hydrochloric acid (OmniTrace, 34−37%) were purchased from VWR and used as received. Potassium carbonate (K_2CO_3, 99.995%) was purchased from Beantown Chemical and used as received. Platinum wire and mesh (99.995%) used as driving electrodes were purchased from VWR. The commercial bipolar membrane Fumasep FBM was purchased from Fuel Cell Store and stored in Millipore water before use. The

CEMs Nafion 212, 115, 117 and 1110, and the AEM Fumasep FAA-3-50 were purchased from Fuel Cell Store and stored dry prior to use. Nafion D2020 (1000 EW, 20 wt% in alcohols) dispersion was purchased from Fuel Cell Store and used as received. Graphene oxide (GO) dispersion (4 wt%) was purchased from Graphenea and used as received. Dialysis tubing (molecular weight cut-off of 14,000 Da) was obtained from Ward's Science and thoroughly rinsed with Millipore water prior to use. All aqueous electrolyte solutions were prepared with type I water (EMD Millipore, 18.2 MΩ·cm resistivity). Glass Ag/AgCl reference electrodes were obtained from CH Instruments and stored in 1 M KCl solution before measurements.

Preparation of Poly(4-Styrenesulfonic Acid) (PSS–H)

PSS–H was prepared in a similar manner to a previous report.[37] To prepare PSS–H samples, 200 mL of a nominal 0.5 M PSS–Na solution were prepared by dilution from the purchased stock solution, transferred into dialysis tubing, and dialyzed against 800 mL of 1 M HCl for 1 h. The HCl was then discarded and replaced with fresh 1 M HCl solution. This procedure was repeated for a total of four times, with the final dialysis step carried out overnight. The dialysis tubing was then thoroughly rinsed and exhaustively dialyzed against Millipore water (with at least 10 exchanges with 1.2 L water) to remove excess HCl. The PSS–H solution was finally concentrated under reduced pressure at 50 °C on a rotary evaporator. An aliquot of this solution was analyzed as is using ICP-OES for S content, and the total volume was adjusted using the measured S concentration to prepare a 1 M PSS–H solution. ^{1}H NMR characterization performed using a 500 MHz Bruker spectrometer was consistent with a previous preparation.[37] The Cl^- content was measured using a chloride ion selective electrode (ISE) (Hach IntelliCAL^{TM} ISECL181 Probe) and found to be negligible (ca. 6.8 mM).

Preparation of Bipolar Membranes

In this study, two types of bipolar membranes were used: commercial Fumasep FBMs, and homemade BPMs. The commercial FBM was typically used in scenarios where quantitative comparisons of limiting currents were required, since it was less prone to sample-to-sample variation, whereas homemade BPMs were used when there was a need to vary the characteristics (e.g. thickness) of one of the ionomer components of the BPM.

Homemade BPMs were prepared by sequential layering of a GO water dissociation catalyst onto an AEM followed by a Nafion ionomeric binder and a CEM. The GO and Nafion dispersions were separately sonicated for at least 1 hour before being coated onto membranes. The FAA-3-50 AEM (3 cm x 3 cm) was heated on a hot plate at 70 °C for 5 minutes while keeping the PET backing intact. 0.5 mL of the GO dispersion were then airbrushed onto the AEM (GO loading = 0.15 – 0.2 mg/cm^2) using an Iwata CM-SB spray gun manipulated with a custom CNC set-up. GO was included as a water dissociation reaction (WDR) catalyst in order to facilitate WDR kinetics and pin the WDR onset potential to ca. −830 mV, and the loading used here was found to be optimal based on a previous report.[62] The GO | AEM composite was then mounted on a glass slide using Kapton tape, and 0.35 mL of Nafion dispersion was spin-coated on at 3000 rpm for 30 s. The Nafion-coated GO | AEM was subsequently dried at 60 °C for 2 min. The Nafion ionomer coating was included to improve the interfacial contact between the CEM and the GO | AEM layers and improve the reproducibility of electrochemical measurements. The Nafion CEM was pressed by hand onto the Nafion-coated GO | AEM between a pair of clean glass slides. Caution was taken to prevent the trapping of air bubbles. The Kapton tape and backing foil on the AEM were then removed, yielding the ready-to-use BPM.

To prepare the 9 μm CEM for the thickness dependence study in **Figure 4.6(a)**, 2 mL of a 3.15 wt% Nafion D2020 dispersion made by dilution of the 20 wt% stock with isopropyl alcohol was airbrushed onto the GO | AEM composite in place of the spin-coated D2020 layer. The resulting BPM was then dried at 60 °C for 15 min prior to electrochemical measurements. The thickness of the CEM layer was determined via profilometry (Bruker DektakXT) on a silicon wafer coated with a Nafion film prepared in the exact same manner.

General Electrochemical Methods

The voltage across the BPM was probed using a four-electrode setup (**Figure S4.1**). For all experiments, the area of the BPM exposed between the two solution compartments was 2 cm^2. In polarization experiments, two glass Ag/AgCl reference electrodes were installed at the ends of the Luggin capillaries. The tips of the capillaries were positioned about 0.5 cm from the BPM surface. Platinum meshes or wires were used as cathode and anode, and each compartment was vented to prevent the build-up of gas during polarization. Acid solutions were added to the compartment facing the CEM, and base solutions were added to the compartment facing the AEM. All electrochemical measurements were performed on either a BioLogic VMP-300 or Gamry Reference 600 potentiostat, and were conducted at ambient temperature (24 ± 1 °C). All glassware and Pt meshes/wires used were cleaned by soaking in a 1:1 mixture by volume of concentrated HNO_3 and H_2SO_4 for at least 30 min before use. For all electrochemical experiments, the V_{mem}

values reported were compensated by the drift between the Ag/AgCl reference electrodes measured in a two-electrode setup in 1 M KCl beforehand (typically < 5 mV).

Galvanodynamic Polarization

To obtain the forward and reverse bias polarization curves, galvanodynamic scans were recorded using a scan rate of 10 μA cm^{-2} s^{-1} on either a BioLogic VMP-3 or Gamry REF 600 potentiostat. This scan rate was compared to independent chronopotentiometry measurements and determined to be sufficiently slow to capture steady-state polarization behavior. In cases for which both forward and reverse bias curves needed to be collected, the latter was always collected first since the formation of water and other products in forward bias could delaminate the BPM and affect performance. All polarization curves were typically corrected for Ohmic losses (iR_u) post-experiment using 80 – 90% of uncompensated resistance (R_u) values determined using the Current Interrupt (CI) program on the BioLogic VMP-3 or the galvanostatic electrochemical impedance spectroscopy (GEIS) program on the Gamry REF 600.

Quantitative ^{1}H NMR for Determination of Acetic Acid Concentration and Faradaic Efficiency

Experiments to determine the Faradaic efficiency for AcOH production in the various regions of the forward bias polarization curve were performed as follows. A BPM cell containing 20 mL solutions in the acid and base compartments respectively was polarized galvanostatically until a given quantity of charge had been passed. For the data point in the limiting region, the cell was polarized potentiostatically instead to ensure that it would fall within the narrow current range of the limiting region. The duration of polarization was chosen to ensure that the resulting concentration of AcOH produced in the acid compartment would be well above the limit of detection for NMR quantitation assuming a 1% Faradaic efficiency (FE). For all polarizations, this 1% FE threshold represented > 1 mM of AcOH produced in the cell. 250 µL aliquots were collected from the acid compartment of the cell at the end of each polarization, and 50 µL of each aliquot were added to 450 µL of a calibrant mixture composed of 8 parts 1 M HCl, 1 part D_2O, and 1 part 0.1 M DMSO (aq) as the internal standard. All NMR spectra were collected on a 500 MHz Bruker spectrometer.

Faradaic efficiencies for AcOH production were calculated as follows.

$$\text{Faradaic Efficiency for AcOH}$$

$$= 2 * \frac{\text{Concentration of AcOH produced} * \text{Volume of acid compartment}}{\text{Charge passed} * F} * 100\%$$

where the factor of 2 is included under the assumption that AcOH produced has equal probability of diffusing either through the CEM into the acid compartment or through the AEM into the base compartment. The volumes used in these calculations were adjusted according to the changes that occurred upon withdrawing aliquots.

Polyelectrolyte Advection Experiment

The influence of polyelectrolyte advection was examined by flowing the anolyte in the cell set-up depicted in **Figure S4.2**. 0.4 M PSS–H + 0.6 M PSS–NH_4 solution was prepared by addition of 0.639 mL of 28% ammonium hydroxide solution to 15 mL of 1 M PSS–H solution. Advection of the PSS–H/NH_4 electrolyte mixture was carried out by flowing the solution with a peristaltic pump through a custom 3D-printed adapter (Formlabs Form 3+) attached in-between the ports of a glass H-cell (**Figure S4.2(a)**). An additional CEM was installed in order to confine advection to a small pocket of electrolyte contained within the adapter, between the CEM and the AEM. Electrolyte was recirculated between the flow adapter and a glass half-cell containing a reservoir of PSS–H/NH_4. The voltage measurement was performed between a reference electrode in contact with the PSS–H/NH_4 solution within the flow adapter (RE1) and a reference electrode in the KOH solution (RE2), and hence was not sensitive to any potential drops between the CEM and PSS–H/NH_4 solution. The exposed AEM surface area was 1 cm^2. The assembled cell with its electrolyte flow circuit is shown in **Figure S4.2(b)**.

4.8 Supplementary Information

4.8.1 Supplementary Discussions

Supplementary Discussion 4.1. V_{mem} is both an electrostatic reporter and experimental handle for the interfacial acid-base chemistry

The thermodynamic voltage for the dissociation/recombination of the AcOH/ OAc⁻ couple, $\boldsymbol{V}_{\mathbf{p}\boldsymbol{K}\mathbf{a}\,(\mathbf{AcOH})}$, can be derived as follows.

The acid dissociation reaction for AcOH is given by the following equation.

$$\mathbf{AcOH} \rightarrow \mathbf{H}^{+} + \mathbf{OAc}^{-}$$

The diffusive flux for H^+ is given by

$$N_{\text{H+,diffusion}} = -D_{\text{H+}} \frac{\partial c_{\text{H+}}}{\partial \text{x}} \qquad \textbf{Equation S4.1}$$

where $c_{\text{H+}}$ and $D_{\text{H+}}$ are the concentration and diffusion coefficient of H^+, respectively.

The migration flux for H^+ is given by

$$N_{\mathrm{H+,migration}} = -\frac{z_{\mathrm{H+}}F}{RT} c_{\mathrm{H+}} D_{\mathrm{H+}} \frac{\partial \phi}{\partial \mathrm{x}} \qquad \textbf{Equation S4.2}$$

where $z_{\mathrm{H+}}$ is the charge of H^+, F is Faraday's constant, R is the molar gas constant, T is temperature and ϕ is the electrostatic potential.

Under standard conditions, the concentrations of all species involved are unity. Hence, 1 M of both a strong acid (e.g., H_2SO_4) and AcOH is present in the acid solution interfaced with the CEM, and 1 M of both KOAc and AcOH are present in the base solution interfaced with the AEM (i.e. 1 M H_2SO_4 + 1 M AcOH | 1 M KOAc + 1 M AcOH). To simplify the problem, the CEM and AEM are assumed to have fixed charge concentrations of 1 M.

At equilibrium, the net flux for H^+ is 0, i.e.

$$N_{\mathrm{H+}} = 0$$

$$N_{\mathrm{H+,diffusion}} + N_{\mathrm{H+,migration}} = 0$$

$$\boldsymbol{N}_{\mathbf{H+,diffusion}} = -\boldsymbol{N}_{\mathbf{H+,migration}} \qquad \textbf{Equation S4.3}$$

$$-D_{\mathrm{H+}}\frac{\partial c_{\mathrm{H+}}}{\partial \mathrm{x}} = \frac{z_{\mathrm{H+}}F}{RT}c_{\mathrm{H+}}D_{\mathrm{H+}}\frac{\partial \phi}{\partial \mathrm{x}}$$

Integrating,

$$-\int_{c_{\mathrm{H+,\ AEM}}}^{c_{\mathrm{H+,\ CEM}}}\frac{1}{c_{\mathrm{H^+}}}\frac{\mathrm{d}c_{\mathrm{H^+}}}{\mathrm{dx}}\cdot\mathrm{dx} = \int_{\phi_{\mathrm{AEM}}}^{\phi_{\mathrm{CEM}}}\frac{F}{RT}\cdot\frac{\mathrm{d}\phi}{\mathrm{dx}}\cdot\mathrm{dx}$$

$$-[\ln c]_{c_{\mathrm{H+,\ AEM}}}^{c_{\mathrm{H+,\ CEM}}} = \frac{F}{RT}\cdot[\phi]_{\phi_{\mathrm{AEM}}}^{\phi_{\mathrm{CEM}}}$$

$$-2.303\cdot(\mathrm{pH}_{\mathrm{AEM}} - \mathrm{pH}_{\mathrm{CEM}}) = \frac{F}{RT}\cdot(\phi_{\mathrm{CEM}} - \phi_{\mathrm{AEM}})$$

Since 1 M KOAc and 1 M AcOH are present in the AEM,

$$\mathrm{pH}_{\mathrm{AEM}} = \mathrm{p}K_{\mathrm{a}}(\mathrm{AcOH})$$

$$-2.303\cdot(\mathrm{p}K_{\mathrm{a}}(\mathrm{AcOH}) - \mathrm{pH}_{\mathrm{CEM}}) = \frac{F}{RT}\cdot(\phi_{\mathrm{CEM}} - \phi_{\mathrm{AEM}})$$

$$(\phi_{\mathrm{CEM}} - \phi_{\mathrm{AEM}}) = -\frac{2.303RT}{F}\cdot(\mathrm{p}K_{\mathrm{a}}(\mathrm{AcOH}) - \mathrm{pH}_{\mathrm{CEM}})$$

$$\mathrm{pH_{CEM}} = 0$$

Therefore,

$$V_{\mathrm{p}K\mathrm{a\ (AcOH)}} = -59\ \mathrm{mV} \cdot \mathrm{p}K_{\mathrm{a}}(\mathrm{AcOH})$$

Rigorously speaking, this derivation applies to the bipolar junction voltage, V_{J}, that occurs at the CEM | AEM interface. In addition, the concentrations of fixed charges within the CEM and AEM are usually larger than 1 M. However, the actual value of V_{mem} is sensitive only to the concentrations in the solutions and not to the fixed charge concentrations in the ion exchange membranes. This is due to the changes in the Donnan potentials at the two membrane-solution interfaces offsetting any changes in V_{J}. This is discussed in more detail in a preceding publication.[37]

The derivation above can be applied to other weak acids and bases. Generally, the thermochemical voltage for HA/A⁻ dissociation-recombination in a 1 M H_2SO_4 + 1 M HA | 1 M KA + 1 M HA cell is given by

$$V_{\mathrm{p}K\mathrm{a\ (HA)}} = -59\ \mathrm{mV} \cdot \mathrm{p}K_{\mathrm{a}}(\mathrm{HA}) \qquad \textbf{Equation S4.4}$$

Similarly, the thermochemical voltage for BH^+/B dissociation-recombination in a 1 M BHCl + 1 M B | 1 M KOH + 1 M B cell is given by

$$V_{\mathrm{p}K\mathrm{b\,(B)}} = -59\ \mathrm{mV} \cdot \mathrm{p}K_\mathrm{b}(\mathrm{B}) \qquad \textbf{Equation S4.5}$$

Profiles of the concentration of H^+, $c_{\mathrm{H+}}$, and the electrostatic potential, ϕ, across the BPM are plotted in **Figure S4.13**. As illustrated, the thermochemical voltage scales with the K_a for 1 M H_2SO_4 + 1 M HA | 1 M KA + 1 M HA cells.

The effect of polarizing a 1 M H_2SO_4 + 1 M HA | 1 M KA + 1 M HA (e.g., HA = AcOH or H_2O) cell is shown in **Figure S4.14**. When the cell is polarized to $V_{\mathrm{mem}} > V_{\mathrm{p}K\mathrm{a}}$ in forward bias, the applied electric field in solution drives the migration of H^+ and A^- into the CEM and AEM, respectively, towards the bipolar junction. (Note that this is a migration flux induced by the applied field, and distinct from the migration flux due to the potential drop at the bipolar junction.) The concentration of H^+ (and A^-) at the bipolar junction increases, causing the diffusion flux, $N_{\mathrm{H+,diffusion}}$, to increase, such that $N_{\mathrm{H+,diffusion}} > -N_{\mathrm{H+,migration}}$. This leads to net recombination at the bipolar junction.

Conversely, when the cell is polarized to $V_{\mathrm{mem}} < V_{\mathrm{p}K\mathrm{a}}$ in reverse bias, the applied electric field in solution drives the migration of H^+ and A^- out of the CEM and AEM, respectively. This leads to a decrease in the concentration of H^+ (and A^-) at the bipolar junction, which leads to $N_{\mathrm{H+,diffusion}} < -N_{\mathrm{H+,migration}}$. Consequently, HA undergoes net dissociation to equilibrate with the lowered concentrations of H^+ and A^-.

Hence, the origin of recombination and dissociation reactions at the bipolar junction is the perturbation in local ion concentrations due to the additional migration fluxes induced by the applied electric field during polarization. For this reason, in the absence of other ionic processes, V_{mem} is a good electrostatic reporter of and experimental handle for controlling acid-base chemistry at the bipolar junction.

Supplementary Discussion 4.2. Voltage gating for the neutralization of cationic weak acids

For BPM cells where the mixture of strong and weak electrolytes occurs in the acid compartment, the membrane voltage that gates the takeoff of current for acid neutralization for a given cationic acid, BH^+, is dictated by the pK_b, i.e. V_{pK_b}, such that

$$V_{pK_b} = -59\ \mathrm{mV} \cdot pK_b(\mathrm{B}) = -59\ \mathrm{mV} \cdot (14 - pK_a(\mathrm{BH^+}))$$

An example is given in **Figure S4.4** for the cells, x M H_2SO_4 + y M NH_4Cl | CEM | AEM | 1 M KOH (where x + y = 1), where NH_4^+ neutralization onsets at $V_{mem} > V_{pKb(NH3)}$.

For the cell 0.5 M H_2SO_4 + 0.5 M KCl | FBM | 1 M KOH, we suggest that the pK_a of K^+ can be treated as that for H_2O, which is 14. This would imply that "K^+ protonation" occurs at $V_{mem} > -59\ \mathrm{mV} \cdot (14 - V_{pKa(H2O)}) = -59\ \mathrm{mV} \cdot (14 - V_{pKb(OH-)}) = = -59\ \mathrm{mV} \cdot (14 - 14) = 0\ \mathrm{mV}$. Instead of K^+ participating in any actual acid-base chemistry, we suggest that the bipolar interface becomes uncharged in net at 0 mV, permitting rapid movement of K^+, which then clears the ionic blockade that K^+ was imposing on H^+ neutralization.

Supplementary Discussion 4.3. Mechanism of AcOH-mediated OH^- protonation

As discussed in the main text, an alternative pathway for the protonation of OH^- within the limiting region proceeds via AcOH mediation. The mechanistic sequence is laid out in **Figure S4.18.** The steps illustrated in panels (a) and (c) in **Figure S4.18** correspond to the following reactions.

$$\mathrm{H^+ + OAc^- \rightarrow AcOH}$$

$$\mathrm{AcOH + OH^- \rightarrow H_2O}$$

The overall reaction hence corresponds to OH^- protonation.

$$\mathrm{H^+ + OH^- \rightarrow H_2O}$$

Notwithstanding the viable mechanistic pathway described above, the observation of a limiting region for the 0.5 M H_2SO_4 + 0.5 M KCl | 1 M KOH cell (**Figure 4.3(c)**), where no neutralization product can be produced from the blocking ion K^+, implies that a mechanism based on the exchange of charged electrolytes is fully able to explain the results presented. Furthermore, within the ca. 650 mV span of the limiting region, interfacial pH gradients and hence the AcOH concentration would be expected to vary by ca. 11 units and orders of magnitude respectively, yet the limiting current density barely changes in value (**Figure 4.2(a)**). Although we cannot completely rule out partial contributions from this AcOH/OH^- exchange mechanism here, we posit that its contribution is likely to be negligible, and base our discussion in this work on the dominant OAc⁻/OH⁻ exchange mechanism.

Supplementary Discussion 4.4. Derivation of expression for relative migration fluxes

The migration flux for a given species i is given by

$$N_{i,\mathrm{migration}} = -\frac{z_i F}{RT} c_i D_i \frac{\partial \phi}{\partial x} \qquad \textbf{Equation S4.6}$$

where F is Faraday's constant, R is the molar gas constant, T is temperature, $\frac{\partial \phi}{\partial x}$ is the electric potential gradient, and z_i, c_i, D_i are the charge, concentration and diffusion coefficient of $\underline{i}$ respectively.

The ratio of migration fluxes for OH⁻ and OAc⁻ can be expressed as follows

$$\frac{N_{\mathrm{OH-,migration}}}{N_{\mathrm{OAc-,migration}}} = \frac{-\frac{z_{\mathrm{OH-}} F}{RT} c_{\mathrm{OH-}} D_{\mathrm{OH-}} \frac{\partial \phi}{\partial x}}{-\frac{z_{\mathrm{OAc-}} F}{RT} c_{\mathrm{OAc-}} D_{\mathrm{OAc-}} \frac{\partial \phi}{\partial x}}$$

Since $z_{\mathrm{OH-}} = z_{\mathrm{OAc-}} = -1$, and many of the terms repeat in the numerator and denominator, the expression simplifies into

$$\frac{N_{\mathrm{OH-,migration}}}{N_{\mathrm{OAc-,migration}}} = \frac{c_{\mathrm{OH-}} \cdot D_{\mathrm{OH-}}}{c_{\mathrm{OAc-}} \cdot D_{\mathrm{OAc-}}}$$

which is given in **Equation 4.3**.

Supplementary Discussion 4.5. Site competition controls the open-circuit V_{mem} for 1 M H_2SO_4 | FBM | x M KOH + y M KOAc (x + y = 1) cells

To investigate the effect of the OH^-:OAc^- concentration ratio on the open-circuit V_{mem}, we measured the open-circuit voltage for cells of the type 1 M H_2SO_4 | x M KOH + y M KOAc (x+y = 1). The open-circuit V_{mem} traces recorded for cells of the type 1 M H_2SO_4 | FBM | x M KOH + y M KOAc (x + y = 1) are shown in **Figure S4.21**. For the cells with KOAc:KOH concentration ratios of 80:20, 85:15 and 90:10, there is an apparent two-stage behavior: V_{mem} initially drifts towards negative values, before reaching a minimum value and then drifting towards less negative values. We suggest that the initial drift towards a minimum value is due to the exchange of Cl^- ions initially charge-paired with the AEM with OH^- and OAc^- entering the AEM. Subsequently, the drift towards less negative values is due to the accumulation of OAc^- ions in the near-interfacial region of the AEM and consequently AcOH accumulation at the bipolar interface due to the ionic short-circuiting mechanism described previously.[37] This is consistent with the above mentioned traces tending towards ca. −59 mV·pK_a (AcOH) at later times.

Due to this two-stage behavior, we interpreted only the region of the traces leading up to the minimum V_{mem} as the period whereby there is competition between the diffusive fluxes of OH^- and OAc^- for sites in the AEM. The most negative V_{mem} value attained for each cell was plotted against the concentration ratio of $[OAc^-]:[OH^-]$ (**Figure S4.22**). A sigmoidal curve was obtained, whereby low $[OAc^-]:[OH^-]$ ratios led to $V_{\mathrm{mem}} \approx V_{\mathrm{p}K\mathrm{a}\ (\mathrm{H2O})} \approx -770$ mV, high $[OAc^-]:[OH^-]$ ratios led to $V_{\mathrm{mem}} \approx V_{\mathrm{p}K\mathrm{a}\ (\mathrm{AcOH})} \approx -300$ mV, suggesting that these compositions led to the near-interfacial region of the AEM being predominantly OH^-- and predominantly OAc^--occupied respectively. Notably, the inflection point connecting the two bounds occurred at 80% KOAc, or $[OAc^-]:[OH^-]$ = ca. 4:1, which is the reciprocal of the ratio of the diffusion coefficient of OAc^- to that of OH^- (i.e. $D_{\mathrm{OAc}-}$: $D_{\mathrm{OH}-}$ = 1:4). These data suggest that, under open-circuit conditions, the relative transport properties of the constituent ions in a mixed electrolyte controls the free charge composition at the bipolar interface.

We suggest that the open-circuit V_{mem} data could be explained by the relative diffusive fluxes of OH^- and OAc^-. The diffusive flux for a given species *i* is given by

$$N_{i,\mathrm{diffusion}} = -D_i \frac{\partial c_i}{\partial x} \qquad \textbf{Equation S4.7}$$

where c_i and D_i are the concentration and diffusion coefficient of $\underline{i}$ respectively.

The ratio of diffusive fluxes for OH^- and OAc^- can be expressed as follows

$$\frac{N_{OH-,\text{diffusion}}}{N_{OAc-,\text{diffusion}}} = \frac{-D_{\text{OH}-}\frac{\partial c_{\text{OH}-}}{\partial x}}{-D_{\text{OAc}-}\frac{\partial c_{\text{OAc}-}}{\partial x}}$$

The $\frac{\partial c_i}{\partial x}$ term describes the concentration gradient for a given species *i*. We assume that the concentration gradient is linear and extends over the same distance, *δ*, for both OH⁻ and OAc⁻. In addition, we assume that the concentration of OH⁻ or OAc⁻ is ca. 0 in the near-interfacial region of the AEM. Hence,

$$\frac{N_{\text{OH}-,\text{diffusion}}}{N_{\text{OAc}-,\text{diffusion}}} = \frac{-D_{\text{OH}-}\frac{\Delta c_{\text{OH}-}}{\delta}}{-D_{\text{OAc}-}\frac{\Delta c_{\text{OAc}-}}{\delta}}$$

$$= \frac{D_{\text{OH}-} \cdot \Delta c_{\text{OH}-}}{D_{\text{OAc}-} \cdot \Delta c_{\text{OAc}-}}$$

$$= \frac{D_{\text{OH}-} \cdot (c_{\text{OH}-,\ \text{solution bulk}} - 0)}{D_{\text{OAc}-} \cdot (c_{\text{OAc}-,\ \text{solution bulk}} - 0)}$$

$$\frac{N_{\text{OH}-,\text{diffusion}}}{N_{\text{OAc}-,\text{diffusion}}} = \frac{D_{\text{OH}-} \cdot c_{\text{OH}-,\ \text{solution bulk}}}{D_{\text{OAc}-} \cdot c_{\text{OAc}-,\ \text{solution bulk}}}$$

Equation S4.8

This is the same expression as **Equation 4.3**.

At open-circuit, since there is no applied polarization, the relative diffusive fluxes, which are also represented by **Equation 4.3**, control the OH^{-}:OAc^{-} composition of the AEM as the Cl^{-} initially present are exchanged out. The relative diffusive fluxes of OH^{-} and OAc^{-} hence determine the near-interfacial composition of the AEM and the resulting V_{mem}. This explains the occurrence of the inflection point at $[OAc^{-}]:[OH^{-}]$ = ca. 4:1, or the reciprocal of $D_{OAc-}: D_{OH-} = 1:4$, as this is the concentration ratio at which OH^{-} and OAc^{-} fluxes are equal, and whereby small excursions lead to drastically different interfacial pH gradients and V_{mem}. The dependence of V_{mem} on the relative diffusion coefficients of OH^{-} and OAc^{-} here is consistent with the mechanistic model and migration trends observed under polarization as described in the main text.

Supplementary Discussion 4.6. Limiting currents cap the power density of forward bias BPM redox flow batteries

BPMs can also be employed in redox flow batteries to increase the operating voltage, and the energy and power density as a result.[28,29] The use of buffer electrolytes is often required in order to minimize degradation of the redox-active species storing the charge.[63–65] To maintain the composition of both the posolyte and negolyte solutions and avoid crossover of the buffer and redox-active species, it would be ideal to operate in a polarization region in both forward and reverse bias whereby only acid and base equivalents are exchanged across the BPM. **Figure S4.24** shows an archetypal example of a BPM redox flow battery under discharging (**Figure S4.24(a)**) and charging (**Figure S4.24(b)**) conditions. Here, the posolyte is operated in strong acid, whereas the negolyte is buffered with a phosphate buffer. Posolyte and negolyte redox-active ions have been chosen to have the same charge (i.e. co-ions) as the membranes they are interfaced with such that Donnan exclusion can serve to minimize undesired crossover. As illustrated, undesirable crossover of redox-active and buffer species can be mitigated by operating the BPM such that only $H_2PO_4^-/HPO_4^{2-}$ buffering reactions are occurring. Polarization curves for this BPM redox flow battery based on our experiments (**Figure S4.5**) are shown in **Figure S4.24(c)**). The cell is expected to contain predominantly the KH_2PO_4 form of the phosphate buffer in the fully discharged state and K_2HPO_4 in the fully charged state. Hence, the forward and reverse bias polarization curves for this BPM cell are expected to resemble the forward bias curve for K_2HPO_4 and the reverse bias curve for KH_2PO_4, respectively, in **Figure S4.5**. The voltage region for operating the cell so that only dissociation-recombination reactions of the $H_2PO_4^-/HPO_4^{2-}$ couple occur at the bipolar interface during discharging and charging cycles is delineated by $V_{pKa}(H_3PO_4)$ and $V_{pKa}(HPO_4^-)$. This entails operating at $V_{mem} < V_{pKa\,(H3PO4)}$ (K_2HPO_4 trace, forward bias, **Figure**

S4.5) in forward bias and at $V_{\mathrm{mem}} > V_{\mathrm{p}K\mathrm{a}\ (\mathrm{HPO4}(2-))}$ (KH_2PO_4 trace, reverse bias, **Figure S4.5**) in reverse bias. Hence, the maximum discharging ($j_{\mathrm{dchg,max}}$) and charging ($j_{\mathrm{chg,max}}$) current densities, corresponding to the limiting currents for HPO_4^{2-} protonation and $H_2PO_4^-$ dissociation, respectively. Below $j_{\mathrm{chg,max}}$, the production of OH^- from water dissociation can increase the pH of the negolyte and lead to degradation of the redox-active species; above $j_{\mathrm{dchg,max}}$, the formation of neutral H_3PO_4 can lead to loss and redistribution of buffering phosphate equivalents from the negolyte into the posolyte. This constraint serves to limit the power density of the flow battery due to the ionic blockade phenomenon.

As a final note, since the electrode reactions considered here involve only electron transfer and not proton-coupled transformations, the pH values in either compartments are not held at a steady value during discharging and charging as hydronium and hydroxide ions are not produced or consumed at either electrode to compensate for the consumption or production of acid and base equivalents at the bipolar junction. Consequently, the compositions of both compartments are expected to change as a function of the state of charge (e.g. the pH of the posolyte increases and the pH of the negolyte decreases during discharging), and will influence the features of the forward and reverse polarization curves. Regardless, the limiting current in forward bias, which originates from the ionic blockade phenomenon explained above, sets the upper-limit on the power density at any given state of charge.

4.8.2 Supplementary Figures & Tables

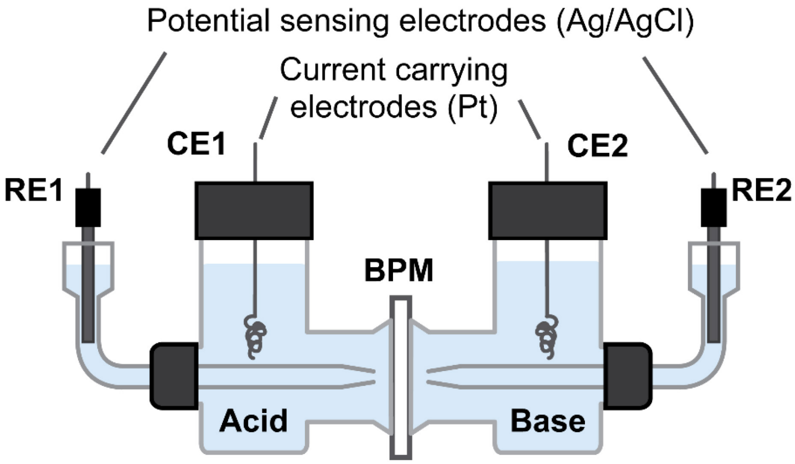

Figure S4.1. Illustration of the four-electrode set up used for electrochemical measurements, showing the placement of the counter electrodes (CEs) and reference electrodes (REs).

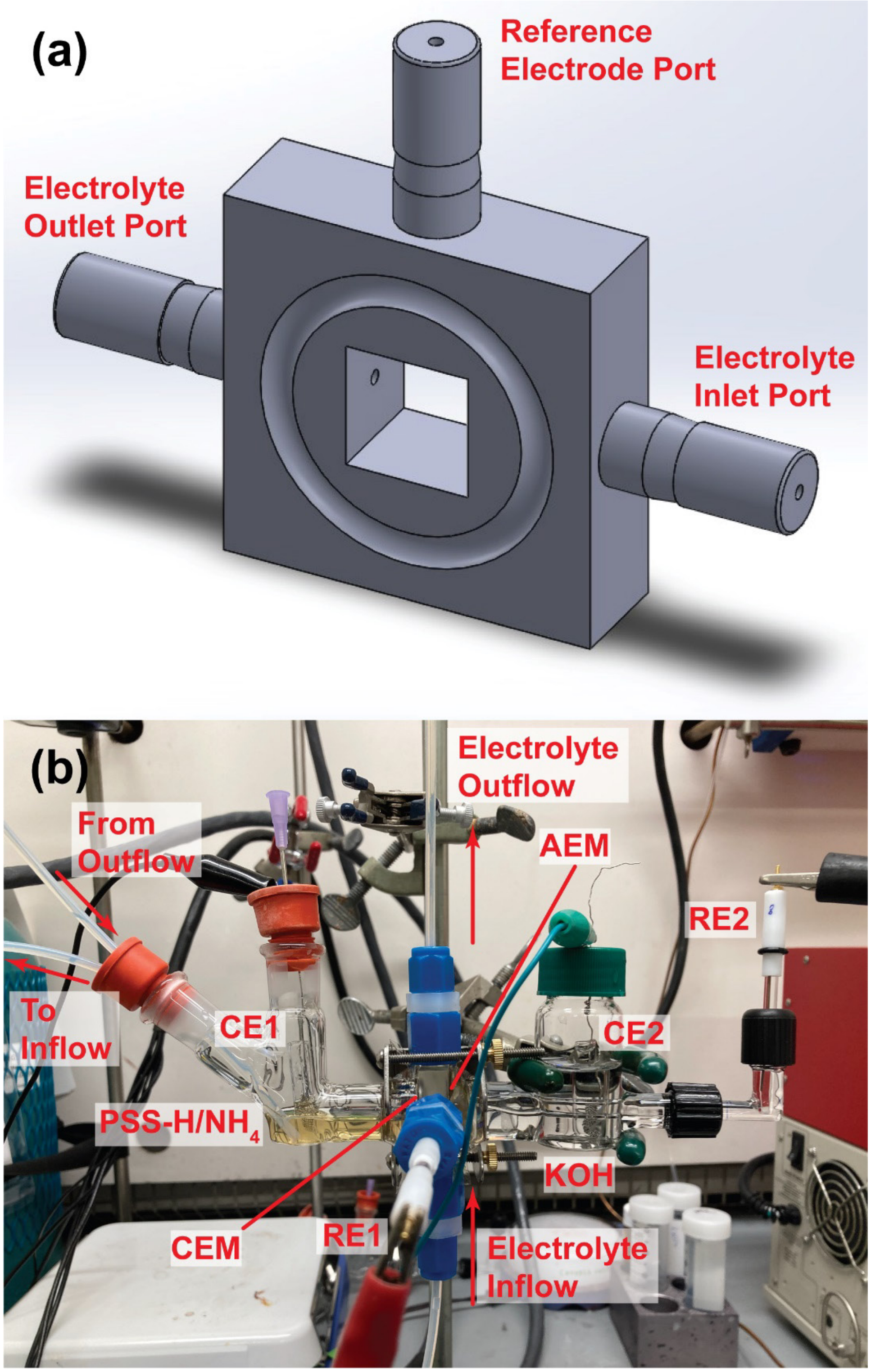

Figure S4.2. Experimental setup for polyelectrolyte advection experiments. **(a)** 3D model of custom-made 3D-printed flow adapter. The exposed surface area is 1 cm^2 and the liquid flow channels are 0.11 cm in diameter. **(b)** Electrochemical cell setup used for polyelectrolyte flow experiments.

Table S4.1. Diffusion coefficients of various ions in dilute aqueous solutions.[39]

Ion	**D_i / 10^{-5} cm^2 s^{-1}**
OH^-	5.273
OAc^-	1.089
H^+	9.31
NH_4^+	1.957
K^+	1.957

Table S4.2. pK_a values for various species in aqueous solutions.[39]

Species	**pK_a**
H_3O^+	0
AcOH	4.76
$nBuCO_2H$	4.83
H_2CO_3	6.35
NH_4^+	9.25
HCO_3^-	10.33
H_2O	14

Table S4.3. List of membranes used in this study and their corresponding thicknesses (as reported by their respective manufacturers).

Membrane	**Thickness / µm**
Fumasep FBM	130 – 160
Nafion 117	175
Fumasep FAA-3-50	45 – 55
Nafion 212	50.8
Nafion 115	125
Nafion 1110	254

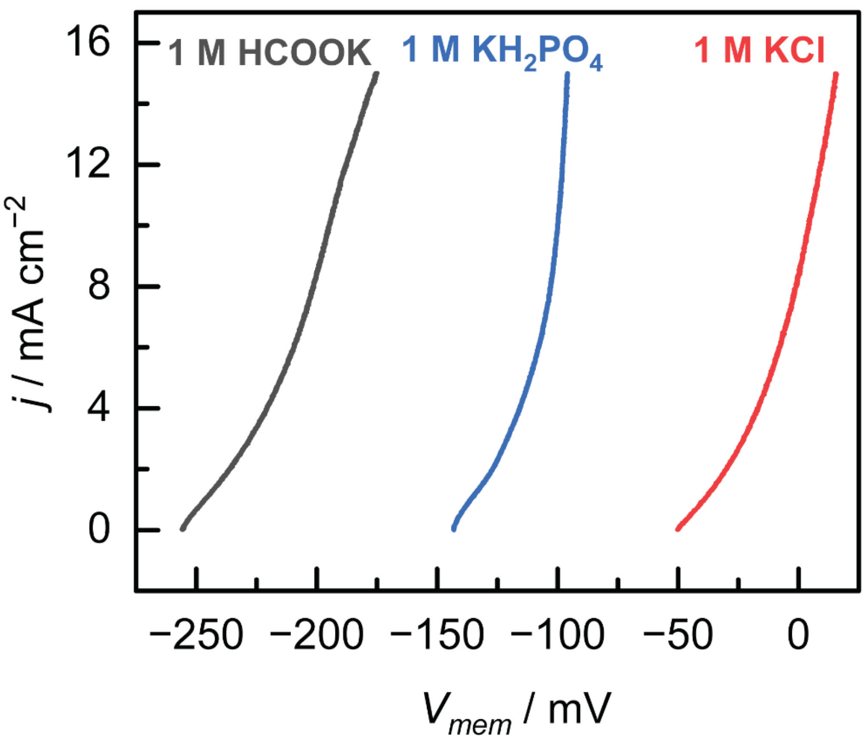

Figure S4.3. Forward bias polarization curves of 1 M H_2SO_4 | CEM | AEM | 1 M KA (where A = $HCOO^-$, $H_2PO_4^-$, Cl^-).

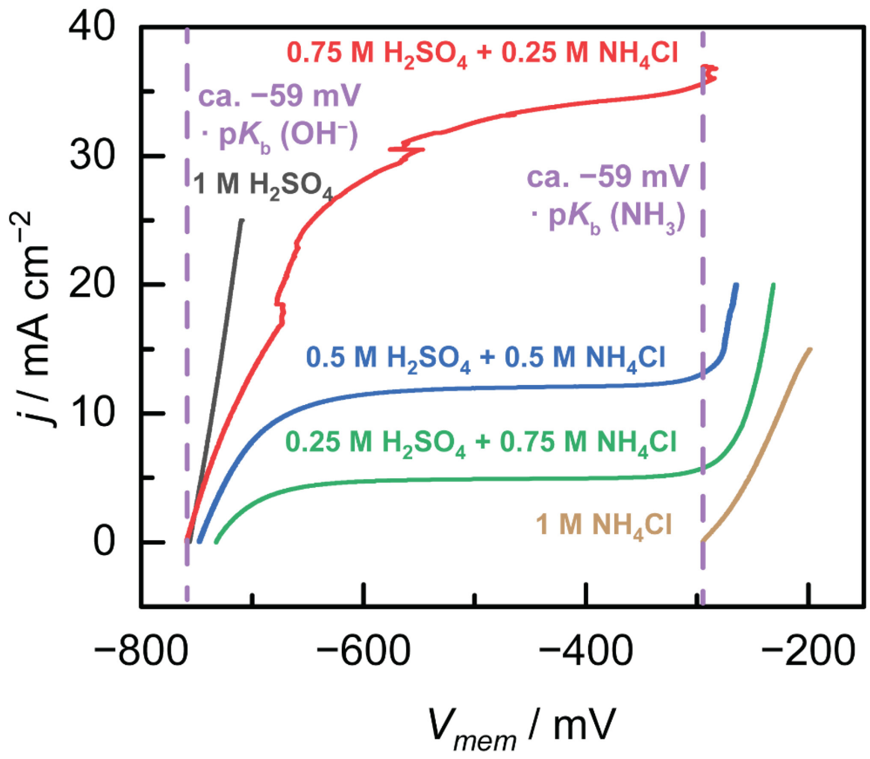

Figure S4.4. Forward bias polarization curves of x M H_2SO_4 + y M NH_4Cl | CEM | AEM | 1 M KOH (where x + y = 1).

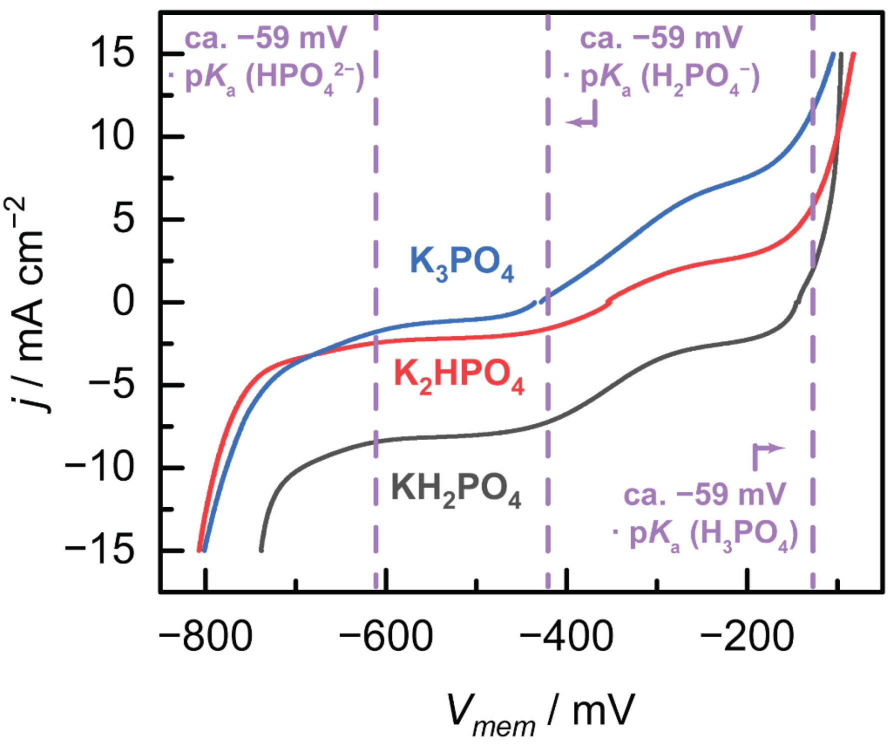

Figure S4.5. Forward bias polarization curves of 1 M H_2SO_4 | CEM | AEM | 1 M $K_xH_yPO_4$ (where x + y = 3).

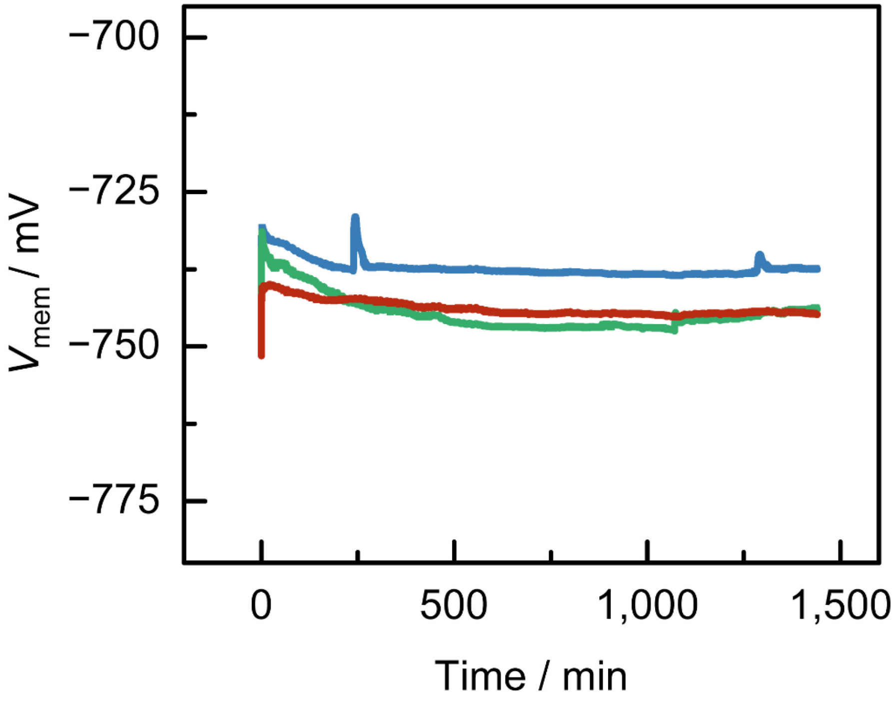

Figure S4.6. Overlay of the iR-corrected chronopotentiograms collected for three replicate 1 M H_2SO_4 | FBM | 0.5 M KOH + 0.5 M KOAc cells polarized at 2 mA cm^{-2}.

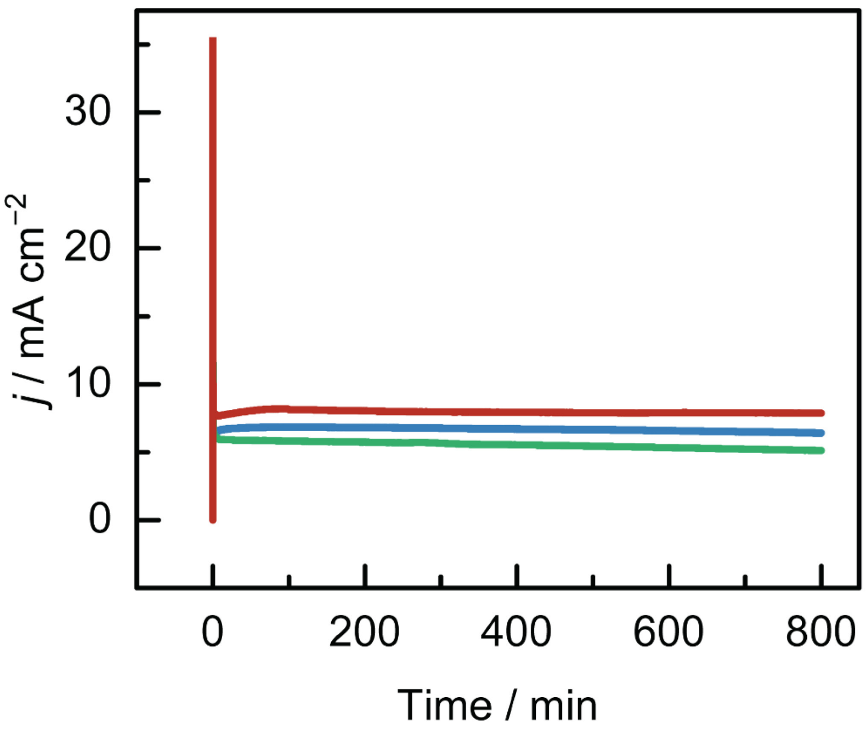

Figure S4.7. Overlay of the chronoamperograms collected for three replicate 1 M H_2SO_4 | FBM | 0.5 M KOH + 0.5 M KOAc cells polarized at ca. −480 mV. iR-corrected steady-state V_{mem} values were −480 (blue), −482 (red) and −479 (green) mV, respectively.

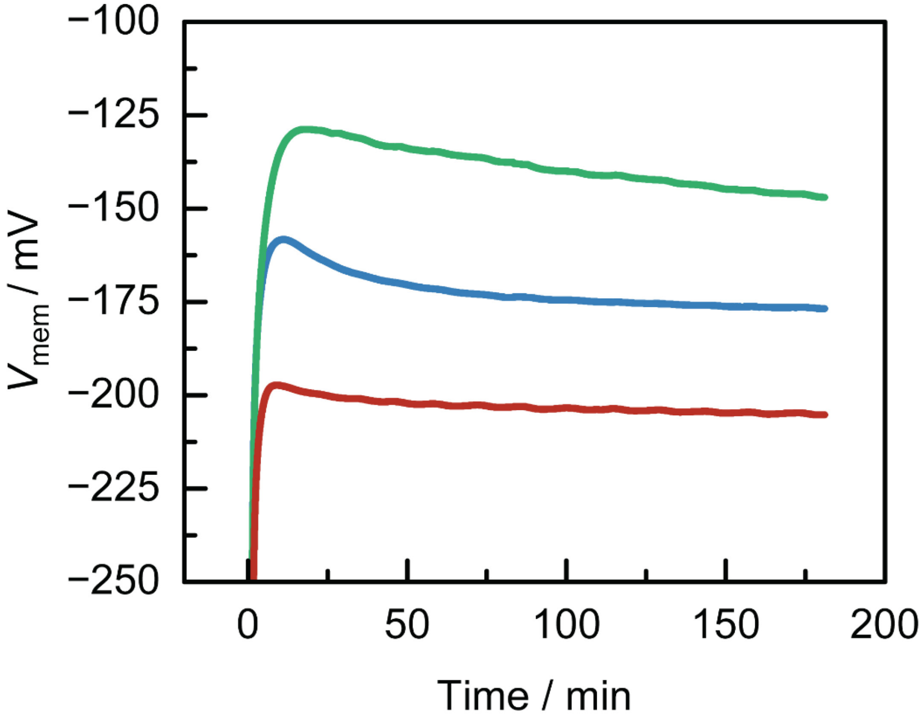

Figure S4.8. Overlay of the iR-corrected chronopotentiograms collected for three replicate 1 M H_2SO_4 | FBM | 0.5 M KOH + 0.5 M KOAc cells polarized at 11 mA cm^{-2}.

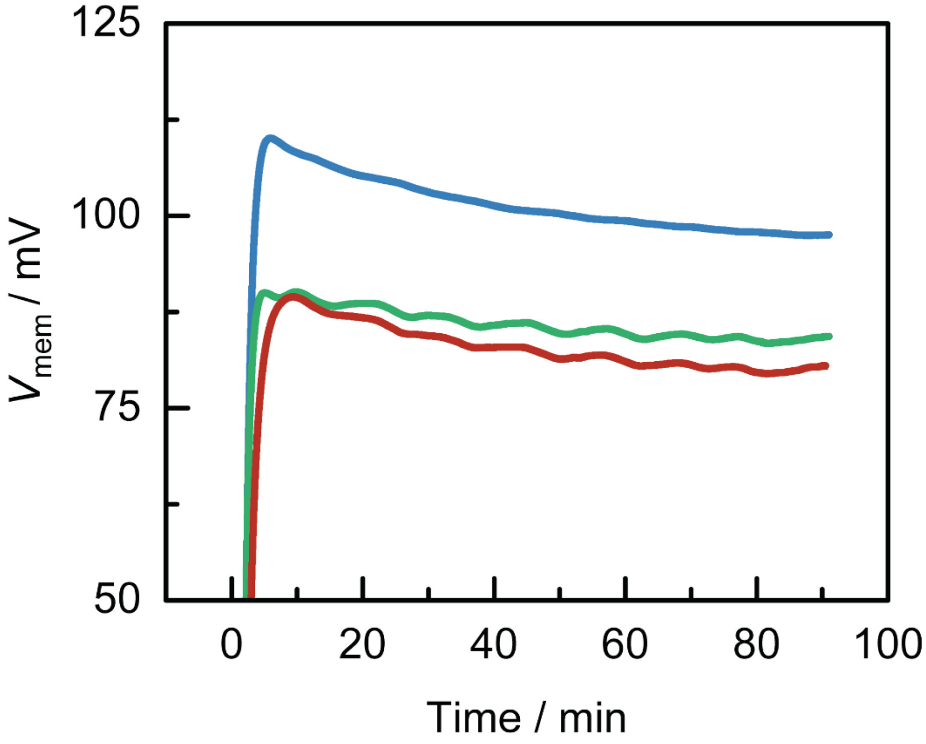

Figure S4.9. Overlay of the iR-corrected chronopotentiograms collected for three replicate 1 M H_2SO_4 | FBM | 0.5 M KOH + 0.5 M KOAc cells polarized at 22 mA cm^{-2}.

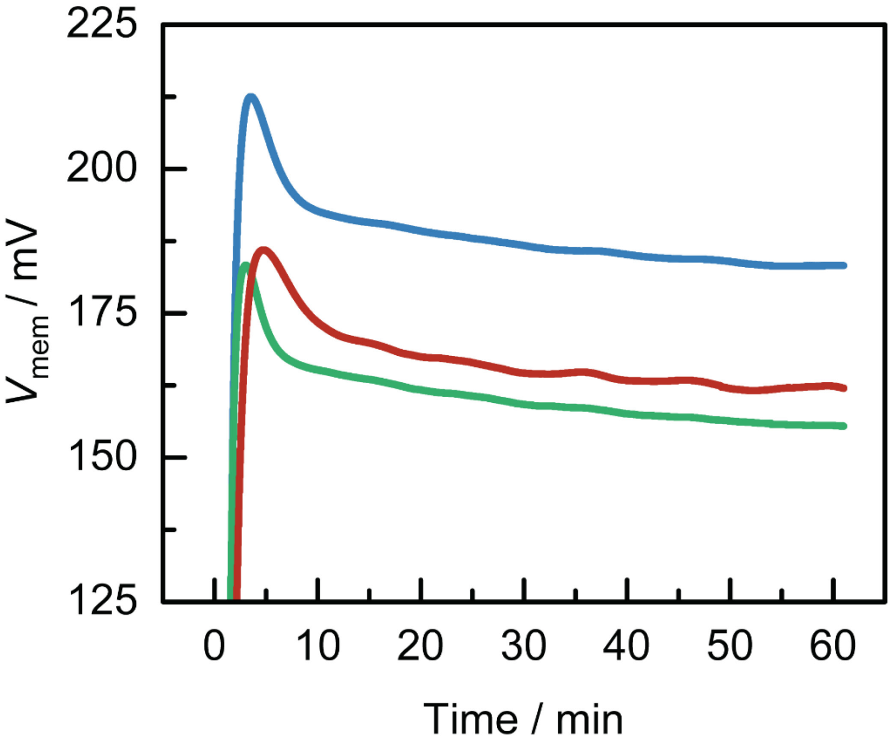

Figure S4.10. Overlay of the iR-corrected chronopotentiograms collected for three replicate 1 M H_2SO_4 | FBM | 0.5 M KOH + 0.5 M KOAc cells polarized at 33 mA cm^{-2}.

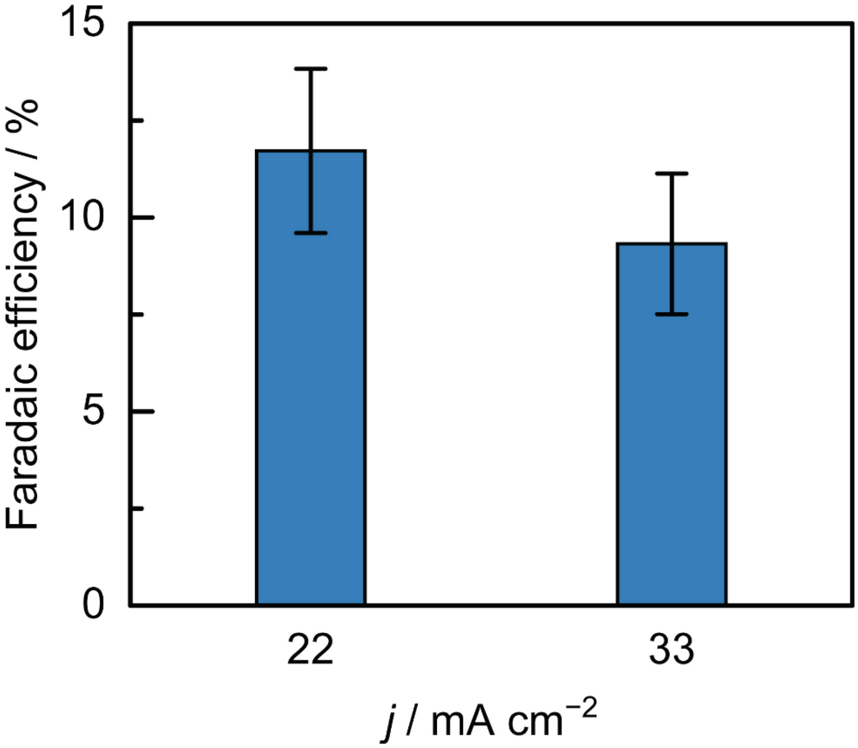

Figure S4.11. Faradaic efficiency for AcOH production in a 1 M H_2SO_4 | FBM | 0.5 M KOH + 0.5 M KOAc cell for galvanostatic polarization at 22 and 33 mA cm^{-2} in the overlimiting region of the polarization curve. The error bars represent standard deviations of three independent replicates.

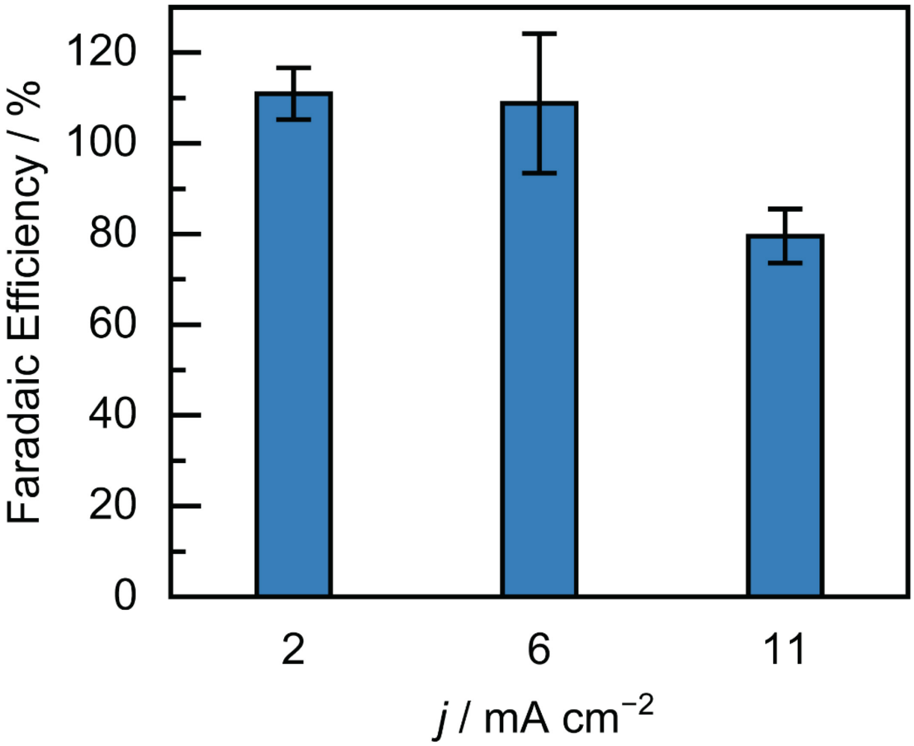

Figure S4.12. Faradaic efficiency for AcOH production in a 1 M H_2SO_4 | FBM | 1 M KOAc cell for galvanostatic polarization at 2, 6, and 11 mA cm^{-2}, corresponding to the same current densities reached for the 1 M H_2SO_4 | FBM | 0.5 M KOH + 0.5 M KOAc cell in the three distinct regions of its polarization curve. The error bars represent standard deviations of three independent replicates. The less-than-unity Faradaic efficiency at 11 mA cm^{-2} is attributed to partial oxidation of the AcOH produced at the Pt anode that becomes appreciable at the high AcOH concentrations attained.

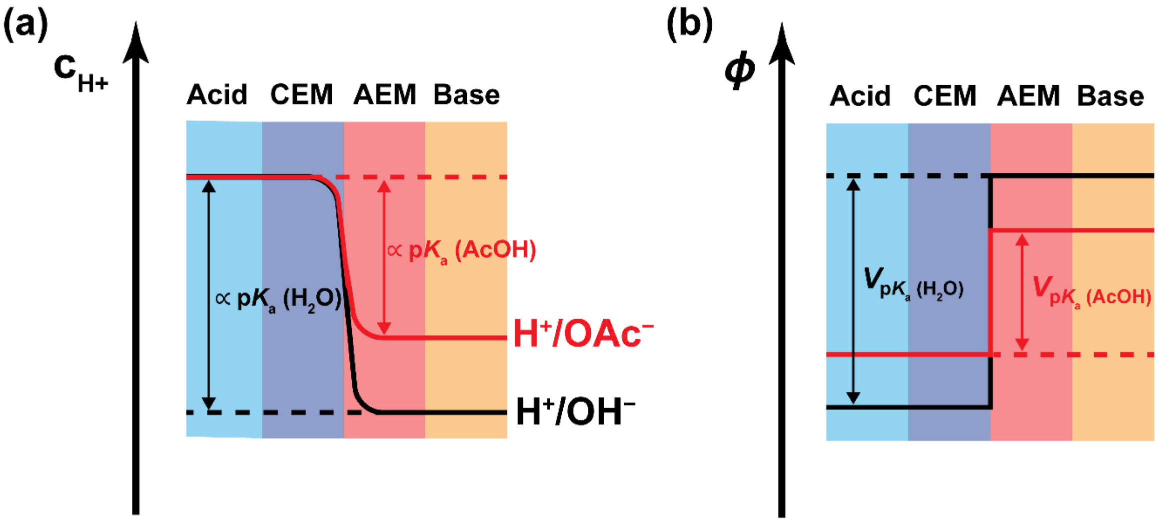

Figure S4.13. Profiles of **(a)** the concentration of H^+, c_{H+}, and **(b)** the electrostatic potential, ϕ, across the BPM.

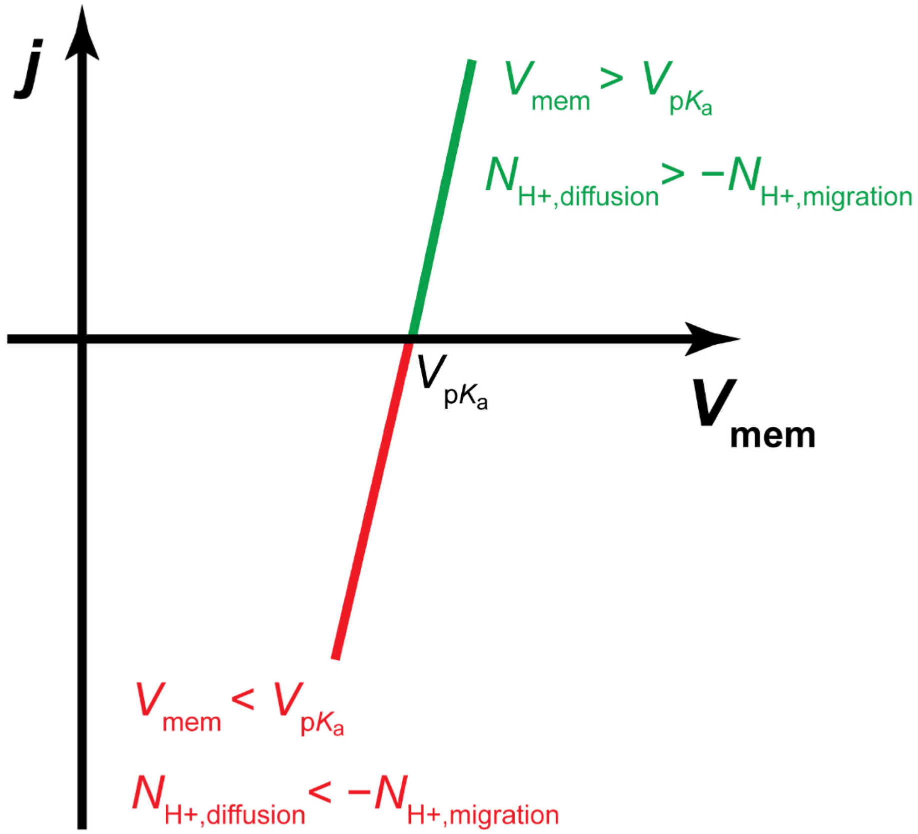

Figure S4.14. Theorized polarization curve for a 1 M H_2SO_4 | CEM | AEM | 1 M KA cell in forward bias (green) and reverse bias (red).

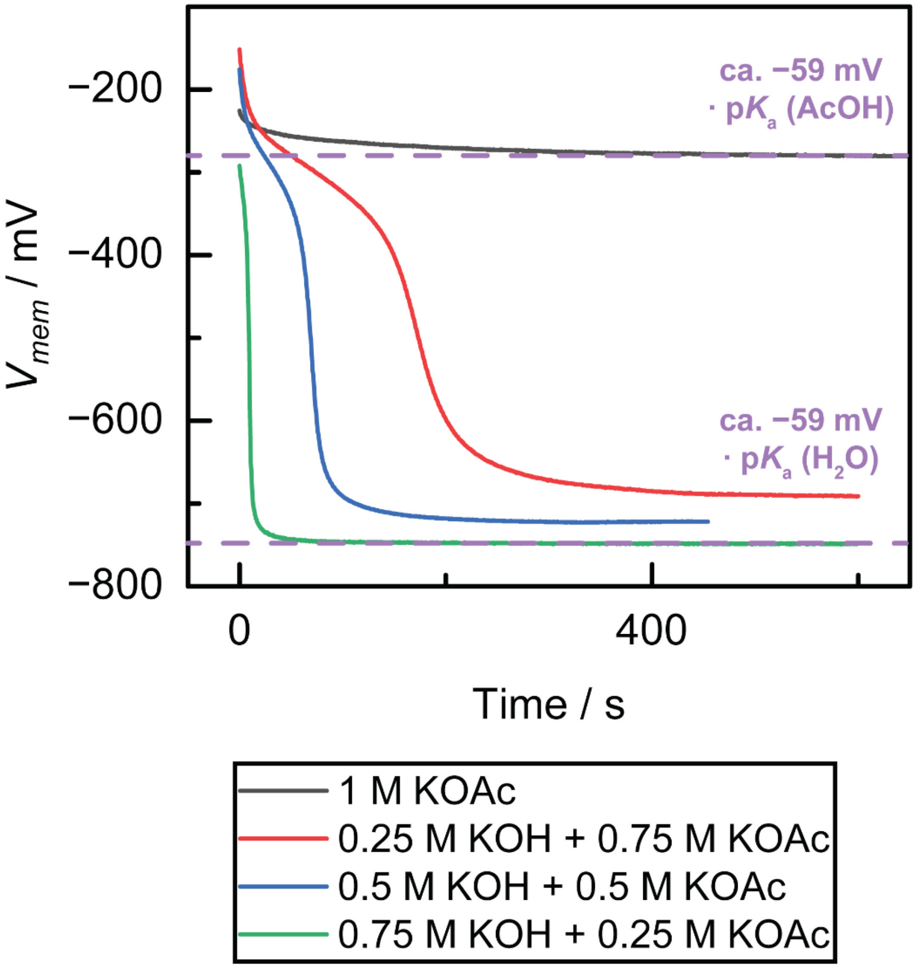

Figure S4.15. Open-circuit measurements of V_{mem} immediately following collection of forward bias polarization curves for 1 M H_2SO_4 | CEM | AEM | x M KOH + y M KOAc (x + y = 1) cells.

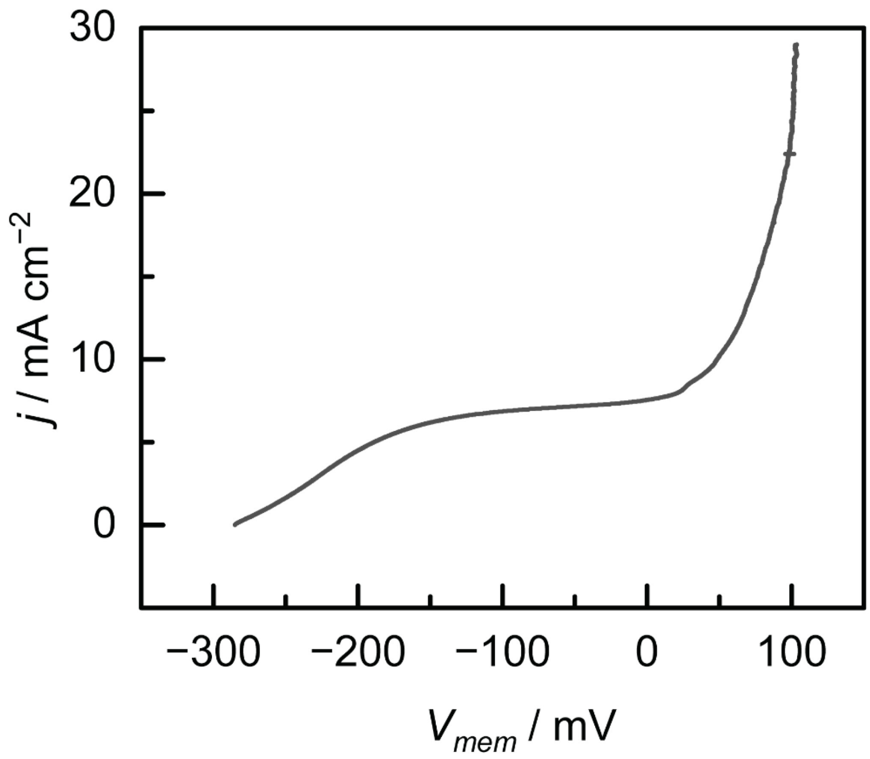

Figure S4.16. Forward bias polarization curve of 0.5 M NH_4Cl + 0.5 M KCl | FBM | 1 M KOH.

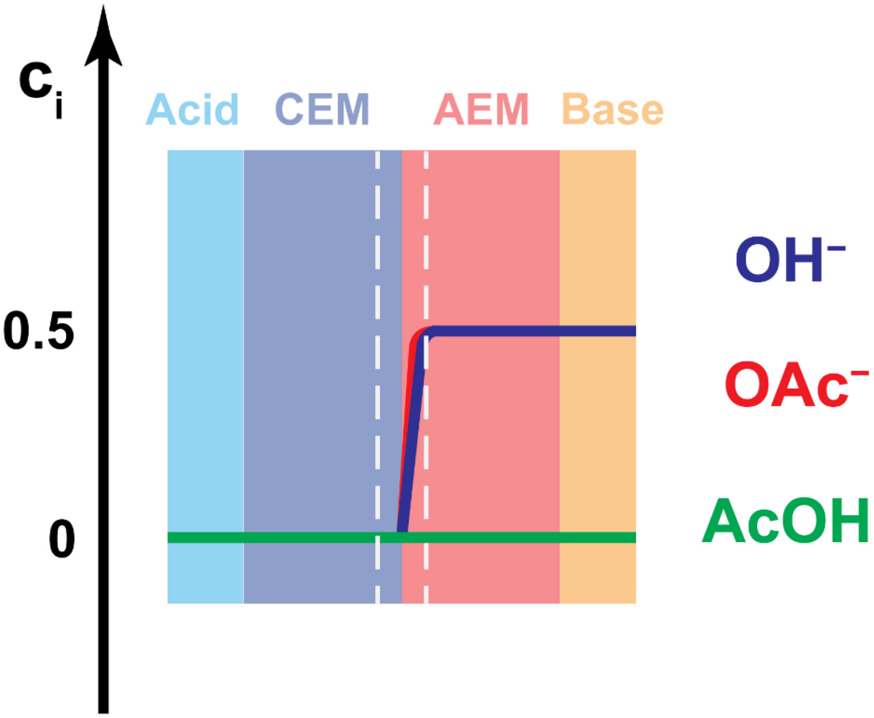

Figure S4.17. Concentration profiles for OH^-, OAc^- and AcOH across the BPM at open-circuit for a 1 M H_2SO_4 | 0.5 M KOH + 0.5 M KOAc cell.

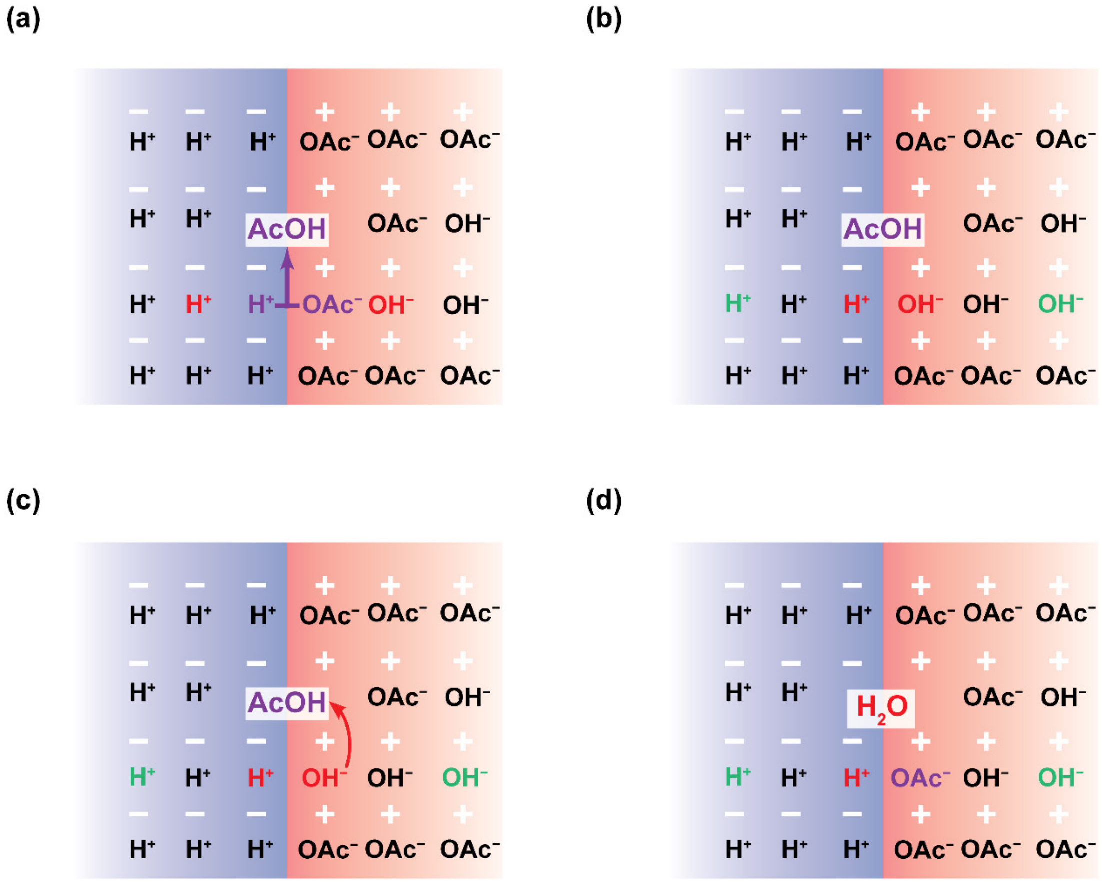

Figure S4.18. Alternative mechanistic pathway for the protonation of OH^- within the limiting region via AcOH mediation. **(a)** H^+ and OAc^- recombine at the bipolar junction to generate AcOH (purple); **(b)** ionic current flows as more H^+ and OH^- (or OAc^-) (green) flow to fill the vacant sites left by AcOH recombination; **(c)** AcOH (purple) reacts with a proximal OH^- (red); **(d)** this acid-base reaction leaves behind an OAc^- ion (purple) and produces H_2O (red).

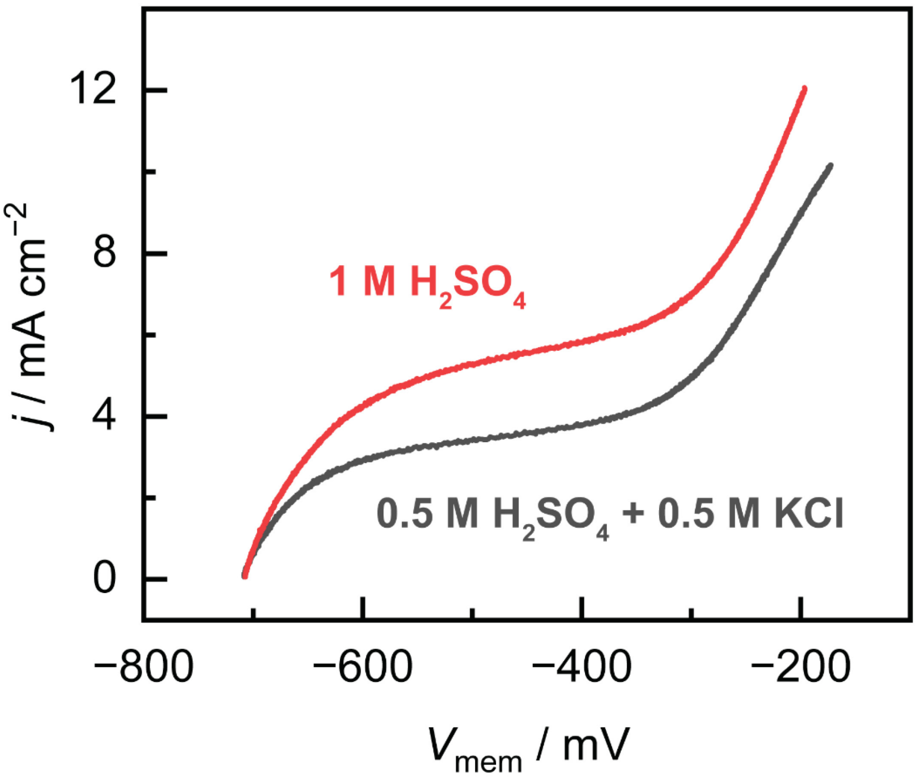

Figure S4.19. Overlay of forward bias polarization curves for 0.5 M H_2SO_4 + 0.5 M KCl | FBM | 0.5 M KOH + 0.5 M KOAc and 1 M H_2SO_4 | FBM | 0.5 M KOH + 0.5 M KOAc. The takeoff voltage for the overlimiting region is roughly similar between the two curves due to the small difference in pH between 1 M H_2SO_4 and 0.5 M H_2SO_4 (~0.2 – 0.3 units higher).

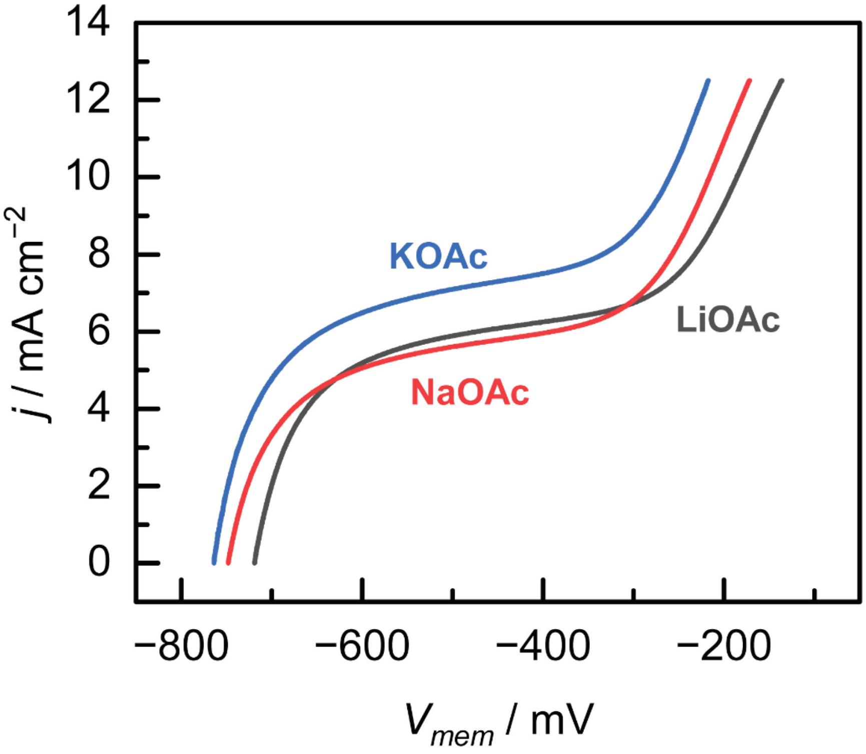

Figure S4.20. Forward bias polarization curve of 1 M H_2SO_4 | FBM | 0.625 M MOH + 0.375 M MOAc ($M^+ = Li^+$, Na^+ or K^+). Note that j_{lim} only increases by ~18% from $M^+ = Li^+$ to K^+ despite the nearly twofold increase in D_{M+} ($1.029\ x\ 10^{-5}$ and $1.957\ x\ 10^{-5}$ cm^2 s^{-1}, respectively), suggesting a minor role of co-ions in controlling j_{lim}.

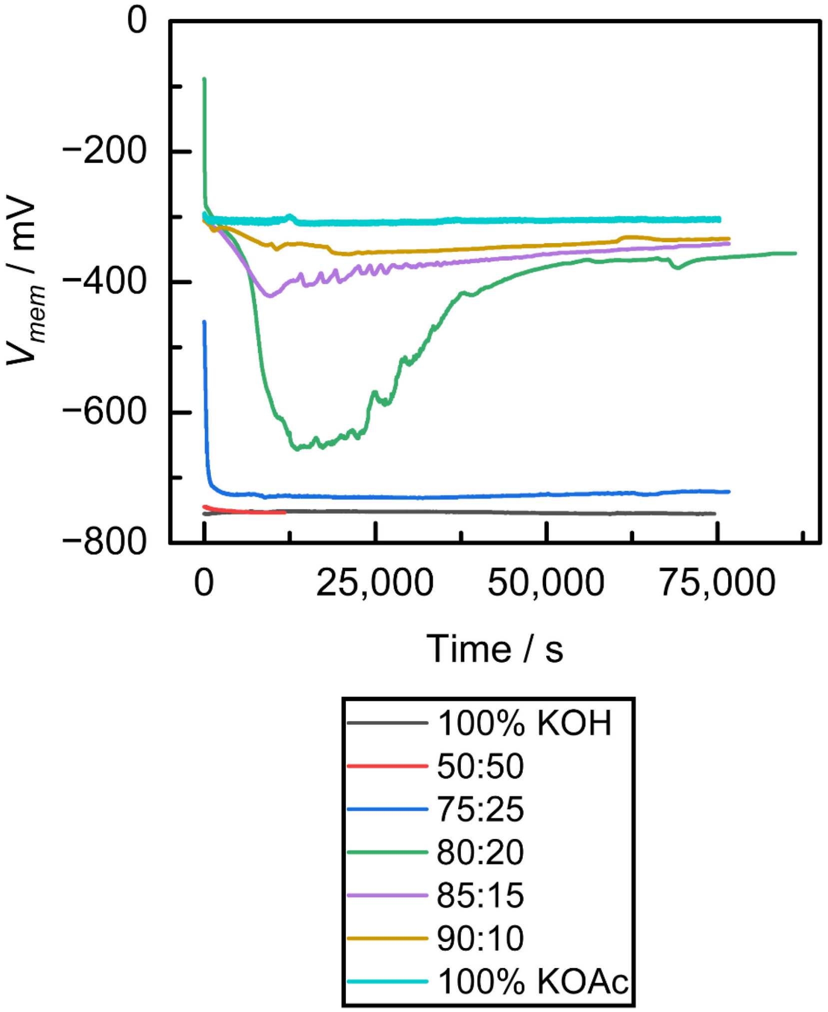

Figure S4.21. Open-circuit V_{mem} traces recorded for 1 M H_2SO_4 | FBM | x M KOH + y M KOAc (x + y = 1) cells. The legend indicates the varying concentration ratio of KOAc:KOH for each trace.

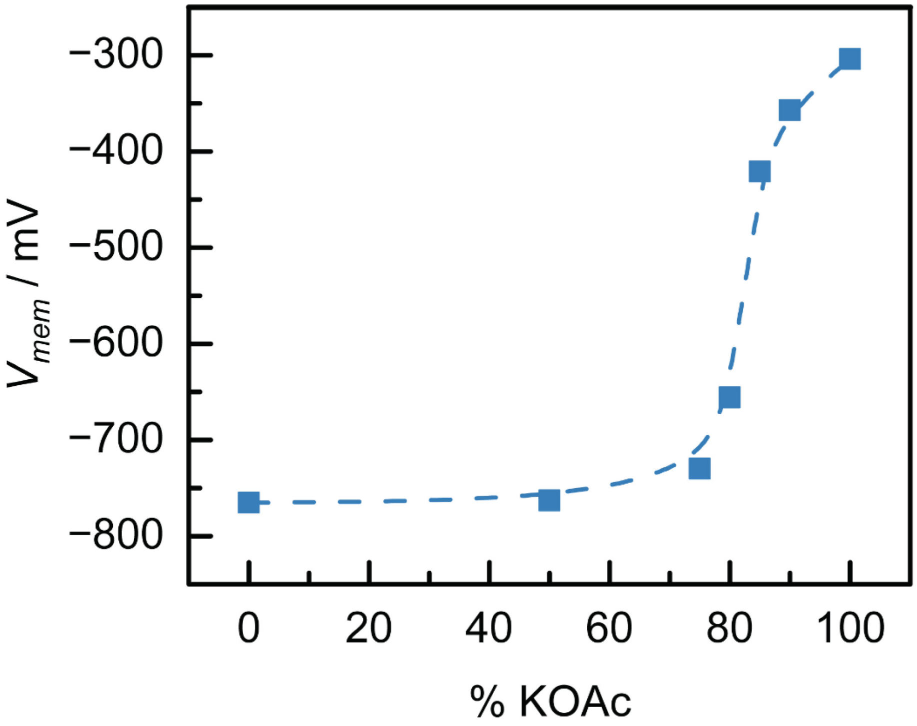

Figure S4.22. Variation of open-circuit V_{mem} as a function of % KOAc out of the total base amount for the cells 1 M H_2SO_4 | FBM | x M KOH + y M KOAc (x + y =1). Dashed line shown is a spline drawn to guide the eye.

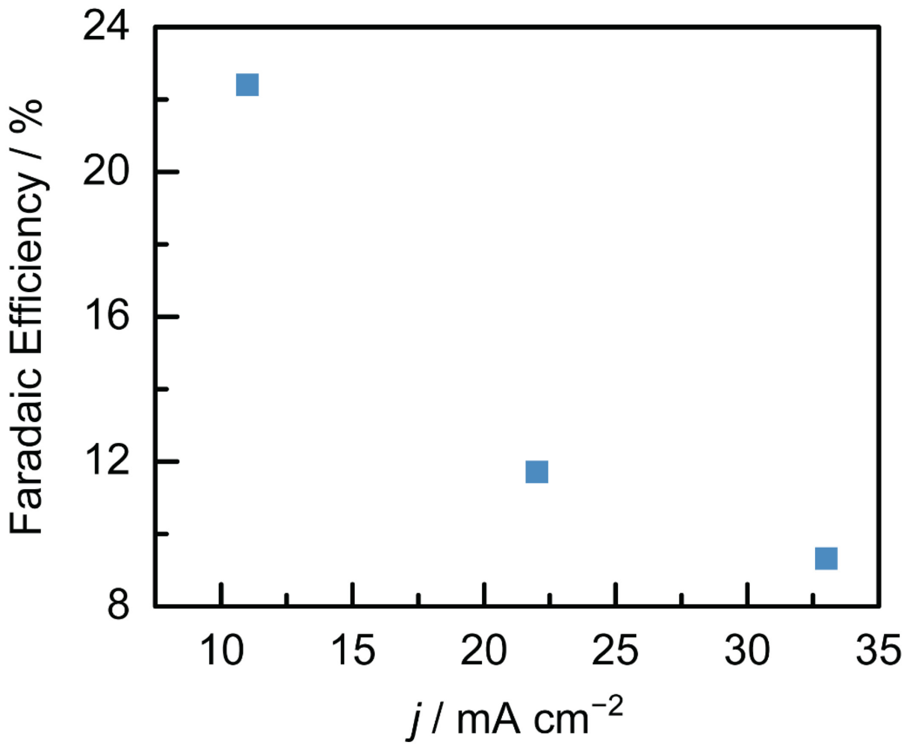

Figure S4.23. Plot of the mean Faradaic efficiency for AcOH production as a function of the applied current density in the overlimiting region of the polarization curve in **Figure 4.2(b)**.

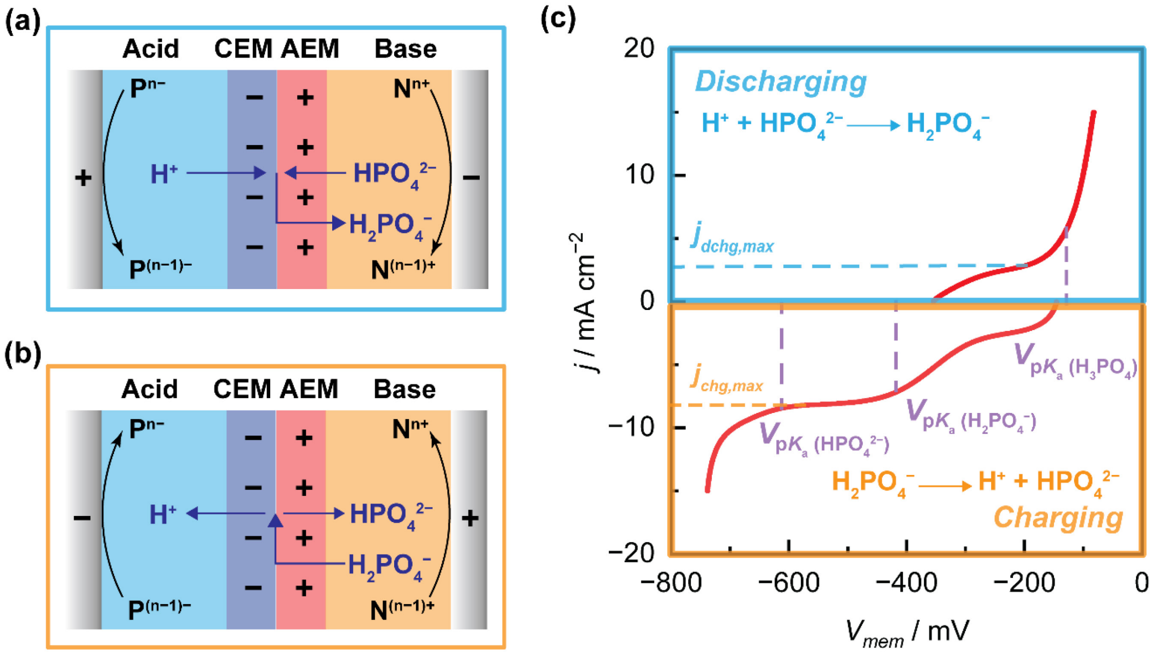

Figure S4.24. Cell schematic showing a BPM redox flow battery in **(a)** forward bias operation during a discharge cycle and in **(b)** reverse bias operation during a charge cycle. $P^{n-}/P^{(n-1)-}$ and $N^{n+}/N^{(n-1)+}$ are the redox-active species present in the posolyte and negolyte respectively. (c) Polarization curves for the redox flow battery shown in **(a)** and **(b)** for discharging and charging with a negolyte containing predominantly the $KHPO_4$ and K_2HPO_4 forms of phosphate buffer, respectively, taken from **Figure S4.5**. $j_{dchg,max}$ and $j_{chg,max}$ represent the maximum discharging and charging current densities, respectively, for BPM operation involving only dissociation-recombination reactions of the $H_2PO_4^-/HPO_4^{2-}$ couple.

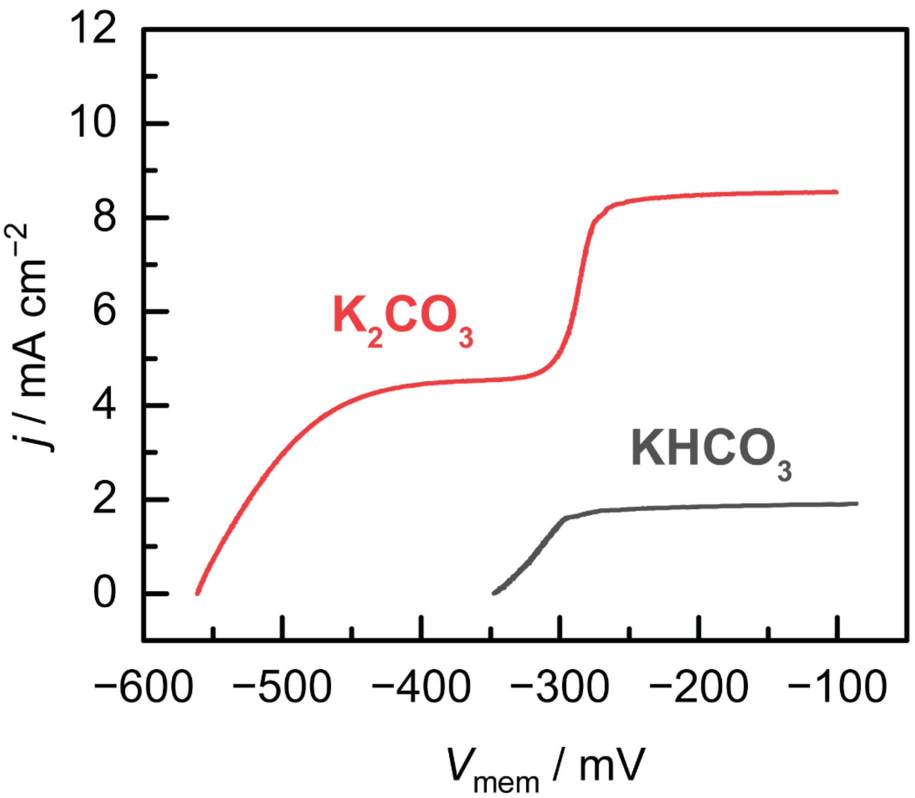

Figure S4.25. Forward bias polarization curve of 1 M H_2SO_4 | CEM | AEM | 1 M $K_xH_yCO_3$ (where x + y = 1). The second limiting region observed here but absent for data collected with FBM is attributed to trapped CO_2 bubbles reducing interfacial area and leading to some degree of membrane delamination for the more loosely attached homemade BPMs.

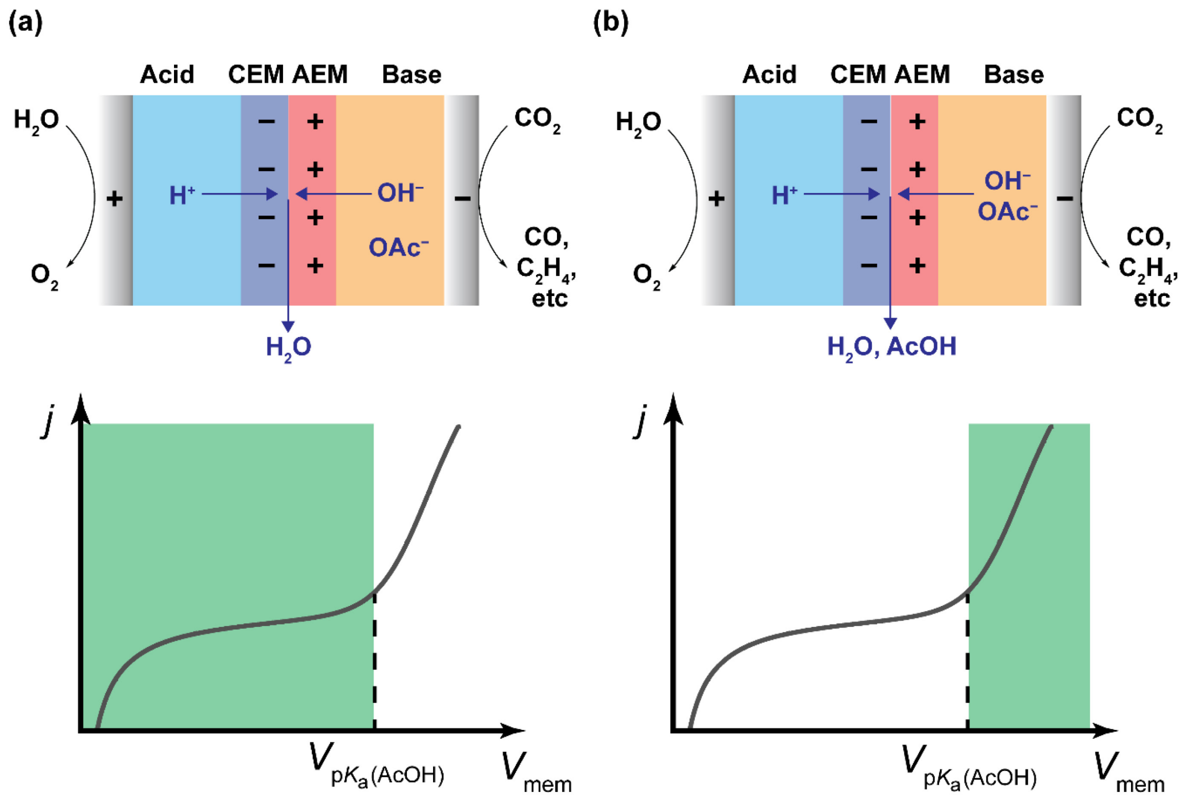

Figure S4.26. Cell schematics and polarization curves for a forward bias BPM CO_2 electrolyzer producing liquid CO_2RR products (AcOH is used as an example here) in an alkaline catholyte operating in **(a)** the under-limiting and limiting regions and **(b)** the over-limiting region. The relevant regions of operation are shaded in green.

4.9 References

(1) Gileadi, E. *Physical Electrochemistry: Fundamentals, Techniques and Applications*; Wiley-VCH: Weinheim, 2011.

(2) Tributsch, H.; Pohlmann, L. Electron Transfer: Classical Approaches and New Frontiers. *Science.* **1998**, *279* (5358), 1891–1895.

(3) Kontturi, K.; Murtomäki, L.; Manzanares, J. A. *Ionic Transport Processes*; Oxford University Press, 2008; Vol. 9780199533.

(4) Pärnamäe, R.; Mareev, S.; Nikonenko, V.; Melnikov, S.; Sheldeshov, N.; Zabolotskii, V.; Hamelers, H. V. M.; Tedesco, M. Bipolar Membranes: A Review on Principles, Latest Developments, and Applications. *J. Memb. Sci.* **2021**, *617*, 118538.

(5) Giesbrecht, P. K.; Freund, M. S. Recent Advances in Bipolar Membrane Design and Applications. *Chem. Mater.* **2020**, *32* (19), 8060–8090.

(6) Blommaert, M. A.; Aili, D.; Tufa, R. A.; Li, Q.; Smith, W. A.; Vermaas, D. A. Insights and Challenges for Applying Bipolar Membranes in Advanced Electrochemical Energy Systems. *ACS Energy Lett.* **2021**, *6*, 2539–2548.

(7) Tufa, R. A.; Blommaert, M. A.; Chanda, D.; Li, Q.; Vermaas, D. A.; Aili, D. Bipolar Membrane and Interface Materials for Electrochemical Energy Systems. *ACS Appl. Energy Mater.* **2021**, *4* (8), 7419–7439.

(8) Yan, Z.; Mallouk, T. E. Bipolar Membranes for Ion Management in (Photo)Electrochemical Energy Conversion. *Accounts Mater. Res.* **2021**, *2* (12), 1156–1166.

(9) Simons, R.; Khanarian, G. Water Dissociation in Bipolar Membranes: Experiments and Theory. *J. Membr. Biol.* **1978**, *38* (1–2), 11–30.

(10) Ramírez, P.; Rapp, H.-J.; Mafé, S.; Bauer, B. Bipolar Membranes under Forward and Reverse Bias Conditions. Theory vs. Experiment. *J. Electroanal. Chem.* **1994**, *375* (1–2), 101–108.

(11) Oener, S. Z.; Foster, M. J.; Boettcher, S. W. Accelerating Water Dissociation in Bipolar Membranes and for Electrocatalysis. *Science.* **2020**, *369* (6507), 1099–1103.

(12) McDonald, M. B.; Ardo, S.; Lewis, N. S.; Freund, M. S. Use of Bipolar Membranes for Maintaining Steady-State PH Gradients in Membrane-Supported, Solar-Driven Water Splitting. *ChemSusChem* **2014**, *7* (11), 3021–3027.

(13) Vargas-Barbosa, N. M.; Geise, G. M.; Hickner, M. A.; Mallouk, T. E. Assessing the Utility of Bipolar Membranes for Use in Photoelectrochemical Water-Splitting Cells. *ChemSusChem* **2014**, *7* (11), 3017–3020.

(14) Luo, J.; Vermaas, D. A.; Bi, D.; Hagfeldt, A.; Smith, W. A.; Grätzel, M. Bipolar Membrane-Assisted Solar Water Splitting in Optimal PH. *Adv. Energy Mater.* **2016**, *6* (13), 1600100.

(15) Mayerhöfer, B.; McLaughlin, D.; Böhm, T.; Hegelheimer, M.; Seeberger, D.; Thiele, S. Bipolar Membrane Electrode Assemblies for Water Electrolysis. *ACS Appl. Energy Mater.* **2020**, *3* (10), 9635–9644.

(16) Oener, S. Z.; Twight, L. P.; Lindquist, G. A.; Boettcher, S. W. Thin Cation-Exchange Layers Enable High-Current-Density Bipolar Membrane Electrolyzers via Improved Water Transport. *ACS Energy Lett.* **2021**, *6* (1), 1–8.

(17) Vermaas, D. A.; Smith, W. A. Synergistic Electrochemical CO2 Reduction and Water Oxidation with a Bipolar Membrane. *ACS Energy Lett.* **2016**, *1* (6), 1143–1148.

(18) Li, Y. C.; Zhou, D.; Yan, Z.; Gonçalves, R. H.; Salvatore, D. A.; Berlinguette, C. P.; Mallouk, T. E. Electrolysis of CO2 to Syngas in Bipolar Membrane-Based Electrochemical Cells. *ACS Energy Lett.* **2016**, *1* (6), 1149–1153.

(19) Zhou, X.; Liu, R.; Sun, K.; Chen, Y.; Verlage, E.; Francis, S. A.; Lewis, N. S.; Xiang, C. Solar-Driven Reduction of 1 Atm of CO2 to Formate at 10% Energy-Conversion Efficiency by Use of a TiO2-Protected III–V Tandem Photoanode in Conjunction with a Bipolar Membrane and a Pd/C Cathode. *ACS Energy Lett.* **2016**, *1* (4), 764–770.

(20) Salvatore, D. A.; Weekes, D. M.; He, J.; Dettelbach, K. E.; Li, Y. C.; Mallouk, T. E.; Berlinguette, C. P. Electrolysis of Gaseous CO2 to CO in a Flow Cell with a Bipolar Membrane. *ACS Energy Lett.* **2018**, *3* (1), 149–154.

(21) Pătru, A.; Binninger, T.; Pribyl, B.; Schmidt, T. J. Design Principles of Bipolar Electrochemical Co-Electrolysis Cells for Efficient Reduction of Carbon Dioxide from Gas Phase at Low Temperature. *J. Electrochem. Soc.* **2019**, *166* (2), F34–F43.

(22) Blommaert, M. A.; Sharifian, R.; Shah, N.; Nesbitt, N.; Smith, W.; Vermaas, D. A. Orientation of Bipolar Membrane Determines the Dominant Ion and Carbonic Species Transport in Membrane Electrode Assemblies for CO2 Reduction. *J. Mater. Chem. A* **2021**.

(23) Siritanaratkul, B.; Forster, M.; Greenwell, F.; Sharma, P. K.; Yu, E. H.; Cowan, A. J. Zero-Gap Bipolar Membrane Electrolyzer for Carbon Dioxide Reduction Using Acid-Tolerant Molecular Electrocatalysts. *J. Am. Chem. Soc.* **2022**, *144* (17), 7551–7556.

(24) Xie, K.; Miao, R. K.; Ozden, A.; Liu, S.; Chen, Z.; Dinh, C.; Huang, J. E.; Xu, Q.; Gabardo, C. M.; Lee, G.; Edwards, J. P.; O'Brien, C. P.; Boettcher, S. W.; Sinton, D.; Sargent, E. H. Bipolar Membrane Electrolyzers Enable High Single-Pass CO2 Electroreduction to Multicarbon Products. *Nat. Commun.* **2022**, *13* (1), 3609.

(25) Sullivan, I.; Goryachev, A.; Digdaya, I. A.; Li, X.; Atwater, H. A.; Vermaas, D. A.; Xiang, C. Coupling Electrochemical CO2 Conversion with CO2 Capture. *Nat. Catal.* **2021**, *4* (11), 952–958.

(26) Sharifian, R.; Wagterveld, R. M.; Digdaya, I. A.; Xiang, C.; Vermaas, D. A. Electrochemical Carbon Dioxide Capture to Close the Carbon Cycle. *Energy Environ. Sci.* **2021**, *14* (2), 781–814.

(27) Ding, Y.; Cai, P.; Wen, Z. Electrochemical Neutralization Energy: From Concept to Devices. *Chem. Soc. Rev.* **2021**, *50* (3), 1495–1511.

(28) Yan, Z.; Wycisk, R. J.; Metlay, A. S.; Xiao, L.; Yoon, Y.; Pintauro, P. N.; Mallouk, T. E. High-Voltage Aqueous Redox Flow Batteries Enabled by Catalyzed Water Dissociation and Acid–Base Neutralization in Bipolar Membranes. *ACS Cent. Sci.* **2021**, *7* (6), 1028–1035.

(29) Metlay, A. S.; Chyi, B.; Yoon, Y.; Wycisk, R. J.; Pintauro, P. N.; Mallouk, T. E. Three-Chamber Design for Aqueous Acid–Base Redox Flow Batteries. *ACS Energy Lett.* **2022**, *7* (3), 908–913.

(30) Pärnamäe, R.; Gurreri, L.; Post, J.; van Egmond, W. J.; Culcasi, A.; Saakes, M.; Cen, J.; Goosen, E.; Tamburini, A.; Vermaas, D. A.; Tedesco, M. The Acid–Base Flow Battery: Sustainable Energy Storage via Reversible Water Dissociation with Bipolar Membranes. *Membranes (Basel).* **2020**, *10* (12), 409.

(31) Al-Dhubhani, E.; Pärnamäe, R.; Post, J. W.; Saakes, M.; Tedesco, M. Performance of Five Commercial Bipolar Membranes under Forward and Reverse Bias Conditions for Acid-Base Flow Battery Applications. *J. Memb. Sci.* **2021**, *7*, 119748.

(32) Bui, J. C.; Digdaya, I.; Xiang, C.; Bell, A. T.; Weber, A. Z. Understanding Multi-Ion Transport Mechanisms in Bipolar Membranes. *ACS Appl. Mater. Interfaces* **2020**, *12* (47), 52509–52526.

(33) Mitchell, J. B.; Chen, L.; Langworthy, K.; Fabrizio, K.; Boettcher, S. W. Catalytic Proton–Hydroxide Recombination for Forward-Bias Bipolar Membranes. *ACS Energy Lett.* **2022**, *7* (11), 3967–3973.

(34) Sokirko, A. V.; Ramírez, P.; Manzanares, J. A.; Mafés, S. Modeling of Forward and Reverse Bias Conditions in Bipolar Membranes. *Berichte der Bunsengesellschaft für Phys. Chemie* **1993**, *97* (8), 1040–1048.

(35) Ziv, N.; Mustain, W. E.; Dekel, D. R. The Effect of Ambient Carbon Dioxide on Anion-Exchange Membrane Fuel Cells. *ChemSusChem* **2018**, *11* (7), 1136–1150.

(36) Lee, M.-Y.; Park, K. T.; Lee, W.; Lim, H.; Kwon, Y.; Kang, S. Current Achievements and the Future Direction of Electrochemical CO2 Reduction: A Short Review. *Crit. Rev. Environ. Sci. Technol.* **2020**, *50* (8), 769–815.

(37) Dinh, H. Q.; Toh, W. L.; Chu, A. T.; Surendranath, Y. Neutralization Short-Circuiting with Weak Electrolytes Erodes the Efficiency of Bipolar Membranes. *ACS Appl. Mater. Interfaces* **2023**, *15* (3), 4001–4010.

(38) Vermaas, D. A.; Wiegman, S.; Nagaki, T.; Smith, W. A. Ion Transport Mechanisms in Bipolar Membranes for (Photo)Electrochemical Water Splitting. *Sustain. Energy Fuels* **2018**, *2* (9), 2006–2015.

(39) Haynes, W. M.; Lide, D. R.; Bruno, T. J. *CRC Handbook of Chemistry and Physics*, 97th ed.; CRC Press, 2016.

(40) Grew, K. N.; McClure, J. P.; Chu, D.; Kohl, P. A.; Ahlfield, J. M. Understanding Transport at the Acid-Alkaline Interface of Bipolar Membranes. *J. Electrochem. Soc.* **2016**, *163* (14), F1572–F1587.

(41) Marioni, N.; Zhang, Z.; Zofchak, E. S.; Sachar, H. S.; Kadulkar, S.; Freeman, B. D.; Ganesan, V. Impact of Ion–Ion Correlated Motion on Salt Transport in Solvated Ion Exchange Membranes. *ACS Macro Lett.* **2022**, *11* (11), 1258–1264.

(42) Ünlü, M.; Zhou, J.; Kohl, P. A. Hybrid Anion and Proton Exchange Membrane Fuel Cells. *J. Phys. Chem. C* **2009**, *113* (26), 11416–11423.

(43) Daud, S. S.; Norrdin, M. A.; Jaafar, J.; Sudirman, R. The Effect of Material on Bipolar Membrane Fuel Cell Performance: A Review. *IOP Conf. Ser. Mater. Sci. Eng.* **2020**, *736* (3), 032003.

(44) Bard, A. J.; Faulkner, L. R. *Electrochemical Methods: Fundamentals and Applications*, 2nd ed.; John Wiley & Sons: New York, 2001.

(45) Chu, S.; Cui, Y.; Liu, N. The Path towards Sustainable Energy. *Nat. Mater.* **2017**, *16* (1), 16–22.

(46) De Luna, P.; Hahn, C.; Higgins, D.; Jaffer, S. A.; Jaramillo, T. F.; Sargent, E. H. What Would It Take for Renewably Powered Electrosynthesis to Displace Petrochemical Processes? *Science.* **2019**, *364* (6438).

(47) Zhang, Y.-J.; Sethuraman, V.; Michalsky, R.; Peterson, A. A. Competition between CO 2 Reduction and H 2 Evolution on Transition-Metal Electrocatalysts. *ACS Catal.* **2014**, *4* (10), 3742–3748.

(48) Wuttig, A.; Yaguchi, M.; Motobayashi, K.; Osawa, M.; Surendranath, Y. Inhibited Proton Transfer Enhances Au-Catalyzed CO 2 -to-Fuels Selectivity. *Proc. Natl. Acad. Sci.* **2016**, *113* (32), E4585–E4593.

(49) Ooka, H.; Figueiredo, M. C.; Koper, M. T. M. Competition between Hydrogen Evolution and Carbon Dioxide Reduction on Copper Electrodes in Mildly Acidic Media. *Langmuir* **2017**, *33* (37), 9307–9313.

(50) Goyal, A.; Marcandalli, G.; Mints, V. A.; Koper, M. T. M. Competition between CO 2 Reduction and Hydrogen Evolution on a Gold Electrode under Well-Defined Mass Transport Conditions. *J. Am. Chem. Soc.* **2020**, *142* (9), 4154–4161.

(51) Rabinowitz, J. A.; Kanan, M. W. The Future of Low-Temperature Carbon Dioxide Electrolysis Depends on Solving One Basic Problem. *Nat. Commun.* **2020**, *11* (1), 5231.

(52) Xie, K.; Ozden, A.; Miao, R. K.; Li, Y.; Sinton, D.; Sargent, E. H. Eliminating the Need for Anodic Gas Separation in CO2 Electroreduction Systems via Liquid-to-Liquid Anodic Upgrading. *Nat. Commun.* **2022**, *13* (1), 3070.

(53) Huang, J. E.; Li, F.; Ozden, A.; Sedighian Rasouli, A.; García de Arquer, F. P.; Liu, S.; Zhang, S.; Luo, M.; Wang, X.; Lum, Y.; Xu, Y.; Bertens, K.; Miao, R. K.; Dinh, C.-T.; Sinton, D.; Sargent, E. H. CO 2 Electrolysis to Multicarbon Products in Strong Acid. *Science.* **2021**, *372* (6546), 1074–1078.

(54) O'Brien, C. P.; Miao, R. K.; Liu, S.; Xu, Y.; Lee, G.; Robb, A.; Huang, J. E.; Xie, K.; Bertens, K.; Gabardo, C. M.; Edwards, J. P.; Dinh, C.; Sargent, E. H.; Sinton, D. Single Pass CO2 Conversion Exceeding 85% in the Electrosynthesis of Multicarbon Products via

Local CO2 Regeneration. *ACS Energy Lett.* **2021**, *6* (8), 2952–2959.

(55) Xu, Y.; Miao, R. K.; Edwards, J. P.; Liu, S.; O'Brien, C. P.; Gabardo, C. M.; Fan, M.; Huang, J. E.; Robb, A.; Sargent, E. H.; Sinton, D. A Microchanneled Solid Electrolyte for Carbon-Efficient CO2 Electrolysis. *Joule* **2022**, *6* (6), 1333–1343.

(56) Kim, J. Y. 'Timothy'; Zhu, P.; Chen, F.-Y.; Wu, Z.-Y.; Cullen, D. A.; Wang, H. Recovering Carbon Losses in CO2 Electrolysis Using a Solid Electrolyte Reactor. *Nat. Catal.* **2022**, *5* (4), 288–299.

(57) Ozden, A.; García de Arquer, F. P.; Huang, J. E.; Wicks, J.; Sisler, J.; Miao, R. K.; O'Brien, C. P.; Lee, G.; Wang, X.; Ip, A. H.; Sargent, E. H.; Sinton, D. Carbon-Efficient Carbon Dioxide Electrolysers. *Nat. Sustain.* **2022**, *5* (7), 563–573.

(58) Qiao, Y.; Lai, W.; Huang, K.; Yu, T.; Wang, Q.; Gao, L.; Yang, Z.; Ma, Z.; Sun, T.; Liu, M.; Lian, C.; Huang, H. Engineering the Local Microenvironment over Bi Nanosheets for Highly Selective Electrocatalytic Conversion of CO 2 to HCOOH in Strong Acid. *ACS Catal.* **2022**, *12* (4), 2357–2364.

(59) Fan, L.; Xia, C.; Zhu, P.; Lu, Y.; Wang, H. Electrochemical CO2 Reduction to High-Concentration Pure Formic Acid Solutions in an All-Solid-State Reactor. *Nat. Commun.* **2020**, *11* (1), 3633.

(60) Miao, R. K.; Xu, Y.; Ozden, A.; Robb, A.; O'Brien, C. P.; Gabardo, C. M.; Lee, G.; Edwards, J. P.; Huang, J. E.; Fan, M.; Wang, X.; Liu, S.; Yan, Y.; Sargent, E. H.; Sinton, D. Electroosmotic Flow Steers Neutral Products and Enables Concentrated Ethanol Electroproduction from CO2. *Joule* **2021**, *5* (10), 2742–2753.

(61) Iddya, A.; Zarzycki, P.; Kingsbury, R.; Khor, C. M.; Ma, S.; Wang, J.; Wheeldon, I.; Ren, Z. J.; Hoek, E. M. V.; Jassby, D. A Reverse-Selective Ion Exchange Membrane for the Selective Transport of Phosphates via an Outer-Sphere Complexation–Diffusion Pathway. *Nat. Nanotechnol.* **2022**, *17* (11), 1222–1228.

(62) Chen, Y.; Wrubel, J. A.; Klein, W. E.; Kabir, S.; Smith, W. A.; Neyerlin, K. C.; Deutsch, T. G. High-Performance Bipolar Membrane Development for Improved Water Dissociation. *ACS Appl. Polym. Mater.* **2020**, *2* (11), 4559–4569.

(63) Xie, Z.; Su, Q.; Shi, A.; Yang, B.; Liu, B.; Chen, J.; Zhou, X.; Cai, D.; Yang, L. High Performance of Zinc-Ferrum Redox Flow Battery with Ac−/HAc Buffer Solution. *J. Energy Chem.* **2016**, *25* (3), 495–499.

(64) McCulloch, W. D.; Yu, M.; Wu, Y. PH-Tuning a Solar Redox Flow Battery for Integrated Energy Conversion and Storage. *ACS Energy Lett.* **2016**, *1* (3), 578–582.

(65) Liu, B.; Tang, C. W.; Jiang, H.; Jia, G.; Zhao, T. Carboxyl-Functionalized TEMPO Catholyte Enabling High-Cycling-Stability and High-Energy-Density Aqueous Organic Redox Flow Batteries. *ACS Sustain. Chem. Eng.* **2021**, *9* (18), 6258–6265.

Acknowledgments

It's hard to believe that I'm actually coming to the end of my PhD. There was a time when it felt like this would go on forever, in a good way. The whole experience was at times exciting, and oftentimes trying, but ultimately rewarding. I owe thanks to the many people who have supported me along the way, and I think this section is the most important piece of writing I will have done in these five years.

I want to start off by offering my utmost gratitude to my academic advisor, Prof Yogesh Surendranath. Yogi has been the most fantastic advisor to work with, and if I had to summarize what I learnt from Yogi in the past five years, I'd say this: he taught me how to be more thoughtful about my science. In my five years in the group, across the many projects I've worked on, Yogi has consistently engaged deeply with my science, questioning my assumptions and providing helpful suggestions. He was always very generous with his time and wisdom, being willing to entertain my questions and proposals for new research directions. The incredible thing about Yogi is that you can ask him what he thinks about a given scientific problem at any time during the day and he'll be happy to give you the time of day and ponder deeply on it right away (sometimes at the expense of his punctuality at meetings). I think this is the hallmark of a great academic, and I'm thankful that (I think) some of his intellectual curiosity and academic rigor has rubbed off on me. I believe that my ability to pick good research problems, approach an unfamiliar research project, and to write effective scientific papers benefited greatly under Yogi's meticulous tutelage. I could not have asked for a more holistic scientific training, and for that I'm immensely grateful to Yogi. I wish you, Athma, and the Anu-man well from the bottom of my heart.

I would like to extend my gratitude to the members of my thesis committee as well. Prof Mircea Dincă (thesis chair), Prof Yuriy Román, and Prof Karthish Manthiram (formerly) – thank you all for taking the time to engage with my research, providing an external perspective to my projects, and making sure I'm on the right trajectory during our meetings and my oral exams.

I am also grateful to the entirety of the inorganic division of the Department of Chemistry. Prof Alex Radosevich, Prof Kit Cummins, and Prof Dan Suess among many others – thank you for the enriching classes that you all so passionately taught, and for the critical but constructive feedback that you provided during my 3rd year oral exam.

It would be remiss of me to not acknowledge the many mentor figures I'd had before starting my PhD. Prof Jia Min Chin (now at University of Vienna), Prof Yin Thai Chan (NUS), Prof Joel Yang (SUTD), Prof Kazunari Akiyoshi and Dr Tomoki Nishimura (Kyoto), Dr Andy Ashley and (now) Dr Adam Piascik (Imperial), Dr Yugen Zhang and Dr Jinquan Wang (A*STAR) – your patient and meticulous guidance was formative in shaping me into the scientist I am today. Thank you all for seeing the potential in me and preparing me to take on this PhD journey.

In my many years here, I count myself very fortunate to have had the opportunity to interact with some of the most brilliant and lovely people I know. These include collaborators both from within the lab and other labs, members of the lab in general, and the many capable students I have had the chance to mentor. Through our many conversations, they have challenged and enriched my perspectives, not just in science, but on a broad spectrum of topics.

During these five years, through the auspices of a number of collaborative research grants, I got the chance to know and work closely with folks from all over the country. Through our Department of Energy grant on carbonate management for CO_2 electrolysis, I worked with Prof Matt Kanan, Prof Ali Mani, Prof Dan Nocera, and Prof Yuriy Román, among others. Through the Center for Interfacial Ionics (CI^2), I had the good fortune to meet Prof Shannon Boettcher, Prof Shane Ardo, Prof Nien-Hui Ge; Prof Niya Sa, and Prof Yixian Wang, among others. Interacting with these amazing professors has truly broadened my scientific horizons. I'm also grateful to their many incredible team members for the collaborative work we did together. Sadly, there are too many folks to call out by name, but I'd like to give a big shout-out to Raj Balaji (Mani); Josh Rabinowitz, Dr Rishi Agarwal, Yuxuan Chen, and Ben Charnay (Kanan); Dr Suyong Han (Román); and Dr Zhifei Yan (Nocera), with whom I had an opportunity to interact extensively. Special shout-out to Dr Rain Mariano, a former Kanan Lab member who helped me out a lot when he was a postdoc here at MIT. I really enjoyed working with each and every one of you and you have all taught me so much in our meetings together. I wish you all the very best!

My collaborators in the group have been a huge contributor to my success in my PhD. Team BPM consisted of myself, An, Hieu, Ethan, Ryan, Daniel and Jaeyune. The efforts of every single one of you led to our group's now sizable body of cutting-edge work on a topic we barely even understood just three years ago. I would like to thank An and Hieu for their tireless efforts helping to collect insightful electrochemical data; Ethan for his help and advice with tricky novel polyelectrolyte syntheses; Ryan for his suggestions and advice on electrolyzer setups; Daniel for his help with cell design and a hairbrained DEMS experiment; and Jae for contributing to the original proposal, building a foundation for this work. Our Carbon Mineralization efforts started with Kunal and I crafting a proposal together with Yogi, and later expanded, inducting Tolik into the in situ mineralization thrust, while An, Ethan and I, along with folks from the Kanan Lab, focused on an ex situ thrust. Whether it was on the in situ or ex situ front, it was so exciting working towards a (possibly) commercial solution for CO_2 capture and storage. More so, it was gratifying to see the strength of each team member come through, whether it was formulating hypotheses and building a mechanistic picture for natural weathering processes, or screening and optimizing candidate electrode materials and electrolytes to build a salt-splitting device with. Without all of your help, we would not have been able to do all this beautiful work today. I am grateful to have been able to work in such brilliant and creative teams.

Lab life has been a dominant and integral part of my PhD journey, and I couldn't be more thankful to the people who contributed to creating the conducive and cordial environment I was so lucky to have while working in lab. Starting with our illustrious alumni, I would like to thank former postdocs Marcel, Patrick, Mike, Daniel, and Ryan; former graduate students Megan, Bing, Seokjoon, Jeff, Soyoung, Corey, Jaeyune, Jo, Travis, Andrew, Will, Onyu, and Thejas; our visiting student, Simon; and our former undergraduates, Sasha and Hieu. In particular, I'd like to give a shout-out to Mike, for his patient mentorship in my first two years; Ryan, for never hesitating to offer help, and being a perennial source of positivity in lab; Bing, for her help and advice on my first project on ion intercalation oxides; Soyoung, for being a friendly face who helped me adjust to working in the group when I'd just started out (thanks for inviting us to your wedding! Congrats on your new life with Harry and baby Samuel!); Corey, for inspiring us with her can-do attitude, for her advice on synthetic preps, and for our nerdy exchanges about musicals in lab (I'm glad you graduated! Now I hope I graduate!); Jae, for his wisdom on the structure of the electrified interface, and for the company on those late nights in my third and fourth year; and Thejas, for his cheeky sense of humor, and for our many conversations about the state of labor in the US and beyond. I have enjoyed being in the lab with all of you, and I can confidently say that each and every one of you taught me something in your time here. Although you may have left, you have all left an indelible mark on the lab, and I believe you have all changed me and the lab for the better. I hope you are all doing well in your new lives!

Needless to say, the current members in the group have played a huge part in defining my experience in the lab. My fellow fifth years/Brillouin zoners, in particular, have weathered the past five years with me and I think this experience has created a lasting friendship between us.

An, your unwavering work ethic, your technical competence with instruments and ability to rig makeshift experimental setups together, and your oratorical skills have always impressed me. Our collaborations have certainly benefited from them. Thank you for teaching me about your *bun* scale for rating Vietnamese restaurants, and what you call 'clean' and 'dirty' EDM (though I've forgotten the distinction). All the best for your new life in Livermore, California (may your catalytic converter not get stolen)!

Noah, ~~we will always blame your 2nd year orals practice talk for starting the pandemic~~ I will miss our goofing around in lab, where it was always raining men, as well as the many cultural exchanges we had. If we were to meet for a picnic in the future and I bring kopi luwak, will you bring matzo balls, or just a very big tub of pasta? Jokes aside, I wish you and Yonina all the best in your new life together.

Bryan, it was a breath of fresh air to meet someone else who also spoke Commonwealth English – frankly, there are too many missing u's, and it's aluminium, not aluminum! While our shared sense of humour (see what I did there) has revealed how regressed our mental ages are relative to our physical ones, I'd like to think that my scientific critical thinking has been honed through our many discussions and thought experiments. All the best for your postdoc at Harvard – gassy bubbly water don't make itself!

I will also miss the company of our incredibly talented and capable younger students, whose explosive growth I've been fortunate enough to witness. Alright, here goes! Sophia, your organization and strong work ethic impresses me, and has really helped support the operation of our lab. I like to think we were trauma-bonded through our shared fear of ion contamination. I will miss your sarcastic wit and our jogs together. Deiaa – *so, what time?* Thanks for being my reliable gym buddy. I will never forget the time we spent together in the gym. You showed me the way of the Sigma Grindset, but I'm still not sure whether my heels should be on the ground or in the sky. In lab, your passion for science inspires me! I enjoyed the candor of our conversations and constantly learning something new about Egyptian culture from you. I wish you and Mariam happiness! Kunal, it's hard to believe you're starting your fourth year soon. You've become a true leader in lab, leading not only our LSC efforts but also our volleyball team. You are truly wise beyond your years and have an infectious energy that uplifts everyone. Thanks for always offering to give us a ride. Let's go! Vennela, you've been an awesome nook buddy (or nuddy) for the past two years. I will miss our silly conversations and unnecessarily highly coordinated bamboo watering sessions. I hope my humble words of wisdom (as well as Deiaa's), which I leave as a parting gift, can be a compass for your own life (or at least the remainder of your PhD). Always remember: Systematize the Science (JT, c. Feb 2023)! Monetize the Model (DMH, c. Mar 2023)! Formalize the Friendship (JT, c. Jun 2023)! Karl, my man, it was motivational to watch you hustle so hard in your first two years, both in lab and on the volleyball court. I'm sure your hard work and dedication will pay off soon! ~~Big T~~ Tolik, thanks for taking a bet on our group and stepping up to lead the rock project. You've made such incredible strides so far and really broadened our understanding of carbon mineralization mechanisms. Also, thank you for stepping up to become safety officer. You've done such a great job on both fronts so far and I know it's only going to get better, king. India, thanks for being my life mentor – the *growth mindset* you imparted to me shall stick with me for life (or at least until I forget). Good luck with your molten amides! Joel, thanks for taking over the interfacial ion transfer project. I will miss the goofy times we had at the CI^2 retreat at Endicott House (but, alas, not the many bug bites I was afflicted with). I wish we had more time to work together and goof around, but I know you will carry this project to greater heights. Your voracious appetite for books has also inspired me to read more! Hye Won, I love your work hard, play hard approach, and I'll miss our conversations on Korean culture and gossiping about the Korean students. Don't hang around in lab too late chatting with HX!

Our postdocs have been phenomenal too, and I'm grateful for the many fruitful exchanges I've had with you all. Ethan, the best polymer chemist from Canada, you somehow always have a way of making me laugh, just by the way you deliver lines. I had fun working with you on our collaborative projects. Can't believe I know one of the top 300 Pokémon™ GO players in the world. Best wishes to you and Jenny! HX, I enjoyed chatting with you about all kinds of science, and learning about Chinese memes. ~~Even~~ Especially on those weekends when we were the only ones around. 666! Max, you're probably the only other person who enjoys the durian candies in lab. I'll miss our jogs and jolly conversations together. Congratulations to you and Huiying on your impending miracle! Don't get too Schmidt-faced! Neil, I will never not be impressed by how good you are at math. Congrats on getting that job – I know you'll do great! Rui, your unwavering dedication to your projects is incredible. I'm looking forward to the exciting work you'll publish! Anton, you're probably the most brilliant EPR spectroscopist I know. Good luck with your MNC project! Jon, our overlap was short but I enjoyed learning about your work on clusters from UW and am so excited to see what you'll come up with in our lab.

The undergraduate and Master's students whom I've had the pleasure to work with were also a big part of my PhD experience. Hieu, your curiosity and drive to answer the questions in your project were truly remarkable. You were able to grasp concepts in the BPM project space so well when so few could, and I enjoyed our many late-night discussions on what we thought was going on inside the BPM. Your hard work and dedication contributed greatly to our success in the BPM space, and An and I enjoyed 'co-parenting' you very much. I will miss your inquisitiveness and candor, and working in lab with you while Dragostea Din Tei or "chemistry laboratory music" is playing in the background. Good luck with your PhD at Harvard! Andy, you amazed me with how quickly you picked up electrochemistry concepts as a freshman. I'm so proud of how you took intellectual ownership of your project over the course of the past year, and started asking questions and suggesting experiments I'd not thought of before. You've really come into your own as a scientist. I will miss your carefree youthfulness, and working in lab with you while Pokémon™ battle music or the OST of La La Land is playing in the background. I hope you figure out what you want to do after you graduate! Simon, despite only being with us for a short span of six months as a visiting Master's student, you took on a project that was only starting to take shape, and were able to make so much progress. Your tenacity paid off and taught us so much about the fundamental kinetics of ion transfer at solid-liquid interfaces. I will miss your upbeat attitude and good-tempered nature. Good luck with your internship in Zürich, and I hope I'll get to see you when I visit Vienna/Europe sometime!

I will miss each and every one of you in the Yogi Lab. Thank you all for galvanizing me to reach my full potential (see what I did there?). You're all gonna do such awesome work individually and together, and I can't wait to read all about it in the future.

Some of these brilliant labmates have also turned out to be awesome roommates. An, our long chats on life and the commonalities and contrasts in what we each want out of it have shaped my perspectives in helpful ways and I will miss them. Bryan, I will miss our morning and evening conversations in the kitchen, both the intellectual, and the incredibly unintellectual. As to my non-coworker roommates – Donavan, it was great having another Singaporean in the house to chat about contemporary Singaporean affairs and complain about America with. The food and public transport abit jialat ah. Peter, we were only roommates for a year but I enjoyed our jogs together and gossiping about An's love life with you. Thank you all for being fantastic roommates and for sticking it out with me. Good luck with the next phase of your lives!

A lot of the work we did in the Yogi Lab would not have been possible without the incredible support staff around us. I want to thank Joanne Baldini for always being a champ and so on top of things like organizing retreats and reimbursements; Brian Pretti for your help with lab renovations and repairs over the years; Ed Mitchell for always entertaining my (sometimes) impossible glassblowing requests (case-in-point: that ITIES cell) and for always having time for a friendly chat whenever you drop by; Sibora Cjapi and Chris Kriofske for keeping our lab on the good side of financial auditors; Gang Liu for your technical wizardry, having resuscitated innumerable pieces of equipment in our lab; Scott Ide, Steve Monstur and Rick Kayser for all your safety advice and help with waste management over the years; Tim McClure for your help with the ICP-OES in DMSE; Kurt Broderick, Gary Riggott and Jim Daley for your help and advice with instruments in MIT.nano. Your combined efforts kept our work going without hiccup and allowed us to keep our focus on doing the best science that we could.

The solidarity and camaraderie I shared with my classmates helped propel me through these trying years. First off, to the other Inorganic students outside of my group: Griff, Trever, Ruomeng, Soohyun, Will and Roger – I learnt from each and every one of you in the classes we took together, and have been so inspired by the diverse paths you have taken. Jet, Jinyi, Alex, and Maria – you were the best fellow 5.310 TAs I could ask for for the gruelling task we had. Hopefully we never have to collect water samples from the Charles River ever again! Gil, it was always great hanging out with you back at Sid-Pac, on the fourth floor of building 18, and in movie theaters. Jinyi, Xiyun, Xin, Qilin, Chuchu and Yongli – I will miss the times we hung out at hotpot and making dumplings over the new year. When's our cross-cutting Chinese startup gonna happen? I hope we can all stay in touch, and I can't wait to see what you guys are gonna accomplish in the future.

The Singaporeans whom I go way back with and who started their PhDs at around the same time as me under the auspices of the A*STAR fellowship were also an important source of strength for me in these five years. Daniel, Boon Siong, Jerald, Kang Yong, Matthew, Qingyun, Wearn Xin, Quyen, Erin, Sheryl… there are so many of you, and I'm thankful I could tap on this support network whenever I needed to. I'm so glad to known most of you for most of the past decade! We even embarrassed ourselves on national television together! *Creating Growth, Enhancing Lives* – can we do it? I look forward to seeing you guys back in the motherland in the not-so-distant future to do great science together!

I can't forget to give a shout-out to my Saturday night Zoom buddies, who started pursuing professional degrees around the same time as I did. Alex (and Ella), congratulations on your PhD from Northwestern! Jerry, congratulations on your MD from USyd! I'm finally gonna join the crew and be a Dr. too! Our Zoom sessions kind of evolved into pseudo-therapy sessions when we would vent our frustrations freely, and they were a really important source of support for me, especially during lockdown days. Can't believe it's been seven years since we first met in Kyoto. Amgen really got a bumper crop with us huh. I wish you guys all the best. Can't wait to see you guys again!

I'm also thankful to the community of friends I'd made in Boston outside of MIT. Frank, Allison, and Theresa (and Riley!), I really enjoyed our annual berry/apple picking trips in the summer/fall, and making fun of Allison together (sorry!). Amelia, it was awesome going to see all those musicals and occasionally films together. Yes, even Spongebob the Musical. How much money have we collectively spent on Playbills?! Good luck with completing your PhD! Kazumi-san, I will miss our lunch conversations about startup culture and salaryman life in Japan. Hope you're doing well at Eisai HQ in Tokyo! Faith, thanks for the solidarity in the last stretch of my PhD, and for bursting my bubble and reminding me that corporate life is not all glamor. I'm keeping my fingers crossed that you make the transition to a job that you'd enjoy more! Thank you all for helping to keep me sane and taking me out of my ivory tower. Let's hang out again sometime.

Last but not least, my family and friends back home in Singapore played a huge part in getting me where I am today. To my mom and dad, my sister Winnie and my brother Wei Li – your unconditional love and support for me kept me going all these years (even though we were at each other's necks during the quarantine at the start of the pandemic). To my childhood friends whom I've known more than half my life: Yi Wei, Shao Huan, Jason x 2, and Shalyn – it's always comforting and exciting whenever we hang out and you catch me up on how you're doing or we while the time away on board games or long walks. I feel like I can always be myself around you guys. We're getting old now huh (nervous laughter). To my friends from secondary school: Cindy, Jun Wei, Jason, and Kai Ting – I can always count on you guys to look for good food or fun things to do back home. Yes, especially you, Jun Wei. And no, Cindy, my Mandarin's still pretty good. To my friends from college who rode the struggle bus with me: Wan Qing, Kian Chong, Shijia, and Teresa – we ended up picking such different paths despite graduating with the same degree, so I always enjoy hearing about the stories from your personal and work lives. So who's getting married next? There're so many others whose friendship I'm thankful for but I won't be able to name them all. Thank you all for having been a constant in my life for a huge part of it. Whenever I come home and meet with any of you, it often feels like I'd never left. I've finally made it!

Thank you all for having been an irreplaceable part of my PhD journey. I wish you all the very best from the bottom of my heart and hope we will have a chance to meet and laugh about all this again in the future.

Wei Lun "James" Toh

Cambridge, MA

August 31, 2023